

NOAA Technical Memorandum OAR ARL-266

doi:10.7289/V5/TM-OAR-ARL-266



**WIND MEASUREMENT FROM AIRCRAFT, 1993
ANNOTATED AND UPDATED, 2013**

J.A. Leise ¹

J. Masters ²

Aircraft Operations Center, NOAA/OMAO
McDill Air Force Base, Tampa, Florida

R. Dobosy, Annotator

Atmospheric Turbulence and Diffusion Division, NOAA/OAR/ARL
and Oak Ridge Associated Universities (ORAU)
Oak Ridge, Tennessee

¹ *Deceased*

² *Current affiliation: Weather Underground, LLC*

Air Resources Laboratory
Atmospheric Turbulence and Diffusion Division
Oak Ridge, Tennessee
August 2013

noaa

NATIONAL OCEANIC AND
ATMOSPHERIC ADMINISTRATION

Office of Oceanic and
Atmospheric Research

NOAA Technical Memorandum OAR ARL-266

doi:10.7289/V5/TM-OAR-ARL-266

WIND MEASURE FROM AIRCRAFT, 1993 ANNOTATED AND UPDATED, 2013

J.A. Leise ¹

J. Masters ²

Aircraft Operations Center, NOAA/OMAO
McDill Air Force Base, Tampa, Florida

R. Dobosy , Annotator

¹ *Deceased*

² *Current affiliation: Weather Underground, LLC*

Air Resources Laboratory
Atmospheric Turbulence and Diffusion Division
Oak Ridge, Tennessee
August 2013



**UNITED STATES
DEPARTMENT OF COMMERCE**
Penny S. Pritzker
Secretary

NATIONAL OCEANIC AND
ATMOSPHERIC ADMINISTRATION
Dr. Kathryn D. Sullivan (Acting)
Under Secretary for Oceans
And Atmosphere/Administrator

Office of Oceanic and
Atmospheric Research
Dr. Robert Detrick
Assistant Administrator

Notice

This document was prepared as an account of work sponsored by an agency of the United States Government. The views and opinions of the authors expressed herein do not necessarily state or reflect those of the United States Government. Neither the United States Government, nor any of their employees, makes any warranty, express or implied, or assumes any legal liability or responsibility for the accuracy, completeness, or usefulness of any information, product, or process disclosed, or represents that its use would not infringe privately owned rights. Mention of a commercial company or product does not constitute an endorsement by NOAA/OAR. Use of information from this publication concerning proprietary products or the tests of such products for publicity or advertising purposes is not authorized.

Contents

Abstract	vii
List of figures	viii
List of tables	x
List of acronyms	xi
I Annotations	1
1 Annotations to Chapter 2 and following chapters	2
1.1 Introduction	2
1.2 Aircraft kinematics and the wind equation	3
1.2.1 Geocentric Coordinate System (ECEF)	4
1.2.2 Global Geodetic Coordinates (GGC)	5
1.2.3 Local Geodetic Coordinates (LGC)	6
1.2.4 Local Astronomic Coordinates	11
1.2.5 Aircraft's (Probe's) Coordinates (PBC)	11
1.2.6 Reference Frames	11
1.2.7 Reference frames and wind measured from aircraft . . .	13
1.2.8 Lagrangian approach of Leise and Masters	14
1.3 Geometry of relative-wind computation	17
1.4 Basic atmospheric thermodynamics	17
1.4.1 Theory of dew point and vapor pressure	19
1.5 Theory of true-airspeed measurement	24
1.6 Theory of flow-angle measurement	27
1.7 Some calibration practices	27

1.7.1	Temperature recovery factor	28
1.7.2	Ambient pressure measurement	28
1.7.3	True airspeed computation	29
1.7.4	Dew point and vapor pressure	29
1.7.5	Offsets: Links to ground measurements	30
1.8	Calibration of flow angles	30
1.9	In-flight examples	31
1.10	Adiabatic and hydrostatic approximation	32
1.11	P-3 data acquisition	32
1.12	Corrections with filters	33
1.13	Horizontal wind computation	33
1.14	Vertical wind computation	33
1.15	Flow distortion and phase	34
1.16	Conclusions and Recommendations	34
1.17	Appendices	35
1.A	P-3 Instrumentation	35
1.B	Incompressible flow past a sphere	35
1.C	Digital filters and symmetry	35
1.D	Sampling and interpolation	35
1.E	Enhanced triangle filters	35
1.F	A mirror-image filter algorithm	36
1.G	Filtered interpolation	36
1.H	Statistical editing	36
	Annotator's Acknowledgements	36
	Annotations' References	37
II	Leise and Masters 1993	42
2	Aircraft kinematics and the wind equation	43
3	Geometry of relative-wind computation	52
4	Basic atmospheric thermodynamics	58
5	Theory of true-airspeed measurement	64

6	Theory of flow-angle measurement	69
7	Some calibration practices	79
8	Calibration of flow angles	86
9	In-flight examples	93
10	Adiabatic and hydrostatic approximation	107
11	P-3 data acquisition	114
12	Corrections with filters	123
13	Horizontal wind computation	130
14	Vertical wind computation	136
15	Flow distortion and phase	144
16	Conclusions and Recommendations	150
	Original Acknowledgements	152
III	Appendices	153
A	P-3 Instrumentation	154
B	Incompressible flow past a sphere	155
C	Digital filters and symmetry	158
D	Sampling and interpolation	165
E	Enhanced triangle filters	174
F	A mirror-image filter algorithm	178
G	Filtered interpolation	186

H Statistical editing	198
Original references	206
I Papers citing Leise and Masters before 2013	208

Abstract

James Leise of NOAA's Aircraft Operations Center (AOC) devoted many years to fundamental analysis and development of wind measurement from aircraft. When he died in 1990 shortly before completing this thorough documentation of his work, Jeffrey Masters, who had worked with him completed the manuscript. Since some of the work was experimental and departed significantly from operational practice at AOC, they decided not to publish the manuscript.

The strong theoretical footing and thorough nature of the work, however, nurtured the development of wind measurement from small aircraft, beginning in the late 1980s. Much of the document remains relevant still, and publications in significant and still-growing numbers have cited this manuscript despite its remaining unpublished (see Appendix I). The recent appearance of several publications citing the work motivated NOAA's Air Resources Laboratory (ARL) to publish the 1993 original verbatim, adding a chapter of annotations to update the original where appropriate.

Topics covered include geodetic and aircraft coordinate systems, relation between airflow measured from an airplane and wind experienced on the ground, relevant thermodynamics, three-component airflow measurements at high speed by pressure sphere, calibration practices, data acquisition, data processing, and quality control. The primary lasting value of this work lies in the background understanding of procedures provided by its theoretical depth, which is impossible to reach in journal publications except by reference to work such as this.

List of Figures

1.1	Aircraft coordinates, earth-science convention	8
2.1	Aircraft coordinates, aeronautical engineering convention . . .	44
2.2	Coordinate transformation, aircraft to earth, FORTRAN listing	46
2.3	Lagrangian position of air parcel in aircraft coordinates	48
2.4	Computing rotational velocities, FORTRAN listing	51
3.1	Aircraft coordinate axes and angles of attack and sideslip . . .	52
3.2	Aircraft angles of heading and sideslip; and drift and track . .	53
6.1	Geometry of flow-angle measurement	72
9.1	P-3 calibration-flight plots	94
9.2	Radar altitude vs. relative humidity	96
9.3	Vertical wind and true airspeed, time series	100
9.4	Yaw maneuver, drift angle and slip angle	102
9.5	Diagnosis of error in reported wind	104
9.6	Checking angles of attack and sideslip	105
10.1	Checking reported ambient-temperature	108
10.2	Wingtip corrections for reported dynamic pressure	110
11.1	Frequency response of Butterworth prefilter	116
11.2	Frequency response, triangle filter vs block average	119
11.3	Frequency response, anti-alias filter vs simpler candidates . . .	121
11.4	Coherence between pairs of sensors with and without anti-alias filter	122
12.1	Effect of one-sided (predictive) filters vs filters symmetrical in time	125

13.1	INS position error	131
14.1	Vertical velocity, time series	136
14.2	Vertical velocity, flow chart for computation	137
14.3	Radar altitude on polar ice cap, time series	138
14.4	Filter response computing vertical velocity of aircraft	139
14.5	Vertical wind using different filter lengths	140
14.6	Vertical wind error possibly due to phase lag	141
14.7	Phase lag between relative wind and aircraft motion in vertical	143
15.1	Mismatch in uncalibrated ambient pressure sensors, wingtip and fuselage	145
15.2	Static and dynamic pressure comparison, fuselage with wingtip in hurricane	146
15.3	Dynamic pressure comparison, fuselage with wingtip in yaw maneuver	147
15.4	Coherence of pairs of dynamic pressure measurements from different places	148
16.1	Oscillation in bank angle	151
A.1	Location of P-3 instruments	154
D.1	Response Curves Bessel interpolation filters	169
F.1	Cubic mirror-image filter, FORTRAN listing	181
G.1	TREND algorithm, flow chart	191
G.2	TREND algorithm, FORTRAN listing	193
G.3	Filtered interpolation, FORTRAN listing	195
G.4	Latitude discrepancy LORAN-C vs INS	197
H.1	Statistical editing, two parameters, flow chart	199
H.2	Updating procedure, statistical editing	200
H.3	Pitch angles compared, two independent INS	203
H.4	Statistical editing, two parameters, FORTRAN listing	204

List of Tables

1.1	Editorial Comments, Chapter 4	18
9.1	Computed calibration coefficients P-3, 1987	98
9.2	Computed calibration coefficients P-3, 1989	98
9.3	Wet calibration model	99
9.4	Selected calibration results	99
9.5	Analysis of attack-angle offset parameter 1987	101
9.6	Analysis of attack-angle offset parameter 1989	101
9.7	Noisy slip-angle offset parameter	103
D.1	Coefficients for Bessel's midpoint interpolation	167
G.1	Filter characteristics	189
H.1	Total points edited, 1989 calibration flight	201
H.2	Percentage of points removed	201
H.3	Editing by 10-min intervals	202

List of acronyms

AOC	Aircraft Operations Center, OMAO, NOAA, McDill Air Force Base, Tampa, Florida, USA
ARL	Air Resources Laboratory, OAR, NOAA, College Park, Maryland
ATDD	Atmospheric Turbulence and Diffusion Division, ARL, OAR, NOAA, Oak Ridge, Tennessee
BAT	Best Airborne Turbulence probe, developed by ARL and Airborne Research Australia (Crawford and Dobosy, 1997)
CW	Continuous Wave (LIDAR, RADAR), radiating continuously rather than in pulses
ECEF	Earth-Centered Earth-Fixed (Geocentric) coordinates, Section 1.2.1
FRD	Field Research Division, ARL, OAR, NOAA, Idaho Falls, Idaho
FFT	Fast Fourier Transform
GGC	Global Geodetic Coordinates, Section 1.2.2
GPS	Global Positioning System
GPS/INS	Inertial Navigation system guided by the Global Positioning System
IERS	International Earth Rotation Service
INS	Inertial Navigation System
LGC	Local Geodetic Coordinates, Section 1.2.3
L&M	Leise and Masters, referring to the original manuscript in Parts II and III

Continued on next page

List of Acronyms, continued from last page

LIDAR	LIght (usually LASER) Detection And Ranging, analogous to RADAR, but using light rather than microwaves
LORAN	Long-Range Navigation
N42RF	Registration number for one of NOAA's P-3 aircraft. N43RF is the other P-3
NAERS	Network of Airborne Environmental Research Scientists
NASA	US National Aeronautics and Space Administration
NCAR	National Center for Atmospheric Research, US National Science Foundation, Boulder, Colorado
NOAA	National Oceanic and Atmospheric Administration, US Department of Commerce
OAR	Office of Oceanic and Atmospheric Research, NOAA
OMAO	Office of Marine and Aviation Operations, NOAA
P-3	P-3 Orion, Lockheed Martin maritime patrol aircraft, four turboprop engines, wingspan 30 m, weight 50 Tonnes, maximum endurance 16 hr
PBC	Probe's (aircraft's) coordinates, Section 1.2.5
SA	(Australian State of) South Australia
SNR	Signal-to-Noise Ratio
UAV	Unmanned Aerial Vehicle
WGS	World Geodetic System

Part I
Annotations

Chapter 1

Annotations to Chapter 2 and following chapters

1.1 Introduction

This volume documents the life work of the late Dr. James A. Leise of the Aircraft Operations Center (AOC) of NOAA. Jim Leise (pronounced like lease) died in August 1990 shortly before completing the work. Jeffrey Masters completed the work in 1993 with support from the AOC, as he notes in his acknowledgements section at the end of the main text. In subsequent review, the AOC determined that the work departed in significant ways from their practices in measuring wind from aircraft. Thus they decided not to publish it as a NOAA Technical Memorandum from their organization.

Meanwhile, NOAA's Air Resources Laboratory (ARL) began developing an airborne capability in the late 1980s to measure boundary-layer turbulence and exchange from small single-engine aircraft having mass considerably less than 1000 kg. This project was inspired and led by the late Dr. Timothy L. Crawford, branch manager at ARL's Atmospheric Turbulence and Diffusion Division (ATDD) in Oak Ridge, Tennessee, and later director of ARL's Field Research Division (FRD) in Idaho Falls, Idaho. Crawford's group, of which Ronald Dobosy was a member, drew heavily on Leise's work with its strong theoretical footing and explicit focus on airborne wind measurement. This group developed the Best Airborne Turbulence (BAT) probe, collaborating on later improvements with Dr. Jörg M. Hacker's group of Flinders University and Airborne Research Australia, Adelaide SA, Australia (Crawford and

Dobosy, 1992, 1997; Hacker and Crawford, 1999).

The BAT probe is now in use by multiple groups worldwide. Parallel efforts of other groups to measure boundary-layer turbulence from small aircraft, with both fixed and rotary wings, have also flourished. The Network of Airborne Environmental Research Scientists (NAERS) was formed by Crawford and Hacker in January 2002. This Leise and Masters work was put on the group's web site and became important source material.

Since the work remained unpublished, however, it was difficult to cite in publications. Nevertheless, Leise's clear physical insight, mathematical rigor, and coverage of a wide range of airborne wind-measurement issues formed such a rich foundation, especially for the BAT probe, that it was difficult to avoid including Leise's work by reference. A number of papers have therefore cited the work. A list of these is provided in Appendix I. Because of the enduring nature of much of Leise's theoretical work and the breadth of his coverage of wind measurement from aircraft, NOAA/ARL has decided to publish the manuscript verbatim as a Technical Memorandum. This first chapter was added to provide updates where later development has superseded or otherwise departed from what is reported in the original manuscript. This chapter also includes a list of references to subsequent work. Section numbers and letters in this chapter correspond to chapters and appendices in the original manuscript in Parts II and III.

Disclaimer: Since much of the work of Leise and Masters in the late 1980s was experimental, specific formulas and procedures in their manuscript do not necessarily represent current or past usage by NOAA/Aircraft Operations Center unless otherwise noted.

1.2 Aircraft kinematics and the wind equation

Chapter 2 derives expressions to determine airflow relative to the earth (*i.e.* wind) from airflow measured relative to a moving vehicle. Leise and Masters (L&M) use an approach which they call Lagrangian to derive the formulations. Their approach is sound, but the argument leading to (2.7) and (2.8) needs some tightening. This is provided in Section 1.2.8. An alternate ap-

proach is sketched in Sections 1.2.6 and 1.2.7 based on reference frames, a natural and general approach to environmental measurements from aircraft.

The two approaches produce an unfortunate nomenclature clash. In Chapter 2 L&M use “frame” to indicate a system of axes, and “coordinates” to mean the ordered triplet of numbers locating a point relative to these axes. This intuitively helpful usage is also found in geodesy (*e.g.*, Soler and Hothem, 1988). On the other hand L&M’s argument requires no distinction between reference frames and axis systems.

In the annotations’ approach, reference frames must be distinct from coordinates. A reference frame is primarily concerned with the perception of an observer. This can be quantified in any number of axis and coordinate systems depending on convenience. The annotations, therefore, prefer the term “reference frame” over “frame.” They sharply distinguish a reference frame from a coordinate system but do not particularly distinguish coordinates from axis systems. Both the annotations and Chapter 2 will be better understood by paying attention to the differing definitions of “frame” and “coordinate” provided in each.

The definitions of the various coordinate systems mentioned by L&M (and sometimes called “frames”) in Chapter 2 are expanded in the annotations to better incorporate GPS and to address a mismatch of units between local and global geodetic coordinates in L&M’s (2.7). For background, see Soler and Hothem (1988) or any basic geodesy text. Section 1.2.8 in this chapter fleshes out the argument linking L&M’s (2.7) and (2.8) and expands somewhat on L&M’s approach.

1.2.1 Geocentric Coordinate System (ECEF)

At the time of L&M’s writing, the Global Positioning System (GPS) was immature. Since then, GPS-based inertial navigation systems (GPS/INS) have become far more effective and less expensive. They are now integral to airborne wind measurement, even from small Unmanned Aerial Vehicles (UAV) weighing less than 100 kg (van den Kroonenberg et al., 2008; Thomas et al., 2012; Reineman et al., 2013). Therefore, the Geocentric or Earth Centered, Earth Fixed coordinate system (ECEF), in which the satellites operate, is conceptually useful. The ECEF is rectangular Cartesian with its origin at the earth’s center of mass (known within a few centimeters). The z_{ec} -axis passes through the Conventional Terrestrial (North) Pole, as defined by the International Earth Rotation Service (IERS). The x_{ec} -axis

is perpendicular to z_{ec} and passes through the IERS-defined zero longitude. The y_{ec} -axis completes a right-hand system. At GPS satellites' distance from earth, the surfaces of constant geopotential (“level” surfaces) are very nearly spherical, centered on the earth’s center of mass.

Wind measurement from aircraft, however, happens on the earth’s surface, still essentially spherical, but not to the required precision. The earth’s true shape is the business of geodesy ($\gamma\epsilon\omega\delta\alpha\iota\sigma\acute{\iota}\alpha$ *geodaisia*: division of earth).

1.2.2 Global Geodetic Coordinates (GGC)

Longitude, Latitude, Height (λ, ϕ, h): The Global Geodetic Coordinate System (GGC) is synonymous with L&M’s **Geographic Coordinate System**. Position is usually converted from ECEF to GGC by GPS/INS before reporting. The coordinate directions are defined relative to a flattened ellipsoid approximating the earth’s shape. The fit may be optimized for the whole earth or some favored part.

The earth’s actual shape is taken to be the level surface of geopotential most closely approximating the mean sea level (and not terrain height). It is technically called the *geoid*, but often simply “mean sea level,” whether over land or sea. Vertical is defined normal to the ellipsoid’s (not the geoid’s) surface. The horizontal coordinates, latitude and longitude, are also defined on the ellipsoid, hence constant in this vertical. Under such definitions GGC are orthogonal in the limit $h \rightarrow 0$.

The geoid model depends on the reference ellipsoid selected. It also changes over time as the earth slowly changes or new information is acquired. The World Geodetic System (WGS) is an international global standard, based on a global reference ellipsoid. Its latest revision, WGS 84, dates from 1984 and was revised in 2004. Since 1987, GPS has used WGS 84 as its standard model for conversion from ECEF to geodetic coordinates.

The height of mean sea level at a given location, called the *geoid height*, may have either sign relative to $h = 0$. The gravity vector is normal to the geoid not strictly “vertical.” The small angle between gravity and vertical defines the shape of the geoid, which is affected by the local distribution of mass due to mountains (on land or under the sea) or nearby density variations in the earth. The actual mean ocean surface departs slightly from mean sea level due to tides, salinity gradients, and atmospheric circulation.

A point’s height h is zero on the ellipsoid and is usefully viewed as the sum of the geoid height and the height above or below the geoid. Usually the

GPS/INS reports only the height relative to the geoid (*i.e.*, to mean sea level). Height defined along the geodetic vertical will differ slightly from height defined parallel to gravity. Likewise the longitude and latitude determined by celestial methods will differ slightly from these geodetic values.

Quantitative application of these geodesic concepts is rendered transparent to the user by modern GPS navigation, but awareness of the assumptions made by the particular system one is using for airborne wind measurement is important to interpretation of the results.

1.2.3 Local Geodetic Coordinates (LGC)

East, North, Up (x, y, z) in atmospheric science. Local geodetic coordinates (LGC) correspond to L&M's **geodetic frame**. Velocity and attitude are usually converted from ECEF to LGC by GPS/INS before reporting. Likewise, conversion of velocity and acceleration from PBC (Section 1.2.5) to “earth coordinates” will always be to LGC. This contrasts with position, which is normally converted to GGC (Section 1.2.2).

Local Geodetic are the coordinates of everyday experience, a rectangular Cartesian system measured in meters. They are tangential and normal to the earth's surface at a particular location \mathbf{p} , given by the GGC's (λ, ϕ, h) . The atmospheric science convention, also used by L&M is, however, not universal. Sometimes (x, y, z) are North, East, and Down or another ordering. L&M advise alertness in reading the literature, configuring a system, or analyzing data.

Important to a simple relation between LGC and GGC is the orthogonality of both. Although GGC are strictly orthogonal only in the limit $h \rightarrow 0$ (Featherstone and Cläßen, 2008), tropospheric values of h are small enough compared to the earth's radius to justify the assumption for ordinary purposes. Navigation solutions by GPS do use the full WGS 84 geoid, but these are transparent to the general user.

Further simplification for ordinary use is possible. The earth's equatorial and polar diameters differ by only 20 *km* (one part in 300). Ordinary conversion of infinitesimal displacements from GGC to LGC can safely assume the earth to be a sphere of radius $r = 6370 \text{ km}$. Furthermore, tropospheric

h/r is smaller yet, allowing to good approximation $r + h \rightarrow r$. Thus

$$\begin{aligned} d\mathbf{x} &= \mathbf{F}(r, \phi) d\boldsymbol{\xi} \\ \begin{pmatrix} dx \\ dy \\ dz \end{pmatrix} &= \begin{pmatrix} r \cos \phi & 0 & 0 \\ 0 & r & 0 \\ 0 & 0 & 1 \end{pmatrix} \begin{pmatrix} d\lambda \\ d\phi \\ dh \end{pmatrix} \end{aligned} \quad (1.2.1)$$

where $d\mathbf{x}$ is in LGC, $d\boldsymbol{\xi}$ is in GGC, and $\mathbf{F}(r, \phi)$ is the spherical approximation to the conversion matrix at latitude ϕ . Because the transformation matrix \mathbf{F} is diagonal, its inverse is simply the same matrix with its diagonal elements inverted.

The convenient diagonal form is the gift of orthogonality of both systems and the locality of LGC. At its unique location $\mathbf{p}(\lambda, \phi, h)$, the LGC can be rotated to align its coordinates (eastward, northward, upward) with those of the GGC. Any basis vector in either system is then parallel to exactly one basis vector in the other system and perpendicular to all other basis vectors (in either system). The same orthogonality properties hold for the reference ellipsoid of the GGC but not the full WGS 84 geoid (mean sea level). That surface is not exactly orthogonal to the geodetic vertical, as noted in Section 1.2.2. For WGS 84, the last row of \mathbf{F} contains a weak but complicated dependency of dz on λ and ϕ in the first and second columns.

Note that \mathbf{F} is a singular matrix at the North and South Poles, where $\cos \phi$ is zero. In operation near a pole this singularity could cause rapid fluctuation of reported λ if the pole is in or near the GPS's region of horizontal uncertainty. This region, however, has a diameter only on the order of 10 m. Furthermore, GPS-native ECEF have no such singularity. It is an artifact of the GGC.

Like the velocity, the attitude of the aircraft, hence the probe, is reported by a GPS/INS in LGC. The sign convention used by L&M appears in Section 1.2.5 and Figure 2-1. Unfortunately, it again differs from that used by flux aircraft in the boundary layer, as is evident in Figure 1.1.

Finite displacement in local geodetic coordinates

The discussion above involves only infinitesimal displacement, including velocity. A finite displacement (path) is an integral of velocity over time. Let $\mathbf{x}_p(t)$ trace the aircraft's track over the earth. The unit vector tangent to

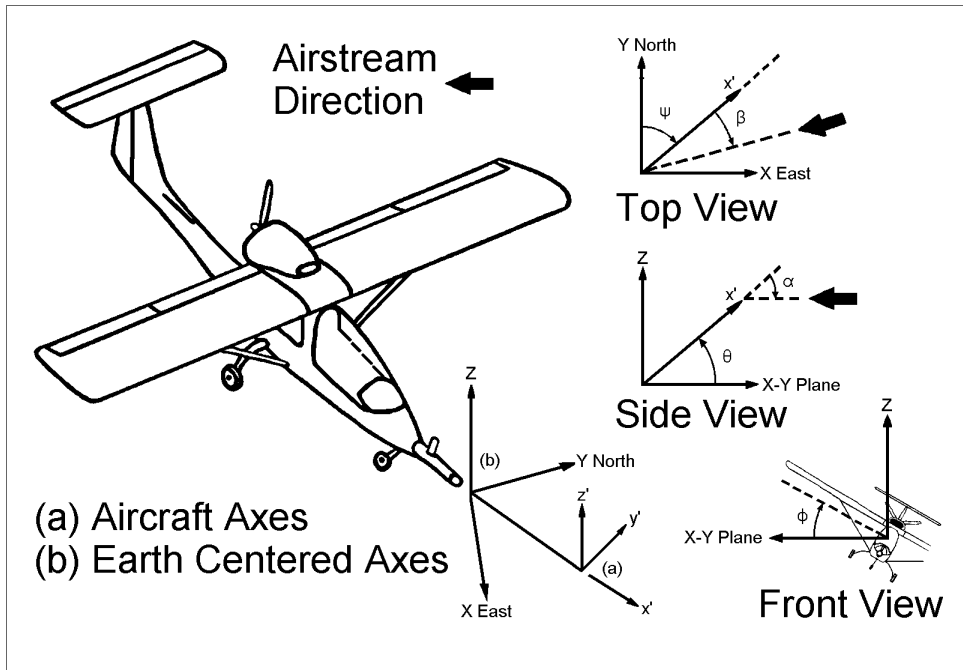


Figure 1.1: Sky-Arrow schematic showing axes of the earth's (LGC) and probe's (PBC) coordinate systems in the earth-science convention. Earth's coordinates (b) are East, North, Up: $(x, y, z) = z_r; r = 1, 2, 3$. PBC(a) are Forward, Lateral (to port), Normal (generally upward): $(\hat{x}, \hat{y}, \hat{z}) = \hat{z}_m; m = 1, 2, 3$. Angles are roll ϕ , pitch θ , and yaw ψ ; attack α and sideslip β . From Hall et al. (2006), see also Vellinga et al. (2013)

this path in LGC is

$$\boldsymbol{\tau} = \frac{d\mathbf{x}_p}{dt} \left(\left| \frac{d\mathbf{x}_p}{dt} \right| \right)^{-1} = \mathbf{u}_p \left(\frac{ds}{dt} \right)^{-1} \quad (1.2.2)$$

and the path is

$$\int_C \boldsymbol{\tau} ds = \int_{t_s}^{t_f} \boldsymbol{\tau} \frac{ds}{dt} dt = \int_{t_s}^{t_f} \mathbf{u}_p dt \quad (1.2.3)$$

Here \mathbf{u}_p is the velocity of the aircraft along the track.

Motion along a finite path implies relocation. Because of gravity, this normally follows the curvature of the earth. It would seem natural, then, to represent \mathbf{u}_p in the curvilinear GGC. By (1.2.1), however, a unit of length in GGC changes with location and direction of travel. Most applications require a uniform length unit. Calculating everything in ECEF would provide this, but at the sacrifice of GGC's simpler mathematical forms [*e.g.*, (1.2.1)].

The long history of navigation gives the resolution. Mariners on sailing vessels took a fix (found their position) at local noon in GGC by clock, horizon, and maximum solar elevation. They also measured their course and speed (relative to the water) in LGC to estimate \mathbf{u}_p in knots. Over the 24 *hr* until the following noon they determined their position by dead reckoning, integrating their velocity using (1.2.3) in rectangular coordinates (LGC) or converting to GGC using (1.2.1) evaluated at their latest fix. With their low speed and high error tolerance they could plot the track on the sea (GGC) within acceptable error until their next fix. Over a voyage of N days, their path over the curved earth in constant units (nautical miles or meters) is the vector sum of N successive segments, each with its own instance of LGC determined by the fix at the start time t_{si} of the each segment:

$$P_{xy}(t) = \sum_{i=1}^N \int_{t_{si}}^{t_{fi}} \mathbf{u}_p dt, \quad (1.2.4a)$$

or in degrees longitude and latitude to plot on a map:

$$P_{\lambda\phi}(t) = \sum_{i=1}^N \int_{t_{si}}^{t_{fi}} \mathbf{F}^{-1}(\phi; h = 0) \mathbf{u}_p dt, \quad (1.2.4b)$$

where \mathbf{F} is defined for most practical purposes by (1.2.1). Note that \mathbf{u}_p in the i^{th} segment is in the LGC of the i^{th} fix.

In real life, of course, these mariners made many refinements to adjust for the long time between fixes, especially when they were near shore. Modern navigation is by brute force. Accurate fixes (samples) come as often as once per second, each new sample a new instance of LGC. Relative to the radius of the earth, this displacement of 100 m or less between fixes is vanishingly small. Because of turbulence, aircraft measuring wind normally then interpolate by dead reckoning to intervals of 10 m, or even 1 m, measuring the aircraft's motion with onboard accelerometers. In mathematical terms, the frequent accurate fixes form a very fine integration mesh giving the integrated path to high accuracy. The curvature of the path over the earth is, in fact, a very slow drift relative to the signal from turbulence. The low error tolerance primarily serves accurate turbulence measurement. Accurate navigation is subsumed.

Acceleration in local geodetic coordinates

High-frequency motions (*e.g.*, vibrations) are best measured as acceleration and integrated. Although the probe is moving over the curved earth during the measured accelerations, the naive integral

$$\mathbf{u}_p = \int_{t_{i-1}}^{t_i} \frac{d\mathbf{u}_p}{dt} dt \quad (1.2.5a)$$

realized as

$$\mathbf{u}_p = \sum_{i=1}^N \mathbf{u}'_p(t) \delta t \quad (1.2.5b)$$

where $\mathbf{u}'_p = d\mathbf{u}_p/dt$, produces the expected velocity. Because \mathbf{u}'_p is in LGC, however, each new fix (GPS report) is a new position. This implies a new set of basis vectors, but no basis vectors appear anywhere in the sum. This may be unsettling, but in fact the velocity and acceleration components here (1.2.5) and in the previous subsection (1.2.4) are those tangential and normal to the earth's surface at each location, much like the surface integrals in the theorems of Gauss and Stokes. A rigorous proof of (1.2.4) and (1.2.5) by simple methods rapidly gets messy. More advanced approaches involving geodesic lines on an ellipsoid (Riemann geometry) are needed. It must suffice here that the expressions' validity is demonstrated by centuries of navigation.

1.2.4 Local Astronomic Coordinates

East, North, Up. These are a right-handed rectangular Cartesian system differing only slightly from the local geodetic coordinates in that the z axis is opposite gravity. They are mentioned only for completeness. If the difference is found to matter, alertness is again appropriate both in the literature and in setting up the navigation solution for the GPS unit being used. The “astronomic” label refers to the sextant and plumb bob (or horizon if at sea) traditionally used to measure position relative to the stars.

1.2.5 Aircraft’s (Probe’s) Coordinates (PBC)

Forward, Port, Up ($\hat{x}, \hat{y}, \hat{z}$): The aircraft’s coordinates PBC form a rectangular Cartesian system fixed to the aircraft and moving with it. L&M follow the aeronautical-engineering convention for the axes: *Forward, Starboard* (pilot’s right), *Down* (see Fig. 2.1 in Chapter 2). Flux aircraft in the boundary layer often use *Forward, Port, Up* (Figure 1.1), analogous to the earth-science convention. L&M use cursive (script) font to represent quantities in PBC. In these annotations they wear hats for want of a suitable cursive font.

1.2.6 Reference Frames

Reference frames are generally associated with Einstein’s Relativity Theory (*e.g.*, Einstein, 1956). They efficiently express the counter-intuitive implications of Michelson’s and Morely’s (Michelson and Morley, 1887) demonstration that the speed of light (in a vacuum) is an absolute constant relative to any observer moving at whatever speed. Reference frames, however, are also useful at low speed (compared to light) to account for the differing perceptions of observers depending on their position and motion. In particular, the reference-frame concept is a natural and intuitive approach to finding wind from aircraft.

A reference frame is defined by a reference object which an associated observer considers fixed (immobile). To an observer on an airplane, the airframe is such an object, here assumed rigid. Anything attached to the airframe, such as a wind sensor, is thus also fixed. Any body such as the earth which moves relative to the airframe is in motion. To an observer on the ground, the earth is a fixed object, and other objects attached to it (such as wind sensors) are thus fixed. Air, being attached neither to the earth nor to the

airframe, is free to move in either reference frame. By Relativity Theory, physical laws valid in one reference frame are valid in all reference frames. Thus one may choose the reference frame most convenient for measurement of a phenomenon and by proper transformation make that information available in the reference frame most convenient for interpretation. The spatial structure of wind and turbulence is often productively measured from aircraft but best interpreted relative to the earth. That is, one seeks to infer wind velocity in the earth's¹ reference frame from measurements made in the aircraft's reference frame.

A reference frame's definitive "fixed object" is its associated native coordinate system, relative to which all objects' positions are defined and tracked in time. Aside from being fixed in the reference frame, the coordinate system can take any convenient form. Importantly, however, an object's position and motion relative to a given reference frame can be described using any coordinate system. That is, transformation of coordinates is a different activity from change in reference frame.

Coordinate transformations are covered in detail in Chapter 2. Change of reference frame for "slow" motion relative to light uses Galilean, as opposed to Lorentz, transformations. As a classic example of Galilean transformation, suppose a mosquito on a train is flying at a constant $\hat{\mathbf{v}}(\text{T}) = 1 \text{ m s}^{-1}$ toward the starboard wall. The argument (T) indicates her location in the train's reference frame. The hat indicates the train's coordinates. The mosquito's motion viewed from the ground outside the train is then her motion relative to the train plus the train's motion relative to the earth.

Suppose the train moves northward at a constant $\mathbf{V}(\text{E}) = 30 \text{ m s}^{-1}$, where the argument (E) and the unadorned symbol indicate, respectively, the earth's reference frame and coordinates. Here the difference between coordinates and reference frames becomes apparent. Adding the two vectors requires their components to be given in a common set of coordinates, say the earth's. Let \mathbf{G} be the transformation matrix from the train's coordinates to the earth's. Then $\mathbf{G}\hat{\mathbf{v}}(\text{T}) = \mathbf{v}(\text{T}) = 1 \text{ m s}^{-1}$ toward *east*. The mosquito is still viewed from onboard the train, but her motion is now tracked in the earth's coordinates. The mosquito's motion $\mathbf{v}(\text{E})$ viewed from the ground

¹Any reference to "earth's reference frame" or the "earth coordinates" fixed in it always means LGC (Section 1.2.3).

outside can now be computed:

$$\begin{aligned}\mathbf{v}(\mathbf{E}) &= \mathbf{v}(\mathbf{T}) + \mathbf{V}(\mathbf{E}) \\ &\cong 30.5 \text{ m s}^{-1} \text{ toward } 002^\circ.\end{aligned}\tag{1.2.6}$$

In this example an idealized train moves at constant speed and direction relative to the earth. A real aircraft's reference frame is in continual acceleration in six degrees of translational and rotational freedom with respect to the earth's reference frame. Reference-frame changes for acceleration are more complex than for the instantaneous velocity given here. The full procedure, relying on high-sample-rate specification of the aircraft's linear and angular velocity vectors, is sketched in the next section.

1.2.7 Reference frames and wind measured from aircraft

Wind sensors such as the Rosemount and BAT probes directly measure the airflow $\hat{\mathbf{v}}_a(P)$ relative to their sensor heads in the probe's PBC reference frame and coordinates.² Likewise, the aircraft's (probe's) instantaneous velocity $\mathbf{U}_p(\mathbf{E})$ in the ECEF reference frame and coordinates can be directly determined by measuring the Doppler shifts in the GPS carrier frequency as the satellites and aircraft move relative to each other. Highly accurate conversion from ECEF to GGC or LGC is transparent with modern GPS, as noted at the end of Section 1.2.2.

Returning to (1.2.6) one can substitute

$$\mathbf{v}_a(\mathbf{E}) = \mathbf{v}_a(\mathbf{P}) + \mathbf{U}_p(\mathbf{E}),\tag{1.2.7}$$

where the reference frame has become the wind probe (P), and the mosquito has become an air parcel $\mathbf{v}_a(\mathbf{P}) = \mathbf{G}(t)\hat{\mathbf{v}}_a(\mathbf{P})$. Transformation $\mathbf{G}(t)$ is now between PBC and LGC. Note that the $\mathbf{v}_a(\mathbf{P})$ remains in the probe's reference frame. All quantities are now understood to be variable in time, but in particular the coordinates LGC are not fixed in the PBC reference frame. This is emphasized by the explicit time argument for $\mathbf{G}(t)$.

²Reference frames will be identified by their native coordinate system. Note from Section 1.2.6, however, that a given quantity need not be expressed in its reference frame's native coordinates, *e.g.*, $\mathbf{v}_a(\mathbf{P})$ of (1.2.7) is in the PBC (probe's) reference frame but the LGC (earth's) coordinates

The probe need not be at the origin of its coordinate system, in which case it's more intuitive use the term "aircraft coordinates." Since an aircraft has three degrees of rotational freedom about its origin (roll, pitch, yaw), the velocity of a probe $\mathbf{U}_p(\mathbf{E}_p)$ displaced $\hat{\mathbf{R}}_p$ from the origin will be the vector sum of the velocity of the origin $\mathbf{U}_p(\mathbf{E}_0)$ and the tangential velocity of rotation $\boldsymbol{\Omega}_p(\mathbf{E}) \times [\mathbf{G}(t)\hat{\mathbf{R}}_p]$ about the origin at $\hat{\mathbf{R}}_p$:

$$\mathbf{U}_p(\mathbf{E}_p) = \mathbf{U}_p(\mathbf{E}_0) + \boldsymbol{\Omega}_p(\mathbf{E}) \times \mathbf{R}_p. \quad (1.2.8)$$

Location $\hat{\mathbf{R}}_p$ is a vector constant because the probe is attached to the aircraft. In earth's coordinates (as \mathbf{R}_p) it retains its length, but its orientation depends on the aircraft's attitude (bank, elevation, and heading).³ Since the aircraft is assumed rigid, the rotation of the airframe, $\boldsymbol{\Omega}_p(\mathbf{E})$, is the same at all points, hence the generic symbol (\mathbf{E}). Substitute (1.2.8) into (1.2.7) to obtain the full expression to compute wind (air motion in the earth's reference frame and coordinates) from measurement of airflow in the aircraft's reference frame and coordinates and measurement of the airplane's own linear and rotational motion.

$$\mathbf{v}_a(\mathbf{E}) = \mathbf{v}_a(\mathbf{P}) + \mathbf{U}_p(\mathbf{E}_0) + \boldsymbol{\Omega}_p(\mathbf{E}) \times \mathbf{R}_p, \quad (1.2.9)$$

It remains to determine $\boldsymbol{\Omega}_p(\mathbf{E})$ from the roll, pitch, and heading usually reported by the GPS/INS. This is covered by L&M in Chapter 2 along with development of the equivalent of (1.2.9) with greater detail and by another approach.

1.2.8 Lagrangian approach of Leise and Masters

As discussed in the introduction to this Section 1.2, L&M approach wind measurement from aircraft along a different path to arrive at (1.2.9) without explicitly invoking reference-frame concepts. Accordingly, they use different nomenclature from that in Sections 1.2.6 and 1.2.7. In particular, "frame" means a system of coordinate axes, and "coordinates" means an ordered triplet locating a point on these axes. The approach is Lagrangian only in the sense that during the derivation it approximates the wind velocity as the finite displacement of a single air parcel from one measurement time t_0 to another time t before taking the limit as $t_0 \rightarrow t$.

³Note that bank, elevation, and heading are used here as nouns while roll, pitch, and yaw are used as verbs. To roll, for example, is to change bank angle.

The general issue is to determine some state quantity at some particular location on the earth by measuring from an aircraft in flight. A scalar state such as temperature can be directly measured at any given point, after which one need only locate that point on the earth. Suppose the aircraft is at point $\mathbf{p}(t_0)$ in GGC: (λ, ϕ, h) when its sampler measures the temperature. The sampler's position relative to the aircraft's origin is fixed and known in the PBC: $(\hat{x}, \hat{y}, \hat{z}) = \hat{\mathbf{R}}$. This can be converted to GGC and added to the origin's position to find the sampler's (and measured parcel's) position.

$$\begin{aligned}\boldsymbol{\xi}(t_0) &= \mathbf{p}(t_0) + \mathbf{G}_\xi[t_0, \mathbf{p}(t_0)]\hat{\mathbf{R}} \\ &= \mathbf{p}(t_0) + \mathbf{R}(t_0)\end{aligned}\tag{1.2.10}$$

Here $\mathbf{R}(t_0)$ is the displacement in GGC $(\Delta\lambda, \Delta\phi, \Delta h)$ of the sensor from the aircraft's origin. The $\mathbf{G}_\xi[t_0, \mathbf{p}(t_0)]$ is the coordinate transformation from PBC to GGC, the GGC being represented by ξ as in (1.2.1). The explicit dependence of \mathbf{G}_ξ on $\mathbf{p}(t_0)$ declares the relation of PBC through LGC to GGC in conversion to $\mathbf{R}(t_0)$. The second step, from LGC to GGC, can use the spherical approximation from [the inverse of] (1.2.1) because of the few meters' magnitude of $\hat{\mathbf{R}}(t_0)$. The sensors' displacement from the origin of PBC, though significant to the measurement, is small compared to the radius of the earth. Note that this implies a need for double-precision arithmetic in conversion between LGC and GGC.

A vector state such as wind velocity, the primary interest of this report, must be determined both in magnitude and in direction. Wind velocity is a (directed) displacement of air over the earth during a specified time interval. Starting with a finite representation of this vector helps physical intuition and mathematical rigor. It is Lagrangian in that it requires knowing the position of the same parcel at two different times. The procedure, as for temperature, is to measure a property of the parcel [its velocity $\hat{\mathbf{u}}(t_0; t_0)$ relative to the sensor] at time t_0 . Since the parcel is at the sensor when measured, its location in the aircraft's coordinates is known, and its location $\boldsymbol{\xi}(t_0; t_0)$ in the earth's GGC can be found from (1.2.10). Later, at $t = t_0 + \Delta t$, its position in the aircraft's coordinates, which move with the airplane, is estimated as

$$\hat{\mathbf{x}}(t; t_0) = \hat{\mathbf{R}} + \hat{\mathbf{u}}(t_0; t_0)\Delta t.\tag{1.2.11}$$

The initial time t_0 tags the parcel with its time of measurement by the sensor. Thus $\hat{\mathbf{x}}(t; t_0)$ [in PBC] is the position at time t of the parcel that was measured at time t_0 . By time t this parcel is somewhere aft of the sensor

because airflow relative to an aircraft in flight is by definition the airspeed, typically 50 m s^{-1} to 100 m s^{-1} , primarily from directly ahead. This second location corresponds to a second position in GGC, which is computed using (1.2.10) with two significant differences both due to the aircraft's own motion during Δt :

$$\begin{aligned}\boldsymbol{\xi}(t; t_0) &= \mathbf{p}(t) + \mathbf{G}_\xi[t, \mathbf{p}(t)]\hat{\mathbf{x}}(t; t_0) \\ &= \mathbf{p}(t) + \mathbf{R}(t; t_0).\end{aligned}\tag{1.2.12}$$

This is L&M's (2.7). Note that $\mathbf{p}(t)$ and $\mathbf{G}_\xi[t, \mathbf{p}(t)]$ apply to the current time and place in GGC and that the parcel's position in PBC $\hat{\mathbf{x}}(t; t_0)$ is no longer the constant $\hat{\mathbf{R}}$.

The wind velocity (over the earth) is obtained by taking the limit

$$\lim_{\Delta t \rightarrow 0} \frac{\boldsymbol{\xi}(t; t_0) - \boldsymbol{\xi}(t_0; t_0)}{\Delta t}\tag{1.2.13}$$

where $\boldsymbol{\xi}(t_0; t_0)$ comes from (1.2.10) and $\boldsymbol{\xi}(t; t_0)$ from (1.2.12). Since we are following the same parcel between t_0 and t , this is straightforward. All quantities in (1.2.12) in this ordinary physical setting (no shock waves or other discontinuities) are safely assumed differentiable allowing unobstructed passage to the limit as $\Delta t \rightarrow 0$ (and $t_0 \rightarrow t$). The result after some manipulation matches L&M's (2.8) and is equivalent to (1.2.9):

$$\mathbf{u}(t) = \mathbf{U}_0(t) + \mathbf{G}'(t)\hat{\mathbf{x}}(t) + \mathbf{G}(t)\hat{\mathbf{u}}(t).\tag{1.2.14}$$

Note that (1.2.14) has been converted to LGC. The time derivative $\mathbf{p}'(t)$ in GGC converts directly to $\mathbf{U}_0(t)$ in LGC using (1.2.1). The $\mathbf{G}(t)$ need convert only from PBC to LGC and can drop subscript ξ . The $\mathbf{G}'(t)$ represents the aircraft's attitude changes in LGC (the rotation $\boldsymbol{\Omega}_p(\mathbf{E})$ of Section 1.2.7). One practical method for its evaluation, if required, is provided in Chapter 2 following (2.9). Although the time-variant $\mathbf{G}(t)$ and $\mathbf{G}'(t)$ include the necessary adjustments to follow the curvature of the earth's surface, the dominant agent of attitude change, especially in the boundary layer, is turbulence (see discussion in Section 1.2.3). The last term of (1.2.14) uses $\hat{\mathbf{x}}'(t) = \hat{\mathbf{u}}(\mathbf{t})$ from (1.2.11).

In operation, much of (1.2.14) is directly measured at the high frequency required. The $\mathbf{U}_0(t)$ is available in LGC from the GPS/INS as noted in Sections 1.2.7 and 1.2.3. The attitude angles required for $\mathbf{G}(t)$ likewise come

directly from the GPS/INS. Recall also that $\hat{\mathbf{u}}(\mathbf{t})$ in PBC is directly measured by the probe.

The discussion by L&M following (2.9) is instructive. Although L&M's $\Delta\mathbf{U}(t)$ of (2.9) is recognized as the tangential velocity of the probe in the earth's reference frame due to rotation about the PBC's origin (Section 1.2.7), its actual computation in practice may be troublesome. L&M offer an approach they found to produce better accuracy with less computation than explicit differentiation of $\mathbf{G}(t)$. In (2.13), however, the vector \mathbf{d}_k seems to come from nowhere. In fact, it is an artificial construction of a vector identically perpendicular to \mathbf{r}_k , regardless of the magnitude or directions of \mathbf{r}_{k-1} or \mathbf{r}_{k+1} . Since the unit vector $\hat{\mathbf{i}}_k$ of (2.12) is already known by the argument following (2.9) (as well as Subsection 1.2.7) to be perpendicular to \mathbf{r}_k this artifice is justified.

1.3 Geometry of relative-wind computation

Relative wind $\hat{\mathbf{U}}_r(t)$ at a point $\hat{\mathbf{r}}$ is measured by definition in PBC and the aircraft's reference frame. Here L&M introduce the important angles α and β , which define the wind direction relative to the aircraft. They also account for measuring the magnitude and direction of the relative wind at locations on the aircraft separate from each other and separate from the origin of the PBC. The true airspeed $\|\hat{\mathbf{U}}_r\|$, denoted τ , might be measured on a boom protruding from a wing tip, or remotely by Doppler sodar or lidar. The direction $\hat{\mathbf{i}}_r$ might meanwhile be measured close to the fuselage. With any rotational motion (roll, pitch, or yaw), measured quantities τ and $\hat{\mathbf{i}}_r$ will then both need to be adjusted to determine the airspeed and direction at the origin of the PBC.

1.4 Basic atmospheric thermodynamics

This is a very informative treatment of the thermodynamic foundation for wind measurement from aircraft. This chapter was unique in having a few editorial errors and other specific issues on which comments are provided in Table 1.1.

Table 1.1: Editorial Comments, Chapter 4

Page	Paragraph	Remark
17	1	288.16 K is 15°C, about 60°F, not 70°F.
17	2	“Specific” generally means normalized by mass, not by molecular weight. <i>Multiply</i> a “specific” quantity by molar weight μ to get the “molar” quantity, normalized by the number of moles.
17	3	Last line: replace “more accurately” with “ <i>i.e.</i> ” The dw is accurate, just not an exact differential.
18	2	Division by 3 is because only the component $\langle u_\eta^2 \rangle$ normal to any boundary exerts the force on that boundary. Since molecular motion is random, all three orthogonal components are equal parts of the total $\langle u^2 \rangle$. Multiplication by 2 accounts for the force required in an <i>elastic</i> (not in-elastic) collision with that boundary. The inbound momentum changes by twice its magnitude in reversing its direction.
18	2	In the ideal-gas context, temperature has meaning at a point as the ensemble-average translational kinetic energy over all gas molecules that have non-zero probability of occupying that point. Boltzmann’s constant converts this to normal engineering units such as Kelvins. Heat is a bulk manifestation of the molecules’ total energy. It can cause increase in any combination of pressure, temperature, or volume. Changing volume does mechanical work (think steam engine). Centers of elevated molecular energy (high temperature) will diffuse that energy, ultimately through collisions with lower-energy molecules (conduction).

1.4.1 Theory of dew point and vapor pressure

Leise and Masters give some practical expressions in Chapter 7, equations (7.21, 7.22), to find the ambient vapor pressure e given the dewpoint temperature T_d , or *vice versa*. These most closely match expressions reported by Murray (1967).

It is striking to see how many expressions exist for these computations. All are evidently empirical in various mathematical forms, some very complex, all of them bristling with significant digits. How can they all be equivalent? Since the issue is fundamentally thermodynamic, a discussion at length is provided here as an extension to Chapter 4.

Except for the simplest, all expressions including L&M's (7.21, 7.22) give results within 1% of each other, perfectly valid for any but the most exacting microphysical applications well beyond the scope of wind measurement from aircraft. In fact the more esoteric of these expressions amount from a meteorologist's standpoint to an overfit, applying specifically to a two-phase gravity-segregated system consisting of a planar surface of liquid (or solid) pure water in equilibrium under pure water vapor. Those willing to accept (7.21 and 7.22) at face value are therefore justified. For those puzzled by the multiplicity of apparently competing expressions, the following development should be satisfying.

All expressions relating ambient vapor pressure to the temperature T_d parameterize integrals of the Clapeyron equation

$$\frac{dp_s}{dT} = \frac{\delta h}{T\delta v}, \quad (1.4.1)$$

which describes pressure p_s as a function of absolute temperature T in a multi-phase system (liquid, solid, gas, etc.) at equilibrium (also called saturation) among the phases. The latent heat δh of transition from one phase to another and the associated change in volume δv are given as molar quantities (*i.e.*, per mole).

The Clapeyron equation applies to any multi-phase equilibrium, but apart from high-precision applications (1.4.1) better suits systems restricted to solid and liquid phases because then δv is approximately constant. A variant appropriate to atmospheric water, draws on two approximations: 1) Atmospheric water vapor is nearly an ideal gas, and 2) the specific volume of liquid water or ice is a tiny fraction (0.001) of that of the vapor. Applying these approximations leads to the Clausius-Clapeyron equation, entirely adequate

for ordinary meteorology:

$$\frac{d \ln(p_s)}{dT} = \frac{L}{RT^2}. \quad (1.4.2)$$

The molar quantities $R [J K^{-1} mol^{-1}]$ and $L [J mol^{-1}]$ are the universal gas constant and the (molar) latent heat of evaporation/sublimation from water/ice. Note that both (1.4.1) and (1.4.2) are properly seen as mapping the temperature to the pressure in a multi-phase system *at equilibrium*. By thermodynamic theory, this equilibrium pressure depends on temperature alone. However, if one abruptly changes the temperature and/or pressure, these expressions will be violated during an adjustment period to a new equilibrium state.

Knowing the equilibrium vapor pressure at a convenient temperature, say the triple point of water ($273.16K$) one can, in principle, integrate (1.4.2) upward to any atmospheric temperature to determine the saturation (*i.e.*, equilibrium) vapor pressure at that temperature. Or specifying L to be the latent heat of sublimation of ice or vaporization of supercooled water, one can integrate downward to any desired sub-freezing temperature. However, beyond coarse approximation or short integration range, the temperature dependence of L becomes important. Furthermore, water vapor departs slightly, but significantly from an ideal gas.

The familiar equation of state assumes an ideal gas, having point-like particles that interact with each other only by elastic collision. Using statistical mechanics, one may generalize the equation of state to account for the effect on pressure of additional interactions among two or more particles. This effect is quantified as a virial expansion, from Latin *viris*: “manly” strength or force. This is a power series in density ρ [molecules m^{-3}] of the form

$$\frac{p}{\rho k_B T} = \frac{pv}{RT} = 1 + \sum_{r=1}^{\infty} B_{r+1}(T) \rho^r, \quad (1.4.3)$$

where $k_B [J K^{-1}]$ is Boltzmann’s constant. If N_a is Avagadro’s number, $R = N_a k_B [J K^{-1} mol^{-1}]$ is the universal gas constant, and $v [m^3 mol^{-1}] = N_a \rho^{-1}$ is the molar volume. The $B_{r+1}(T)$ are the virial coefficients, functions in general of temperature. Multiplying by RT specifying $A_{r+1}(T) = N_a (k_B T)^{1-r} B_{r+1}(T)$, and using $p = \rho k_B T$ provides an equation of state for saturated water vapor generalized to include particles’ interaction in pairs:

$$p_s v_s = RT - A_2(T) p. \quad (1.4.4)$$

Further generalization includes intra-molecular vibrations, small at atmospheric temperatures, but measurable. Interactions in triplets, interactions with gases of unlike chemical species (*e.g.*, N₂, O₂), and more can be accounted by higher-order terms if the data show significance.

By mid-Twentieth Century, accurate and detailed measurements were available of actual water substance over a wide range of temperature. Osborne et al. (1939) considered three processes involving carefully measured input of electrical energy to an otherwise adiabatic calorimeter containing pure water (no air) in both liquid and vapor phases, which met at a planar interface. The calorimeter's pressure and temperature were also carefully measured. For each process the investigators applied electrical energy and then, for process α measured the resulting temperature rise; for β maintained constant temperature by withdrawing saturated liquid (*i.e.*, liquid in equilibrium with the vapor); and for γ maintained constant temperature by withdrawing saturated vapor. Giauque and Stout (1936) obtained similarly accurate measurements for ice and water vapor.

Goff and Gratch (1946), in a very detailed and thorough study, took advantage of these measurements to develop semi-empirical closed-form expressions which fit the measurements within 0.02%—less than these measurements' own (quite small) uncertainty. The accuracy of the data was sufficient to describe quantitatively among other things the non-ideal characteristics of water vapor represented in the second virial coefficient $A_2(T)$ of (1.4.4).

Murphy and Koop (2005) surveyed data and schemes available by the turn of the present century and proposed new data-based numerically integrated expressions for saturation vapor pressure over plane surfaces of liquid water, ice, and for the first time, supercooled water. The numerical results were well approximated as closed-form functions of T , parameterized by the four coefficients of the formal integral of the Clausius-Clapeyron equation (1.4.2) using a second-order polynomial for $L(T)$:

$$\ln p_s = b_0 + b_1 T^{-1} + b_2 \ln T + b_3 T. \quad (1.4.5)$$

The parameters were statistically fit to numerical integrations of the more general Clapeyron equation (1.4.1) using the (very precise) data to specify the changes in molar enthalpy and molar volume across the phase transition.

For ice, the integration proceeded downward from the triple point of water $[(p_t, T_t) = (611.657 \pm 0.01 Pa, 273.16 K)]$ using the best known measurements of the molar heat of sublimation and of the molar heat capacity of ice and

vapor as functions of the temperature. The integration incorporated non-ideal characteristics of water vapor, including the second virial coefficient and molecular vibrations. The four-parameter fit,

$$\ln p_{ice} = 9.550426 - 5723.265T^{-1} + 3.53068 \ln T - 0.00728332T \quad (1.4.6)$$

$$T \in [110K, 273.16K],$$

stays within 0.025% of the numerical integration between 111 K and the triple point, well within the uncertainties of the integration itself. Given the ambient vapor pressure e_a the frost-point temperature is

$$T_{frost} = (1.814625 \ln e_a + 6190.134)(28.120 - \ln e_a)^{-1} \quad T > 115K \quad (1.4.7)$$

to within $\pm 0.04K$ for T above 115K.

With liquid water one encounters the possibility of super cooling, where water remains liquid although the temperature is below, sometimes well below, the triple point. The parameterizations by Goff and Gratch (1946), Goff (1965), or Hyland and Wexler (1983) applied within 0.02% either to liquid water above the triple point or to ice below. Parameterization over supercooled water was impossible for want of measurements. This meteorologically significant region had to be covered by risky extrapolation of liquid-water parameterizations. When measurements became available they revealed trouble.

The molar heat capacity of supercooled water was found to rise rapidly with decreasing temperature below about 250K, a feature not found in the extrapolations. The current measurements extend down to about 235K, below which homogeneous nucleation to crystalline ice has so far been unavoidable. Amorphous (noncrystalline) ice can exist below 155K, perhaps because internal energy is low enough to leave a metastable structure undisturbed. Between 235K and 155K non-crystalline water is unobtainable. Amorphous ice is prepared by plunging liquid water through the range between these two temperatures within a fraction of a millisecond.

At least three hypotheses propose to describe non-crystalline water through this unstable range, the simplest being thermodynamic continuity. If this proves true, a curve can be completed between the measured molar heat capacity of supercooled liquid above 235K and amorphous ice below 155K. The simplest such curve reaches a maximum just below 235K. Two four-parameter curves of the form of (1.4.5) can represent the slopes up either side

toward the maximum. Murphy and Koop (2005) used a hyperbolic-tangent patch over the maximum to produce a ten-parameter fit from $123K$ to $332K$:

$$\begin{aligned} \ln p_{liq} = & 54.842763 - 6763.22T^{-1} - 4.210 \ln T + 0.000367T + \\ & \tanh [0.0415(T - 218.8)] \times \\ & (53.878 - 1331.22T^{-1} - 9.44523 \ln T + 0.014025T). \end{aligned} \quad (1.4.8)$$

The warm side of this fit continues upward beyond the triple point to include vapor pressure over liquid water using the results from Wagner and Pruß (1993). The cold side is less certain, relying on the thermodynamic-continuity hypothesis to model saturation vapor pressure over supercooled water and amorphous ice. The range of (1.4.8) covers saturation vapor pressure over liquid water from -150°C to $+60^\circ\text{C}$, though its reliability deteriorates below $235K$ (-38°C).

All data applied to developing the forgoing parameterizations come from systems of pure water under its own vapor in two phases separated by a planar interface. In the atmosphere, water is a minority constituent. Furthermore, boundaries between vapor and condensed phases are typically strongly curved, the condensed phase represented by cloud droplets or crystals of several micrometers' diameter or less. Hydrophilic chemical species present in aerosols introduce further complexity. Such questions are major issues in climate dynamics and are currently active topics of research in microphysics of clouds and aerosols.

For many practical purposes, including most research in the boundary layer, the primary value of these rather complex expressions is the convenience of their validity over the entire atmospheric temperature range. With modern computers such expressions are easily evaluated. As noted at the beginning of this section, all except the simplest give results within 1% of each other over wide ranges of temperature. The multiplicity of expressions need not give concern for ordinary use. The expressions (1.4.6–1.4.8) have advantages of relative simplicity and of grounding in actual data for supercooled water, at least above (-38°C). At their native level of detail, however, additional processes in the wild introduce uncertainty often well beyond that of the vapor pressure. These include an air-dominated gas phase, curved phase boundaries, hydrophilic gases and aerosols, and chemical reactions.

Finally, from an aviation perspective, supercooled water is called “known icing conditions.” Only large or sophisticated aircraft, such as NOAA’s P-3 aircraft for which this technical memorandum was originally written, are

equipped to operate safely in known icing. Small environmental research aircraft are rarely certified for such operation.

1.5 Theory of true-airspeed measurement

Here the Bernoulli equation is derived in the form of an energy balance by taking the scalar product of the Euler equation of motion with the wind velocity. The energy form facilitates imposition of the adiabatic constraint to simplify the equations. Since a wind probe's pressure distribution is usually assumed to be in steady state, the authors express some concern about the adjustment time to a new equilibrium state after a change in ambient conditions.

They provided no estimate of the adjustment time, but plausibly the adjustment time is comparable to the travel time of an idealized gust (step change in incident velocity) across the probe's upstream-influence region to engulf the probe in the new ambient conditions. All quantities here are given and calculated in the probe's reference frame and coordinates. That is, the air is moving relative to a fixed probe. Transient acoustic waves are expected during the change, but at the small scale of the probe and the low Mach numbers of the flow they should have low amplitude and should dissipate quickly. During the change, the state quantities (flow, pressure, and temperature) around the probe will depart from the steady state assumed to prevail when deriving the flow velocity from the pressure distribution. If the adjustment time is short compared to the time scale of encounter with the significant eddies in the air, the assumption of equilibrium flow over the probe is justified. Otherwise, the degree of residual dis-equilibrium in the flow and its effect on the measurements must be determined, a challenge beyond the current scope.

To attempt a justification of the assumption of equilibrium flow, consider a somewhat simplified structure where the incident air far upstream (relative to the probe's diameter) is moving uniformly. The speed is equal to the airplane's true airspeed. The direction is near but not necessarily on the probe's axis. Everything is initially in steady-state equilibrium expressed by

$$\frac{D}{Dt} \left(\frac{1}{2} U^2 + c_p \bar{T} + \mathbf{g} \cdot \mathbf{X} \right) = 0. \quad (1.5.1)$$

Here $U^2 = \mathbf{U} \cdot \mathbf{U}$ and \mathbf{U} , \bar{T} , and \mathbf{X} are the (initial) equilibrium values, respectively, of the incident flow velocity, ambient temperature, and position

vector (probe's coordinates). The specific heat at constant pressure is c_p . The gravity vector (probe's coordinates) is \mathbf{g} . The D/Dt is the material derivative, also called the total time derivative (see (5.1) in Chapter 5). The local time derivative is zero here because of the steady state.

Expression (1.5.1) is slightly more carefully stated than L&M's (5.5) and (5.6). The geopotential term, involving gravity, only appears if the probe is not horizontal. Then $\mathbf{U} = D\mathbf{X}/Dt$ has a component parallel to gravity, and geopotential energy enters the exchange with the kinetic and thermodynamic energy along the steady flow path.

Suppose this steady state is now altered by the arrival of a strong updraft typical of the convective boundary layer. The updraft can be modeled as a step change \mathbf{u} perpendicular to the initial equilibrium flow and having magnitude 10% of the initial equilibrium speed. This produces a direction change of about 6° and a speed increase of 5%, amenable to perturbation analysis. Being bouyant, it also brings an increase, less than 5%, in temperature and a corresponding decrease in density. Let the gust's incremental quantities be expressed in lower-case or primed symbols:

Perturbation Increments

Steady State Add an abrupt
 increment

\mathbf{U}	$\mathbf{U} + \mathbf{u}$	wind
ρ	$\rho + \rho'$	density
P	$P + p$	pressure
\bar{T}	$\bar{T} + T$	temperature
\mathbf{X}	$\mathbf{X} + \mathbf{x}$	position vector, probe's coordinates

The temperature increment T is a small capital to avoid confusion with time t .

An equation expressing the (non-steady) adjustment to the new equilibrium can be computed by using the incremental quantities to expand L&M's (5.5) with gz replaced by $\mathbf{g} \cdot \mathbf{X}$. The products of incremental terms can be ignored as being small, the incremental density ρ' likewise, except when it multiplies gravity (Boussinesq approximation). Subtracting (1.5.1) yields, after some algebra,

$$\frac{D}{Dt} (\mathbf{u} \cdot \mathbf{U} + c_p T) + \mathbf{g} \cdot \left(\mathbf{u} + \frac{\rho'}{\rho} \mathbf{U} \right) + c_p \mathbf{u} \cdot \nabla \bar{T} = \frac{1}{\rho} \frac{\partial p}{\partial t}. \quad (1.5.2)$$

Being in a non-steady state, these incremental quantities include transient local change, including $\partial p / \partial t$.

Numerical, and perhaps analytical, solutions to (1.5.2) could be found, but a heuristic argument will be considered sufficient here. The gust first appears far upstream of the probe. Near the probe, \mathbf{u} and p , (equivalently τ because adiabatic) are initially zero. As the gust approaches the probe it begins to move the stagnation point, and its faster air packs against the probe's head developing an adverse perturbation-pressure gradient ∇p . This brings the \mathbf{u} , like the equilibrium \mathbf{U} , to a stop (relative to the probe) at the stagnation point, but also generates acoustic waves. While a new equilibrium pressure pattern is developing, $\partial p/\partial t > 0$ in the region around the probe. In the new steady state, the incident flow becomes $\mathbf{U} + \mathbf{u}$, and the pressure at the new stagnation point becomes $P + p$.

The adjustment time Δt , over which the local pressure tendency is nonzero, is comparable to the transit time of the initial perturbation across the probe's upstream influence region and around the probe's hemispherical head plus time for the acoustic waves to dissipate. At a typical Mach number $\text{Ma} < 0.3$, the acoustic waves' dissipation time will be assumed small compared to the transit time. The width of the upstream influence region may be estimated from potential-flow theory. The transit speed across this upstream region is estimated as half the incident flow speed because of its steady decrease along a streamline to become zero at the stagnation point.

In spherical polar coordinates for streaming flow past a sphere of radius a , having boundary conditions of zero normal flow at the sphere's surface ($r = a$) and uniform flow speed U far from the sphere, the velocity potential for potential flow is

$$\phi = U \left(r + \frac{a^3}{2r^2} \right) \cos \theta, \quad (1.5.3)$$

where r is the radial distance from the sphere's center and θ is the angular distance around any great circle of the sphere which passes through the stagnation point at $\theta = \pi$. The flow is radially symmetrical in any plane perpendicular to the undisturbed uniform flow. The radial component of the flow follows

$$\frac{\partial \phi}{\partial r} = U \left(1 - \frac{a^3}{r^3} \right) \cos \theta. \quad (1.5.4)$$

At $r = 5a$, two diameters upstream of the sphere's center, the normal velocity on the stagnation streamline ($\cos \theta = -1$) is reduced by $(U + u)(1 - 1/125)$, about 1%. Since the pressure increase goes as the square of the velocity, the pressure two diameters upstream is about $(P + p)(1 + 2/125)$

or about 2% above ambient. If the base-state airspeed is 60 m s^{-1} , and the perturbation travels on average 30 m s^{-1} over the 2.5 probe diameters along the stagnation streamline, adjustment will require less than 15 ms for the BAT probe's diameter of 0.15 m. The Rosemount probes used by NOAA/AOC on the P-3 have a diameter of 0.025 m, and the transit speed is on average 50 m s^{-1} , giving an estimate of less than 1.5 ms.

During 15 ms an airplane at 60 m s^{-1} travels 0.9 m. A sample rate of 50 s^{-1} minimally detects fluctuations on scales of 2.5 m, but operational resolution is about 6 m. The P-3 travels 0.15 m in 1.5 ms. A sample rate of 50 s^{-1} corresponds to 4 m minimal detection scale and 10 m scale operationally. Most important gusts have larger length scale than this. The concern of L&M about their (5.6) thus appears unnecessary, but not by a huge margin.

Their other concerns are significant, yet airborne turbulence measurement works remarkably well. Helping this result are the amazing accuracy of the GPS, the high capacity of data storage and computer throughput, and the high sample rate and accuracy of current sensors. Much of this development has come since the time of L&M's writing.

1.6 Theory of flow-angle measurement

In Chapter 8 L&M report not being able to utilize the nuanced results of Chapter Six. This chapter, however, has been enormous help in developing the BAT probe (Crawford and Dobosy, 1992; Eckman, 1999; Dobosy et al., 2013) and derivative instruments (Eckman et al., 2007). Eckman (1999), drawing on Chapter 6, derived a method explicit to the BAT probe. Later, Dobosy et al. (2013) and Vellinga et al. (2013) found discernable improvement from modifying Eckman's scheme to account for the BAT probe's actual hemisphere-cylinder shape. Our group owes a debt to L&M's original work, especially that found in this chapter.

1.7 Calibration of temperature, pressure, and airspeed

This chapter describes some practical calibration practices developed by Leise and Masters in the 1990s. New instrumentation, especially GPS has enabled several improvements, but the thought behind these practices is instructive.

Also in this chapter is the set (7.20) of equations currently used by NOAA/AOC to compute the wind velocity from their P-3s.

1.7.1 Temperature recovery factor

Currently NOAA/AOC computes a total temperature offset based on airspeed, moisture, and altitude, by a process different from that presented here. In fact, *this section's stated purpose is an in-flight sanity check on the entire temperature-measurement system.* It is not meant for operational use. In this section L&M simply assume a constant temperature-recovery factor. The usual temperature sensor's recovery factor varies with the Mach number in a way that can only be determined in a wind tunnel. Another discussion of the recovery factor for a particular temperature sensor, including its variation with Mach number, is given by Khelif et al. (1999), also in connection with NOAA/AOC's P-3 aircraft as equipped at the time.

The maneuver described uses a pair of racetracks at two significantly different known airspeeds. Since direct determination of the airspeed requires knowledge of the ambient air's temperature, the ground speed on each straight leg provides a proxy. To achieve the simplest possible relation between airspeed and ground speed, the patterns are flown directly upwind and downwind, always at the same altitude. Maintaining constant airspeed is important as is knowing the wind direction and successfully finding a time and place of homogeneous wind over the whole pattern. Such a set of conditions appears difficult to meet.

Small boundary-layer aircraft typically fly at Mach numbers less than 0.2. Since the adiabatic heating of the air at the temperature sensor depends on the square of the Mach number, knowledge of the recovery factor only to within 10% may be acceptable for them (Vellinga et al., 2013).

1.7.2 Ambient pressure measurement

The aircraft's reported ambient pressure is tested in relation to a cone trailed on a long tube in undisturbed air behind the aircraft and carrying a pressure sensor. Khelif et al. (1999) compared the departure of the ambient pressure reported at the cone to the pressure reported by the aircraft's ambient (static) pressure ports as a function of the measured dynamic pressure q_m . They fit a polynomial to sixth order in $q_m^{0.5}$ which, apart from density fluctuations, varies directly with true airspeed τ . NOAA/AOC's current practice in correcting the

measured ambient pressure fits an empirical expression in altitude as well as airspeed, also based on trailing-cone measurements from each of their two P-3 aircraft.

1.7.3 True airspeed computation

The error in dynamic pressure is estimated in flight using racetrack patterns similar to (or the same as) those used to check the temperature-recovery factor. Again the ground speed is used as proxy for the unknown airspeed. The same requirements and complexities apply. System (7.20), however, is an excellent path from dynamic pressure to true airspeed, which bypasses the Mach number. It is currently used by NOAA/AOC (Damiano, personal communication, 2012). Our scheme (Dobosy et al., 2013; Vellinga et al., 2013) uses the Mach number, with which we have similar success.

1.7.4 Dew point and vapor pressure

L&M give practical expressions (7.21) relating the ambient vapor pressure e to the dewpoint temperature T_d . These most closely match expressions reported by Murray (1967) and are currently in use by NOAA/AOC for $T_d \geq 0^\circ\text{C}$. Current NOAA/AOC practice for $T_d < 0^\circ\text{C}$ is to go the other direction, determining the vapor pressure from specific humidity measured directly by laser absorption. The frost point ($T_d < 0^\circ\text{C}$) can then be found from L&M's (7.22) or equivalent (Barry Damiano, personal communication, 2013).

More recent work (Murphy and Koop, 2005) incorporates results from new measurements over supercooled water at least down to -38°C as noted in Section 1.4.1. However, aviators read supercooled water as “known icing conditions.” Only large or sophisticated aircraft, such as NOAA's P-3 aircraft for which this technical memorandum was originally written, are equipped to operate safely in known icing. Furthermore, as stated in Section (1.4.1) the level of detail in the expression of Murphy and Koop (2005) amounts to an overfit for measurements in the real atmosphere. Thus either expression (7.21) of L&M or that of Murphy and Koop (2005) is fully suitable for humidity measurement in all but the most demanding microphysical applications, beyond the scope of airborne measurement of wind and turbulence.

1.7.5 Offsets: Links to ground measurements

L&M note the need for checking offsets as well as scale (slope) parameters and recommend flying close to fixed measurement sites. In airborne boundary-layer measurements, this practice is important for two reasons. The first is the reason given by L&M in this section. The second is a synergy whereby the fixed surface measurements provide high-resolution, long-term coverage of the temporal variation at their location, while the airborne measurements link one location to another. Thus a productive deployment requires both fixed and airborne measurement even in its normal operation (Crawford and Dobosy, 2004; Crawford et al., 1996b; Isaac et al., 2004; Kirby et al., 2008; Vellinga et al., 2010; Zulueta et al., 2011, 2013).

1.8 Calibration of flow angles

Much work has been done in calibration of flow angles. As in 1993, differential pressure measurements are the normal data from which the flow direction is determined. Two general approaches are followed.

The first approach was used by L&M in this chapter. It uses forms derived from L&M's (B.10) or (6.9) parameterized by slopes K_α and K_β and by offsets A_0 and B_0 .

$$\begin{aligned}\tan \alpha &= K_\alpha(\delta_\alpha p/q_\alpha) + A_0 \\ \tan \beta &= K_\beta(\delta_\beta p/q_\beta) + B_0.\end{aligned}\tag{1.8.1}$$

Here $\delta_\alpha p$ and $\delta_\beta p$ are, respectively, the pressure differences in the aircraft's vertical and lateral directions measured over the approximately spherical head(s) of the wind sensor(s).

Separate sensors are used by NOAA/AOC for attack and sideslip angle as shown in L&M's Appendix A. The q_α and q_β are associated measurement(s) of dynamic pressure. The parameters K_α , K_β , A_0 , and B_0 are fit to data from appropriate flight maneuvers. L&M describe some of these. Barry Damiano (personal communication 2013) added a third racetrack maneuver at 210 kt for NOAA/AOC's P-3s around the year 2000. This demonstrably improved the derived K_α and A_0 .

Related maneuvers are described by Lenschow (1986); Lenschow et al. (2007); Khelif et al. (1999); Kalogiros and Wang (2002b). These procedures

suit airborne systems, typically on larger, more complex aircraft having pressure sensors on a radome (Brown et al., 1983) or along the fuselage (L&M).

The second approach separates the model for the flow over the probe from the models for the aircraft's distortion of that flow (Crawford et al., 1996a,b; Kalogiros and Wang, 2002a; Garman et al., 2008; Vellinga et al., 2013). This approach suits simpler, smaller aircraft, often explicitly configured to minimize and simplify flow distortion. The two approaches have many flight maneuvers in common, though the analysis is different. Kalogiros and Wang (2002a) also introduce acceleration maneuvers to address distortion by thrust.

This second approach allows consideration of the sensor independent of the aircraft's distortion. The sensor may then be calibrated in a wind tunnel (Garman et al., 2006; Dobosy et al., 2013) and can be strongly aspherical (van den Kroonenberg et al., 2008). If a spherical shape is retained, the second approach can meaningfully apply the refinements of Chapter 6 [see L&M, Chapter 8 after (8.5)].

L&M recognize the importance of considering roll. Often, one simply minimizes roll by flying straight and level. Lenschow et al. (2007), whose airborne measurements of divergence and vorticity require both nonzero roll and accuracy at high precision, have developed promising maneuvers and analysis for calibration considering nonzero roll.

Although NOAA/AOC's P-3s have pressure ports on their radomes (Khelif et al., 1999), these are not currently used (Damiano, NOAA/AOC, personal communication 2012). They are not configured to provide measurements during rain or icing, which characterize many of the P-3s' missions.

1.9 In-flight examples

The stairsteps described by L&M in Chapter 9 provide calibration parameters over a useful range of altitudes, but require considerable time to execute. If multiple altitudes are impractical, flights should at least be in sufficiently smooth air (minimal vertical motion) to control contamination of the calibrated parameters.

Having GPS navigation makes knowledge of the aircraft's velocity very reliable. Accurate knowledge of the vertical component of the aircraft's velocity is vital to calibration of the parameters describing the lift-induced upwash (Crawford et al., 1996a; Vellinga et al., 2013). Accurate knowledge of the

aircraft’s horizontal velocity relaxes the requirement to fly directly upwind and downwind to calibrate the direction offset and the error parameter for dynamic pressure.

The K_β has proven a relatively awkward parameter in simpler measurement systems than the P-3 (Vellinga et al., 2013), but see Lenschow et al. (2007), who also have a reliable way to determine B_0 . Having the angle sensors farther forward as L&M suggest, however, has been found beneficial in aircraft so equipped (Kalogiros and Wang, 2002a,b; Khelif et al., 1999; Lenschow et al., 2007; Vellinga et al., 2013).

1.10 Adiabatic and hydrostatic approximation

This chapter demonstrates the utility of adiabatic and hydrostatic approximations to enable sanity checks on quantities derived from calculations complex and hard to interpret in their precise form. Several examples are presented. They apply to the NOAA/AOC P-3s of L&M’s direct interest, but can be mined for useful concepts more generally. The current ubiquitous use of the Global Positioning System changes the game considerably. GPS with carrier-phase differential correction can, for instance, readily determine the error in the reported static pressure to a few Pascals (0.1 m – 0.3 m)—given the hydrostatic approximation.

1.11 P-3 data acquisition

Discussion starts with filters and sampling, including aliasing of samples. This chapter does not describe NOAA/AOC’s current real-time data-acquisition system, which has been upgraded since L&M’s writing. The issues and concepts are, however, still relevant. The topic of computational aliasing is little discussed or covered in data acquisition, at least among atmospheric scientists. That was true in L&M’s time and is likely still true. Nonlinear computations introduce additional frequencies above those present in the input signals. Even if the input is free of aliased components, these new frequencies may be above the input’s Nyquist frequency and appear as alias modes below the Nyquist frequency. For practical use L&M recommend an additional filter having a response that vanishes at the Nyquist frequency of the

digital sample. This removes additional aliased components and mitigates computational aliasing. However, they also offer procedures of interpolation and filtering in Appendix D that are more effective and likely practical with current computing power. Again, however, these do not explicitly reflect current practice at NOAA/AOC.

1.12 Corrections with filters

This is a very important chapter about more than corrections. Current standard procedure is to mix the signal from an instrument accurately responsive to high frequencies with the signal from an instrument accurately drift free at low frequencies to obtain an output signal of broad band width (Crawford and Dobosy, 2004, 1997). We used Leise’s cubic mirror-image replacement filter, Appendix F, in this service for many years and found it to work very well. L&M addressed filter optimization and several other important issues: shot noise, boundaries, and missing data. They also include Appendices C-F with details of filtering and its applications, including the filter in Appendix F.

1.13 Horizontal wind computation

This chapter is largely obsolete, but historically interesting. The recommendations L&M make at the end of it are basically the way horizontal winds are now measured. GPS and fast computers have completely changed the game and produced major improvements in wind-measurement accuracy. Subsequent developments in (relatively) low-cost single-antenna GPS/INS have conquered the Schuler oscillation. Obtaining a high-precision heading-angle reference still requires multi-antenna GPS, as L&M foresaw. See the more extensive discussion in Appendix G, also Vellinga et al. (2013); Dobosy et al. (2013).

1.14 Vertical wind computation

NOAA/AOC normally uses the method of Jorgensen and LeMone (1989) to determine the vertical wind (B. Damiano, Personal communication, 2012), entirely sufficient for their missions. With GPS now fully three-dimensional and capable of direct measurement of velocity from the Doppler shift on the

carrier wave, all three components of the probe's motion can be determined to high precision by the same computation. There is no need to separate horizontal from vertical wind. The issues of complementary filtering and phase matching discussed by L&M in this chapter remain, however. See also Section 1.12.

1.15 Flow distortion and phase

Flow distortion can be treated in bulk as in the approach using the two parameters discussed by L&M in Chapter 8. This can be quite serviceable for horizontal wind, if all the instruments are physically near each other and away from locations of serious flow distortion. As L&M show, however, the synchrony between instruments should not be taken for granted, but should be tested to the extent possible.

The second approach mentioned in the annotation to Chapter 8 models the most important contributions to flow distortion directly. Using the second approach requires explicit treatment of the flow distortion. This may become quite complex unless the instrument configuration simplifies the flow distortion as much as possible (Crawford and Dobosy, 1992; Crawford et al., 1996a,b; Kalogiros and Wang, 2002a). A good configuration has the probe centered laterally as far forward from both engines and wings as possible. A pusher configuration is nearly ideal because the propeller is behind the wing, leaving the nose clean for mounting the wind sensor on a boom. The center of mass, hence the wing, is aftward allowing the nose to protrude farther forward of both thrust and lift. A twin-engine tractor aircraft at least moves the center of thrust off the aircraft's longitudinal axis and frees the nose. The four-engine P-3 has this same advantage if the probe can be mounted on a boom ahead of the nose. Flow distortion for pusher aircraft has been treated by Crawford et al. (1996a); Vellinga et al. (2013) and for a twin tractor by Kalogiros and Wang (2002a).

1.16 Conclusions and Recommendations

Many of these have been adopted and/or superseded. This chapter, however, is interesting for historical reasons.

1.17 Appendices

These appendices contain a wealth of detailed background information that can be mined for useful insights into important aspects of airborne-data processing and quality control.

1.A P-3 Instrumentation

1.B Incompressible flow past a sphere

This section provides theoretical justification for ignoring the flow acceleration in determining the relative wind from pressure-sphere measurements. It is basically a restatement for incompressible potential flow of the problem of local pressure tendency handled in Section 1.5 for adiabatic flow.

1.C Digital filters and symmetry

Many toolkits for building digital filters exist, but this appendix helps develop a basic understanding of how filters work and how their properties are analysed.

1.D Sampling and interpolation

This appendix addresses aliasing and gap filling, helping theoretical understanding of what is happening. Current practice at NOAA/AOC has, of course, progressed independently since this writing.

1.E Enhanced triangle filters

With ready filter-building kits and fast computers, these may be old fashioned. They are, however, very efficient filters. This appendix also provides background to understanding Leise's Cubic Mirror-Image Filter, which is powerful, efficient, and not likely found in a filter toolbox.

1.F A mirror-image filter algorithm

Here the Cubic Mirror-Image Filter itself is described in detail with its algorithm worked out in Fortran. Developing this algorithm required a major balancing act. Having it explicitly worked out saves a lot of tedious detailed work for someone who would use the filter.

1.G Filtered interpolation

Here several interpolation schemes are analysed theoretically providing theoretical understanding and potentially saving a lot of tedious work.

1.H Statistical editing

We have called such algorithms as these despikers. Spikes in data must be removed before any filtering or they will be propagated widely, rendering many good data useless. Often the spikes are simply single missed samples, but spike removal in general is one of the more difficult issues in data processing. Wavelet theory, not covered by L&M is a powerful tool as well, if one properly understands and applies it.

Annotator's Acknowledgements

Director Bruce Baker of ARL/ATDD supported the annotation and publication of this work of Leise and Masters. James McFadden and Barry Damiano of gave NOAA/AOC's clearance to publish the manuscript as annotated. Barry Damiano, in particular, reviewed the manuscript and annotations. Drawing on his long experience with AOC, including work with Jim Leise, he provided information and many valuable comments. Also highly valued were the review comments of Richard Eckman and Edward Dumas of NOAA/ARL. Librarian Maggie Robinson of ARL/ATDD provided major help with literature surveys and in obtaining old manuscripts, difficult to find. Author Jeffrey Masters, currently of Weather Underground, LLC, supplied the high-quality hard copy of the original that is reproduced in Parts II and III. There was no electronic copy extant.

Annotations' References

- Brown, E. N., C. A. Friehe, and D. H. Lenschow, 1983: The use of pressure fluctuations on the nose of an aircraft for measuring air motion. *Journal of Applied Meteorology*, **22** (1), 171–180.
- Crawford, T. and R. Dobosy, 2004: Accuracy and utility of aircraft flux measurements. *Vegetation, Water, Humans and the Climate: A New Perspective on an Interactive System*, P. Kabat, M. Claußen, P. Dirmeyer, H. Gash, L. DeGuenni, M. Meybeck, R. Pielke Sr., C. Vörösmarty, R. Hutjes, and S. Lutkemeier, Eds., Springer Verlag, Berlin, Heidelberg, New York, 566–571.
- Crawford, T. L. and R. J. Dobosy, 1992: A sensitive fast-response probe to measure turbulence and heat flux from any airplane. *Boundary-Layer Meteorology*, **59** (3), 257–278.
- Crawford, T. L. and R. J. Dobosy, 1997: Pieces to a puzzle: Air-surface exchange and climate. *GPS World*, **8** (11), 32–39, URL <http://www.atdd.noaa.gov/>.
- Crawford, T. L., R. J. Dobosy, and E. J. Dumas, 1996a: Aircraft wind measurement considering lift-induced upwash. *Boundary-Layer Meteorology*, **80** (1), 79–94.
- Crawford, T. L., R. J. Dobosy, R. T. McMillen, C. A. Vogel, and B. B. Hicks, 1996b: Air-surface exchange measurement in heterogeneous regions: extending tower observations with spatial structure observed from small aircraft. *Global-Change Biology*, **2** (3), 275–286.

- Dobosy, R., et al., 2013: Calibration and quality assurance of an airborne turbulence probe in an aeronautical wind tunnel. *Journal of Atmospheric and Oceanic Technology*, **30** (2), 182–196.
- Eckman, R., 1999: Computation of flow angles and dynamic pressure on a BAT Probe. ARL/FRD contribution, Available on web, NOAA, Air Resources Laboratory, Field Research Division, 4 pp., Idaho Falls (Idaho), USA. URL <http://www.noaa.inel.gov/Personnel/Eckman/docs/flowangles.pdf>.
- Eckman, R., R. Dobosy, D. Auble, T. Strong, and T. Crawford, 2007: A pressure-sphere anemometer for measuring turbulence and fluxes in hurricanes. *Journal of Atmospheric and Oceanic Technology*, **24** (6), 994–1007.
- Einstein, A., 1956: *The meaning of relativity*. Fifth edition ed., Princeton University Press, Princeton, New Jersey, 166 pg pp.
- Featherstone, W. and S. Cläßen, 2008: Closed-form transformation between geodetic and ellipsoidal coordinates. *Studia geophysica et geodaetica*, **52** (1), 1–18.
- Garman, K., P. Wyss, M. Carlsen, J. Zimmerman, B. Stirm, T. Carney, R. Santini, and P. Shepson, 2008: The contribution of variability of lift-induced upwash to the uncertainty in vertical winds determined from an aircraft platform. *Boundary-Layer Meteorology*, **126** (3), 461–476, URL <http://dx.doi.org/10.1007/s10546-007-9237-y>.
- Garman, K. E., et al., 2006: An airborne and wind tunnel evaluation of a wind turbulence measurement system for aircraft-based flux measurements. *Journal of Atmospheric and Oceanic Technology*, **23** (12), 1696–1708.
- Giauque, W. and J. Stout, 1936: The entropy of water and the third law of thermodynamics. the heat capacity of ice from 15 to 273 K. *Journal of the American Chemical Society*, **58** (7), 1144–1150.
- Goff, J., 1965: Saturation pressure of water on the new Kelvin scale. *Humidity and Moisture Measurement and Control in Science and Industry*, H. Wexler and W. Wildhack, Eds., Reinhold Publications, Vol. 3, 289–292.

- Goff, J. and S. Gratch, 1946: Low-pressure properties of water from -160 to 212 F. *Trans. Amer. Soc. Heat. Vent. Eng.*, **51**, 125–164.
- Hacker, J. M. and T. L. Crawford, 1999: The BAT-Probe: The ultimate tool to measure turbulence from any kind of aircraft (or sailplane). *Technical Soaring*, **23** (2), 42–45.
- Hall, P. G., E. J. Dumas, and D. L. Senn, 2006: NOAA ARL Mobile Flux Platform instrumentation integration on University Of Alabama Sky Arrow environmental aircraft. NOAA Technical Memorandum ARL-257, Air Resources Laboratory, National Oceanic and Atmospheric Administration, 41 pp., Oak Ridge (Tennessee), USA. URL http://aero.eng.ua.edu/equipment/noaa_tm.pdf.
- Hyland, R. and A. Wexler, 1983: Formulations for the thermodynamic properties of saturated phases of H₂O from 173.15 K to 473.15 K. *ASHRAE Transactions*, **89**, 500–519.
- Isaac, P., J. McAneney, R. Leuning, and J. Hacker, 2004: Comparison of aircraft and ground-based flux measurements during OASIS95. *Boundary-layer meteorology*, **110** (1), 39–67.
- Jorgensen, D. P. and M. A. LeMone, 1989: Vertically velocity characteristics of oceanic convection. *Journal of the Atmospheric Sciences*, **46** (5), 621–640, doi:10.1175/1520-0469(1989)046<0621:VVCOOC>2.0.CO;2.
- Kalogiros, J. A. and Q. Wang, 2002a: Aerodynamic effects on wind turbulence measurements with research aircraft. *Journal of Atmospheric and Oceanic Technology*, 1567–1576, doi:10.1175/1520-0426(2002)019<1567:AEOWTM>2.0.CO;2.
- Kalogiros, J. A. and Q. Wang, 2002b: Calibration of a radome-differential GPS system on a Twin Otter research aircraft for turbulence measurements. *Journal of Atmospheric and Oceanic Technology*, 159–171, doi:10.1175/1520-0426(2002)019<0159:COARDG>2.0.CO;2.
- Khelif, D., S. P. Burns, and C. A. Friehe, 1999: Improved wind measurements on research aircraft. *Journal of Atmospheric and Oceanic Technology*, **16**, 860–875, doi:10.1175/1520-0426(1999)016<0860:IWMORA>2.0.CO;2.

- Kirby, S., R. Dobosy, D. Williamson, and E. Dumas, 2008: An aircraft-based analysis method for discerning individual fluxes in a heterogeneous agricultural landscape. *Agricultural and Forest Meteorology*, **148** (3), 481–489.
- Lenschow, D. H., 1986: Aircraft measurements in the boundary layer. *Probing the Atmospheric Boundary Layer*, D. H. Lenschow, Ed., American Meteorological Society, 39–55.
- Lenschow, D. H., V. Savic-Jovicic, and B. Stevens, 2007: Divergence and vorticity from aircraft air motion measurements. *Journal of Atmospheric and Oceanic Technology*, 2062–2072, doi:10.1175/2007JTECHA940.1.
- Michelson, A. A. and E. W. Morley, 1887: On the relative motion of the earth and the luminiferous ether. *American Journal of Science*, **203**, 333–345.
- Murphy, D. and T. Koop, 2005: Review of the vapour pressures of ice and supercooled water for atmospheric applications. *Quarterly Journal of the Royal Meteorological Society*, **131**, 1539–1565.
- Murray, F., 1967: On the computation of saturation vapor pressure. *Journal of Applied Meteorology*, **6**, 203–204.
- Osborne, N., H. Stimson, and D. Ginnings, 1939: Measurements of heat capacity and heat of vaporization of water in the range of 0° to 100° C. *Journal of Research, National Bureau of Standards*, **23**, 197–260.
- Reineman, B. D., L. Lenain, N. M. Statom, and W. K. Melville, 2013: Development and testing of instrumentation for UAV-based flux measurements within terrestrial and marine atmospheric boundary layers. *Journal of Atmospheric and Oceanic Technology*, **30** (7), 1295–1319, doi:10.1175/JTECH-D-12-00176.1.
- Soler, T. and L. D. Hothem, 1988: Coordinate systems used in geodesy: Basic definitions and concepts. *Journal of surveying engineering*, **114** (2), 84–97.
- Thomas, R., K. Lehmann, H. Nguyen, D. Jackson, D. Wolfe, and V. Ramanathan, 2012: Measurement of turbulent water vapor fluxes using a lightweight unmanned aerial vehicle system. *Atmospheric Measurement Techniques*, **5** (1), 243–257.

- van den Kroonenberg, A., T. Martin, M. Buschmann, J. Bange, and P. Vörsmann, 2008: Measuring the wind vector using the autonomous mini aerial vehicle M²AV. *Journal of Atmospheric and Oceanic Technology*, **25** (11), 1969–1982, doi:10.1175/2008JTECHA1114.1.
- Vellinga, O. S., R. J. Dobosy, E. J. Dumas, B. Gioli, J. A. Elbers, and R. W. A. Hutjes, 2013: Calibration and quality assurance of flux observations from a small research aircraft. *Journal of Atmospheric and Oceanic Technology*, **30** (2), 161–181.
- Vellinga, O. S., B. Gioli, J. A. Elbers, A. A. M. Holtslag, P. Kabat, and R. W. A. Hutjes, 2010: Regional carbon dioxide and energy fluxes from airborne observations using flight-path segmentation based on landscape characteristics. *Biogeosciences*, **7** (4), 1307–1321, URL <http://www.biogeosciences.net/7/1307/2010/>.
- Wagner, W. and A. Pruß, 1993: International equations for the saturation properties of ordinary water substance: Revised according to the international temperature scale of 1990. *Journal of Physical and Chemical Reference Data*, **22**, 783–787.
- Zulueta, R., W. Oechel, H. Loescher, W. Lawrence, and K. T. Paw U, 2011: Aircraft-derived regional scale CO₂ fluxes from vegetated drained thaw-lake basins and interstitial tundra on the Arctic Coastal Plain of Alaska. *Global Change Biology*, **17** (9), 2781–2802.
- Zulueta, R. C., W. C. Oechel, J. G. Verfaillie, S. J. Hastings, B. Gioli, W. T. Lawrence, and K. T. Paw U, 2013: Aircraft regional-scale flux measurements over complex landscapes of mangroves, desert, and marine ecosystems of Magdalena Bay, Mexico. *Journal of Atmospheric and Oceanic Technology*, 1266–1294, doi:10.1175/JTECH-D-12-00022.1.

Part II

Leise and Masters 1993

2. AIRCRAFT KINEMATICS AND THE WIND EQUATION

In this section, we analyze required geometry and motion compensation associated with aircraft measurement. Of special importance is the wind equation used to compute ambient wind from aircraft velocity and the relative wind. Our approach is to derive this equation in Lagrangian coordinates before converting to Eulerian coordinates. An advantage of this approach is that corrections to compensate for spatial separation of sensors are derived in a rigorous way. Finally, an algorithm for required motion compensation is presented along with a FORTRAN subroutine.

We begin with a discussion of coordinate systems. Of central importance is the familiar **geographic coordinate system** in which a vector position \mathbf{p} is given as a latitude, a longitude, and an elevation above mean sea level; in principle, these quantities are referenced to the earth geoid. Velocities require additional structure; they are tangent vectors to curves and must be referenced to a Euclidean frame that moves with geographic position \mathbf{p} . In meteorology (and other earth sciences), the convention is for the x , y , and z axes to have unit direction vectors $\mathbf{i}_E(\mathbf{p})$, $\mathbf{i}_N(\mathbf{p})$, and $\mathbf{i}_Z(\mathbf{p})$ that point toward geodetic east, north, and up respectively. This is called the **geodetic frame**. We remark that in navigation, there is an alternate convention (that goes by the same name) in which the x , y , and z axes point north, east, and *down*. Needless to say, some care must be exercised in using the literature. In any case, the geodetic frame is used to measure positions and velocities *relative* to the geographic position \mathbf{p} . It is a right-hand system and so the local vertical $\mathbf{i}_Z(\mathbf{p})$ is the vector product of $\mathbf{i}_E(\mathbf{p})$ and $\mathbf{i}_N(\mathbf{p})$: $\mathbf{i}_Z(\mathbf{p}) = \mathbf{i}_E(\mathbf{p}) \times \mathbf{i}_N(\mathbf{p})$. The plane spanned by $\mathbf{i}_E(\mathbf{p})$ and $\mathbf{i}_N(\mathbf{p})$ is the (local) **horizontal**.

On board an aircraft, geographic position \mathbf{p} is obtained from navigation equipment, principally the inertial navigation system (INS). Note, however, that with the advent of sophisticated Global Positioning System (GPS) receivers and high precision accelerometers, it is possible to make the required extremely precise measurements of \mathbf{p} required for aircraft science without an INS (Crawford and Dobosy, 1992). In either case, it is natural to equate aircraft parameters with the navigation equipment used. Thus, the origin of the geodetic frame is the position of the navigation instrumentation, and aircraft velocity is the velocity of the navigation instrumentation. In straight and level flight, all points on an aircraft move at the same speed; however, in maneuvers, this is not the case. For example, in a turn, the outside wing tip moves faster than the inside wing tip. Thus,

2. Aircraft Kinematics and the Wind Equation

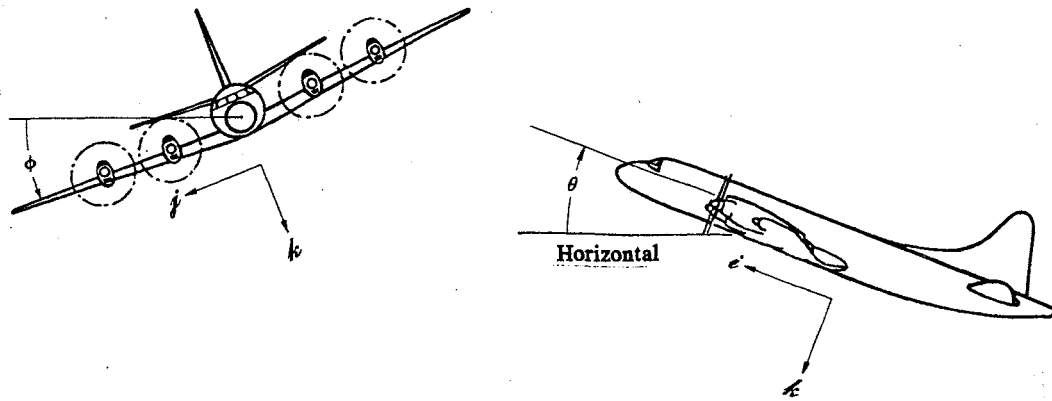


Fig. 2-1. Aircraft coordinates i, j, k , and their relation to pitch angle θ and roll angle ϕ .

corrections must be made to aircraft measurements made at locations other than that of the navigation equipment. We study this next.

The aircraft frame (also the platform frame) is another Euclidean frame that is rigidly attached to the aircraft and moves with it; the origin is again taken as the INS. Aircraft coordinates (also platform coordinates) are the positions in this frame. This can be confusing insofar as the geographic position p is still required for a complete description. We adopt the convention of using script for quantities measured in aircraft coordinates; in particular i, j , and k denote the unit direction vectors; i points forward along the axis of the fuselage, j points in the direction of the right wing (relative to the pilot), and k points down (under normal flight conditions) as shown in Fig. 2-1. Again, this is a right-hand system $k=i \times j$. To help see the relationship to the geodetic frame, suppose an observer on the ground sees a cloud as stationary; its geographic position stays the same. However, when viewed from inside an aircraft, the cloud is seen to go by at the speed of the aircraft; in this situation, the cloud has a vector velocity in the aircraft frame that is precisely the *negative* of the aircraft velocity in the geodetic frame.

Because most aircraft measurement is done in the aircraft frame, data must be transformed to the geodetic frame. Parameters used consist of three attitude angles: the yaw or heading ψ , the pitch θ , and the roll ϕ ; these angles are supplied by the INS. Heading tells us the horizontal direction of flight; pitch tells us how much the nose is pointed up (or down), and roll tells us how much the aircraft is banked (e.g. when turning). Pitch and roll

2. Aircraft Kinematics and the Wind Equation

are also illustrated in Fig. 2-1 .

The transformation required to convert *observed data* between frames is computed in factored form by sequentially removing the dependence on roll, pitch, and heading together with a relabeling of axes. The way in which these angles are expressed is a matter of convention. Heading is measured clockwise from geodetic north, like on a compass; pitch is measured from the local horizontal to a line through the fuselage, it is positive when the nose is pointed up; finally, roll is measured in the $j-k$ plane, it is positive in a right-hand, clockwise turn (right wing down).

The first rotation $\mathbf{T}_1(\phi)$ removes roll; it is a rotation about the i axis with matrix representation:

$$(2.1) \quad \mathbf{T}_1(\phi) = \begin{bmatrix} 1 & 0 & 0 \\ 0 & \cos \phi & -\sin \phi \\ 0 & \sin \phi & \cos \phi \end{bmatrix} .$$

Thus, a vector position \mathbf{r}_0 observed in the aircraft frame is transformed into a new position $\mathbf{r}_1 = \mathbf{T}_1(\phi)\mathbf{r}_0$ computed as the product of a matrix and a column vector; it is the hypothetical position that would be observed if the aircraft was flying without roll (wings horizontal). To check orientation, an aircraft flying to the north and on its side $\phi = \pi/2$ (right wing down), will result in the k -axis pointing west; after rotation, positions west will be off the left wing and will have negative values as required by (2.1).

The next rotation $\mathbf{T}_2(\theta)$ removes the pitch:

$$(2.2) \quad \mathbf{T}_2(\theta) = \begin{bmatrix} \cos \theta & 0 & \sin \theta \\ 0 & 1 & 0 \\ -\sin \theta & 0 & \cos \theta \end{bmatrix} .$$

Now, $\mathbf{r}_2 = \mathbf{T}_2(\theta)\mathbf{r}_1$ is the position observed from a hypothetical aircraft flying horizontally (no pitch and no roll).

The last rotation $\mathbf{T}_3(\psi)$ removes the heading:

$$(2.3) \quad \mathbf{T}_3(\psi) = \begin{bmatrix} \cos \psi & -\sin \psi & 0 \\ \sin \psi & \cos \psi & 0 \\ 0 & 0 & 1 \end{bmatrix} .$$

Now $\mathbf{r}_3 = \mathbf{T}_3(\psi)\mathbf{r}_2$ is the position observed by a hypothetical aircraft flying horizontally and due north. This would be the answer except that the axes are reversed; present coordinates of the hypothetical aircraft frame point north, east, and down, and must be transformed to east, north and up. This is done with the permutation \mathbf{T}_4 :

2. Aircraft Kinematics and the Wind Equation

$$(2.4) \quad \mathbf{T}_4 = \begin{bmatrix} 0 & 1 & 0 \\ 1 & 0 & 0 \\ 0 & 0 & -1 \end{bmatrix}.$$

Thus, the wanted position in the geodetic frame is $\mathbf{r} = \mathbf{T}_4 \mathbf{b}_3$. Sometimes, these last two transformations are combined into $\tilde{\mathbf{T}}_3(\psi)$:

```

SUBROUTINE TRAN(XA,XG,CS,SN,MODE)
C *****Jim Leise 6/85.
C Transform position data XA(3) from the aircraft frame to the
C geodetic frame XG(3) using the rotation implicit in the
C direction cosines CS(3) and sines SN(3). Mode specifies
C the transformation or its inverse.
C   MODE= 1 ... Aircraft ==> Geodetic ... XA ==> XG.
C   MODE=-1 ... Geodetic ==> Aircraft ... XG ==> XA.
C Also, the code is configured so that the replacement implicit
C in "CALL TRAN(Z,Z,CS,SN,MODE)" is valid.
DIMENSION XA(3),XG(3),CS(3),SN(3)
C
  IF(MODE.EQ.1)THEN
C....   Aircraft ==> Geodetic.
        XRL= XA(1)                ! Take out the roll.
        YRL= CS(1)*XA(2) - SN(1)*XA(3)
        ZRL= SN(1)*XA(2) + CS(1)*XA(3)
C
        XPC= CS(2)*XRL + SN(2)*ZRL    ! Take out the pitch.
        YPC= YRL
        ZPC=-SN(2)*XRL + CS(2)*ZRL
C
        XG(1)= SN(3)*XPC + CS(3)*YPC    ! Take out the heading
        XG(2)= CS(3)*XPC - SN(3)*YPC    ! & flip vertical.
        XG(3)=-ZPC
  ELSE
C....   Geodetic ==> Aircraft.
        XPC= SN(3)*XG(1) + CS(3)*XG(2) ! Put in the heading
        YPC= CS(3)*XG(1) - SN(3)*XG(2) ! & flip vertical.
        ZPC=-XG(3)
C
        XRL= CS(2)*XPC - SN(2)*ZPC    ! Put in the pitch.
        YRL= YPC
        ZRL= SN(2)*XPC + CS(2)*ZPC
C
        XA(1)= XRL                ! Put in the roll.
        XA(2)= CS(1)*YRL + SN(1)*ZRL
        XA(3)=-SN(1)*YRL + CS(1)*ZRL
  ENDIF
END

```

Fig. 2-2. FORTRAN listing of basic transformation relating aircraft coordinates to earth coordinates.

2. Aircraft Kinematics and the Wind Equation

$$(2.5) \quad \tilde{\mathbf{T}}_3(\psi) = \mathbf{T}_4 \mathbf{T}_3(\psi) = \begin{bmatrix} \sin \psi & \cos \psi & 0 \\ \cos \psi & -\sin \psi & 0 \\ 0 & 0 & -1 \end{bmatrix}.$$

which has the slight computational advantage of saving a step. In any case, the total transformation \mathbf{G} between frames is the matrix product:

$$(2.6) \quad \boxed{\mathbf{G} = \mathbf{T}_4 \mathbf{T}_3(\psi) \mathbf{T}_2(\theta) \mathbf{T}_1(\phi) = \tilde{\mathbf{T}}_3(\psi) \mathbf{T}_2(\theta) \mathbf{T}_1(\phi)}.$$

Thus, an observed position \mathbf{r}_0 in the aircraft frame is transformed to the vector position $\mathbf{r} = \mathbf{G} \mathbf{r}_0$ in the geodetic frame.

A FORTRAN subroutine for (2.6) together with the inverse is given in Fig. 2-2; in this code, attitude angles are given in trigonometric form, that is,

$$\begin{array}{ll} \text{CS}(1) = \text{COS}(\phi) & \text{SN}(1) = \text{SIN}(\phi) \\ \text{CS}(2) = \text{COS}(\theta) & \text{SN}(2) = \text{SIN}(\theta) \\ \text{CS}(3) = \text{COS}(\psi) & \text{SN}(3) = \text{SIN}(\psi) \end{array}$$

which helps avoid redundant computation and saves time.

Analysis of Lagrangian Motions We denote the Lagrangian position of an air parcel observed in *aircraft coordinates* as $\mathbf{x}(t; t_0)$. Note that geographic position \mathbf{p} as well as attitude angles depend on time t , and the parameter t_0 is used to distinguish a parcel as "arriving" at a given position \mathbf{r} when $t = t_0$, that is, $\mathbf{r} = \mathbf{x}(t_0; t_0)$. To fix ideas, suppose that \mathbf{r} is the position (in aircraft coordinates) of a boom on the left wing tip as illustrated in Fig. 2-3. The sensor will pass through the given air parcel at time $t = t_0$. Then the **Lagrangian trajectory** of this parcel, relative to the earth, is

$$(2.7) \quad \boxed{\mathbf{x}(t; t_0) = \mathbf{p}(t) + \mathbf{G}(t) \mathbf{x}(t; t_0)}.$$

This equation uses the flat earth approximation insofar as $\mathbf{p}(t)$ is geographic position on a curved earth while $\mathbf{G}(t) \mathbf{x}(t; t_0)$ is a vector in a Euclidean frame, and addition requires a common set of units. A velocity equation then results by differentiating (2.7) with respect to time

$$(2.8) \quad \mathbf{u}(t; t_0) = \mathbf{U}_0(t) + \dot{\mathbf{G}}(t) \mathbf{x}(t; t_0) + \mathbf{G}(t) \mathbf{u}(t; t_0).$$

where $\mathbf{u}(t; t_0) = \dot{\mathbf{x}}(t; t_0)$ is the (true) parcel velocity as observed from the ground; $\mathbf{U}_0(t) = \dot{\mathbf{p}}(t)$ is the aircraft velocity supplied by the INS, and $\mathbf{u}(t; t_0) = \dot{\mathbf{x}}(t; t_0)$ is the parcel velocity observed from the aircraft frame. Note that, although we started from an approximation (2.7), this equation is exact

2. Aircraft Kinematics and the Wind Equation

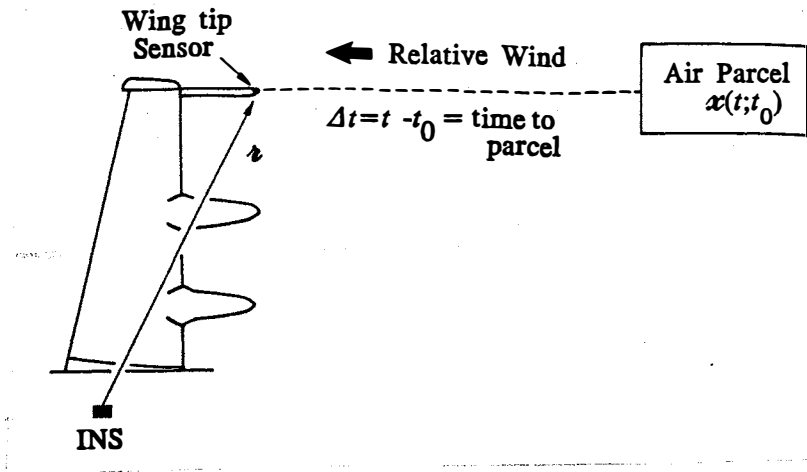


Fig. 2-3. Illustration of the Lagrangian position of an air parcel observed in aircraft coordinates. The wingtip sensor (at position \mathbf{r} in aircraft coordinates) passes through an air parcel located at $\mathbf{x}(t; t_0)$ at time t_0 .

because velocities are tangent vectors in the geodetic frame.

Now, at time $t=t_0$, the relative wind vector $\mathbf{u}_r(t)$ measured at \mathbf{r} on the boom is the parcel velocity $\mathbf{u}_r(t_0)=\dot{\mathbf{x}}(t_0; t_0)$. Also, at time $t=t_0$, the incremental velocity of the wing tip due to changing attitude angles is $\Delta\mathbf{U}(t_0)=\dot{\mathbf{G}}(t_0)\mathbf{x}(t_0; t_0)=\dot{\mathbf{G}}(t_0)\mathbf{r}$. The important observation is that by changing the indexing time t_0 , all measured winds $\mathbf{u}_r(t_0)$ are accounted for. In other words, every parcel of air that intersects the wing tip can be described as being part of a trajectory indexed by some t_0 . The deduced ambient wind resulting from such measurement is then abbreviated $\mathbf{u}(t_0)=\mathbf{u}(t_0; t_0)$. At this point, subscript notation is superfluous, and we change t_0 to t . Substitution into (2.8) then gives the wind equation used to compute the ambient-wind vector $\mathbf{u}(t)$ at the point of relative-wind measurement:

(2.9)

$$\mathbf{u}(t) = \mathbf{U}_0(t) + \mathbf{U}_r(t) + \Delta\mathbf{U}(t)$$

where, as above, $\mathbf{U}_0(t)=\dot{\mathbf{p}}(t)$ is the aircraft velocity supplied by the INS, $\mathbf{U}_r(t)=\mathbf{G}(t)\mathbf{u}_r(t)$ is the relative wind vector and $\Delta\mathbf{U}(t)=\dot{\mathbf{G}}(t)\mathbf{r}$ is the incremental velocity of a sensor located at \mathbf{r} . Ideally, this sensor is located next to the INS ($\mathbf{r} \cong 0$) and $\Delta\mathbf{U}(t)$ can be neglected. Unfortunately, this is often not the case. For example, if as on the P-3's, the velocity sensor is located on the left wing tip which extends, say, 15m from the fuselage (where the INS is located), then in a maneuver consisting of a two minute circle (bank angle 30°), the incremental velocity $\Delta\mathbf{U}(t)$ is in excess of 50 cm/s which is competitive with desired accuracy.

2. Aircraft Kinematics and the Wind Equation

At this point we need some matrix and vector-space concepts. First, a (square) matrix \mathbf{A} is **orthogonal** if its inverse is the matrix transpose $\mathbf{A}^{-1} = \mathbf{A}^T$; thus, $\mathbf{A}\mathbf{A}^T = \mathbf{A}^T\mathbf{A} = \mathbf{I}$ where \mathbf{I} is the identity matrix. It is easily verified that the above \mathbf{T}_k are orthogonal; consequently, so is the total transformation \mathbf{G} of (2.6). In passing, it is worth observing that the rotation matrices \mathbf{T}_1 , \mathbf{T}_2 , and \mathbf{T}_3 also have the (group) properties:

$$\mathbf{T}_k(\omega_1 + \omega_2) = \mathbf{T}_k(\omega_1)\mathbf{T}_k(\omega_2) \quad \text{and} \quad \mathbf{T}_k^{-1}(\omega) = \mathbf{T}_k(-\omega); \quad k=1,2,3$$

which are properties not shared by $\tilde{\mathbf{T}}_3(\psi)$.

Recall that the dot (or inner) product $\mathbf{x} \cdot \mathbf{y}$ of two (column) vectors of real numbers $\mathbf{x} = (x_1, x_2, x_3)^T$ and $\mathbf{y} = (y_1, y_2, y_3)^T$ is defined

$$(2.10) \quad \mathbf{x} \cdot \mathbf{y} = \mathbf{x}^T \mathbf{y} = x_1 y_1 + x_2 y_2 + x_3 y_3,$$

and the Euclidean length (or norm) is $\|\mathbf{x}\| = \sqrt{\mathbf{x} \cdot \mathbf{x}}$. It follows that for any set of attitude angles that $\|\mathbf{G}\boldsymbol{\zeta}\| = \|\boldsymbol{\zeta}\|$. This is because \mathbf{G} is orthogonal, and orthogonal transformations always preserve dot products:

$$\mathbf{G}\boldsymbol{\zeta} \cdot \mathbf{G}\boldsymbol{\zeta} = (\mathbf{G}\boldsymbol{\zeta})^T \mathbf{G}\boldsymbol{\zeta} = (\boldsymbol{\zeta}^T \mathbf{G}^T) \mathbf{G}\boldsymbol{\zeta} = \boldsymbol{\zeta}^T (\mathbf{G}^T \mathbf{G}) \boldsymbol{\zeta} = \boldsymbol{\zeta}^T \mathbf{I} \boldsymbol{\zeta} = \boldsymbol{\zeta} \cdot \boldsymbol{\zeta}.$$

We remark that the distinction between row and column vectors is only relevant in matrix calculations; vectors are usually given as row vectors.

With this background, we now estimate the incremental velocity $\Delta \mathbf{U}(t) = \dot{\mathbf{G}}(t)\boldsymbol{\zeta}$. One way to do this is to differentiate $\mathbf{G}(t)$ by parts. However, it is more direct to difference positions $\mathbf{r}(t) = \mathbf{G}(t)\boldsymbol{\zeta}$ directly: $\Delta \mathbf{U}(t) = \dot{\mathbf{r}}(t)$. Thus, numerical estimates of $\Delta \mathbf{U}(t_k)$ can be obtained from the (3-point) difference

$$(2.11) \quad \Delta \mathbf{U}(t_k) = \dot{\mathbf{r}}_k \cong (\mathbf{r}_{k+1} - \mathbf{r}_{k-1}) / (t_{k+1} - t_{k-1})$$

where $\mathbf{r}_k = \mathbf{G}(t_k)\boldsymbol{\zeta}$ and $\dot{\mathbf{r}}_k = \dot{\mathbf{G}}(t_k)\boldsymbol{\zeta}$. This is a difference of vectors and two kinds of errors can occur, errors in amplitude and errors in direction. Of the two, errors in direction are the more serious because incremental velocities in the horizontal could end up in the vertical. It is therefore useful to model the velocity estimate as

$$(2.12) \quad \boxed{\Delta \mathbf{U}(t_k) = \|\Delta \mathbf{U}(t_k)\| \mathbf{i}_k}$$

where the amplitude $\|\Delta \mathbf{U}(t_k)\|$ is computed from (2.11) and the direction vector \mathbf{i}_k is yet to be determined. A better estimate of \mathbf{i}_k can be obtained from the condition that \mathbf{i}_k be orthogonal to \mathbf{r}_k , that is, $\mathbf{i}_k \cdot \mathbf{r}_k = 0$. To understand this condition, first observe from (2.12) that \mathbf{i}_k should point in the same direction as $\dot{\mathbf{r}}_k = \Delta \mathbf{U}(t_k)$; consequently, $\mathbf{i}_k \cdot \mathbf{r}_k = 0 \Leftrightarrow \dot{\mathbf{r}}_k \cdot \mathbf{r}_k = 0$. But $\mathbf{G}(t)$ is

2. Aircraft Kinematics and the Wind Equation

orthogonal and preserves lengths; hence,

$$\dot{\mathbf{r}}(t) \cdot \mathbf{r}(t) = \frac{1}{2} \frac{d}{dt} [\mathbf{r}(t) \cdot \mathbf{r}(t)] = \frac{1}{2} \frac{d}{dt} [r \cdot r] = 0,$$

and the conclusion $\mathbf{i}_k \cdot \mathbf{r}_k = 0$ follows. A good estimate of \mathbf{i}_k can then be constructed as the following linear combination of \mathbf{r}_{k+1} and \mathbf{r}_{k-1} :

$$(2.13) \quad \mathbf{i}_k = \mathbf{d}_k / \|\mathbf{d}_k\| \quad \text{where} \quad \mathbf{d}_k = (\mathbf{r}_k \cdot \mathbf{r}_{k-1}) \mathbf{r}_{k+1} - (\mathbf{r}_k \cdot \mathbf{r}_{k+1}) \mathbf{r}_{k-1}$$

Indeed, a simple calculation verifies that $\mathbf{i}_k \cdot \mathbf{r}_k = 0$. Should the denominator $\|\mathbf{d}_k\|$ vanish, it is consistent to simply set $\mathbf{i}_k = 0$. In turn, this direction is used in (2.12) to complete the estimate of $\Delta \mathbf{U}(t_k)$. While this may seem unduly complicated, it is still considerably easier and less prone to error than differentiating $\mathbf{G}(t)$ by parts. We remark that this same procedure is well suited for real-time application, i.e., applications which use data only from the past, say, at times t_k and t_{k-1} . In this case, formulas are obtained by simply setting $k+1$ to k in (2.11) and (2.12). Clearly, orthogonality has a stronger effect in this situation.

A FORTRAN listing for such a real-time algorithm is given in Fig. 2-4. This subroutine in tandem with the transformation of Fig. 2-2, form the basis of all motion compensation presented in this work. However, note that this motion compensation is incomplete insofar as it cannot correct for the vertical bobbing motion of a wing, or other vibrations of the aircraft. The best solution for motion compensation is not to have to do any at all, by mounting all of one's sensors at the location of the navigation instrumentation. This approach has been used by Crawford and Dobosy [1992].

2. Aircraft Kinematics and the Wind Equation

```

SUBROUTINE VROT(PROBE, PLAST, UROT, CS, SN)
C *****Jim Leise 6/85.
C Real-time method for computing rotational velocities due
C to changing attitude angles. This algorithm uses the
C condition that velocity direction is orthogonal to position.
C   PROBE(3) =Probe position in aircraft coordinates.
C   PLAST(3) =Stored value from last call.
C   UROT(3)  =Answer: rotational velocity in earth coordinates.
C   CS(3)   =Attitude cosines.
C   SN(3)   =Attitude sines.
C   DIMENSION PROBE(3), PLAST(3), UROT(3), CS(3), SN(3), Pnow(3)
C
C.... First, rotate the PROBE position to geodetic coordinates.
C =====
C CALL TRAN(PROBE, Pnow, CS, SN, 1)
C =====
C
C.... Store velocity energy (=amp**2) in Vamp.
C   Pdot=0. ! Initialize.
C   Pmag=0. ! ...
C   Vamp=0. ! ...
C   DO 10 K=1,3
C   Pdot=Pdot+Pnow(K)*PLAST(K) ! Compute inner product.
C   Pmag=Pmag+Pnow(K)**2 ! Used to orthogonalize.
C 10 Vamp=Vamp+(Pnow(K)-PLAST(K))**2 ! Get velocity energy.
C
C.... Get orthogonal direction UROT.
C   Erot=0.
C   DO 20 K=1,3
C   UROT(K)=Pdot*Pnow(K)-Pmag*PLAST(K) ! Orthogonalize.
C 20 Erot=Erot+UROT(K)**2 ! Used to normalize.
C
C.... Put amplitude and direction together.
C   Vnorm=0. ! Default.
C   IF(Erot.GT.0.)Vnorm=SQRT(Vamp/Erot) ! Get normalization.
C   DO 30 K=1,3
C   UROT(K) =Vnorm*UROT(K) ! Do normalization.
C 30 PLAST(K)=Pnow(K) ! Save: Pnow ==> PLAST.
C
END

```

Fig. 2-4. FORTRAN listing of subroutine used to compute rotational velocities caused by changing attitude angles.

3. GEOMETRY OF RELATIVE-WIND COMPUTATION

Recall that the relative wind $\mathcal{U}_r(t)$ at a point \mathcal{r} (aircraft coordinates) is the parcel motion relative to the aircraft frame. With in-situ measurement, \mathcal{r} is a point on (or near) the aircraft, and the relative wind is the motion of the airstream in the immediate vicinity of the aircraft; with remote measurement, say from a Doppler radar or lidar, \mathcal{r} is some distance away. Although measurement techniques vary, there is much overlap in the equations and analysis.

The scheme of interest here is one in which the amplitude and direction are measured independently. The amplitude $\|\mathcal{U}_r(t)\|$ is called **true airspeed** and will be denoted τ ; the vector direction is $\hat{e}_r = \mathcal{U}_r / \|\mathcal{U}_r\|$ and satisfies $\mathcal{U}_r(t) = \tau(t)\hat{e}_r(t)$. The standard way to measure τ is indirect; it is inferred from dynamic pressure using Bernoulli's equation for an ideal gas (derived latter in Sec. 5). Direct measurement of τ can be achieved with Doppler lidar; as a direct measurement there is no theoretical limitation on accuracy.

The standard way of obtaining the direction \hat{e}_r is with **flow-angle** sensors that measure the pressure gradient field. Although flow-angle measurement is also model dependent, it is more direct than using Bernoulli's equation. In any case, two angles are required to resolve direction: the **attack angle** α and the **slip angle** β ; both are measured in aircraft coordinates as illustrated in Fig. 3-1.

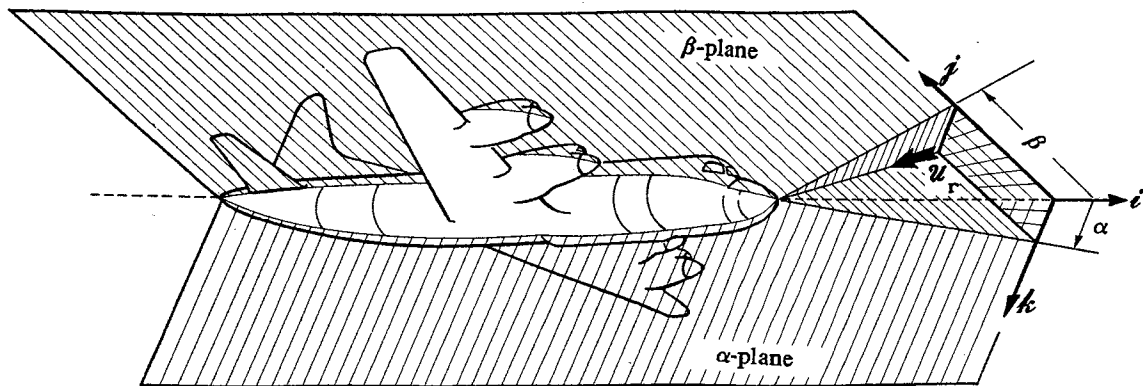


Fig. 3-1. Aircraft attack angle α , slip angle β , and aircraft coordinate axes i , j , and k used to compute relative wind \mathcal{U}_r .

3. Geometry of Relative-Wind Computation

In straight and level flight, the attack angle is measured in the same vertical plane as the pitch angle. Under normal flight conditions and with no ambient wind, pitch and attack are nearly the same; in particular, they have the same sign.

To understand slip, we need the track angle ζ which is the angle (measured clockwise in the horizontal) between geodetic north and the direction of horizontal aircraft velocity $\mathbf{U}_H = (U_0, V_0, 0)$ as shown in Fig. 3-2; more precisely, $\zeta = \tan^{-1}(U_0/V_0)$. The polar form $\mathbf{U}_H = U_H \mathbf{i}_\zeta$ of horizontal velocity is also useful where $U_H = \|\mathbf{U}_H\| = (U_0^2 + V_0^2)^{1/2}$ is the horizontal groundspeed, and \mathbf{i}_ζ is the track direction $\mathbf{i}_\zeta = \mathbf{U}_H / U_H = \sin \zeta \mathbf{i}_E + \cos \zeta \mathbf{i}_N$.

For present purposes, track is needed to describe the drift angle d which is computed as the difference between track and heading $d = \zeta - \psi$. Note that under normal flight conditions and with no ambient wind, drift and slip are nearly the same; in particular they also have the same sign.

Now suppose that ambient wind is changing and/or the aircraft is in a maneuver. Then the attack and slip will depart from the pitch and drift. This is due to such things as aircraft inertia and related flight characteristics. For example, when an aircraft is "shocked", say with a turbulent updraft, the effect on the flow angles is immediate; however it takes some time for other parameters to adjust.

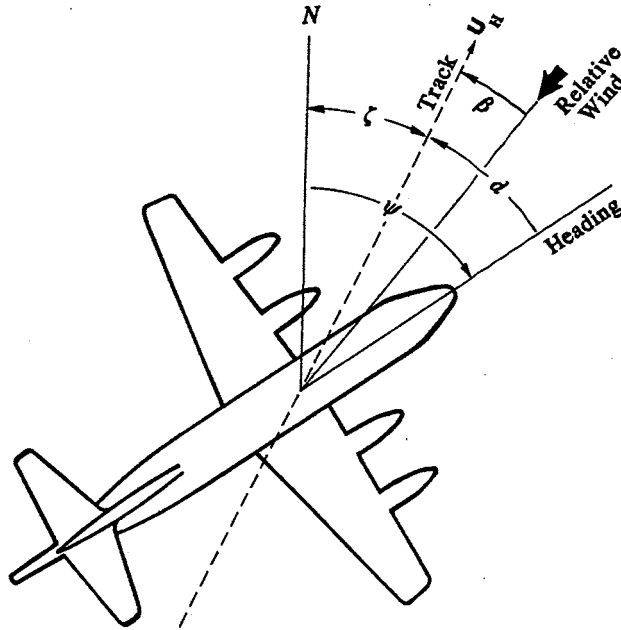


Fig. 3-2. Geometrical relationship of aircraft heading angle ψ , slip angle β , drift angle d , and track angle ζ to horizontal aircraft velocity (groundspeed) \mathbf{U}_H , and relative wind.

3. Geometry of Relative-Wind Computation

In more detail, attack angle α is the angle between the fuselage direction \hat{i} and the projection of the relative wind onto the $\hat{i}\hat{k}$ plane. The slip angle β is the angle between \hat{i} and the projection of the relative wind onto the $\hat{i}\hat{j}$ plane. If we expand the the relative-wind vector \mathcal{U}_r in terms of its vector components:

$$(3.1) \quad \mathcal{U}_r = \mathcal{U}_r \hat{i} + \mathcal{V}_r \hat{j} + \mathcal{W}_r \hat{k},$$

the attack and slip angles must satisfy:

$$(3.2) \quad \tan \alpha = \mathcal{W}_r / \mathcal{U}_r \quad \text{and} \quad \tan \beta = \mathcal{V}_r / \mathcal{U}_r.$$

Note that sign conventions for α and β are implicit in these equations. Consider an aircraft to flying nose up with (small) positive pitch in a quiet atmosphere; the relative wind will be observed as coming primarily from the front ($\mathcal{U}_r < 0$) and slightly from below ($\mathcal{W}_r < 0$), and (3.2) requires attack α to be positive. Thus, as stated above, attack and pitch generally have the same sign.

Now, because $\mathcal{U}_r < 0$, the vector $\mathcal{U}_r / \mathcal{U}_r = (\mathcal{U}_r / \mathcal{U}_r, \mathcal{V}_r / \mathcal{U}_r, \mathcal{W}_r / \mathcal{U}_r)$ has direction opposite to \mathcal{U}_r ; thus, normalization and a change of sign gives the direction of the relative wind

$$(3.3) \quad \hat{i}_r = -(\hat{i} + \tan \beta \hat{j} + \tan \alpha \hat{k}) / D$$

$$\text{where } D = \sqrt{1 + \tan^2 \beta + \tan^2 \alpha}$$

Note that D is simply the normalization required for a unit vector.

Doppler We next consider the case where true airspeed is (implicitly) measured using back scatter from a Doppler radar or lidar. To fix ideas, suppose that a CW lidar with a fixed beam is focused a few meters in front of the aircraft. Such a sensor can only measure the radial velocity component (i.e., velocity in the direction of the transmission beam). In other words, if the beam direction is \hat{i}_D (aircraft coordinates), then the measured Doppler velocity \mathcal{V}_D is the projection of the relative wind onto \hat{i}_D ; thus, $\mathcal{V}_D = \mathcal{U}_r \cdot \hat{i}_D$. If, in addition, we know \hat{i}_r from flow-angle sensors, then the equation obtained from the dot product of the relative wind $\mathcal{U}_r = \tau \hat{i}_r$ with \hat{i}_D can be solved for true airspeed $\tau = \mathcal{U}_r \cdot \hat{i}_D / \hat{i}_r \cdot \hat{i}_D$. Thus, true airspeed can be computed from the Doppler velocity \mathcal{V}_D as

3. Geometry of Relative-Wind Computation

$$(3.4) \quad \tau = \mathcal{V}_D / (\dot{\mathbf{i}}_r \cdot \dot{\mathbf{i}}_D)$$

Note, that although $\dot{\mathbf{i}}_D$ is a fixed direction, both \mathcal{V}_D and $\dot{\mathbf{i}}_r$ vary with time t .

Motion Compensation So far, we have been working with the tacit assumption that the true airspeed τ and the direction $\dot{\mathbf{i}}_r$ are both measured in the same place, from a single sensor. We now consider the situation where this is not the case. To fix ideas, suppose that true airspeed is measured from a boom mounted on the left wing tip at position \mathbf{r}_w (relative to the INS). Also suppose that the vector direction is measured near the nose of the aircraft at position \mathbf{r}_n . To help visualize the problem, note that in a turn, true airspeed measured at the wing tip and at the nose are not the same. Consequently, the true airspeed must be adjusted before it can be combined with the vector direction. Because spurious or unwanted motion is the source of the problem, this adjustment is an example of what is generally referred to as motion compensation.

Recall that in the wind equation (2.9), the incremental velocity $\Delta \mathbf{U}$ (computed in geodetic coordinates) is the velocity adjustment for differences in sensor location; computational formulas were given in (2.11) and (2.13). These same incremental velocities will now be used to adjust for lack of spatial contiguity in the true airspeed and direction measurements. To begin, suppose that $\Delta_w \mathbf{U}$ is the incremental velocity of the position \mathbf{r}_w on the left wing tip and $\Delta_n \mathbf{U}$ is the incremental velocity of the position \mathbf{r}_n near the nose. Then $\Delta_{wn} \mathbf{U} = \Delta_w \mathbf{U} - \Delta_n \mathbf{U}$ is the velocity of position \mathbf{r}_w relative to position \mathbf{r}_n . To use this correction, the direction vector $\dot{\mathbf{i}}_{r,n}$ measured at \mathbf{r}_n must be transformed to the geodetic frame $\mathbf{i}_{r,n} = \mathbf{G} \dot{\mathbf{i}}_{r,n}$ where \mathbf{G} is the transformation (2.6); because \mathbf{G} preserves lengths, $\mathbf{i}_{r,n}$ is also a direction vector. Suppose next that τ_w is the measured true airspeed at \mathbf{r}_w and $\hat{\tau}_n$ is the (unknown) true airspeed at \mathbf{r}_n . Then $\tau_w = \|\mathbf{U}_{r,w}\|$ is the amplitude of the relative wind at \mathbf{r}_w , and $\mathbf{U}_{r,n} = \hat{\tau}_n \mathbf{i}_{r,n}$ is the relative wind at \mathbf{r}_n . Finally, an equation relating these quantities can be derived from the wind equation (2.9). To do this, we model the ambient wind \mathbf{u} measured on the wing tip and on the nose as being the same; thus,

$$(3.5) \quad \begin{aligned} \mathbf{u} = \mathbf{U}_0 + \mathbf{U}_{r,w} + \Delta_w \mathbf{U} = \mathbf{U}_0 + \mathbf{U}_{r,n} + \Delta_n \mathbf{U} &\Rightarrow \mathbf{U}_{r,w} - \mathbf{U}_{r,n} + (\Delta_w \mathbf{U} - \Delta_n \mathbf{U}) = 0 \\ &\Rightarrow \mathbf{U}_{r,w} = \mathbf{U}_{r,n} - \Delta_{wn} \mathbf{U} \end{aligned}$$

where, as above, $\Delta_{wn} \mathbf{U} = \Delta_w \mathbf{U} - \Delta_n \mathbf{U}$. This equation relates the relative wind at any

3. Geometry of Relative-Wind Computation

two points \hat{e}_w and \hat{e}_n on (or near) the aircraft; the wing tip and nose have been used as an aid to exposition. A true airspeed equation then results by taking amplitudes:

$$(3.6) \quad \begin{aligned} \tau_w^2 &= \|\mathbf{U}_{r,w}\|^2 = \|\mathbf{U}_{r,n} - \Delta_{wn} \mathbf{U}\|^2 = \|\hat{\tau}_n \hat{\mathbf{i}}_{r,n} - \Delta_{wn} \mathbf{U}\|^2 \\ &= (\hat{\tau}_n \hat{\mathbf{i}}_{r,n} - \Delta_{wn} \mathbf{U}) \cdot (\hat{\tau}_n \hat{\mathbf{i}}_{r,n} - \Delta_{wn} \mathbf{U}) \\ &= \hat{\tau}_n^2 - 2\hat{\tau}_n (\hat{\mathbf{i}}_{r,n} \cdot \Delta_{wn} \mathbf{U}) + \|\Delta_{wn} \mathbf{U}\|^2 \end{aligned}$$

which is a quadratic equation in $\hat{\tau}_n$ with exact solutions; all other quantities: τ_w , $\hat{\mathbf{i}}_{r,n}$, and $\Delta_{wn} \mathbf{U}$ are known. A good approximation is

$$(3.7) \quad \boxed{\hat{\tau}_n \cong \tau_w + (\hat{\mathbf{i}}_{r,n} \cdot \Delta_{wn} \mathbf{U})}$$

which will be further analyzed in Sec. 10. As a check on signs, note that in a right turn the left wing tip will be traveling faster than the nose

$$\tau_w > \hat{\tau}_n,$$

and $\Delta_{wn} \mathbf{U}$ will be in the direction of aircraft motion \mathbf{U}_0 . Because $\hat{\mathbf{i}}_{r,n}$ is opposite to \mathbf{U}_0 , it follows that $(\hat{\mathbf{i}}_{r,n} \cdot \Delta_{wn} \mathbf{U}) < 0$ and (3.7) is consistent. In any case, the relative wind at the nose can now be computed as $\mathbf{U}_{r,n} = \hat{\tau}_n \hat{\mathbf{i}}_{r,n}$ and the ambient wind (at \hat{e}_n) is obtained from the wind equation (2.9) as $\mathbf{u}(t) = \mathbf{U}_0(t) + \mathbf{U}_{r,n}(t) + \Delta_n \mathbf{U}$.

Doppler Measurement The last level of complexity is to replace the true-airspeed sensor with a Doppler sensor. If, as above, the sensor is located on the wing tip, then the true-airspeed computation $\tau_w = \mathcal{V}_D / (\hat{\mathbf{e}}_{r,w} \cdot \hat{\mathbf{e}}_D)$ also requires the relative-wind direction $\hat{\mathbf{e}}_{r,w}$ on the wing tip. Again, we convert to geodetic coordinates. Because \mathbf{G} is orthogonal, it preserves dot products and so $\tau_w = \mathcal{V}_D / (\hat{\mathbf{i}}_{r,w} \cdot \hat{\mathbf{i}}_D)$ where $\hat{\mathbf{i}}_{r,w} = \mathbf{G} \hat{\mathbf{e}}_{r,w}$ and $\hat{\mathbf{i}}_D = \mathbf{G} \hat{\mathbf{e}}_D$. With notation as above, measured parameters on the wing tip and on the nose still satisfy (3.5) and substitution gives

$$(3.8) \quad \boxed{\mathcal{V}_D \hat{\mathbf{i}}_{r,w} / (\hat{\mathbf{i}}_{r,w} \cdot \hat{\mathbf{i}}_D) = \hat{\tau}_n \hat{\mathbf{i}}_{r,n} - \Delta_{wn} \mathbf{U}}$$

The unknowns, $\hat{\mathbf{i}}_{r,w}$ and $\hat{\tau}_n$, (together) comprise three degrees of freedom. As a vector equation, (3.8) consists of three equations, and the (nonlinear) problem of computing both $\hat{\mathbf{i}}_{r,w}$ and $\hat{\tau}_n$, although nonlinear, is well posed. While a closed-form solution appears unlikely, a convergent sequence of approximations can be obtained with iterative "improvement" of $\hat{\mathbf{i}}_{r,w}$ and $\hat{\tau}_n$. In

3. Geometry of Relative-Wind Computation

any case, putting a Doppler sensor on the wing tip is not very realistic. In practice, such a sensor would be put closer to the flow-angle sensor, in which case (3.8) might not even be needed.

A question of some relevance is "Do sensors at different locations really measure the same thing?" The problem here is one of scale sizes. For a nominal airspeed of 100m/s and data acquired at 1Hz (one sample per second), a separation between sensors up to about 20m could be expected to give meaningful results. That is, provided features smaller than 100m are filtered out in the data acquisition. In effect, this means that data must be acquired at rates significantly higher than 1Hz and then prefiltered or averaged to the 1-Hz rate. Increasing the sample rate changes these numbers proportionally; for 10Hz data, sensors should not be separated by more than about 2m. To achieve high data rates with a CW lidar focused, say, 10m in front of the aircraft, it is possible to simply delay or phase shift acquired data by 0.1s before combining with directional data near the aircraft nose. In this situation, the relevant separation distance is the distance between the air parcel illuminated by the lidar and the air parcel that will, in fact, impact the flow-angle sensors 0.1s later.

4. BASIC ATMOSPHERIC THERMODYNAMICS

Because of the elusive nature of thermodynamic reasoning, we here review basic concepts and ideas relevant to airborne science. Much of the following material is based on Dutton (1976). It is here useful to use the units decagrams (da g) for density and hecto-Pascals (hPa) for pressures (1 hPa = 1 millibar). A natural place to begin is with the **ideal gas law** (Boyle's-Charles' law) which states that pressure p (hPa) is proportional to density ρ (da g/m³) times temperature T (°K):

(4.1)

$$p = \rho RT$$

where R (J/kg-mole-°K) is the, material dependent, gas constant. It is related to the universal gas constant $R^* = 8.314 \times 10^3$ J/°K by the equation $R = R^*/\mu$ where μ (kg-mole) is the molar weight (kg \times molecular weight). The odd units da g/m³ for density is an artifact of using millibars (hPa) for pressure. For example, the molecular weight of dry air is 28.968 which gives 287.04 J/(kg-mole-°K) for the gas constant R . Thus on a "standard" day, $p = 1013.3$ hPa at sea level and $T = 288.16$ °K (≈ 70 °F), density ρ is computed from (4.1) with stated units as 1.225 kg/m³.

Another useful form of the gas law is $p\alpha = RT$ where the ratio $\alpha = 1/\rho$ is called the **specific volume**; it is the (average) volume per unit mass. In general, "specific" means that quantities are normalized by molar weight μ .

The **first law of thermodynamics** states that heat is a form of energy and that specific energy e , heat q , and mechanical work w are differentially related as

(4.2)

$$de = dq - dw$$

Here, de is a total differential (as a function of the state variables ρ , p and T); however, dq and dw generally are not. For a gas, work is realized through changes in volume; more accurately, $dw = p d\alpha$.

Thermodynamics can be confusing because variables are defined qualitatively, making theoretical distinction more difficult. For example, "What is the fundamental difference between temperature and heat?" In classical thermodynamics, temperature is elusive, defined implicitly through more sensible variables. Curiously, this situation is somewhat reversed in the kinetic theory of gases. Here, temperature is related to particle motion by $\frac{1}{2}mu^2 = \frac{3}{2}kT$ where m is the molecular weight of a *particle* moving with speed u ,

4. Basic Atmospheric Thermodynamics

and k is Boltzmann's universal constant, 1.380×10^{-23} J/(molecule $^\circ$ K). Simply stated, this equation says that *temperature is proportional to translational kinetic energy*.

This result can be interpreted in terms of the ideal gas law (4.1). According to kinetic theory, pressure is $p = \frac{2}{3}[\frac{1}{2}\rho\langle u^2 \rangle] = \frac{1}{3}\rho\langle u^2 \rangle$ where brackets $\langle \bullet \rangle$ denote the ensemble mean or average. Note that the included term $\frac{1}{2}\rho\langle u^2 \rangle$ is kinetic energy per unit volume which just happens to have units of force per unit area. The division by 3 is the result of projecting what is generally a vector force in any of three directions onto the direction normal to a (hypothetical) surface, and the multiplication by 2 is to account for inelastic collisions with a (hypothetical) surface. In any case, substitution into (4.1) gives $\langle u^2 \rangle = 3RT$ which is the same as $\frac{1}{2}mu^2 = \frac{3}{2}kT$ because $R = k/m$. Consequently, *the ideal gas law (4.1) is a statement about translational kinetic energy*.

So what is heat? Unlike temperature, heat only has meaning as a global or statistical quantity. It has the properties of a temperature density. A volume of water vapor has a higher capacity for heat than an equal volume of dry air; more energy in the form of heat is required to raise the temperature. The thermodynamic way of saying this is through change; two dependencies are

$$(4.3) \quad \begin{aligned} dq &= c_v dT && \text{(gas at constant volume)} \\ dq &= c_p dT && \text{(gas at constant pressure)} \end{aligned}$$

where c_v (J/kg $^\circ$ K) and c_p (J/kg $^\circ$ K) are material "constants" called the **specific heat capacities** at constant volume and pressure respectively. However, these relations are only a part of the story. The important relationship between heat and temperature is the **heat equation**

$$(4.4) \quad \boxed{dq = T ds}$$

where s is (specific) **entropy**. Entropy is generally viewed as a measure of statistical disorder. The **second law of thermodynamics** says that, in a closed system, entropy can only increase with time. As a consequence, order cannot be restored from disorder and time cannot be reversed. In particular, heat can only flow from hot regions to cold ones. An important source of entropy is diffusion. Diffusion in a gas is, basically, the result of the chaotic motion of molecules (at microscopic scales); it is a mixing process that generally increases entropy and moves thermodynamic systems toward statistical equilibrium. Processes in which there is no exchange of heat have constant

4. Basic Atmospheric Thermodynamics

entropy ($ds=0$) and are called **adiabatic**. The earth's boundary layer, being well mixed, is often modeled in this way.

Without additional structure, ideal gases are not very useful. The final hypothesis that makes ideal-gas theory work is that *internal energy e depends only on temperature*. In this case, (I) c_v and c_p also depend only on temperature, (II) $R=c_p-c_v$, and (III) $de=c_v dT$. To help understand the energy relation (III), we return to kinetic theory. Recall that temperature is proportional to the (mean) kinetic energy of translation. But molecules can also have internal kinetic energy due to rotation and vibration. Related degrees of freedom are, however, subject to quantum effects and only become available in discrete units as energy is increased. Nonetheless, when available, the principle of **equipartition of energy** states that kinetic energy must be equally balanced among all such degrees of freedom. In this context, the energy equation $de=c_v dT$ begins to take on meaning; it is a statement as to how translational kinetic energy is related to total kinetic energy. In particular, c_v must reflect the availability of energy states with increasing temperature.

Fortunately, for application to atmospheric science, the situation simplifies. At typical atmospheric temperatures, vibration of air molecules can be neglected and there is only one excitation state available for rotation (the ground state). Thus, available degrees of freedom f depend solely on molecular geometry; there are three translational degrees of freedom plus rotational degrees of freedom. Monatomic gases (He, Ne, Ar, ...), are symmetric and have no rotational degrees of freedom, so $f=3$; diatomic gases (H_2, N_2, O_2, \dots), because of their dumbbell shape, have two rotational degrees of freedom, so $f=5$; gases with no special symmetry have three rotational degrees of freedom, so $f=6$. Now, because specific quantities are normalized by molar weight, $\frac{1}{2}\langle u^2 \rangle$ is the specific translational kinetic energy and represents three degrees of freedom. Because energy is equally partitioned, a gas with f degrees of freedom then has specific energy

$$e = \frac{f}{2} \left[\frac{1}{2} \langle u^2 \rangle \right] = \frac{fRT}{2}$$

However, for an ideal gas, $c_v=de/dT$ and $c_p=R+c_v$; thus,

$$(4.5) \quad \boxed{c_v = \frac{f}{2}R \quad \text{and} \quad c_p = \left[1 + \frac{f}{2}\right]R}$$

4. Basic Atmospheric Thermodynamics

We arrive at the important conclusion that at atmospheric temperatures, c_v and c_p are related to the gas constant R by molecular geometry.

With this background, we return to entropy and adiabatic gases. Of importance to the theory of ideal gases is that ds , as (implicitly) defined by the heat equation (4.4), is a total differential of the state parameters p , ρ , and T . Indeed, from the first law (4.2) $dh=de+dw=c_v dT+pd\alpha$ and $d\alpha=d(1/\rho)=-d\rho/\rho^2$. Substitution, together with an application of the ideal gas law (4.1), gives the stated result

$$ds = dq/T = c_v(dT/T) - (p/\rho T)(d\rho/\rho) = d[c_v \ln(T) - R \ln(\rho)] .$$

In turn, this equation can be integrated (with constant of integration s_0):

$$s-s_0 = c_v \log(T) - R \log(\rho) = c_p \log \left[\left(T^{c_v/c_p} \right) \left(\rho^{-R/c_p} \right) \right] .$$

The term in brackets is called the **potential temperature** θ and can be further simplified with (4.1)

$$(4.6) \quad \boxed{\theta = T(p_0/p)^{(\gamma-1)/\gamma}}$$

where p_0 is a reference pressure (usually 1000 hPa), obtained by redefining the integration constant s_0 . Also, $\gamma=c_p/c_v$ is **Poisson's constant**; note that $(\gamma-1)/\gamma=R/c_p$. Kinetic theory provides another representation of Poisson's constant, $\gamma=(f+2)/f$ where f is the number of degrees of freedom used in (4.5). Because a dry atmosphere consists primarily of diatomic molecules, the value $\gamma=7/5=1.4$ can be used; by contrast, water vapor is polyatomic and $\gamma=8/6=1.333$. Needless to say, but something to remember, is that Poisson's constant is "more constant" than the material constants: c_v , c_p , and R . In this sense, physical equations that depend only on γ are more fundamental.

Recall that in an adiabatic process there is no exchange of heat or entropy. Also, potential temperature satisfies $s=s_0+c_p \log(\theta)$, and so $ds=c_p d\theta/\theta$; consequently, $ds=0 \Rightarrow d\theta=0$ and shows that *in an adiabatic process, potential temperature must be constant*. In addition, the adiabatic condition can be put into differential form

$$(4.7) \quad \boxed{dp = \rho c_p dT = \gamma RT d\rho}$$

which are equations useful for fluid dynamics. In passing, it is worth observing that $c^2=\gamma RT$ is the speed of sound squared. Because waves do not, generally, alter the propagation media, there is little change in entropy, and

4. Basic Atmospheric Thermodynamics

sound propagation can be modeled as a pressure-density disturbance.

The final topic to be reviewed here is **mixing theory**. The atmosphere consists of many different kinds of gases and we need to know how to deduce properties of this mixture from its constituents. This task simplifies because atmospheric molecules can be divided into two basic groups, the diatomic molecules of dry air and the polyatomic molecules of water vapor. Thus, our exposition will focus on mixing dry air with water vapor to produce moist air.

We begin with **Dalton's law** which states that *the total pressure of a gas is the sum of the partial pressures of its constituents and each constituent obeys its equation of state as if the others were not present*

$$(4.8) \quad p_d = \rho_d R_d T_d \quad \text{and} \quad e = \rho_v R_v T_v .$$

Here, e is the standard notation for vapor pressure (not to be confused with specific energy above), and subscripts "d" and "v" stand for dry and vapor respectively.

Next, equipartition of energy applies to gas mixtures and, consequently, statistical equilibrium requires that *different species of gas molecules will, as a group, have the same average temperature*. As a consequence $T_d = T_v$ and subscripts on temperature can, and should, be omitted. According to Dalton's law, the moist-air pressure p_s then is

$$(4.9) \quad p_s = p_d + e = (\rho_d R_d + \rho_v R_v) T$$

To complete this development, we need to know how densities mix. The answer is provided by **Avogadro's law** (1811) which states that *under the same external conditions of pressure and temperature, all gas molecules occupy the same space*. To say this another way, "Under standard conditions, a mole of gas always contains the same number of molecules." This number is called Avogadro's number N_0 ; it is 6.023×10^{26} molecules/kg-mole and relates the universal gas constant R^* with Boltzmann's constant k , $R^* = N_0 k$. For present application, the important observation is that moist-air density ρ_s is the sum of the partial densities $\rho_s = \rho_d + \rho_v$. The moist-air gas constant R_s is now easily deduced from (4.9) as

$$(4.10) \quad R_s = (\rho_d R_d + \rho_v R_v) / (\rho_d + \rho_v)$$

Likewise, the specific heats c_p and c_v satisfy the same mixing rule. At this point, it is convenient to introduce the **mixing ratio** $\eta = \rho_v / \rho_d$; from (4.8), it can be expressed $\eta = (R_d / R_v) [e / (p_s - e)]$ which is useful because p_s and e are

4. Basic Atmospheric Thermodynamics

available from measurement. With this notation, the moist-air gas constants are, finally, computed as

$$(4.11) \quad \begin{aligned} R_s &= (R_d + \eta R_v) / (1 + \eta) \\ c_{p,s} &= (c_{p,d} + \eta c_{p,v}) / (1 + \eta) \\ c_{v,s} &= (c_{v,d} + \eta c_{v,v}) / (1 + \eta) \end{aligned}$$

In closing, we give the following "standard" values, in units of (J/kg-°K).

$$(4.12) \quad \begin{aligned} c_{p,d} &= 1004.64, & c_{v,d} &= 717.60 & \Rightarrow & R_d &= 287.04 \\ c_{p,v} &= 1846.00, & c_{v,v} &= 1384.04 & \Rightarrow & R_v &= 461.96 \\ & & \Rightarrow & \eta &= & 0.62135 \cdot e / (p_s - e) \end{aligned}$$

Equations (4.11) together with the constants (4.12) are used for P-3 data processing.

5. THEORY OF TRUE-AIRSPEED MEASUREMENT

To apply thermodynamics to fluids, change must proceed in an orderly fashion, slow enough to keep statistical equilibrium locally intact. This is not as restrictive as it might seem because the numbers are enormous. A cubic centimeter of air contains more than 10^{19} molecules traveling with a mean velocity in excess of the speed of sound ($\sim 350\text{m/s}$). However, because interactions are on the order of 10^9 collisions per second, molecular drift or diffusion associated with Brownian motion is only several meters per second.

Fluid dynamics uses the model of a continuum; required derivatives always exist as continuous functions. If $\mathbf{x}(t)=(x(t),y(t),z(t))$ is the position of a particle as a function of time, then as time varies, the set of related positions is a Lagrangian trajectory. The time derivative of position is the particle velocity $\mathbf{u}(t)=\dot{\mathbf{x}}(t)$. A variable, say density ρ , that "goes with the flow" is parameterized $\rho(\mathbf{x}(t),t)$ and the total time derivative is computed from the chain rule:

$$\begin{aligned}
 \frac{d\rho}{dt} &= \frac{\partial\rho}{\partial t} + \frac{\partial\rho}{\partial x} \frac{dx}{dt} + \frac{\partial\rho}{\partial y} \frac{dy}{dt} + \frac{\partial\rho}{\partial z} \frac{dz}{dt} \\
 (5.1) \qquad &= \frac{\partial\rho}{\partial t} + \frac{\partial\rho}{\partial x} u + \frac{\partial\rho}{\partial y} v + \frac{\partial\rho}{\partial z} w \\
 &= \frac{\partial\rho}{\partial t} + \mathbf{u} \cdot \nabla\rho
 \end{aligned}$$

where $\mathbf{u} \cdot \nabla\rho$ is the dot product of $\mathbf{u}=(u,v,w)$ with the gradient $\nabla\rho$:

$$\nabla\rho = \frac{\partial\rho}{\partial x} \mathbf{i} + \frac{\partial\rho}{\partial y} \mathbf{j} + \frac{\partial\rho}{\partial z} \mathbf{k} .$$

Time derivatives of this kind are called **material derivatives** and are denoted D/Dt ; thus, $D\rho/Dt = \partial\rho/\partial t + \mathbf{u} \cdot \nabla\rho$.

Of central importance is the **momentum equation** which is a modified version of Newton's second law ($\mathbf{f}=\mathbf{ma}$). The most informative statement has integral form:

$$(5.2) \qquad \boxed{\frac{d}{dt} \int_{\mathbf{x} \in V(t)} \rho(\mathbf{x},t) \mathbf{u}(\mathbf{x},t) dV = - \int_{\mathbf{x} \in \partial V(t)} p(\mathbf{x},t) \mathbf{n}(\mathbf{x}) d\sigma} .$$

The volume integral on the left has units of momentum; consequently, the time derivative is a force. Here, the volume $V(t)$ can change in both size and shape as it moves with the flow. The integral on the right is a surface integral over the (smooth) boundary $\partial V(t)$ of $V(t)$; $\mathbf{n}(\mathbf{x})$ is the outward unit normal at $\mathbf{x} \in \partial V(t)$. Consequently, (5.2) says that momentum change in $V(t)$ is opposed to

5. Theory of True-Airspeed Measurement

the net, outward pressure force on the surface $\partial V(t)$; the negative sign is required because motion is towards regions of low pressure. In view of the kinematic theory of gases, modeling pressure as a normal force is very reasonable. However, in a real fluid or gas there are other (tangential) forces due to friction, and can be modeled into the surface integral (as stresses). For present purposes, friction will be neglected.

Although informative, (5.2) is not very useful for computation, and must be converted to a differential equation. This is a purely mathematical procedure requiring the transport theorem and the divergence theorem. The end result is the **Euler equation**:

$$(5.3) \quad \boxed{\rho \frac{D\mathbf{u}}{Dt} = -\nabla p + \rho \mathbf{g}}$$

where gravitational acceleration $g=9.80665 \text{ m/s}^2$ has been added to the force balance. Again, the derivative on the left is the material derivative. Fluids that satisfy (5.3) are called **inviscid**.

To derive Bernoulli's equation, first apply the dot product of velocity \mathbf{u} to (5.3)

$$\rho \mathbf{u} \cdot \frac{D\mathbf{u}}{Dt} = -\mathbf{u} \cdot \nabla p + \rho \mathbf{u} \cdot \mathbf{g}$$

which is mathematically equivalent to

$$(5.4) \quad \frac{D}{Dt} \left(\frac{1}{2} u^2 + gz \right) = -\frac{1}{\rho} \frac{Dp}{Dt} + \frac{1}{\rho} \frac{\partial p}{\partial t}$$

where $u^2 = \mathbf{u} \cdot \mathbf{u}$.

To continue, we need the adiabatic condition. To help understand this model, picture an ideal aircraft (say a glider) going through the air so smoothly that after the flow has been parted, it comes together again as if nothing had happened. In particular, there has been no change in entropy, and flow close to the aircraft must be adiabatic. Also, to reduce friction, aircraft are designed to be as entropy free as possible.

When applied to fluids, the condition of "no entropy change" $ds=0$ can be modified to "no entropy change for a parcel" $Ds/Dt=0$. In this case, flow is called **isentropic**; thus, isentropic flow has adiabatic parcels and the adiabatic condition (4.7) becomes:

$$\frac{1}{\rho} \frac{Dp}{Dt} = c_p \frac{DT}{Dt}$$

5. Theory of True-Airspeed Measurement

Substitution into (5.4) gives an intermediate equation, useful for analysis:

$$(5.5) \quad \boxed{\frac{D}{Dt} \left(\frac{1}{2} u^2 + c_p T + gz \right) = \frac{1}{\rho} \frac{\partial p}{\partial t}}$$

When the right side is zero, $\partial p / \partial t = 0$, this equation can be integrated to get **Bernoulli's equation for isentropic flow**:

$$(5.6) \quad \boxed{\frac{1}{2} u^2 + c_p T + gz = \text{constant along flow lines}}$$

which says that specific energy will be conserved along flow lines, *provided entropy does not change and pressure is stationary*.

At this point, we need to distinguish between ambient or static values ρ_s , p_s , and T_s existing in a hypothetical, quiescent atmosphere from total ones ρ_t , p_t , and T_t observed in the aircraft frame; the difference is due to aircraft motion and ambient wind. The pressures most often measured are the static pressure p_s and the **dynamic pressure** $q_c = p_t - p_s$ ("c" is for compressible). This is advantageous because dynamic pressure can be obtained with better *precision* when measured directly as a differential pressure. Nonetheless, p_t is usually more *accurate* than either p_s or q_c . This is because measurement of p_s is more difficult, requiring special flow conditions; related errors get passed on to q_c , but cancel in the computation of p_t .

True airspeed can now be computed from Bernoulli's equation by balancing energies:

$$(5.7) \quad \frac{1}{2} \tau^2 + c_p T_s + gz = c_p T_t + gz,$$

and solving for τ :

$$(5.8) \quad \tau = \sqrt{2c_p(T_t - T_s)}.$$

But, Bernoulli's equation is a statement about change along flow lines, while (5.8) is a statement about change resulting from aircraft motion. So what is going on? One explanation is to consider the flow as being generated artificially, as in a wind tunnel. In this case, flow around the aircraft has an unambiguous interpretation, and the balance (5.7) can be viewed as conservation of (specific) energy.

Another explanation is provided by kinetic theory. Here, the increase in pressure δp due to *organized* motion is $\delta p = \frac{1}{2} \rho u^2$. If, in addition, change is

5. Theory of True-Airspeed Measurement

adiabatic then $\delta p = \rho c_p \delta T$, and $\frac{1}{2}u^2 = c_p \delta T$. Finally, setting $u = \tau$ and $\delta T = T_t - T_s$, we arrive at the same equation (5.8). Thus, *adiabatic heating can be interpreted as a "thermodynamic" property of organized motion*. Should this be exactly true, the requirement of stationary pressure in (5.5) is superfluous.

Next, T_s is computed from potential temperature (4.6) which is constant under adiabatic conditions:

$$\begin{aligned} T_s (p_0/p_s)^{(\gamma-1)/\gamma} &= T_t (p_0/p_t)^{(\gamma-1)/\gamma} \\ \Rightarrow T_s &= T_t (p_s/p_t)^{(\gamma-1)/\gamma} \\ \Rightarrow T_t - T_s &= P_\gamma T_t \end{aligned}$$

where $P_\gamma = 1 - (p_s/p_t)^{(\gamma-1)/\gamma}$ and substitution into (5.8) gives

$$(5.9) \quad \boxed{\tau = \sqrt{2c_p P_\gamma T_t}}$$

This calculation is often organized to include the Mach number M defined

$$(5.10) \quad M^2 = \frac{2}{\gamma-1} \left[(p_t/p_s)^{(\gamma-1)/\gamma} - 1 \right]$$

$$(5.11) \quad \Rightarrow \quad \boxed{\tau = \sqrt{\gamma R T_s} M}$$

which is the same calculation, but in different form. Note that the Mach number is the ratio of true airspeed to the speed of sound $c_s = (\gamma R T_s)^{1/2}$. Although this is the more standard computation, we prefer (5.9) because it is better suited to both approximation (Sec. 10) and calibration (Sec. 7).

A useful estimate of (5.11) is the indicated airspeed τ_I obtained by modeling the speed of sound; specifically, with $\gamma=7/5$ for dry air and $T_s=0^\circ\text{C}$ (273.16°K), the speed of sound is 331.32 m/s. However, because τ_I is used mostly as an operational parameter, it is here expressed in knots ($1\text{ m/s} = 1.94\text{ kt}$);

$$(5.12) \quad \tau_I = 1477 [(p_t/p_s)^{2/7} - 1]^{1/2} \text{ kt}$$

We remark that this estimate could be improved with a constant lapse rate model $T_s = T_0 - \Gamma z$ (see Sec. 10).

Limitations? In closing this topic, we review possible limitations of the true-airspeed measurement. First, there are some difficulties with the

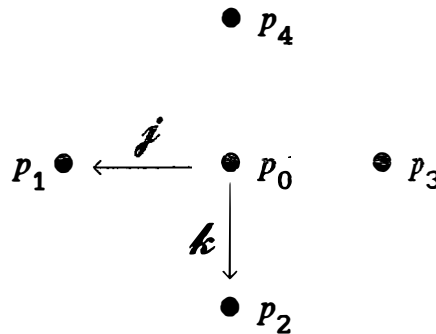
5. Theory of True-Airspeed Measurement

inference model. Bernoulli's equation (5.6) requires that (static) pressure be stationary and possible effects of a changing pressure field are largely unknown. Moreover, possible effects due to friction and/or turbulence are difficult to even address. Second, there are practical difficulties in having to combine different types of measurements. The calculation requires three pressures p_s , q_c , and p_v along with total temperature T_t . Each of these measurements is difficult, requiring in-flight calibration; related analysis is nonlinear and elusive. In addition, such things as dust and water droplets are known to cause problems, especially with temperature.

6. THEORY OF FLOW-ANGLE MEASUREMENT

We now apply preceding results to flow-angle measurement. The basic idea is to measure differential pressures on the surface of a sphere; preceding theory can then be used to infer incidence angles of the relative wind. In the sequel, three different methods will be analyzed; two are supported by Rosemount, the other, developed by Brown, *et.al.* [1983], is used at the National Center for Atmospheric Research (NCAR). In particular, we compute exact, closed-form solutions for the three cases; again, solutions are for potential flow past a sphere.

A good place to begin is with the 858 flow-angle probe manufactured by Rosemount. These probes are about 5" long and 0.5" in diameter, made of hard metal. There are two versions, model 858AJ for mounting on a nose boom, and model 858Y for mounting on the fuselage. The essential feature is that the nose of the probe is spherically shaped. When viewed from the front, there are five holes or ports, a center port and four outside ones; they are aligned (relative to aircraft coordinates j, k) as shown:



where the p_k are the (total) pressures at the respective ports. In turn, differential pressures $\delta_k p$ are defined

$$(6.1) \quad \delta_k p = p_0 - p_k ; k = 1, 2, 3, 4.$$

Pressure differences of this kind can be measured directly, using differential transducers.

This geometry also applies to **radome sensors** which are, basically, scaled up versions of the 858 probe. The idea is to drill similar holes in the nose radome to function as pressure ports; everything else is the same. This, of course, assumes that the front part of the radome is spherically shaped. An obvious question is, "Why go to the trouble?" Recall that with the 858 probe there are two places to mount it, on a boom and on the fuselage. However, booms tend to resonate and bob around; additionally, when mounted near the

6. Theory of Flow-Angle Measurement

nose, they can interfere with other instrumentation such as radar, and when mounted on a wing, data must be corrected for spatial displacement and extraneous motions.

If, on the other hand, the 858 probe is mounted on the fuselage, there is flow distortion to contend with. To help visualize the problem, think of flow distortion over a wing. The wing parts the air; airfoil causes the flow to move faster across the top, pressure is reduced, and lift results. This basic flow behavior is happening everywhere along the skin of the aircraft. Flow distortion of any kind, for any reason, translates to changes in the pressure field, and it is such change that flow-angle sensors monitor. Now, flow distortion along the fuselage is largely unintuitive (stagnation points provide a nice example). By contrast, radomes occupy a position of (flow) symmetry and meet the air first; also, as was seen in the previous section, flow past a "spherically-shaped" nose is largely predictable. As an added bonus, there are no metal parts to interfere with nose radars. In short, the radome sensor converts the liability of flow distortion into an asset.

High-Resolution Method Rosemount gives two basic methods for computing attack and slip. These methods can be characterized as having high and low resolution (more about this later). In the high-resolution method, attack α and slip β are estimated as

$$(6.2a) \quad \alpha = \frac{p_2 - p_4}{K_1 [(p_0 - p_2) + (p_2 - p_4)/2]} = \frac{2}{K_1} \left[\frac{\delta_4 p - \delta_2 p}{\delta_4 p + \delta_2 p} \right]$$

$$(6.2b) \quad \beta = \frac{p_1 - p_3}{L_1 [(p_0 - p_1) + (p_1 - p_3)/2]} = \frac{2}{L_1} \left[\frac{\delta_3 p - \delta_1 p}{\delta_3 p + \delta_1 p} \right]$$

where K_1 and L_1 are calibration constants called **sensitivity coefficients**. Implicitly, these quotients indicate two slightly different procedures of data acquisition. The left quotients (Rosemount's), use differential pressures $(p_1 - p_3)$, $(p_2 - p_4)$, $(p_0 - p_2)$, and $(p_0 - p_1)$; the right ones use the $\delta_k p$. Nonetheless, these procedures are mathematically equivalent.

Low-Resolution Method By contrast, in the low-resolution method, another source of dynamic pressure q_c is used

$$(6.3a) \quad \alpha = \frac{p_2 - p_4}{K_2 q_c} = \frac{\delta_4 p - \delta_2 p}{K_2 q_c}$$

6. Theory of Flow-Angle Measurement

$$(6.3b) \quad \beta = \frac{p_1 - p_3}{L_2 q_c} = \frac{\delta_3 p - \delta_1 p}{L_2 q_c}$$

The advantage here is that q_c is often measured anyway (for true airspeed), and less hardware is required. However, as we shall see, K_2 and L_2 are generally not the same as K_1 and L_1 .

NCAR Method This scheme is somewhere in between the high-resolution method of (6.2) and the low-resolution method of (6.3). It is most easily visualized as being the low-resolution method, but with q_c replaced with $(p_0 - p_s)$

$$(6.4a) \quad \alpha = \frac{p_2 - p_4}{K_3 (p_0 - p_s)} = \frac{\delta_4 p - \delta_2 p}{K_3 (p_0 - p_s)}$$

$$(6.4b) \quad \beta = \frac{p_1 - p_3}{L_3 (p_0 - p_s)} = \frac{\delta_3 p - \delta_1 p}{L_3 (p_0 - p_s)}$$

The pressure p_0 still comes from the probe; but now, the static pressure p_s is imported from another source. For good precision, the difference $(p_0 - p_s)$ must still be measured directly as a differential pressure. In principle, the sensitivity coefficients K_3 and L_3 should agree with K_2 and L_2 .

We remark that for application to the P-3's, this method has the limitation of requiring long pressure lines. This is because $(p_0 - p_s)$ is best measured as a differential pressure, and static pressure along the fuselage is measured aft of the wing, some 30 m behind the radome. Because the speed of sound is about 340 m/s, static pressure is delayed in the pressure lines by about 0.1 s. Additionally, for a nominal airspeed of 100 m/s, it takes about 0.3 s for an air parcel to "move" from the nose to the static port. Even for slow, 1 Hz data this is unacceptable.

Geometric Preliminaries We begin our investigation by setting up needed geometry. Positions are specified with unit direction vectors n_k that point outward from the center of the sphere as illustrated in Fig. 6-1. (Again, script is used to emphasize aircraft coordinates.) Equally important, are the subtended angles between ports, also measured from the center of the sphere. It is useful to think of these angles as design parameters and to treat the vertical and horizontal cases independently. Thus, the two (equal) angles subtending adjacent vertical ports will be denoted Θ ; they are related to the direction vectors as follows:

6. Theory of Flow-Angle Measurement

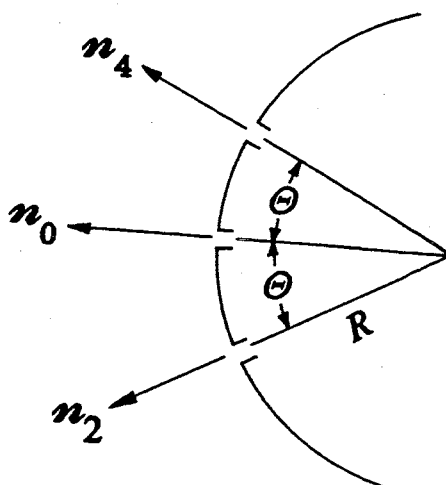


Fig. 6-1. Geometry of flow angle measurement on an aircraft nose radome. The angle between adjacent ports is Θ ; R is the radius of the spherical radome. Normals n_0 , n_2 , n_4 point outward from their respective radome pressure ports.

$$(6.5) \quad n_0 \cdot n_2 = n_0 \cdot n_4 = \cos \Theta; \quad n_2 \cdot n_4 = \cos 2\Theta; \quad 1 - n_2 \cdot n_4 = 2 \sin^2 \Theta.$$

Similarly, the two horizontal angles will be denoted Φ and satisfy

$$(6.6) \quad n_0 \cdot n_1 = n_0 \cdot n_3 = \cos \Phi; \quad n_1 \cdot n_3 = \cos 2\Phi; \quad 1 - n_1 \cdot n_3 = 2 \sin^2 \Phi.$$

Next, radome geometry must be linked to aircraft coordinates i , j , and k . By design, flow-angle probes are aligned with these coordinates, and they should be in precise agreement with navigation instrumentation. But, then there must be constants κ_j and κ_k so that

$$(6.7) \quad i = n_0; \quad j = \kappa_j (n_1 - n_3); \quad k = \kappa_k (n_2 - n_4)$$

where an easy calculation shows

$$\kappa_j = 1/(2 \sin \Phi) \quad \text{and} \quad \kappa_k = 1/(2 \sin \Theta).$$

Note that Crawford and Dobosy [1992] align their flow angle probe at zero angle of attack, and correct for how much the angle of attack is different from the navigation instrumentation. This has the advantage of avoiding possible non-linearities associated with flying at large angles of attack.

Differential Pressures With geometry established, we can now relate differential pressures to flow angles. Recall that these angles are determined by the direction \mathcal{E}_r of the relative wind. To avoid proliferating negative signs, we here change to the direction vector $\mathcal{S} = -\mathcal{E}_r$ that points outward, $\mathcal{U}_r = -\tau \mathcal{S}$. In reference to (3.3), this direction can be written

6. Theory of Flow-Angle Measurement

$$(6.8) \quad \mathcal{N} = Ai + Bj + Ck$$

where: $A=1/D$; $B=\tan\beta/D$; $C=\tan\alpha/D$; and $D=\sqrt{1+\tan^2\beta+\tan^2\alpha}$. At this point we need to know the pressure distribution over the surface of a sphere; but this is derived in (B.14) of Appendix B which can here be written

$$(6.9) \quad p(n) = p_s + \frac{q}{4}[9(\mathcal{N} \cdot n)^2 - 5]$$

where, as before, p_s is static pressure and n is the outward unit normal. In passing, we remark that this equation is often given in trigonometric form. To do this, set $\mathcal{N} \cdot n = \cos\gamma$ where γ is the angle between the wind direction and a surface port measuring pressure p . Then (6.9), takes the form

$$(6.10) \quad p = p_s + q \left[1 - \frac{9}{4} \sin^2 \gamma \right]$$

Of some importance is when the term in brackets vanishes: $\sin^2 \gamma_s = 4/9 \Leftrightarrow \gamma_s \cong 41.81^\circ$. In this case, *measured pressure p at the surface is precisely the static pressure p_s* . However, this is getting ahead of the story.

For present purposes, the useful consequence of (6.9) is that the differential pressures $\delta_k p$ of (6.1) must satisfy

$$(6.11) \quad \delta_k p = \frac{9}{4} q [(\mathcal{N} \cdot n_0)^2 - (\mathcal{N} \cdot n_k)^2],$$

making it possible to compute the following four values:

$$\begin{aligned} \delta_1 p &= \frac{9}{4} q [A^2 - (A \cos \Phi + B \sin \Phi)^2] \\ \delta_2 p &= \frac{9}{4} q [A^2 - (A \cos \Theta + C \sin \Theta)^2] \\ \delta_3 p &= \frac{9}{4} q [A^2 - (A \cos \Phi - B \sin \Phi)^2] \\ \delta_4 p &= \frac{9}{4} q [A^2 - (A \cos \Theta - C \sin \Theta)^2]. \end{aligned}$$

Verification is simple vector arithmetic; for example, to compute $\delta_1 p$, note that $\mathcal{N} \cdot n_0 = A$ and evaluate $\mathcal{N} \cdot n_1$ with (6.3) and (6.5)

$$\begin{aligned} \mathcal{N} \cdot n_1 &= (Ai + Bj + Ck) \cdot n_1 = A(i \cdot n_1) + B(j \cdot n_1) \\ &= A(n_0 \cdot n_1) + B \kappa_j (1 - n_1 \cdot n_3) \\ &= A \cos \Phi + B \sin \Phi. \end{aligned}$$

To continue, required sums and differences simplify to

$$(6.12a) \quad \delta_4 p + \delta_2 p = \frac{9}{2} q (A^2 - C^2) \sin^2 \Theta; \quad \delta_4 p - \delta_2 p = \frac{9}{2} q AC \sin 2\Theta$$

$$(6.12b) \quad \delta_3 p + \delta_1 p = \frac{9}{2} q (A^2 - B^2) \sin^2 \Phi; \quad \delta_3 p - \delta_1 p = \frac{9}{2} q AB \sin 2\Phi$$

6. Theory of Flow-Angle Measurement

The basic use of these equations is to relate differential pressures to flow-angle parameters implicit in A , B , and C .

Exact Solution of High-Resolution Method Curiously, the high-resolution method is the easiest to solve. The approach used here and below is superficially naive, "Compute the quotients of measured parameters and see what happens." In the present case:

$$\frac{\delta_4 p - \delta_2 p}{\delta_4 p + \delta_2 p} = \frac{AC \sin 2\Theta}{(A^2 - C^2) \sin^2 \Theta} = \left[\frac{2 \tan \alpha}{1 - \tan^2 \alpha} \right] \frac{1}{\tan \Theta} = \frac{\tan 2\alpha}{\tan \Theta}$$

$$\frac{\delta_3 p - \delta_1 p}{\delta_3 p + \delta_1 p} = \frac{AB \sin 2\Phi}{(A^2 - B^2) \sin^2 \Phi} = \left[\frac{2 \tan \beta}{1 - \tan^2 \beta} \right] \frac{1}{\tan \Phi} = \frac{\tan 2\beta}{\tan \Phi}$$

At this point, we could simply solve for $\tan 2\alpha$ and $\tan 2\beta$; however, for uniformity of presentation, we compute the solutions in terms of $\tan \alpha$ and $\tan \beta$. We organize this computation by defining (secondary) quantities F_α and F_β as

$$(6.13) \quad F_\alpha = \frac{\tan \Theta}{2} \left[\frac{\delta_4 p - \delta_2 p}{\delta_4 p + \delta_2 p} \right] \quad \& \quad F_\beta = \frac{\tan \Phi}{2} \left[\frac{\delta_3 p - \delta_1 p}{\delta_3 p + \delta_1 p} \right]$$

Note, in particular, that F_α and F_β only depend on measured pressures. Substitution then yields quadratic equations in $\tan \alpha$ and $\tan \beta$

$$(1 - \tan^2 \alpha) F_\alpha = \tan \alpha$$

$$(1 - \tan^2 \beta) F_\beta = \tan \beta$$

Clearly, F_α and F_β are first-order estimates of the exact solutions:

$$(6.14) \quad \boxed{\begin{aligned} \tan \alpha &= 2F_\alpha / \left[1 + \sqrt{1 + 4F_\alpha^2} \right] \\ \tan \beta &= 2F_\beta / \left[1 + \sqrt{1 + 4F_\beta^2} \right] \end{aligned}}$$

Exact Solution of Low-Resolution Method Here required equations follow directly from (6.12)

$$\frac{P_2 - P_4}{q} = \frac{9}{2} AC \sin 2\Theta = \frac{9}{2} (\tan \alpha \sin 2\Theta) / D^2$$

$$\frac{P_1 - P_3}{q} = \frac{9}{2} AB \sin 2\Phi = \frac{9}{2} (\tan \beta \sin 2\Phi) / D^2$$

Now, we define (secondary) quantities G_α and G_β as

6. Theory of Flow-Angle Measurement

$$(6.15) \quad G_\alpha = \frac{2}{9 \sin 2\Theta} \left[\frac{P_2 - P_4}{q} \right] \quad \& \quad G_\beta = \frac{2}{9 \sin 2\Phi} \left[\frac{P_1 - P_3}{q} \right]$$

which, after substitution, result in the following pair of equations:

$$\begin{aligned} (1 + \tan^2 \alpha + \tan^2 \beta) G_\alpha &= \tan \alpha \\ (1 + \tan^2 \alpha + \tan^2 \beta) G_\beta &= \tan \beta . \end{aligned}$$

Note well that this is a coupled set of quadratic equations in $\tan \alpha$ and $\tan \beta$. Fortunately, taking quotients gives $G_\alpha \tan \beta = G_\beta \tan \alpha$ and equations decouple, yielding closed-form solutions:

$$(6.16) \quad \boxed{\begin{aligned} \tan \alpha &= 2G_\alpha / \left[1 + \sqrt{1 - 4(G_\alpha^2 + G_\beta^2)} \right] \\ \tan \beta &= 2G_\beta / \left[1 + \sqrt{1 - 4(G_\alpha^2 + G_\beta^2)} \right] \end{aligned}}$$

Unlike the high-resolution case, these solutions are (weakly) coupled insofar as the term $G_\alpha^2 + G_\beta^2$ is common to both.

Exact Solution of NCAR Method The added complexity here is that the pressure difference $p_0 - p_s$ must also be computed. This is readily accomplished with (6.9); indeed, $\mathcal{M} \cdot n_0 = A = 1/D$, and so

$$(6.17) \quad \begin{aligned} p_0 - p_s &= \frac{q}{4} [9(\mathcal{M} \cdot n_0)^2 - 5] = \frac{q}{4} [9 - 5D^2] / D^2 \\ &= q \left[1 - \frac{5}{4} (\tan^2 \alpha + \tan^2 \beta) \right] / D^2 . \end{aligned}$$

Aside from this, the computation mimics the previous one:

$$\begin{aligned} \frac{P_2 - P_4}{P_0 - P_s} &= \frac{9}{2} (\tan \alpha \sin 2\Theta) / \left[1 - \frac{5}{4} (\tan^2 \alpha + \tan^2 \beta) \right] \\ \frac{P_3 - P_1}{P_0 - P_s} &= \frac{9}{2} (\tan \beta \sin 2\Phi) / \left[1 - \frac{5}{4} (\tan^2 \alpha + \tan^2 \beta) \right] \end{aligned}$$

Again, (secondary) quantities H_α and H_β are defined

$$(6.18) \quad H_\alpha = \frac{2}{9 \sin 2\Theta} \left[\frac{P_2 - P_4}{P_0 - P_s} \right] \quad \& \quad H_\beta = \frac{2}{9 \sin 2\Phi} \left[\frac{P_1 - P_3}{P_0 - P_s} \right] ,$$

and again a coupled pair of quadratics results:

$$\begin{aligned} \left[1 - \frac{5}{4} (\tan^2 \alpha + \tan^2 \beta) \right] H_\alpha &= \tan \alpha \\ \left[1 - \frac{5}{4} (\tan^2 \alpha + \tan^2 \beta) \right] H_\beta &= \tan \beta . \end{aligned}$$

6. Theory of Flow-Angle Measurement

Finally, taking quotients gives $H_\alpha \tan \beta = H_\beta \tan \alpha$, and equations decouple to yield closed-form solutions:

$$(6.19) \quad \begin{cases} \tan \alpha = 2H_\alpha / \left[1 + \sqrt{1 + 5(H_\alpha^2 + H_\beta^2)} \right] \\ \tan \beta = 2H_\beta / \left[1 + \sqrt{1 + 5(H_\alpha^2 + H_\beta^2)} \right] \end{cases}$$

Analysis of Sensitivity Coefficients In retrospect, we can now better understand the sensitivity coefficients in the inversion models (6.2), (6.3), and (6.4). For present purposes, it simplifies things to use the same vertical and horizontal angles $\Theta = \Phi$ so that $K_n = L_n$. Now, in view of the exact solutions (6.14), (6.16), and (6.19), we see that all three models use the small-angle approximation $\tan x \cong x$. This aside, K_1 can be computed by comparing the defining relations (6.2) with the first-order quantity F_α ; thus,

$$(6.20) \quad K_1 = \pi / (45 \tan \Theta) \text{ deg}^{-1}$$

Similarly, the other coefficients can be shown to satisfy

$$(6.21) \quad K_2 = K_3 = (\pi \sin 2\Theta) / 40 \text{ deg}^{-1}$$

We observe in the first case that sensitivity is inversely proportional to port separation while, in the other two cases, sensitivity is directly proportional; note, in particular, that inverse sensitivity goes counter to intuition. Of special interest is the case where these two sets of coefficients agree; again the angle is the "optimal" one deduced from (6.10), $\Theta = \gamma_s \cong 41.81^\circ$; for this angle, $K_1 = K_2 = K_3 = 0.0780535 \text{ deg}^{-1}$.

According to Rosemount, the high-resolution method applied to the 858 flow-angle sensor requires $K_1 = 0.079 \text{ deg}^{-1}$ which, in view of above discussion, corresponds to a separation angle Θ of about 41.5° . By contrast, Rosemount gives $K_2 = 0.088 \text{ deg}^{-1}$ for the low-resolution method which, to the author's knowledge, has no theoretical justification. In any case, for Mach numbers less than about 0.5, Rosemount gives "usable" ranges for these two methods as about $\pm 45^\circ$ for the high-resolution method and about $\pm 12^\circ$ for the low-resolution method. Although these ranges are far too optimistic for wind measurement, they do demonstrate practical differences.

At this point, it should be clear that the approximations (6.2), (6.3), and (6.4) are unnecessary insofar as exact solutions (6.14), (6.16), and

6. Theory of Flow-Angle Measurement

(6.19) are available. An obvious question is, "Are the improvements significant to measurement?" The answer is, "Yes, but only marginally so." For example, with $\tan\beta=0.1$, the net difference between the approximate and exact estimates of $\tan\hat{\beta}$ is only about one percent; however $\tan\beta=0.1$ corresponds to an angle of $\beta\cong 5.7^\circ$ which, in the context of how aircraft actually fly, must be viewed as abnormally large.

Dynamic-Pressure Computation The problem here is to estimate dynamic pressure from measured parameters. Clearly, this excludes the low-resolution method because dynamic pressure is a given quantity.

To begin, the solution for the **NCAR method** is obtained by simply solving (6.17) for q

$$(6.22) \quad q = (p_0 - p_s) \left[1 + \frac{9(\tan^2\alpha + \tan^2\beta)}{4 - 5(\tan^2\alpha + \tan^2\beta)} \right]$$

Clearly, this solution supposes that flow angles have already been computed. Again, this is an exact solution for potential flow past a sphere.

Computing dynamic pressure for the **high-resolution method** is similar. The useful quantity here is the average differential pressure defined:

$$(6.23) \quad \langle \delta p \rangle = (\delta_1 p + \delta_2 p + \delta_3 p + \delta_4 p) / 4 .$$

Note that $\langle \delta p \rangle = p_0 - (p_1 + p_2 + p_3 + p_4) / 4$ which is approximately a difference of the form " $p_0 - p_s$." To continue, we evaluate $\langle \delta p \rangle$ with (6.12):

$$\langle \delta p \rangle = \frac{9}{8} q [(A^2 - B^2) \sin^2 \Phi + (A^2 - C^2) \sin^2 \Theta]$$

which can be solved for q (provided that flow angles are known)

$$(6.24) \quad q = \frac{4 \langle \delta p \rangle}{9 \sin^2 \Theta} \left[1 + \frac{3(\tan^2\alpha + \tan^2\beta)}{2 - (\tan^2\alpha + \tan^2\beta)} \right]$$

where, for simplicity, we have set $\Theta = \Phi$. Note in particular, that when $\Theta = \gamma_s \cong 41.81^\circ$ the leading coefficient simplifies and, to first order, $q \cong \langle \delta p \rangle$.

Static Pressure Estimation Once flow angles α and β together with dynamic pressure \hat{q} have been obtained, static pressure can be computed from (6.17) as:

6. Theory of Flow-Angle Measurement

$$(6.25) \quad p_s = p_0 - q \left[1 - \frac{5}{4} (\tan^2 \alpha + \tan^2 \beta) \right] / D^2 .$$

provided that the center pressure p_0 has been recorded and is available. The advantage of estimating static pressure in this way is that it is contiguous in space and time with other pressure measurements. Also, as we shall see in the next section, static pressure can be calibrated independently, providing a useful check.

In closing this topic, it would be presumptuous to say which method is, in fact, best suited to radome measurement. This is because flow distortion and inexact models can distort predicted results. In the author's opinion, the first-order correction to present theory is in the geometry — radomes are not spheres. Moreover, flow is a global entity and even features behind the radome can influence measured parameters. Nevertheless, the radome sensor is, in principle, an excellent one. The salient observation is that flow-angle measurement is independent of dynamic pressure q which is the quantity most influenced by flow distortion and pressure-dome effects.

7. CALIBRATION OF TEMPERATURE, PRESSURE, AND AIRSPEED

So far we have been working with the tacit assumption that sensors are accurately calibrated and need no correction. In practice, this turns out not to be the case. Some problems arise because of inexact alignment of sensors, others are due to flow distortion, and some are due to inexact theory and models. Alignment errors arise because of difficulties in matching sensor directions and orientations on different parts of an aircraft. For example, the flow-angle sensors for measuring the attack and slip angles must be precisely aligned with inertial navigation. Flow-distortion errors arise because flow near an aircraft is modified in unknown ways, effects may even be turbulent. In any case, dynamic calibration techniques can be broken into three basic parts: (I) in-flight calibration data, (II) calibration models, and (III) appropriate analysis procedures.

Our main focus here is on the calibration of temperature, pressure, and true airspeed, a task made more difficult by the nonlinear equations. Recall that the equation of state $p_s = \rho_s R T_s$ is a good expression of thermodynamic balance in a static atmosphere. For adiabatic change, this balance applies to total quantities as well $p_t = \rho_t R T_t$. In addition, adiabatic processes are governed by the variational equations (4.7) which, for present application, are put in alternate form

$$(7.1) \quad \frac{\delta T}{T} = \left(\frac{\gamma-1}{\gamma}\right) \frac{\delta p}{p} = (\gamma-1) \frac{\delta \rho}{\rho}$$

where it is here useful to model the variations as $\delta T = T_t - T_s$, $\delta p = p_t - p_s$, $\delta \rho = \rho_t - \rho_s$; as above, $q_c = \delta p$ denotes (compressible) dynamic pressure. In turn, these equations can be integrated to get

$$(7.2) \quad T_t / T_s = (p_t / p_s)^{(\gamma-1)/\gamma} = (\rho_t / \rho_s)^{\gamma-1}$$

Note that total quantities can be varied by changing airspeed, and static variables can be held constant by flying a fixed altitude.

Temperature Calibration Measured values $T_{t,m}$ of total temperature T_t often exhibit small errors due to such things as flow distortion and sensor design. A standard calibration model for fixing such problems is to postulate that the **recovery factor** r defined as the quotient

$$(7.3) \quad r = \frac{T_{t,m} - T_s}{T_t - T_s}$$

is essentially constant, at least for small Mach numbers ($M < 1$). To help

7. Calibration of Temperature, Pressure, and Airspeed

understand what this means, consider the following equivalent form

$$(7.4) \quad T_t = T_{t,m} + K_T(T_t - T_s) = T_{t,m} + K_T \delta T$$

where now $K_T = 1 - r$. In this context, the constant recovery-factor model can be interpreted as a scaling adjustment that compensates for lack of sensitivity to adiabatic heating.

We first show that (7.3) is a Mach-number dependence for adiabatic change. Indeed, from (7.2) together with the definition of the Mach number (5.12), we get

$$\begin{aligned} \frac{T_t}{T_s} &= \left(\frac{p_t}{p_s}\right)^{(\gamma-1)/\gamma} = 1 + \frac{\gamma-1}{2} M^2 \\ \Rightarrow T_t - T_s &= \frac{\gamma-1}{2} M^2 T_s \end{aligned}$$

Substitution into (7.3) and solving for T_s then results in the following estimate

$$(7.5) \quad \hat{T}_s = T_{t,m} / \left(1 + r \frac{\gamma-1}{2} M^2\right)$$

which, in turn, leads to an estimate of total temperature

$$(7.6) \quad \hat{T}_t = \hat{T}_s \left(1 + \frac{\gamma-1}{2} M^2\right)$$

and shows that the recovery-factor postulate leads to corrections that depend only on the Mach number. Note, in particular, that when the sensor is standing still ($M=0$), this calibration does nothing $\hat{T}_s = T_{s,m}$. Thus, the sensor must already be calibrated for static conditions.

A somewhat more direct way of obtaining these corrections amounts to bypassing the Mach number by rewriting (7.4) in the form

$$T_t = T_{t,m} / [1 - K_T(1 - T_s/T_t)]$$

which, when combined with (7.2), immediately gives

$$(7.7) \quad \boxed{\hat{T}_t = T_{t,m} / [1 - K_T(1 - P_\gamma)]}$$

where, as in Sec. 5, $P_\gamma = (p_s/p_t)^{(\gamma-1)/\gamma}$. Now, static temperature is obtained as $\hat{T}_s = P_\gamma \hat{T}_t$. Note that this is mathematically equivalent to (7.6).

Recovery-Factor Estimation The accepted method of determining the recovery factor is using conventional wind tunnel testing. Flight test methods can then be used to check the recovery-factor to see if such things as flow

7. Calibration of Temperature, Pressure, and Airspeed

fields, radiation, radio frequency interference, etc. change the calibration of the in-situ sensor. One such flight test check, using reverse-track data, is discussed next.

It is not at all obvious that the recovery factor r can be estimated without knowing either the dynamic pressure or the static pressure. We do this next. To begin, recall that the true-airspeed equation (5.10) says that $\tau^2/2=c_p(T_t-T_s)$, and so the recovery factor (7.3) can be expressed

$$(7.8) \quad r = 2c_p \frac{T_{t,m} - T_s}{\tau^2}.$$

Consequently, by varying τ with constant T_s , we get

$$(7.9) \quad r = 2c_p \left(\frac{\Delta T_{t,m}}{\Delta \tau^2} \right)_{T_s}$$

where the subscript notation is used to emphasize that T_s is held constant. The key step amounts to finding conditions under which true airspeed τ can be replaced with the horizontal groundspeed $U_H = \|\mathbf{U}_H\|$ (as measured by the INS); if this can be done, the need for dynamic pressure is circumvented. Now, the usual way to keep static temperature constant is to fly at fixed altitude. Additionally, "reverse-track" maneuvers are particularly effective in canceling effects due to ambient wind. In more detail, suppose that U_+ and U_- are the horizontal groundspeeds obtained by flying first in the direction of the ambient wind $U_+ = \tau + v$ and then against it $U_- = \tau - v$ where v is the (horizontal) wind speed. Note that both τ and v must be nearly constant over the duration. This is relatively easy to achieve for true airspeed τ by simply flying with constant power. However, atmospheric conditions determine the windspeed v , and acquired data must be from a stable and laminar flow. In any case, data U_+^2 and U_-^2 for the two directions are averaged together to get

$$(7.10) \quad \begin{aligned} U_{\text{AVE}}^2 &= \frac{1}{2}(U_+^2 + U_-^2) = \frac{1}{2}[(\tau+v)^2 + (\tau-v)^2] \\ &= \tau^2 + v^2. \end{aligned}$$

Note that the net effect of averaging over opposite directions is to cancel the cross term τv . As previously stated, true airspeed must be varied to obtain a dynamic range of values. A simple way to do this is to use a high-speed value τ_{HI} and a low-speed one τ_{LO} . Thus, let U_{HI} and U_{LO} denote the average groundspeeds corresponding to the different airspeeds. Observe that *equal amounts of data in opposite directions must be averaged for the problematic cross terms $\pm \tau v$ to cancel*. The difference ΔU^2 is then computed as

7. Calibration of Temperature, Pressure, and Airspeed

$$(7.11) \quad \Delta U^2 = U_{HI}^2 - U_{LO}^2 = (\tau_{HI}^2 + v^2) - (\tau_{LO}^2 + v^2) \\ = \tau_{HI}^2 - \tau_{LO}^2 = \Delta \tau^2 .$$

Now, the small but potentially troublesome term v^2 cancels. Finally, substitution into (7.9) gives the required estimate

$$(7.12) \quad \hat{r} = 2c_P \left(\frac{T_{t,HI} - T_{t,LO}}{U_{HI}^2 - U_{LO}^2} \right)_{T_S}$$

where $T_{t,HI}$ and $T_{t,LO}$ denote the corresponding averages of the measured temperatures $T_{t,m}$ for the different airspeeds. We emphasize that this is an exact equation when maneuvers are precisely executed and when atmospheric conditions are stable. Also, there is no reference to pressure. However, if the sensor has a non-linear recovery-factor for some reason, the evaluation of recovery-factor will be incorrect if only two airspeeds are used.

Static Temperature We next show that *the net effect of temperature calibration is to correct the static temperature T_S* . In part, this follows from (7.5) above. However, it is more convincing to work backwards from the recovery-factor computation (7.12). First, recall that total temperatures $\hat{T}_{t,HI}$ and $\hat{T}_{t,LO}$ as computed from (7.7) satisfy

$$U_{HI}^2 - U_{LO}^2 = \tau_{HI}^2 - \tau_{LO}^2 = 2c_P(\hat{T}_{t,HI} - \hat{T}_{t,LO}) - 2c_P(\hat{T}_{s,HI} - \hat{T}_{s,LO})$$

provided the ambient-wind term u^2 cancels in the difference. But, the recovery factor is computed to force the balance $U_{HI}^2 - U_{LO}^2 = 2c_P(\hat{T}_{t,HI} - \hat{T}_{t,LO})$ which is equivalent to saying that computed static temperature must be the same for the two racetracks, i.e., $\hat{T}_{s,HI} = \hat{T}_{s,LO}$. In any case, the recovery factor is usually close to unity (e.g. $\hat{r}=0.95$), and corrections to static temperature are typically only a few tenths of a degree ($^{\circ}\text{K}$).

Racetrack Maneuvers In practice, data are acquired from **dual racetracks** consisting of two racetrack maneuvers aligned with the wind direction; *one is flown at high speed while the other is flown at low; both are flown at the same altitude and with as little roll as possible (turns excluded)*. Each racetrack has two straight legs consisting of several minutes of data, separated by turns to reverse direction. In principle, the two legs should have opposite tracks, a condition that is made easier by flying directly into and against the wind which has the added advantage of reducing troublesome

7. Calibration of Temperature, Pressure, and Airspeed

correlations with the slip angle. In executing such maneuvers, small variations in altitude (~50 m) are inevitable and can cause small variations in ambient temperature T_s . Corrections can be made by adjusting to a constant altitude via a lapse-rate model. Thus, if $\langle H \rangle$ denotes the average altitude for both race tracks and if Γ is a given lapse rate (typically 0.0065°K/m for moist air), then a corrected value $\tilde{T}_{t,m}$ can be obtained as

$$(7.13) \quad \tilde{T}_{t,m} = T_{t,m} + \Gamma(H - \langle H \rangle).$$

where H is the altitude corresponding to the sample $T_{t,m}$. In principle, (7.13) is not really a correction to total temperature at all, but a static-temperature correction applied to the difference $T_{t,m} - T_s$ occurring in the numerator of (7.8); because the net effect is the same, it is here convenient to attach it to total temperature. As a check on signs, note that if altitude H is greater than the mean $\langle H \rangle$, then the temperature $T_{t,m}$ at H will be smaller than the hypothetical temperature $\tilde{T}_{t,m}$ at $\langle H \rangle$.

Static-Pressure Calibration Here the model to correct for airspeed dependence is:

$$(7.14) \quad \hat{p}_s = p_{s,m} + K_p q_{c,m}.$$

where $p_{s,m}$ and $q_{c,m}$ are the measured static and dynamic pressures respectively; K_p is the calibration constant (the dependence is not necessarily on $q_{c,m}$, but could be upon attack angle or Mach number). Note that this model simply balances two quantities of the same basic type, and when the sensor is standing still ($q_{c,m} = 0$), calibration does nothing $\hat{p}_s = p_{s,m}$. Thus, as with temperature, this sensor must already be calibrated for static conditions. In any case, K_p can be evaluated in flight tests using a reference pressure sensor inside of a trailing cone flown at several different airspeeds and altitudes to compute the range of static errors (Brown, 1988). Such flight testing can reduce static and dynamic errors to ± 0.4 mb and ± 0.53 mb, respectively.

True-airspeed Calibration It remains to calibrate dynamic pressure q_c and with it, true airspeed. Here the model is a simple one:

$$(7.18) \quad \hat{q}_c = K_q q_{c,m}.$$

Now, the constraint on K_q is to optimize the true-airspeed computation. This

7. Calibration of Temperature, Pressure, and Airspeed

is done by comparing computed airspeed with horizontal groundspeed. Again, using racetrack data, constant winds cancel and the constraint is simply stated in terms of sample averages

$$(7.19) \quad \boxed{\langle \tau \rangle = \langle U_H \rangle} .$$

As with the recovery-factor computation, valid application requires data from reverse tracks to be of equal duration. However, dual racetracks are not required – they can either be used separately or in tandem. In particular, they can be used to test whether K_q is, in fact, a constant.

The difficulty in using this condition is that equations are nonlinear and computing a solution requires a search algorithm. To review the computation, recall that known data are $T_{t,m}$, $p_{s,m}$, $q_{c,m}$, and γ , and known calibration constants are $K_T = 1 - r$ and K_p . In particular, static pressure may be considered as already corrected: $p_s = p_{s,m} + K_p q_{c,m}$. Then for a trial value of K_q , true airspeed is computed

$$(7.20) \quad \begin{aligned} q_c &= K_q q_{c,m} \\ P_\gamma &= [p_s / (p_s + q_c)]^{(\gamma-1)/\gamma} \\ T_t &= T_{t,m} / [1 - K_T(1 - P_\gamma)] \\ T_s &= P_\gamma T_t \\ \tau &= \sqrt{2c_p(T_t - T_s)} \end{aligned}$$

This computation is then repeated for all given data, and the average error $e(K_q) = \langle U_H \rangle - \langle \tau \rangle$ is used to indicate whether the trial value K_q was a good one or not. Finally, the whole procedure is repeated for many different values of K_q , and the value \hat{K}_q for which $e(K_q)$ is closest to zero is the answer. In practice, \hat{K}_q must be computed with an iterative root-finding algorithm.

Vapor Pressure and Relative Humidity Vapor pressure e is not measured directly, but inferred from mirror temperature T_{mir} (measured in °C) measured with a cooled-mirror, dew point hygrometer. The exact calculation is:

$$(7.21) \quad e = \begin{cases} 6.1078 \exp[17.6498 T_{\text{mir}} / (243.17 + T_{\text{mir}})], & T_{\text{mir}} \geq 0 \\ 6.1078 \exp[22.4716 T_{\text{mir}} / (272.72 + T_{\text{mir}})], & T_{\text{mir}} \leq 0 \end{cases} .$$

For temperatures above freezing, T_{mir} is better known as dew point temperature T_d , and for temperatures below freezing it is usually converted to frost point temperature (also denoted T_d):

7. Calibration of Temperature, Pressure, and Airspeed

$$(7.22) \quad T_d = \begin{cases} T_{\text{mir}}, & T_{\text{mir}} \geq 0 \\ 243.17 [(\log e - 1.8096)/(19.4594 - \log e)], & T_{\text{mir}} \leq 0 \end{cases}$$

Next, relative humidity is based on an intermediate quantity called the **saturation vapor pressure** e_w (mb); it is computed in a fashion similar to e , but with static temperature T_s in place of T_{mir} :

$$(7.23) \quad e_w = 6.1078 \exp[17.45 T_s / (241.48 + T_s)]$$

where T_s also has units of $^{\circ}\text{C}$. Finally, the relative humidity estimate \mathcal{H} is computed in percent as:

$$(7.24) \quad \mathcal{H} = 100 \eta (p_s - e_w) / e_w$$

where, as in Sec. 4, η is the mixing ratio.

Constant Offsets The last detail in calibrating temperature and pressure is to baseline ambient values. Recall that our calibration models are linear, and slopes have already been computed; it remains to compute the intercepts. This requires comparison of static temperature and pressure along with mirror temperature with in-situ measurements, say from a tower; needed data is acquired with "fly-bys" at different airspeeds. In turn, small corrections are inferred and used to (additively) adjust *measured* parameters.

8. CALIBRATION OF FLOW-ANGLES

In the previous section, we calibrated true-airspeed τ which is the amplitude of the relative wind $\mathcal{W}_r = \tau \hat{e}_r$, it remains to calibrate the direction vector \hat{e}_r which, in view of Sec.3, is the same as calibrating the flow angles.

Not surprising, flow-angle calibration is largely geometric. The easy case is that of straight-and-level flight. However, when roll ϕ is added, the situation becomes more complex; now, both α and β can change with ϕ . Consider the situation where probes are mounted on the fuselage; the attack probe is located, say, near the front and on one side while the slip probe is located nearby, but on the top. This arrangement is poor because it lacks symmetry with respect to roll. When the aircraft is banked in a turn, flow is modified in nonlinear ways, and this distortion gets passed on to the sensors; in particular, affects may not be the same in right and left turns.

Standard Calibration In Sec.6, we showed that the flow angles are, to first order, proportional to quotients of a differential pressure and a dynamic pressure. The calibration model commonly used for straight-and-level flight ($\phi=0$) is

$$(8.1) \quad \begin{array}{l} \tan \alpha = K_\alpha (\delta_\alpha p / q_\alpha) + A_0 \\ \tan \beta = K_\beta (\delta_\beta p / q_\beta) + B_0 \end{array}$$

Here $\delta_\alpha p$, $\delta_\beta p$, q_α , and q_β , denote measured pressures while K_α , K_β , A_0 , and B_0 are the calibration constants. For example, with the high-resolution method (6.2) and (6.14) we would choose $\delta_\alpha p = \delta_2 p - \delta_4 p$, $q_\alpha = (\delta_2 p + \delta_4 p) / 2$, $\delta_\beta p = \delta_3 p - \delta_1 p$, and $q_\beta = (\delta_3 p + \delta_1 p) / 2$. Note, however, that K_α and K_β are inverse to the sensitivity coefficients used before; also A_0 and B_0 are constant offsets that align flow parameters to inertial navigation, in particular, to correct for possible misalignment of sensors. Although required pressures can be obtained in different ways, it is enough here to know that they are supplied by measurement. Also, the small-angle approximations $\tan \alpha \cong \alpha$ and $\tan \beta \cong \beta$ are often used in this model. Not only is this less correct, it is confusing; it suggests that additional trigonometry is required in subsequent relative-wind calculations.

It turns out that dual racetracks provide a good source of calibration data for K_α and B_0 , but *not* for K_β ; data for A_0 is conditional. There is significant correlation of true airspeed with the attack angle, but not with the slip angle. (On the P-3's, changing airspeed from 180 kt to 240 kt results

8. Calibration of Flow Angles

in a change from about 3° to about 0° in the attack angle.) To estimate K_α , observe that *in straight-and-level flight, attack α and pitch θ should have the same dynamic range, and so*

$$(8.2) \quad K_\alpha = \frac{\tan \theta_{HI} - \tan \theta_{LO}}{(\delta_\alpha p/q_\alpha)_{HI} - (\delta_\alpha p/q_\alpha)_{LO}}$$

In turn, A_0 can be estimated

$$(8.3) \quad A_0 = \frac{1}{2} \left\{ \tan \theta_{HI} + \tan \theta_{LO} - K_\alpha \left[(\delta_\alpha p/q_\alpha)_{HI} + (\delta_\alpha p/q_\alpha)_{LO} \right] \right\}$$

which is valid *provided there is no net vertical motion in the atmosphere.* However, vertical velocities on the order of 10 cm/s are common, and such motion is difficult, if not impossible, to isolate or average out. At the same time, A_0 is an important parameter to estimate well; it determines the zero line of the vertical-wind measurement. In the next section, we see that there may be other nonlinear effects as well.

Yaw Maneuvers Slip-angle calibration requires special data taken in yaw maneuvers. Such maneuvers are executed by skidding the aircraft from side to side, in snake-like fashion, to produce variations in the slip angle. Again these maneuvers are flown at constant altitude and with as little roll as possible. Recall that attack is calibrated by comparison with the pitch angle. In a similar way, slip is calibrated by comparison with the drift angle $d = \zeta - \psi$. However, unlike the comparison of attack and pitch, the comparison of slip and drift is an approximation which is only exact in horizontal flight when pitch is zero. Fortunately, pitch is typically small (a few degrees) and this problem can usually be neglected. In any case, data are divided into high and low averages by separating quantities which lie above and below the sample mean. The estimate of K_β is then analogous to the estimate of K_α .

$$(8.4) \quad K_\beta = \frac{\tan d_{HI} - \tan d_{LO}}{(\delta_\beta p/q_\beta)_{HI} - (\delta_\beta p/q_\beta)_{LO}}$$

To continue, we observe that the (strenuous) turning and skidding required in the yaw maneuver is difficult to execute with high precision, making it a poor source of data for B_0 . However, dual racetracks provide a good source of data. Thus, B_0 is estimated using racetrack data as:

8. Calibration of Flow Angles

$$(8.5) \quad B_0 = \frac{1}{2} \left\{ \tan d_{HI} + \tan d_{LO} - K_\beta \left[(\delta_\beta p/q_\beta)_{HI} + (\delta_\beta p/q_\beta)_{LO} \right] \right\}$$

We emphasize that data bases used in (8.4) and (8.5) are completely different and should not be confused.

Improved Calibration Models? The calibration model (8.1) is known to be inexact in several ways. First, none of the refinements of the exact solutions (6.14), (6.16), or (6.19) are reflected in this model. Recall from Sec.6 that net improvements using exact solutions were diagnosed as being marginal except possibly in extreme cases.

Another modeling error, at a similar level of significance, is due to the way that sensor misalignment is corrected. A small error ε in an angle x affects the tangent as $\tan(x+\varepsilon) = [\tan x + \tan \varepsilon] / [1 - \tan x \cdot \tan \varepsilon]$, and the nonlinearity in this denominator is not accounted for in (8.1).

Improved Comparison Angles Recall that our understanding of flow angles is through comparison with pitch and drift. However, when roll is present, this comparison is no longer valid. In fact, even without roll, the comparison of slip with drift is an approximation. Our objective here is to compute more accurate comparison angles, say α_0 and β_0 , that also work when roll is present. Recall from (3.2) that attack and slip satisfy $\tan \alpha = \mathcal{W}_r / \mathcal{U}_r$ and $\tan \beta = \mathcal{V}_r / \mathcal{U}_r$ where $\mathcal{U}_r = (\mathcal{U}_r, \mathcal{V}_r, \mathcal{W}_r)$ is the relative-wind vector expressed in aircraft coordinates. Consequently, first-order approximations to the wanted angles satisfy $\tan \alpha_0 \cong \mathcal{W}_0 / \mathcal{U}_0$ and $\tan \beta_0 \cong \mathcal{V}_0 / \mathcal{U}_0$.

Better approximations can be obtained by transforming computed winds into *aircraft coordinates* where attack and slip are measured. In aircraft coordinates wind is computed, $\mathbf{u} = \mathcal{U}_0 + \mathcal{U}_r$ where $\mathcal{U}_0 = \mathbf{G}^{-1} \mathbf{U}_0 = (\mathcal{U}_0, \mathcal{V}_0, \mathcal{W}_0)$ and \mathbf{G}^{-1} is the inverse of the orthogonal matrix \mathbf{G} in (2.6). Next, remembering that \mathcal{U}_r is always negative,

$$(8.6) \quad \begin{aligned} \mathbf{u} = \mathcal{U}_0 + \mathcal{U}_r &= \mathcal{U}_0 - |\mathcal{U}_r| (\mathcal{U}_r / \mathcal{U}_r) \\ &= (\mathcal{U}_0, \mathcal{V}_0, \mathcal{W}_0) - |\mathcal{U}_r| (1, \tan \beta, \tan \alpha) . \end{aligned}$$

and it becomes apparent that more correct comparison angles should satisfy:

$$(8.7) \quad \begin{aligned} \tan \alpha_0 &\equiv \mathcal{W}_0 / |\mathcal{U}_r| \\ \tan \beta_0 &\equiv \mathcal{V}_0 / |\mathcal{U}_r| \end{aligned}$$

8. Calibration of Flow Angles

With these definitions, (8.6) can be written

$$(8.8) \quad u \cong |\mathcal{U}_r| \left[\left(\mathcal{U}_0 / |\mathcal{U}_r| - 1 \right) \hat{i} + (\tan \beta_0 - \tan \beta) \hat{j} + (\tan \alpha_0 - \tan \alpha) \hat{k} \right]$$

and we can now better understand what is going on. First, $\mathcal{U}_r \cong -\tau$ is a controlled variable (that usually changes slowly), and so wind information is largely contained in the angles. In particular, mean winds are contained in α_0 and β_0 (because airborne platforms tend to advect with the mean flow), and fluctuations are contained in α and β (because flow-angle sensors react more quickly). Clearly, this mixed behavior complicates wind measurement and can be difficult to analyze.

However, the definition (8.7) is somewhat circular (i.e., nonlinear) insofar as \mathcal{U}_r also depends on flow angles; more precisely, $\mathcal{U}_r = -\tau/D$ where D , as defined in (3.3), depends on $\tan \alpha$ and $\tan \beta$. This difficulty can be circumvented by replacing $\tan \alpha$ and $\tan \beta$ with $\tan \alpha_0$ and $\tan \beta_0$ in the definition of D . Now, angles must satisfy the coupled set of quadratic equations:

$$\begin{aligned} \tan^2 \alpha_0 &= (\mathcal{W}_0/\tau)^2 (1 + \tan^2 \alpha_0 + \tan^2 \beta_0) \\ \tan^2 \beta_0 &= (\mathcal{V}_0/\tau)^2 (1 + \tan^2 \alpha_0 + \tan^2 \beta_0) . \end{aligned}$$

Taking quotients shows $\mathcal{V}_0^2 \tan^2 \alpha_0 = \mathcal{W}_0^2 \tan^2 \beta_0$ and this system is readily solved to give:

$$(8.9) \quad \boxed{\begin{aligned} \tan \alpha_0 &\cong \mathcal{W}_0/\Lambda \\ \tan \beta_0 &\cong \mathcal{V}_0/\Lambda \end{aligned}}$$

$$\text{where } \Lambda = \sqrt{\tau^2 - \mathcal{V}_0^2 - \mathcal{W}_0^2} .$$

The tedious part of this computation is inverting the groundspeed: $\mathcal{U}_0 = \mathbf{G}^{-1} \mathbf{U}_0 = (\mathcal{U}_0, \mathcal{V}_0, \mathcal{W}_0)$. Observe that, unlike pitch and drift, these estimates depend on true airspeed τ . Also, Λ is an estimate of $|\mathcal{U}_r|$, and when ambient winds are small, can be replaced with \mathcal{U}_0 .

The calibrations (8.2)-(8.5) for attack and slip can now be improved by replacing θ with α_0 and d with β_0 . However, "improvements" so obtained have been marginal, probably because racetrack maneuvers tend to cancel many of the errors anyway. The main application is to data with nonzero roll.

To use these angles, maneuvers must be flown to make the mean wind $\langle u \rangle$ in (8.8) cancel out. This is possible because ambient wind u in aircraft

8. Calibration of Flow Angles

coordinates has the curious, but useful, property of depending on attitude angles; more precisely, \mathbf{u} is computed as the inverse transformation $\mathbf{u}=\mathbf{G}^{-1}\mathbf{u}$ of ambient wind \mathbf{u} , expressed in geodetic coordinates. For example, circles are usually flown with constant pitch and roll, in which case \mathbf{G} varies only with heading ψ . Thus, $\langle \mathbf{u} \rangle = 0$ when averaged over an integral number of circles, provided that ambient wind \mathbf{u} is constant. (More general conditions can be obtained using Stokes Theorem.)

Calibration for Roll In principle, calibration for roll is possible when flow distortion is laminar (the kind that creates lift). However, in practice, this is seldom done, due to the complexity of the problem.

To help understand the affect of roll, we compute simpler estimates of α_0 and β_0 in the special case when aircraft motion is horizontal and pitch is small. We observe that in horizontal flight, the main affect of roll is to rotate the pitch and drift angles into the attack and slip planes. This rotation can be approximated:

$$(8.10) \quad \begin{bmatrix} \alpha_0 \\ \beta_0 \end{bmatrix} \cong \begin{bmatrix} \cos \phi & -\sin \phi \\ \sin \phi & \cos \phi \end{bmatrix} \begin{bmatrix} \theta \\ d \end{bmatrix} .$$

We remark that this estimate is not meant to be an alternative to (8.6); its main use is for analysis.

Now, parameters most affected by flow distortion due to roll are the "constants" A_0 and B_0 in (8.1). Intuitively, these parameters reflect changes in the mean flow along the skin of the aircraft; when banked in a turn, flow characteristics can change, requiring an adjustment. By contrast, the sensitivity coefficients K_α and K_β are relatively unaffected. Therefore, *the next significant level of complexity in a calibration model is to allow for roll dependence: $A_0=A_0(\phi)$ and $B_0=B_0(\phi)$.*

Lagrangian Circles Data for computing the functions $A_0(\phi)$ and $B_0(\phi)$ can be obtained by flying left and right circles with constant roll ϕ ; additionally, airspeed and altitude should be kept constant. In the absence of ambient wind, this maneuver does, indeed, result in Eulerian circles. However, when wind is present, the Eulerian circles become Lagrangian ones that advect with the mean flow; aircraft tracks, as observed from the ground, consist not of circles but of cycloids.

Experience has shown that at least three circles are required with each value of ϕ for unambiguous interpretation. Thus, a minimal calibration would require three circles to the right and three circles to the left, say, with

8. Calibration of Flow Angles

constant bank angles $\pm 30^\circ$. Then, using the same values of K_α and K_β computed in (8.2) and (8.4), estimates of A_0 and B_0 can be obtained as:

$$(8.11a) \quad A_0(\phi) = \langle \alpha_0 \rangle - K_\alpha \langle \delta_\alpha p / q_\alpha \rangle$$

$$(8.11b) \quad B_0(\phi) = \langle \beta_0 \rangle - K_\beta \langle \delta_\beta p / q_\beta \rangle$$

where, as usual, $\langle \cdot \rangle$ denotes the sample mean or average. Observe that in straight-and-level flight, these equations are equivalent to (8.3) and (8.5) above. Note also that both $\langle \alpha_0 \rangle$ and $\langle \beta_0 \rangle$ are strongly influenced by ambient wind, and so, to minimize unwanted affects, it is important to average over an integral number of circles. We emphasize that (8.11) should be applied to the left and right circles independently; joint application with data from both is not very meaningful. In any case, we now presumably have three sets of estimates corresponding to roll angles ϕ of -30° , 0° , and 30° ; therefore, required calibration functions $A_0(\phi)$ and $B_0(\phi)$ can be modeled as quadratics. Otherwise said, intermediate values can be inferred from quadratic interpolation.

Useful diagnostic quantities are the **track and cross-track components** of the computed wind (also known as the longitudinal and lateral components or as the tangential and radial components). The track component u_ζ is the horizontal wind in the track direction $u_\zeta = \mathbf{u} \cdot \mathbf{i}_\zeta$, and the cross-track component u_x is the remaining orthogonal part, it is positive outward along the right wing. In more detail, suppose that $\mathbf{U}_0 = (U_0, V_0, W_0)$ is the aircraft velocity and $\mathbf{u} = (u, v, w)$ is the computed wind. Then, u_ζ and u_x are computed as

$$(8.12) \quad \begin{aligned} u_\zeta &= (uU_0 + vV_0) / D \\ u_x &= (uV_0 - vU_0) / D \end{aligned}$$

where $D = \sqrt{U_0^2 + V_0^2}$ is the horizontal groundspeed. For circles, these quantities should be sinusoidal and 90° out of phase; in particular, they should have the same amplitude. It turns out that the track component u_ζ depends primarily on true airspeed while the cross-track component u_x depends primarily on flow angles, and this separation is valuable in analysis procedures.

In concluding this material, we remark that flow-angle calibration can often be improved through direct analysis of computed winds. The advantage is that winds are computed using all available transformations and corrections. At the same time, winds tend to be sensitive to calibration errors, and

8. Calibration of Flow Angles

minimizing erroneous correlations with aircraft maneuvers often produces better results. In short, calibration constants are "fine-tuned" using the final product rather than some intermediate one. This can either be done manually or with search algorithms.

9. IN-FLIGHT EXAMPLES

We now apply theory and procedures of the last three sections to the P-3's. We emphasize from the onset that the primary purpose of this exposition is to illustrate basic ideas and theory, and not necessarily to document specific sets of parameters.

Our discussion will focus on two calibration flights, one for each aircraft (N43RF and N42RF); acquired data were taken nearly two years apart, on the 13th of August, 1987 and on the 10th of August, 1989 respectively. Calibration flights of this kind, during the summer, are performed yearly in support of hurricane research and reconnaissance, and generally consist of two basic parts: (I) "high-altitude" maneuvers to determine dynamic parameters and (II) "ground-based" comparisons to determine constant offsets. In the 1987 calibration, the ground-based comparison was done with tower data acquired at a flight-training strip (the Dade-Collier airport), west of Miami and in the Everglades ecosystem. Data so acquired was near the ground (~ 25 m), in the boundary layer, and may not be representative of operational conditions. The 1989 comparison was done using a tethered balloon located at NASA's lightning triggering site on the north tip of Merritt Island, near Cape Canaveral FL. This comparison consisted of fly-bys at altitudes ranging from 150 ft to 4100 ft. Although results were generally consistent with P-3 data, measurement difficulties (on the balloon) obscured accuracies and the comparison. Although such comparisons are important and operationally intricate, they are conceptually straightforward and will not be further discussed here. For present purposes, the important aspect of these flights was that the "high-altitude" maneuvers were performed over open water and away from possible sea-breeze affects.

An identifying feature of in-flight procedures is the **calibration staircase** of race-track maneuvers. Two staircases are shown in Fig. 9-1 for the 1987 calibration (upper left curve) and the 1989 calibration (upper right curve); both curves are plots of *radar* altimetry verses time. Note that the 1987 curve is a descending staircase while the 1989 staircase is an ascending one. It is worth mentioning that such procedures were introduced in 1987 and this was the first staircase used with N43RF. It turns out that ascending staircases are somewhat more effective because aircraft are lighter near the top (due to fuel consumption) and can go higher. (The P-3's operational ceiling is about 25,000 feet.)

In more detail, the 1987 staircase of race tracks consisted of six steps

9. In-Flight Examples

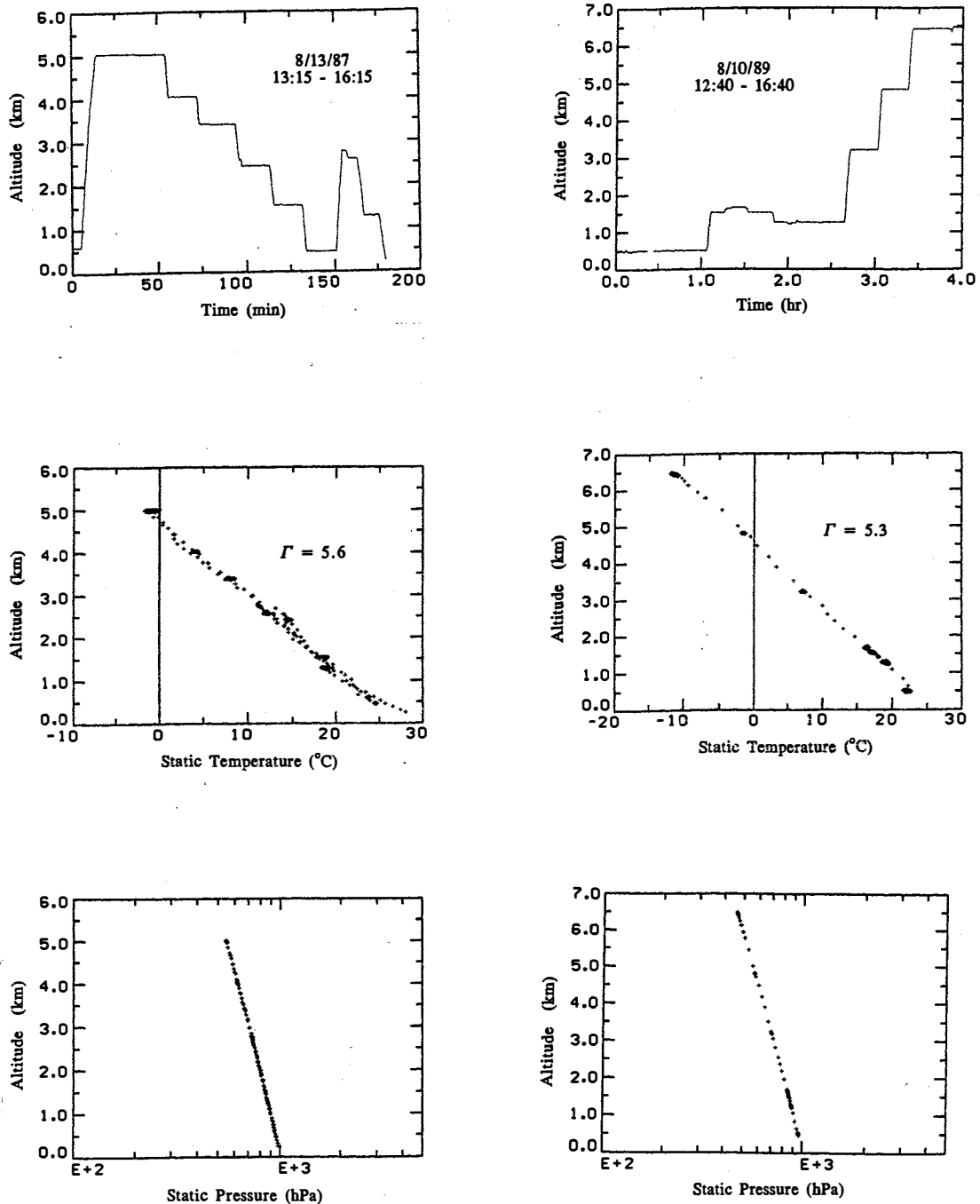


Fig. 9-1. P-3 calibration flight data. The left-hand graphs are from N43RF's calibration flight on 8/13/87; the right-hand graphs are from N42RF's calibration flight on 8/10/89. Radar altitude is plotted versus time in the upper graphs, showing the calibration staircase performed in each flight. Radar altitude vs. static temperature is plotted in the middle graphs, with lapse rates $\Gamma=5.6^{\circ}\text{C}/\text{km}$ and $\Gamma=5.3^{\circ}\text{C}/\text{km}$ shown. Radar altitude vs. static pressure is plotted in the bottom graphs, showing that the atmosphere was approximately hydrostatic in both flights.

9. In-Flight Examples

or levels at approximate altitudes of 15 K, 12 K, 10 K, 8 K, 5 K, and 1.5 K feet respectively; the remaining levels shown in Fig. 9-1 were for other maneuvers. (These altitudes correspond to pressure increments of about 100 mb.) By contrast, the 1989 staircase consisted of fewer altitudes but a greater overall range; altitudes used were 1.5 K, 5 K, 10 K, 15 K, and 20 K feet. The additional levels shown were part of the balloon comparison mentioned above. All things considered, it was probably a mistake to combine the staircase with the balloon comparison. Compromises had to be made; staircase data was more spread out in time and the 8 K altitude was omitted altogether. At the same time, there is more variability in calibration at lower altitudes, and multiple levels help protect against faulty data. Because of this, the author recommends using the *seven* altitudes: 1.5 K, 5 K, 8 K, 10 K, 12 K, 15 K, and 20 K feet in future calibrations.

Another important aspect of calibration is the atmosphere itself; conditions should be as stable and quiescent as possible. In southern Florida, early morning flights are best (to avoid afternoon convection); the basic idea is to start maneuvers as soon as the sun is high enough in the sky to insure good visibility. For the calibrations under consideration, both staircases were started at about 1330 Z (830 EDT).

A good (post-processing) check on atmospheric conditions is supplied by temperature. To this effect, scatter plots of altitude verses computed, static temperature ($^{\circ}\text{C}$) are also shown in Fig. 9-1. The reason for the apparent sparsity of points is, in part, because the 1 Hz data was preaveraged into 19 s bins (1987) and 24 s bins (1989) prior to plotting; additionally, many of the points fall on top of one another and cannot be distinguished. In any case, both scatter plots are roughly straight lines with lapse rates Γ of about $5.6^{\circ}\text{C}/\text{km}$ and $5.3^{\circ}\text{C}/\text{km}$ respectively, showing that conditions were about as homogeneous and stable as could be expected.

Analogous scatter plots of static pressure p_s are shown in the bottom curves of Fig. 9-1, and relative humidity \mathcal{H} , as computed by (7.23), is shown in Fig. 9-2 for the 1989 calibration (only). Here, pressure (upper curve) appears as a nearly perfect straight line when displayed in log-linear fashion. This is the result of the atmosphere being hydrostatic: $dp/dz = -\rho g$, together with the exponential decay of density ρ with height z . Next observe that humidity (lower curve) exceeds 80% at lower altitudes, typical to southern Florida in the summer. Also, note that the plot shows the presence of a dry-air layer at about 5 km (15K ft). Such layers have repeatedly been

9. In-Flight Examples

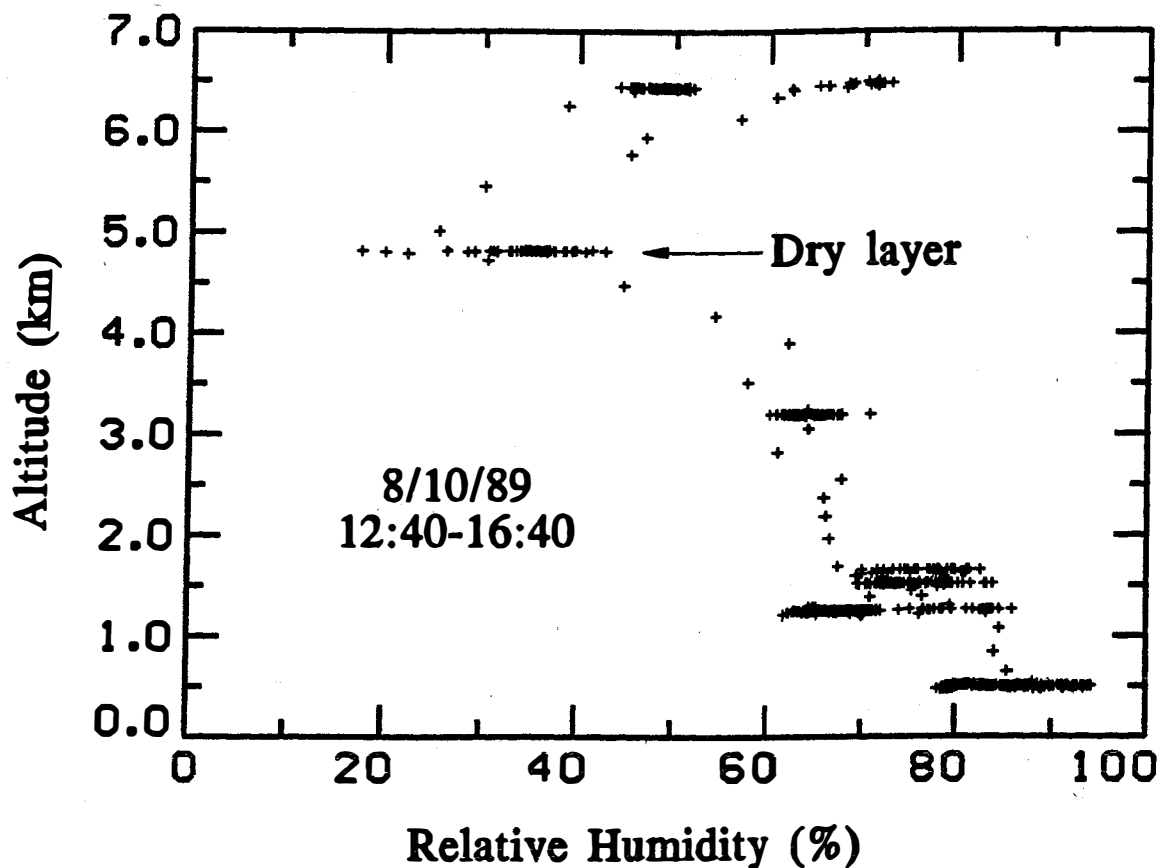


Fig 9-2. Radar altitude vs. relative humidity for N42RF's calibration flight on 8/10/89.

observed, and have been useful in determining humidity dependencies which would otherwise be difficult to distinguish from altitude ones.

With this background, we now turn to the details. First, the basic maneuver executed at each level of the staircase consisted of dual racetracks at (indicated) airspeeds of 240 kt and 180 kt respectively; these airspeeds are, effectively, the limits of P-3 performance (at least, in turbulent air). Racetracks were flown with a two-minute leg flow directly into the wind with a companion leg in the opposite direction; thus, four minutes of straight-and-level data were acquired from each racetrack. We also observe from Fig.9-1 that each step requires about 15-20 minutes of flight time; this time is attributable to the eight minutes of data together with time for wind alignment, turns, and a changes in altitude.

As documented in previous sections, the objective of dynamic calibration is to deduce calibration constants K_T , K_p , K_q , K_α , K_β , A_0 , and B_0 used to correct total temperature \hat{T}_t , static pressure \hat{p}_s , and dynamic pressure \hat{q}_c , as well as to estimate the attack and slip angle tangents $\tan\hat{\alpha}$ and $\tan\hat{\beta}$

9. In-Flight Examples

as summarized in the calibration models:

$$(9.1) \quad \begin{aligned} \hat{T}_t &= T_{t,m} / [1 - K_T(1 - P_{\gamma,m})] \\ \hat{p}_s &= p_{s,m} + K_p q_{c,m} \\ \hat{q}_c &= K_q q_{c,m} \\ \tan \hat{\alpha} &= K_\alpha (\delta_\alpha p / q_\alpha) + A_0 \\ \tan \hat{\beta} &= K_\beta (\delta_\beta p / q_\beta) + B_0 \end{aligned}$$

where $T_{t,m}$, $p_{s,m}$, and $q_{c,m}$ are the measured (total) temperature, static pressure, and dynamic pressure respectively; also, $\delta_\alpha p$, $\delta_\beta p$, q_α , and q_β , are some compatible set of measured differential flow-angle pressures as discussed in Sec. 6. Here, $P_{\gamma,m}$ is an intermediate quantity defined $P_{\gamma,m} = (p_{s,m} / p_{t,m})^{(\gamma-1)/\gamma}$ where γ is the (computed) Poisson constant discussed in Sec. 4.

Before proceeding there is a scaling problem that needs to be mentioned. The difficulty is that calibration constants K_α , K_β , A_0 , and B_0 have traditionally been scaled in degrees which is technically inconsistent unless the small-angle approximation $\tan(x) \cong x$ is used. Also, for historical reasons, P-3 parameters K_α and K_β differ from theoretical ones by a factor of two. Although these are purely formal problems, the reader should be wary when interpreting results.

Recall that, with the exception of K_β , all constants can be estimated for each level of the staircase, from a single pair of dual racetracks. Computed results for K_T , K_p , K_q , K_α are shown in Tables 9-1 and 9-2 for the 1987 and 1989 calibrations respectively. As above, temperature is tabulated in $^\circ\text{C}$, pressure in mb and the mixing ratio η in g/kg; additionally, all values shown are ensemble averages over the full 8 min of racetrack data.

Our first observation is the relatively poor quality of the temperature calibration K_T ; in the 1987 calibration, the 8K and 10K values were discarded because of observed dust (possibly African). Nonetheless, the resulting average $\hat{K}_T = 0.079$ is reasonable and corresponds to a recovery factor of $\hat{r} = 1 - \hat{K}_T = 0.921$. Although amplitudes were similar in the 1989 calibration, values fluctuated in sign for unknown reasons and had to be discarded as erroneous. While it is well known that water droplets adversely affect the temperature measurement, this would indicate that there are other factors as well. In any case, the wisdom of using temperature calibration with these sensors is debatable.

9. In-Flight Examples

H_r (feet)	$p_{s,m}$ (m/s)	$T_{t,m}$ (°C)	η (g/kg)	K_T	K_p	K_q	K_α (deg)
15.0K	555.9	8.14	3.8	0.074	0.030	0.990	6.14
12.0K	627.8	12.51	3.7	0.086	0.027	0.986	6.18
10.0K	679.1	15.97	5.8	0.078	0.027	0.984	6.12
8.0K*	763.2	21.93	3.0	-0.016x	0.028	0.989	6.32
5.0K*	850.1	24.91	9.2	-0.050x	0.027	0.979	6.27
1.5K*	960.1	30.72	14.5	0.079	0.029	0.972	6.17
Averages =				0.079	0.028	0.983	6.20

*=observed dust, x=discarded

Table 9-1. Computed calibration constants for N43RF, 13-Aug-87. Instrumentation: INS=2, Temperature 2, Wingtip pressures.

H_r (feet)	$p_{s,m}$ (m/s)	$T_{t,m}$ (°C)	η (g/kg)	K_T	K_p	K_q	K_α (deg)
1.5K	958.3	28.62	17.9	-0.082	0.024	0.966	6.15
5.0K	852.8	24.33	12.2	0.085	0.030	0.966	6.13
10.0K	698.2	15.88	6.6	0.079	0.028	0.965	6.17
15.0K	571.8	8.22	2.4	-0.024	0.027	0.965	6.04
20.0K	464.3	0.33	2.0	0.028	0.032	0.965	6.08
Averages =				fail	0.028	0.965	6.11

Table 9-2. Computed calibration constants for N42RF, 10-Aug-89. Instrumentation: INS=2, Temperature 1, Wingtip pressures.

We next observe that the true-airspeed calibration K_q is nearly constant in the 1989 data, but varies by several percent in the 1987 data which translates to errors of about ± 1 m/s. This variation was found to be attributable to humidity sensitivity in a Garrett pressure transducer on the N43RF wing tip (which was replaced in 1989), and humidity dependence was modeled empirically as $\tilde{K}_q = K_q / [1 - (p_v/p_{s,m})]$; results of this model are shown in Table 9-3. (Belatedly, it was learned that Garrett recommended routine replacement of a desiccant in the dynamic-pressure line.) Now, because \tilde{K}_q is nearly constant, the value of K_q in (9.1) can be computed as $K_q = 0.994 [1 - (p_v/p_{s,m})]$, and the problem is solved. Note that without data from many different altitudes, this problem could not have been properly diagnosed and parameterized, illustrating the great utility of staircase data.

Some results of pressure calibration and adiabatic temperature compensation are shown in Table 9-4. Although changes in static pressure

9. In-Flight Examples

H_r (feet)	$p_{s,m}$ (mb)	p_v (mb)	\tilde{K}_q
15.0K	555.9	3.37	0.996
12.0K	627.8	3.74	0.992
10.0K	679.1	6.25	0.994
8.0K	763.2	3.70	0.994
5.0K	850.1	12.40	0.993
1.5K	960.1	21.98	0.994
			0.994

Table 9-3. Wet calibration model \tilde{K}_q

H_r (feet)	$p_{s,m}$ (mb)	p_s (mb)	$T_{t,m}$ (°C)	T_s (°C)
1.5K	958.3	960.2	28.62	22.15
5.0K	852.8	855.2	24.33	17.19
10.0K	698.2	700.5	15.88	07.37
15.0K	571.8	574.0	8.22	-01.58
20.0K	464.3	466.8	0.33	-11.29

Table 9-4. Selected results for the 1989 calibration.

are small (~ 2 mb), the correction for adiabatic heating is substantial and requires good precision.

We next turn to flow-angle calibration. To motivate this discussion, we analyze a problem with our vertical-wind measurement. Vertical wind for the 1989 calibration staircase is shown in the upper curve of Fig. 9-3. Here, data was manually adjusted so that data on the far left corresponding to the 1.5K level is centered about zero. We next observe that data on the far right, at the top of the staircase, is about 40 cm/s. However, all who participated in this experiment agreed that such vertical velocities were unrealistic, leading to the conclusion that our vertical-wind measurement is drifting in time by perhaps as much as 5-10 cm/s per hour. This is a very serious problem; clearly, the single most important aspect of vertical measurement is to determine whether net vertical motion is up or down, and our example shows that this cannot be done with any certainty!

One might speculate that vertical measurement is drifting with altitude and/or true airspeed. Indeed, the lower plot in Fig. 9-3 shows that mean airspeed did increase with time; this is due to maneuvers being flown using *indicated* airspeed (5.14). Nonetheless, we next show that this drift is more likely correlated with P-3 fuel consumption.

9. In-Flight Examples

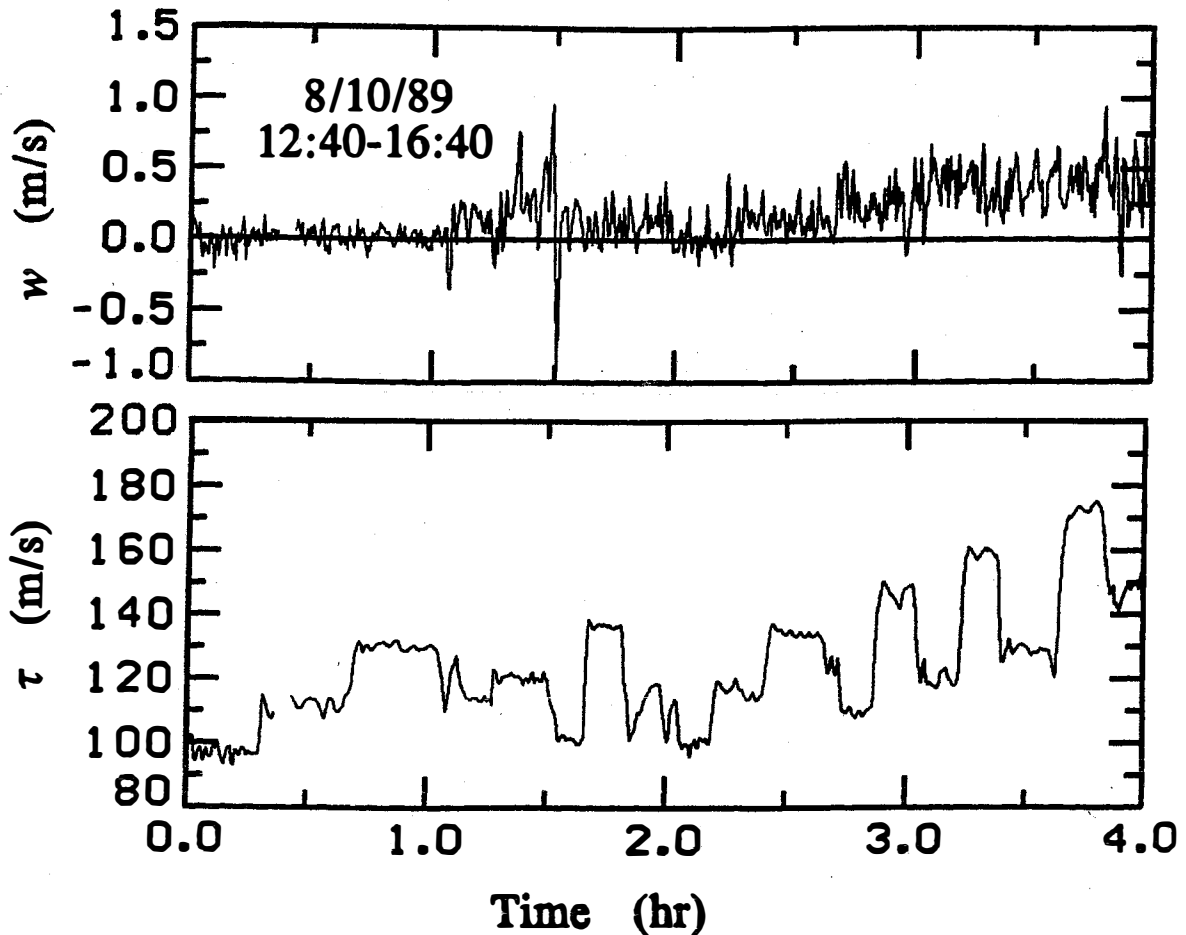


Fig 9-3. Vertical wind, w , and true airspeed, τ , vs. time for N42RF's calibration flight on 8/10/89.

A good place to start is to remember that vertical-wind measurement is largely determined by the attack-angle α , and we look for anomalies in this calibration. First, inspection of Tables 9-1 and 9-2 shows a weak trend in the dynamic parameter K_α . However, such variations are not very significant and can be neglected. By contrast, analogous variations in the offset A_0 cannot be so easily dismissed. Analysis of this important parameter is given in Tables 9-5 and 9-6 for the two calibrations. Because, A_0 also serves to compensate for possible misalignment of sensors, the means $\langle A_0 \rangle$ are first removed to show variations. Analogous variations are also computed for pitch θ and true airspeed τ . (Recall that the mean true airspeed is calibrated to be exactly the same as the mean groundspeed.) Also shown is the mean windspeed v together with its standard deviation $\sigma(v)$. (We remark that the large value of $\langle A_0 \rangle = 2.13$ in the 1989 calibration is consistent with a known alignment problem on N42RF.)

9. In-Flight Examples

H_r (feet)	A_0 (deg)	$A_0 - \langle A_0 \rangle$ (deg)	θ (deg)	$\theta - \langle \theta \rangle$ (deg)	τ (m/s)	$\tau - \langle \tau \rangle$ (m/s)	v (m/s)	$\sigma(v)$ (m/s)
15.0K	-0.79	0.04	1.57	0.12	139.7	13.7	8.8	1.2
12.0K	-0.81	0.02	1.52	0.07	132.4	6.4	8.9	0.8
10.0K	-0.84	-0.01	1.48	0.03	129.1	3.1	10.0	0.9
8.0K	-0.84	-0.01	1.43	-0.02	123.5	-2.5	6.8	0.3
5.0K	-0.86	-0.03	1.41	-0.04	118.0	-8.0	7.6	0.4
1.5K	-0.85	-0.02	1.31	-0.14	113.1	-12.9	5.6	0.6
	$\langle A_0 \rangle = -0.83$		$\langle \theta \rangle = 1.45$		$\langle \tau \rangle = 126.0$			

Table 9-5. Analysis of A_0 for 1987 calibration.

H_r (feet)	A_0 (deg)	$A_0 - \langle A_0 \rangle$ (deg)	θ (deg)	$\theta - \langle \theta \rangle$ (deg)	τ (m/s)	$\tau - \langle \tau \rangle$ (m/s)	v (m/s)	$\sigma(v)$ (m/s)
1.5K	2.24	0.11	1.95	0.57	113.4	-17.0	2.5	0.5
5.0K	2.19	0.06	1.57	0.19	119.0	-11.4	5.9	0.3
10.0K	2.11	-0.02	1.22	-0.16	129.5	-0.9	5.4	0.3
15.0K	2.06	-0.07	1.17	-0.21	138.8	8.4	5.3	0.9
20.0K	2.04	-0.09	1.00	-0.38	151.5	13.1	7.6	0.4
	$\langle A_0 \rangle = 2.13$		$\langle \theta \rangle = 1.38$		$\langle \tau \rangle = 130.4$			

Table 9-6. Analysis of A_0 for 1989 calibration.

We argue next that variations in A_0 matches observed drift in computed vertical winds. Indeed, for an aircraft traveling at 100 m/s, a 0.1° drift in α will result in an error of about $100 \tan(0.1^\circ) \cong 0.2$ m/s. Consequently, the 0.2° variation shown in Table 9.6 corresponds, almost exactly, to the drift observed in Fig. 9-3. Next, observe that $A_0 - \langle A_0 \rangle$ and $\theta - \langle \theta \rangle$ were positively correlated on both flights. At the same time, dependence on true-airspeed can be excluded because $A_0 - \langle A_0 \rangle$ and $\tau - \langle \tau \rangle$ were positively correlated in 1987, but negatively correlated in 1989. Similarly, correlation with altitude and/or pressure can be also be excluded because one staircase was ascending while the other was descending. Finally, there is no evidence of correlation with atmospheric winds, and a reasonable cause for the variation in A_0 is due to fuel consumption. (Unfortunately, this correlation was only discovered in the preparation of this document, and this hypothesis is yet untested.

It remains to calibrate the slip angle β , and here things are very disappointing. The difficulty is that P-3 slip sensors are located on top of the aircraft, and several meters behind the cockpit (see App. A); but the cockpit is known to generate a "rooster tail" and the slip sensor is in the

9. In-Flight Examples

turbulent wake. Because of this, calibration parameters are based more on history and use, rather than on precise computation. In any case, values K_β of about 8.5 (for both aircraft) have been used. In passing, we remark that a yaw maneuver was executed in the 1989 calibration, and precise computation generated a value of about 10.4 for K_β which is much too large for general application, again indicating the the poor performance of this sensor. This discrepancy is shown in Fig. 9-4, where calibrated slip β for the yaw maneuver with $K_\beta=8.5$ is compared with the drift angle. Even the value 8.5 is significantly larger than it should be; indeed, Eq. (6.21) predicts $K_\alpha=K_\beta \cong 6.41$ (note that this value accounts for the "missing" factor of two discussed above).

Further evidence that the sensor is in the turbulent wake, can be found in the data of Table 9-7 which shows computed values of B_0 . Again, this table was compiled using dual-racetrack data; recall that for this to work, the value of K_β must be preset, in this case to 8.5.

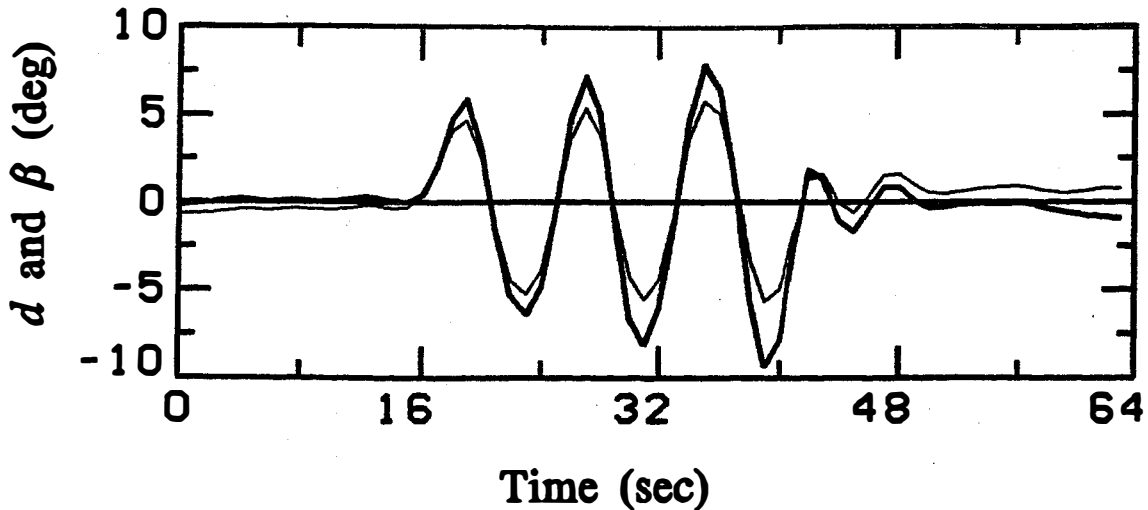


Fig 9-4. Drift angle d (dark line) and slip angle β (light line) during a yaw maneuver executed on N42RF's calibration flight on 8/10/89.

9. In-Flight Examples

H_r (feet)	B_0 (deg)
15.0K	0.063
12.0K	0.236
10.0K	0.020
8.0K	0.143
5.0K	0.096
1.5K	-0.097
Average 0.078	

Table 9-7. Noisy B_0 .

It is easily verified that the estimation procedure (8.5) for B_0 is both accurate and statistically stable (even with an incorrect value of K_β). However, the computed values of B_0 are quite noisy compared to those of A_0 , leading us to the conclusion that the slip measurement is unstable. This behavior has consistently been observed with both aircraft.

In addition to unstable fluctuation, there is also a persistent nonlinear distortion. To demonstrate this we use 1989 calibration data acquired from a circle maneuver consisting of three circles to the left (-30° roll) followed by three circles to the right ($+30^\circ$ roll), flown at about 1.5K ft, prior to the staircase and with constant power. A scatter plot of heading versus groundspeed (mean removed) is given in the upper curve of Fig. 9-5. The strong sinusoidal behavior is the result of the aircraft advecting with the mean flow. In particular, minimums occur when the aircraft is flying against the wind and maximums occur when flying with it; according to the plot, wind is from the east and off the water. Also wind speed can be deduced as about half the peak-to-peak variation which is about 3 m/s. It is fascinating that so much information can be inferred from INS data alone.

Next, the track and cross-track components of the horizontal wind [see Eq. (8.9)], are shown in the lower plot of Fig. 9-5. Here the track component (dark curve) is balanced across both sets of circles; however, the cross-track component (light curve) changes in the mean by nearly 1 m/s. At this point, it is useful to recall that the track component depends primarily on true airspeed while the cross-track component depends primarily on flow angles. We can therefore conclude that one (or both) of the flow angles is incorrect, "But which one?"

For a more detailed analysis, we use the modeled angles α_0 and β_0 computed in (8.6). Recall that these angles depend primarily on INS data, with a weak

9. In-Flight Examples

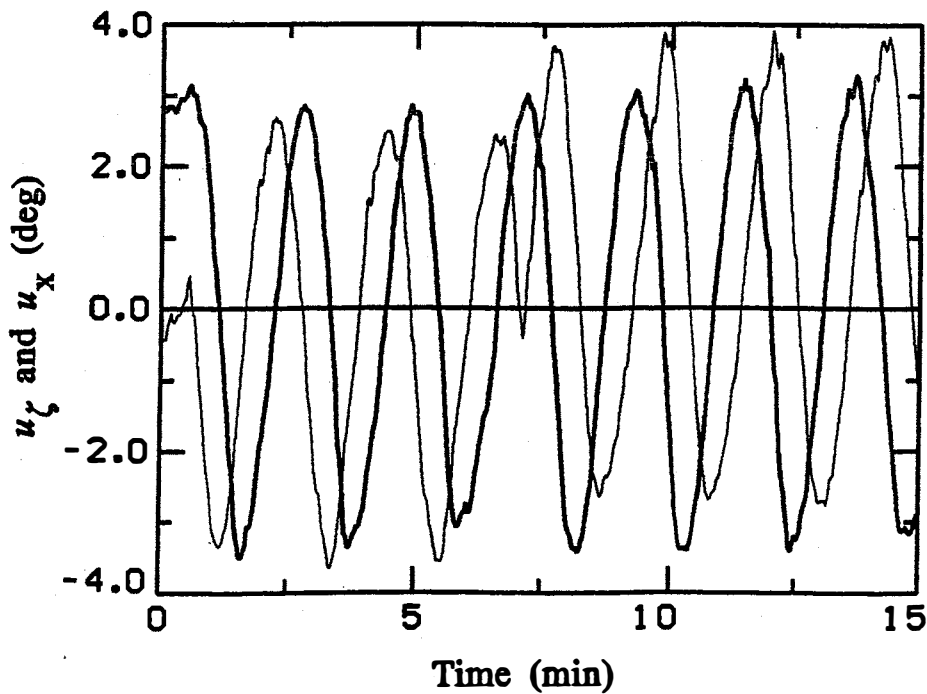
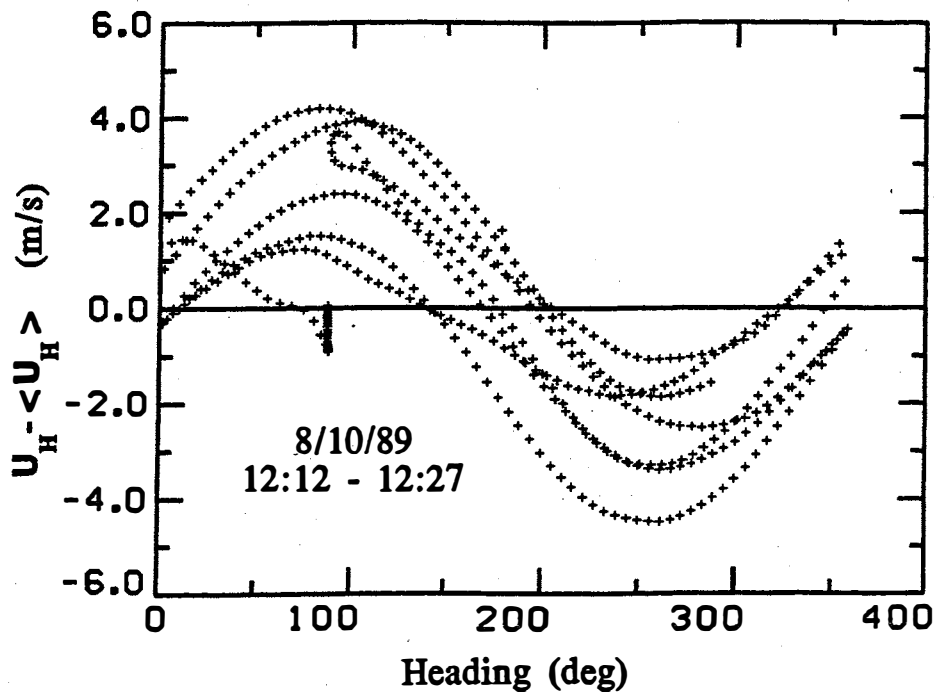


Fig. 9-5. Upper graph: Scatter plot of groundspeed with mean removed ($U_H - \langle U_H \rangle$) vs. heading during a circle maneuver on N42RF's calibration flight on 8/10/89. Lower graph: Track component (u_ζ) and cross-track component (u_x) of the computed horizontal wind (dark and light lines, respectively) from the same circle maneuver.

9. In-Flight Examples

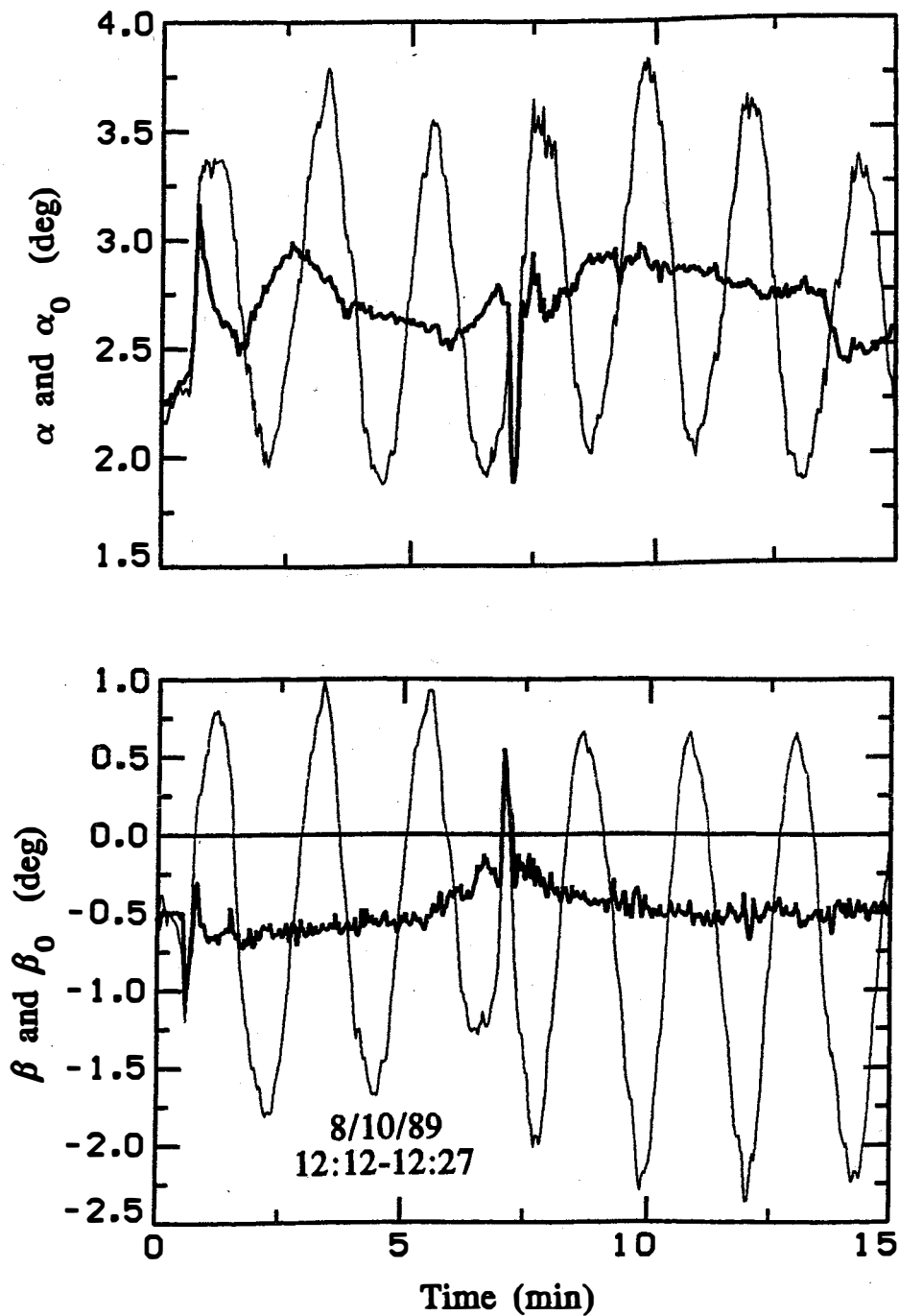


Fig. 9-6. Upper graph: Attack angle α (dark line) and modeled attack angle α_0 (light line) during circle maneuvers on N42RF's calibration flight on 8/10/89. Lower graph: Slip angle β (dark curve) and modeled slip angle β_0 (light line) during the same circle maneuver.

9. In-Flight Examples

dependence on true airspeed τ . Basically, they function much like pitch and drift, but are designed to work in the presence of roll; in particular, they tend to agree with attack and slip *on the average*. We next refer the reader to Fig. 9-6; in the upper plot, α_0 is compared with α , and in the lower plot, β_0 is compared with β . Observe that attack effectively goes down the "middle" of α_0 as it should, but slip is defective in this respect. Thus, error in the cross-track component can be traced to a faulty slip angle.

So what if anything can be done? Clearly, the best answer is to relocate the slip sensor to a position well in front of the cockpit (e.g., a radome sensor). Short of this, calibration for roll, as outlined in Sec. 7, is about all that can be done. In this respect, a preliminary investigation with the same circular data, showed that errors can be reduced by about a factor of two. Nonetheless, such procedures cannot solve the instability problem mentioned earlier, and we are led to the conclusion that roll calibration is, at best, a "band-aid" solution.

10. ADIABATIC AND HYDROSTATIC APPROXIMATION

Considerable insight into the equations for adiabatic change can be gained from their first-order approximations. Often complicated expressions simplify in ways that make interpretation easier. Such approximations are also useful in error-correcting procedures. Of special interest is the adiabatic correction required to transform a dynamic pressure from the wing tip to the fuselage. In tandem with this, the hydrostatic approximation is used to transform wing-tip static pressure to the fuselage.

To begin, we introduce the quotients $Q_s = q_c/p_s$ and $Q_t = q_c/p_t$ which are small, dimensionless quantities, central to this analysis; in particular, $p_t/p_s = 1 + Q_s$ and $p_s/p_t = 1 - Q_t$. In addition, we need the **binomial theorem** which says that for any real number ω and $|x| < 1$, $(1+x)^\omega$ has the following Taylor's series expansion:

$$(10.1) \quad (1+x)^\omega = 1 + \omega x + \frac{\omega(\omega-1)}{2 \cdot 1} x^2 + \frac{\omega(\omega-1)(\omega-2)}{3 \cdot 2 \cdot 1} x^3 + \dots \\ = 1 + \omega x + O(x^2)$$

where the notation $O(x)$ is used to denote a function or error term that remains bounded as x goes to zero. Thus, $f(x) = O(x)$ means there is some constant A so that $|f(x)| < A|x|$ for x sufficiently small. Examples are $\cos(x) = 1 + O(x^2)$, $\sin(x) = x + O(x^3)$, and $1/(1-x) = 1 + x + O(x^2)$. (Note that the "O" notation does not distinguish between terms that differ by multiplicative constants.)

As a first application, we apply this to the adiabatic condition (7.2) relating temperature and pressure. Actually, there are two ways to do this

$$(10.2a) \quad T_s/T_t = (p_s/p_t)^{(\gamma-1)/\gamma} = (1-Q_t)^{(\gamma-1)/\gamma} = 1 - (\gamma-1)Q_t/\gamma + O(Q_t^2)$$

$$(10.2b) \quad T_t/T_s = (p_t/p_s)^{(\gamma-1)/\gamma} = (1+Q_s)^{(\gamma-1)/\gamma} = 1 + (\gamma-1)Q_s/\gamma + O(Q_s^2)$$

Clearly, the first approximation (10.2a) is the better of the two because $Q_t = q_c/(p_s + q_c)$ is uniformly smaller than $Q_s = q_c/p_s$.

Mach number Here, we approximate the the Mach number (squared):

$$M^2 = \frac{2}{\gamma-1} \left[(1+Q_s)^{(\gamma-1)/\gamma} - 1 \right] = \frac{2}{\gamma} Q_s + O(Q_s^2)$$

which says that, to first order, M^2 is proportional to Q_s . An immediate consequence is that the pressure calibration model (7.14), when written in the form $\hat{p}_s = p_{s,m} (1 + K_p q_{c,m}/p_{s,m})$, is essentially a Mach number dependence.

10. Adiabatic and Hydrostatic Approximation

Adiabatic Heating Recall from Sec.3 that $(\gamma-1)/\gamma=R/c_p$ which together with the ideal gas law can be used to rewrite (10.2a) in the form:

$$q_c \cong \rho_t c_p (T_t - T_s) .$$

Taking differentials of both sides of this equation, with T_s held fixed then gives

$$(10.3) \quad \boxed{\Delta q_c \cong \rho_t c_p \Delta T_t} .$$

which is similar to (4.7), except that now ρ is replaced with ρ_t . (Note that total quantities ρ_t , p_t , and T_t usually work better in adiabatic approximations.) This relationship is graphically illustrated in Fig.10-1 which shows data from the dual-racetrack maneuver for the 5K ft level of the 1989 calibration discussed in the previous section. The dark curve is dynamic pressure q_c and the light line is total temperature T_t after means have been removed; additionally, total temperature has been rescaled by a factor of 10 for graphical display. The jumps or steps in these quantities correspond to a change of (indicated) airspeed from 180 kt to 240 kt. With nominal values of

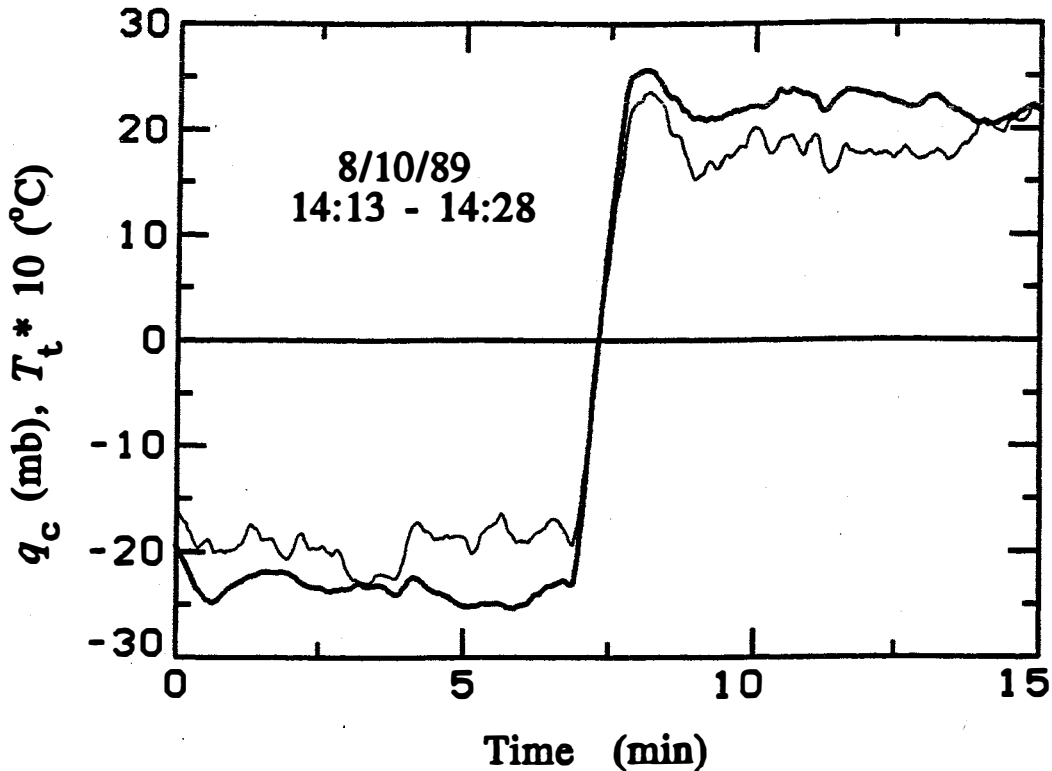


Fig 10-1. Wingtip dynamic pressure q_c (dark line) and total temperature T_t multiplied by 10 (light line) during a change of indicated airspeed from 180 kt to 240 kt. Means have been removed from both quantities.

10. Adiabatic and Hydrostatic Approximation

0.01 (10-g/m³) and 1000 (J/kg-°K) for ρ_t and c_p respectively, we get the approximate relationship $\Delta q_c \cong 10 \Delta T_t$, explaining the scaling used in the figure. Note, in particular, that such temperature changes are due to dynamic heating and must be removed to obtain static temperature T_s .

Adiabatic q_c We next work backwards from the true-airspeed equation to obtain the adiabatic analog of $q = \frac{1}{2} \rho_s \tau^2$ used with incompressible fluids. In detail, (10.2a) combined with the true-airspeed equation (5.10) gives:

$$\begin{aligned} \frac{1}{2} \tau^2 &= c_p (T_t - T_s) = c_p T_t (1 - T_s / T_t) \cong c_p T_t (R / c_p) Q_t \\ &= (T_t R / p_t) q_c = q_c / \rho_t, \end{aligned}$$

and solving for q_c yields the wanted result:

$$(10.4) \quad \boxed{q_c \cong \frac{1}{2} \rho_t \tau^2} .$$

Thus, the essential change has been to replace static density ρ_s with total density ρ_t ; otherwise said, $q_c = (\rho_t / \rho_s) q$.

Wingtip Corrections for q_c With this background, we now turn to the problem of correcting dynamic pressure for extraneous motions. To fix ideas, suppose that because of changing attitude angles, a probe mounted on the wing tip measures the true airspeed τ , but the (hypothetical) true airspeed at some other point on the aircraft (e.g., the INS) is $\tau - \Delta\tau$. Then, according to (10.4), incremental change in dynamic pressure is related to incremental change in true airspeed by the equation: $\Delta q_c = \rho_t \tau \Delta\tau$, and the corrected value q_{NEW} of dynamic pressure q_{WING} on the wing tip is:

$$(10.5) \quad \boxed{\hat{q}_{NEW} \cong q_{WING} - \rho_t \tau \Delta\tau} .$$

Because τ depends on q , this equation is, implicitly, nonlinear. However, when processing sequential data, the previous value of τ works well. In low-wind situations (hurricanes excluded), $\tau \cong \|\mathbf{U}_0\|$ also works.

It remains to estimate $\Delta\tau$. Recall from (3.7) that an estimate $\Delta\tau = \tau_w - \tau_n$ of the difference between true airspeed on the wing tip and near the nose is the dot product $\Delta\tau \cong -\mathbf{i}_{r,n} \cdot (\Delta\mathbf{U}_w - \Delta\mathbf{U}_n)$ where $\mathbf{i}_{r,n}$ is the relative-wind direction and where $\Delta\mathbf{U}_w$ and $\Delta\mathbf{U}_n$ are the incremental velocities due to changing attitude angles. Another estimate is:

$$(10.6) \quad \boxed{\Delta\tau \cong \|\mathbf{U}_0 + \Delta\mathbf{U}_w\| - \|\mathbf{U}_0 + \Delta\mathbf{U}_n\|} .$$

10. Adiabatic and Hydrostatic Approximation

which has considerable geometric appeal; it says that the difference in true airspeeds at different points on the aircraft is about the same as the difference in groundspeeds. Verification again uses the binomial theorem. Indeed, the first term on the right containing $\Delta_w \mathbf{U}$ can be approximated:

$$\begin{aligned} \|\mathbf{U}_0 + \Delta_w \mathbf{U}\| &= \|\mathbf{U}_0\| \left(1 + 2\mathbf{U}_0 \cdot \Delta_w \mathbf{U} / \|\mathbf{U}_0\|^2 + \|\Delta_w \mathbf{U}\|^2 / \|\mathbf{U}_0\|^2 \right)^{1/2} \\ &\cong \|\mathbf{U}_0\| \left(1 + 2\mathbf{U}_0 \cdot \Delta_w \mathbf{U} / \|\mathbf{U}_0\|^2 \right)^{1/2} \\ &\cong \|\mathbf{U}_0\| + (\mathbf{U}_0 \cdot \Delta_w \mathbf{U}) / \|\mathbf{U}_0\| \\ &= \|\mathbf{U}_0\| + \mathbf{i}_0 \cdot \Delta_w \mathbf{U} \end{aligned}$$

where $\mathbf{i}_0 = \mathbf{U}_0 / \|\mathbf{U}_0\|$ is the direction of aircraft motion which, in horizontal flight, is the same as the track direction. The term containing $\Delta_n \mathbf{U}$ is similar, and (10.6) becomes $\Delta\tau \cong \mathbf{i}_0 \cdot (\Delta_w \mathbf{U} - \Delta_n \mathbf{U}) = \mathbf{i}_0 \cdot \Delta_{wn} \mathbf{U}$; in particular, the groundspeed $\|\mathbf{U}_0\|$ cancels in the difference. But, to first order, this is the same as (3.7) because \mathbf{i}_0 and $-\mathbf{i}_{r,n}$ typically agree to one, if not two, significant digits. Thus, (10.6) is a valid, first-order estimate of $\Delta\tau$. In retrospect, we can now better appreciate the complexity of the exact solution (3.6).

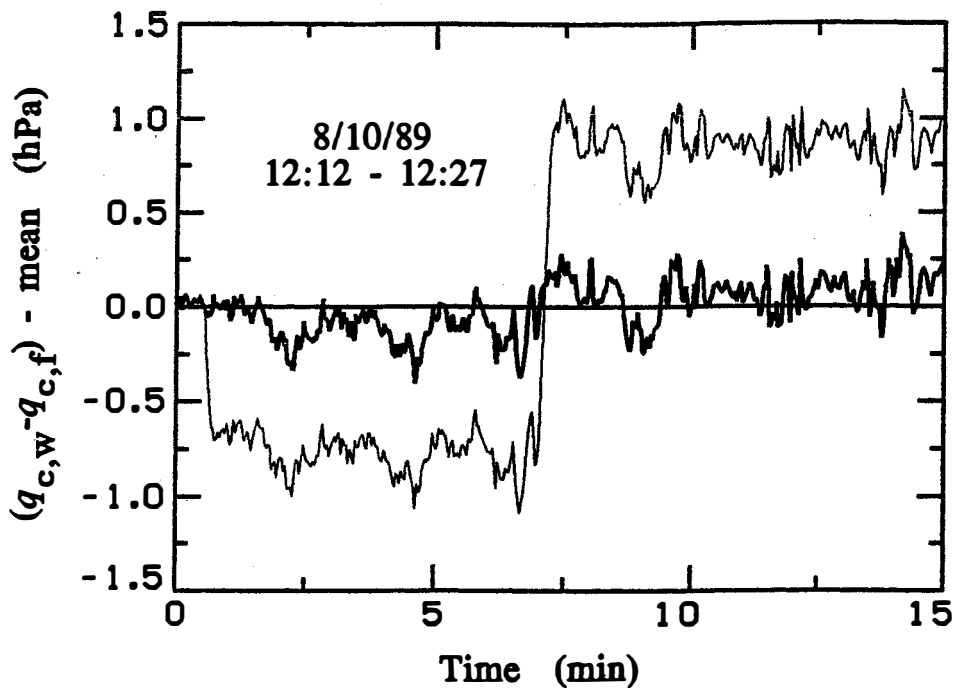


Fig. 10-2. Difference between uncorrected wingtip dynamic pressure $q_{c,w}$ and uncorrected fuselage dynamic pressure $q_{c,f}$ (light line), and the same difference after correcting the wing tip q_c for motion (dark line). Means have been removed from both quantities. Data is from circle maneuvers performed on N42RF's calibration flight on 8/10/89.

10. Adiabatic and Hydrostatic Approximation

This correction procedure is graphically illustrated in Fig.10-2. Here data is from the same calibration consisting of three circles to the left followed by three circles to the right, discussed in the previous section. The light curve shows the difference in dynamic pressures as measured by the (left) wing tip sensor and by the fuselage sensor. Because the left wing tip travels slower in a left turn and faster in a right turn, there is an abrupt jump when circles are reversed. The dark curve is then the result of applying (10.5) and (10.6) to correct the wing tip pressure by translating it to the INS. In this way, the jump is almost entirely removed (dark curve), demonstrating the high precision of this correction.

True-Airspeed Errors It is now easy to analyze sensitivity of true airspeed to errors in dynamic pressure. As a test case, we choose a nominal airspeed τ of 100m/s and $\rho_t=0.01$ (10-g/m³). Again using the differential of (10.4): $\Delta q_c = \rho_t \tau \Delta \tau$, we see that *an accuracy $\Delta \tau$ of 1 m/s in true airspeed requires an accuracy of (about) $\Delta q = 1.0$ mb in dynamic pressure.*

As a check, we again use the circles of the above example. Now, because the wing tip sensor is about 15 m from the INS and because a circle requires about 2 min to complete, the rotational velocity $\Delta \tau$ of the wing tip is about $15 \times 2\pi / 120$ or 0.75 m/s. In addition, present analysis predicts a change of about 0.75 mb in q_c which is close to what is observed in Fig. 10-2.

Next, we analyze humidity-dependent errors. Here, required accuracy in vapor pressure e can be estimated from related error in density $\rho_t = \rho_d + \rho_v$ where $\rho_v = e/RT_t$. To this end, we again take the differential of (10.4), this time allowing density to vary as well:

$$\Delta q_c = \frac{1}{2} \Delta \rho_t \tau^2 + \rho_t \tau \Delta \tau .$$

Furthermore, $\rho_t = \rho_d(1+\eta)$ where $\eta = \rho_v / \rho_d$ is the mixing ratio, and so

$$\begin{aligned} \Delta \rho_t &\cong \rho_d \Delta \eta = \rho_t \Delta \eta / (1+\eta) \cong \Delta \eta \rho_t . \\ \Rightarrow \frac{1}{2} \Delta \rho_t \tau^2 &\cong \Delta \eta [\rho_t \tau^2 / 2] \cong \Delta \eta q_c \end{aligned}$$

However, errors in ρ_t do not effect q_c (because dynamic pressure is an independent measurement); thus, $\Delta q_c = 0$ and the following dependence results:

$$(10.8) \quad \boxed{q_c \Delta \eta \cong -\rho_t \tau \Delta \tau} .$$

Note that underestimating the vapor pressure ($\Delta \eta < 0$) results in computed true airspeed τ being too large. For the test case used above and values of 50mb for q_c and $\Delta \eta = -0.02$ (-20g/kg), the error $\Delta \tau$ is about 1 m/s. Also, this mixing

10. Adiabatic and Hydrostatic Approximation

ratio corresponds to about 30mb of vapor pressure at sea level which is not uncommon to moist climates. Consequently, *neglecting vapor pressure can lead to errors in excess of 1 m/s.*

Temperature Calibration The temperature calibration equation (7.7) can be approximated to obtain a simpler model. First, apply the binomial theorem to $P_\gamma = (p_s/p_t)^{(\gamma-1)/\gamma}$ to get

$$1 - P_\gamma = 1 - (1 - Q_t)^{(\gamma-1)/\gamma} = \frac{\gamma-1}{\gamma} Q_t + O(Q_t^2) .$$

which, in tandem with $1/(1-x) \cong 1+x$, results in the following first-order estimate:

$$\hat{T}_t \cong T_{t,m} (1 + K_T \frac{\gamma-1}{\gamma} Q_t)$$

where, as above, $K_T = 1-r$. Note that the difference between this and the exact equation is a second-order term of the form $O(Q_t^2) \cdot T_{t,m}$. To verify the accuracy of this approximation, computer simulations show that with a recovery factor $r=0.95$ ($K_T=0.05$), the maximum error for Mach numbers $M \leq 0.5$ is $(1.44E-4) \cdot T_{t,m}$, and this error is reduced to $(3.15E-5) \cdot T_{t,m}$ when K_T is replaced with $\tilde{K}_T = 1.05 \cdot K_T$. (This modification works because of convexity in the underlying mathematical functions.) In short, this approximation is sufficiently accurate for direct use as a calibration model.

Wingtip Corrections for p_s It should be clear that laws governing adiabatic change do not generally apply to the atmosphere, and static corrections are based on a different set of physics. Here the model is that of a motionless fluid, governed by the **hydrostatic equation**:

$$(10.9) \quad dp_s = -\rho_s g dz$$

where g is the acceleration of gravity. This equation is recognized as the vertical component of the Euler equation (5.4) for a wind-free atmosphere; it is the first-order balance between pressure, density and altitude. We observe that (10.9) is directly applicable to correct static pressure for differences in elevation, e.g., for sensors on the wing tip. The most accurate way to compute Δz is with the transformation \mathbf{G} of Sec.1. However, for a sensor at position \mathbf{r} , this difference depends primarily on roll ϕ and can be estimated:

$$\Delta z \cong \|\mathbf{r}\| \sin \phi$$

where $\|\mathbf{r}\|$, as before, is the distance to the INS.

10. Adiabatic and Hydrostatic Approximation

Vertical Aircraft Velocity For an ideal gas, (10.9) can be expressed:

$$(10.10) \quad dz = -(R/g)T_s \left(\frac{dp_s}{p_s} \right)$$

which, when differenced in time, gives the vertical-velocity estimate:

$$(10.11) \quad \boxed{\hat{W}_0 \cong -(R/g)T_s \left(\frac{1}{p_s} \frac{dp_s}{dt_s} \right)}$$

which can be used to "stabilize" the vertical-wind computation.

Pressure Altimetry As was seen in the calibration data of Fig. 9-1, the relationship between pressure and altitude is quite predictable. However, to infer altitude from pressure, temperature information is also required. For this purpose it is common to model the troposphere as having a constant lapse rate Γ which simply means that temperature can be modeled $\tilde{T}_s = T_0 - \Gamma z$ where T_0 is some reference value. But then, (10.10) can be rearranged: $dp_s/p_s = -(g/R)dz/\tilde{T}_s$, and a simple integration gives

$$p_s/p_0 = (\tilde{T}_s/T_0)^{g/(\Gamma R)} = \left(1 - \frac{\Gamma z}{T_0} \right)^{g/(\Gamma R)}$$

Finally, replacing z with H_p and solving gives the **pressure altitude equation**:

$$(10.12) \quad \boxed{\hat{H}_p = (T_0/\Gamma) [1 - (p_s/p_0)^{\Gamma R/g}]}$$

which is an estimate of height H_p above mean sea level. Note well that this estimate is not designed for high accuracy. Rather, it is used more as a standard, for comparison with in-flight parameters. Commonly used values are $T_0 = 288.16^\circ\text{K}$ (15°C), $\Gamma = 0.0065^\circ\text{K/m}$, and $p_0 = 1013.25\text{mb}$ (sea level), in which case $T_0/\Gamma = 44332$, $\Gamma R/g = 0.19025$, and H_p is in meters.

Another estimate of vertical aircraft velocity can be obtained by differencing pressure altitude (10.12). We leave it as an exercise to show that this leads to the same estimate as (10.11), but with T_s replaced by $\tilde{T}_s = T_0 - \Gamma z$. The author has no explanation as to why this seemingly inferior estimate is used so often in practice.

11. P-3 DATA ACQUISITION

In its simplest form, data acquisition can be thought of as little more than recording data for subsequent use. In this context, it might seem that the only difficulties would be technical ones related to the mechanics of moving data around. In actuality, data acquisition is one of the most complex topics in signal processing, with a whole theory to support it. Important aspects of this theory are discussed in App. D. Of particular interest here is how symmetric filters are used in "near real time" to prefilter data prior to sampling. Also, aliasing problems related to computation are discussed.

The main difficulty with data acquisition comes in trying to represent a continuous process with a discrete sample. Clearly, it is impossible to capture all the information with instantaneous points; important features may be skipped over or omitted when the step size is too coarse. The problem, therefore, becomes one of obtaining discrete samples that are, in some sense, statistically representative of the greater whole. The basic idea is to average the continuous data into discrete values which are then attached to the time-series grid. Again, such averaging can be modeled with convolution and, again, convolution is the same as filtering.

Aliasing Intuitively, the effect of incorrect sampling is to introduce noise. However, when (almost) periodic functions are sampled with too large a step size, the result is another (almost) periodic function; the difficulty is that it is the wrong one. One periodic structure has been aliased into another. This is what happens when the spokes in wagon wheels appear to move backwards in a western movies; the frame rate is too slow to keep up with actual motions. From the standpoint of data acquisition, it would be better to blur out aliased motions, say, with long exposures. But, this is just another way of saying that it would be better to average or prefilter the aliased images before they are recorded in discrete form.

The mathematical explanation of aliasing begins with the observation that complex exponentials are 2π periodic $e^{ik(\omega+2\pi)} = e^{ik\omega}$; thus, when the continuous functions $e^{i\omega t}$ and $e^{i(\omega+2\pi)t}$ are sampled at times $t=k$, results are identical. More generally, an improperly sampled component will get folded mod(2π) so that it (falsely) appears as a component in the interval $[-\pi, \pi]$; the end point π of this interval is called the **folding or Nyquist frequency** (in radians); by periodicity this is the same as $-\pi$. Strictly speaking, the Nyquist component is not aliased. Nonetheless, it exhibits a related form of uncertainty. Observe that a time series $x(t) = \cos(\pi t + \varphi)$ sampled at times $t=k$

11. P-3 Data Acquisition

results in the Nyquist component of alternating numbers:

$$x_k = x(k) = \cos(\pi k + \varphi) = (-1)^k \cos(\varphi) .$$

Thus, a sample of finite length will have energy proportional to $\cos^2(\varphi)$. But, phase φ is a random variable and dependent only on when the "clock" was started; consequently, energy is also a random variable making the finite sample ambiguous. We conclude that, like other aliased components, *the folding frequency is unsuitable for analysis.*

Normalization A discrete sample x_k of a process $x(t)$ is usually modeled as $x_k = x(k\Delta t)$ where the **sampling increment** or interval Δt has units, say, of time; here, the **sampling rate** is $1/\Delta t$. However, when working with discrete samples, Δt is a nuisance parameter that is usually "scaled out" to obtain normalized time $t_N = t/\Delta t$. To see how frequency ω_N is normalized, we observe that true components and normalized ones must be the same $A \cos(\omega t + \varphi) = A \cos(\omega_N t_N + \varphi)$; thus, $\omega_N t_N = \omega t$ and so $\omega_N = \omega t/t_N = \omega \Delta t$. Additionally, true frequency f , measured in Hertz (cycles-per-second), is related to radian frequency as $\omega = 2\pi f$ and the normalized value is $f_N = f \Delta t$. In particular, the normalized folding frequency $f_N = 1/2$ corresponds to a true folding frequency of $f = 1/(2\Delta t)$ Hz. For example, a 1 Hz sampling rate ($\Delta t = 1.0$ s) has a 1/2 Hz folding frequency while a 10 Hz sampling rate ($\Delta t = 0.1$ s) has a 5 Hz folding frequency.

For a discrete sample, the normalized folding frequency has the simple interpretation of always being two sample points long. However, when a discrete time series is subsampled there are two folding frequencies, one for the given time series and another for the subsampled one, and this can lead to confusion.

Aircraft Data Acquisition The data-acquisition scheme used with the P-3's is designed to produce data at several different rates; data can be sampled at the "slow" rate of 1 Hz (1 point per second) and the "fast" rate of 80 Hz, with an intermediate rate of 10 Hz. Basically, all analog data are prefiltered with a four-pole Butterworth filter prior to sampling at the fast 80 Hz rate; in turn, slower samples are obtained through decimation by digitally filtering and then subsampling the "fast" samples. In more detail, the Butterworth filter shown in Fig.11-1 is a standard (four-pole) analog filter that attenuates the 40 Hz frequency component by about an order of magnitude

11. P-3 Data Acquisition

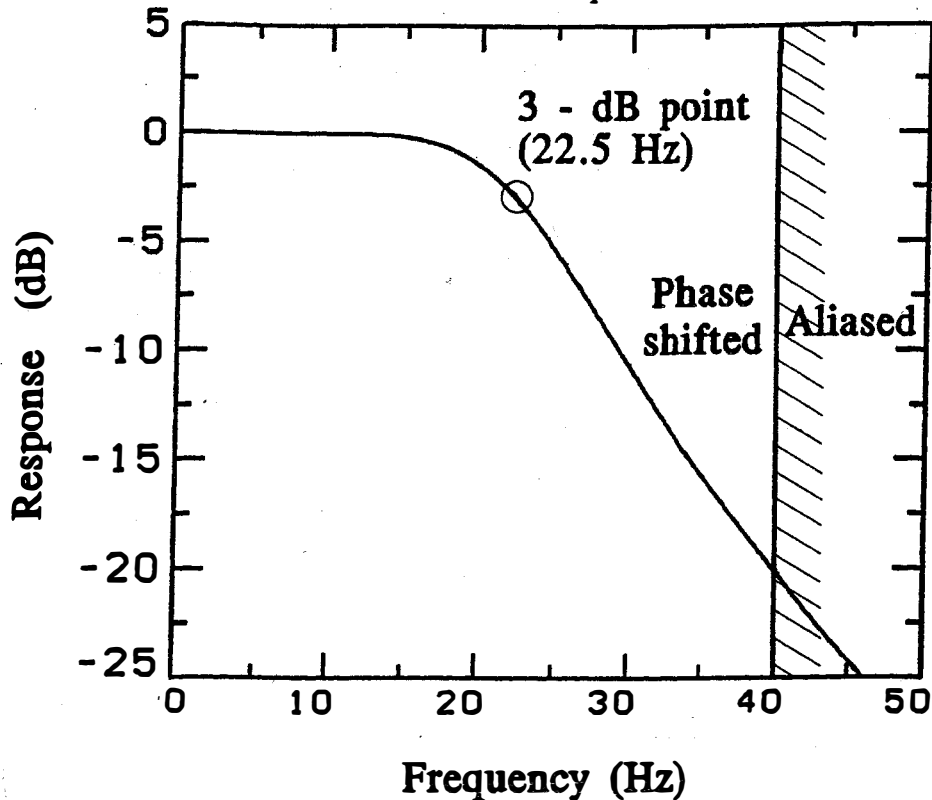


Fig. 11-1. Frequency response of the four-pole Butterworth filter used to prefilter all P-3 analog data.

(20 dB); additionally, the half-power point (3 dB) occurs at about 22.5 Hz. (Recall that an 80 Hz *sample rate* corresponds to a 40 Hz *folding frequency*.)

Next, to obtain the 10 Hz rate, data are digitally averaged ("box-car" averaged) and subsampled. Although this may seem naive, it is useful because some instruments produce digital outputs at different clock speeds, and simple averaging is easily modified to accommodate this. Ideally, all data are brought into sync with a single clock in this way. In any case, the interesting step is in going from the 10 Hz rate to the 1 Hz rate; here, a triangular filter T_{20} having 20 coefficients

$$(11.1) \quad (1, 2, 3, 4, 5, 6, 7, 8, 9, 10, 10, 9, 8, 7, 6, 5, 4, 3, 2, 1)/121$$

is used. Because coefficients sum to unity, T_{20} leaves constant sequences unchanged. Also, this is a symmetric filter provided that resulting values are recorded as delayed in time (by 0.95 s from the end). Also, because the filter uses 20 values (0.1 s of data per value), the resulting 1 Hz time series has adjacent points that are correlated. (More precisely, white noise sampled at 10 Hz, prefiltered, and subsampled at 1 Hz will have a lagged correlation of $4/7 \approx 0.57$.) Nonetheless, *alternate points remain statistically independent*.

Of practical importance is that T_{20} is both easy and efficient to

11. P-3 Data Acquisition

implement. Consider the following FORTRAN loop:

```

S1=0.
S2=0.
DO 100 K=1,10
S1=S1+X(K)
100 S2=S1+S2

```

On exit from this loop, $S2=10X(1)+9X(2)+\dots+X(10)$ and so

$$X(1)+2X(2)+\dots+10X(10)=11*S1-S2$$

The sum $S3=10X(11)+9X(12)+\dots+X(20)$ is computed in analogous fashion from the remaining 10 points and T_{20} is computed as

$$(11.2) \quad \begin{aligned} T_{20} &= [11*S1 - S2 + S3]/121 \\ &= [S1 - [S2-S3]/11]/10 \end{aligned}$$

Thus, only two multiplications are required and shows that, T_{20} has an efficient implementation.

Frequency Response At this point, the reader is referred to App. C for a discussion of basic filter concepts such as the frequency response. Our objective here is to compute the frequency response $\mathcal{R}_{T_{20}}(\omega)$ of T_{20} . The pivotal fact is that the composition $T=A_N A_M$ of an N -point running-average filter A_N with an M -point running-average filter A_M is a filter T with $N+M-1$ coefficients in the shape of a trapezoid. In the special case when $N=M$, we get a triangle with a single vertex; for example,

$$\left[\frac{1}{3}(\mathcal{E}^{-1} + I + \mathcal{E}^1)\right]^2 = \frac{1}{9} [1\mathcal{E}^{-2} + 2\mathcal{E}^{-1} + 3I + 2\mathcal{E}^1 + 1\mathcal{E}^2]$$

where \mathcal{E} is the shift operator $\mathcal{E}x_k = x_{k+1}$; Similarly, when $N=M+1$, the filter is a triangle with two "vertices"; in particular, T_{20} is the product $T_{20}=A_{10}A_{11}$.

To continue, we need the responses of the filters A_L . The easier computation is for the case when L is odd $L=2N+1$ because then the running-average filter is centered and can be summed like a geometric series

$$A_L = \frac{1}{L} \sum_{k=-N}^N \mathcal{E}^k = \frac{1}{L} \frac{(e^{N+1/2} - e^{-N-1/2})}{(e^{1/2} - e^{-1/2})}$$

In turn, the response, say \mathcal{R}_L , of A_L is computed by replacing \mathcal{E} with $e^{i\omega}$:

$$(11.3) \quad R_L(\omega) = \frac{1}{L} \sum_{k=-N}^N e^{ik\omega} = \frac{1}{L} \frac{(e^{i(N+1/2)\omega} - e^{-i(N+1/2)\omega})}{(e^{i\omega/2} - e^{-i\omega/2})}$$

11. P-3 Data Acquisition

$$= \frac{\sin L\omega/2}{L \sin \omega/2}$$

When $L=2N$ is even, the computation of $R_L(\omega)$ is somewhat more involved, but the result is still the same.

Next, the convolution theorem [see (C.15) of App. C] gives $\mathcal{R}_{10}\mathcal{R}_{11}$ for the response \mathcal{R}_{T20} which would be the answer except that decimation from 10 Hz to 1 Hz must also be included; thus,

$$\mathcal{R}_{T20}(\omega) = \mathcal{R}_{10}(\omega/10) \mathcal{R}_{11}(\omega/10)$$

Finally, the response of our data acquisition must include the averaging used to go from 80 Hz to 10 Hz. This is yet another averaging filter with response $\mathcal{R}_8(\omega/80)$. Consequently, the total response $\mathcal{R}_D(\omega)$ of our digital filter is $\mathcal{R}_{T20}(\omega)\mathcal{R}_8(\omega/80)$ or

$$(11.4) \quad \mathcal{R}_D(\omega) = \left[\frac{\sin \omega/2}{10 \sin \omega/20} \right] \left[\frac{\sin 11\omega/20}{11 \sin \omega/20} \right] \left[\frac{\sin \omega/20}{8 \sin \omega/160} \right]$$

This is the response of a symmetric filter provided only that resulting data are recorded as delayed in time. As noted above, computation of the triangle filter results in data being 0.95 s too slow, and decimation from 80 Hz to 10 Hz accounts for another 3.5/80 s; thus, total delay is 0.99375 s.

Analysis of Data Acquisition The response (11.4) is shown in Fig. 11-2 for frequencies between zero and three Hertz with a folding frequency of 1/2 Hz. Also shown is the sinc function $\text{sinc} 2\omega = (\sin 2\omega)/(2\omega)$ which is essentially what the filter would be like if the triangle filter were replaced with simple averaging; note, that our filter significantly reduces the (aliased) peaks or lobes. Finally, the circles are the result of a test in which data of known frequency content was used as input; because data was analog, the (negligible) effect of the Butterworth filter is also present. Although agreement is not exact, it is within experimental error.

To continue, we observe that the most serious aliasing occurs close to the folding frequency of 1/2 Hz, and the interval [1/2 Hz, 3/4 Hz] gets folded or reflected back onto the interval [1/4 Hz, 1/2 Hz]. By contrast, there is little aliased data to fold back to low frequencies around 0 Hz. Consequently,

11. P-3 Data Acquisition

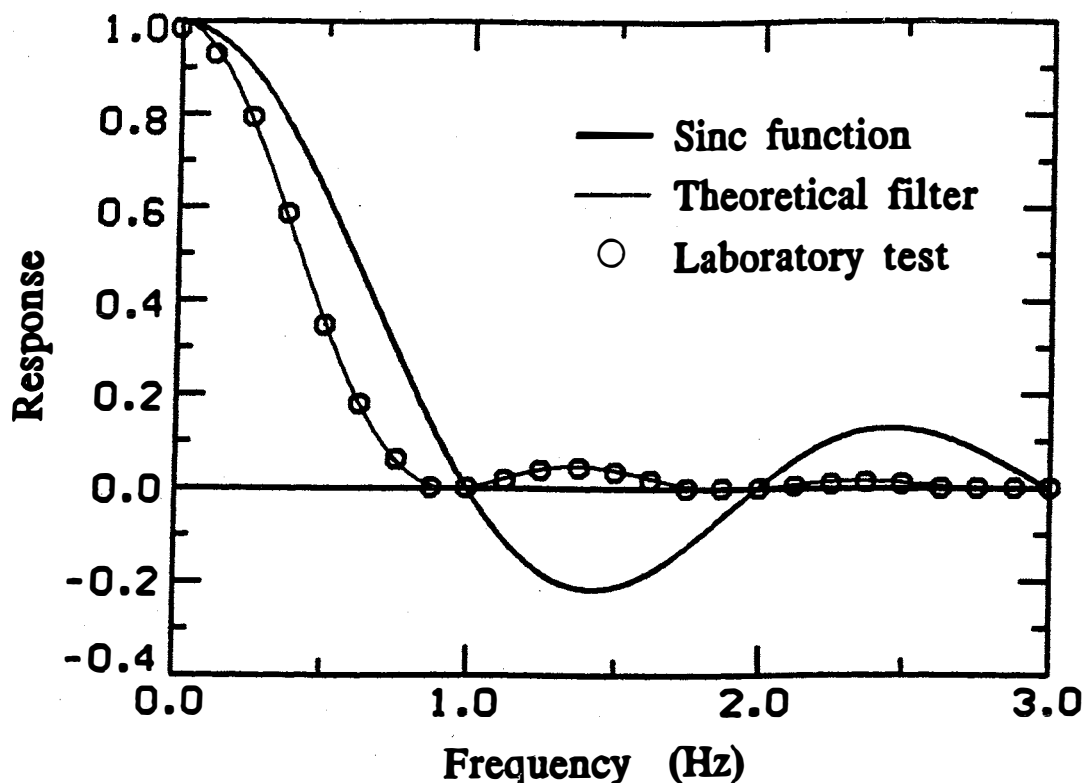


Fig. 11-2. Frequency response of the digital prefilter used to obtain "slow" 1-Hz data from "fast" 80-Hz data (light line), and frequency response of the sinc function, $\text{sinc } 2\omega = (\sin 2\omega)/(2\omega)$ (dark line). Circles are the result of a test in which data of known frequency content was used as input.

residual effects of aliasing are largely confined to the interval $[1/4 \text{ Hz}, 1/2 \text{ Hz}]$ and another low-pass filter can be applied later to the final, "slow" data to remove the contaminated area. More generally, *"The option to further reduce aliasing, in post-processing procedures, only works if the data-acquisition filter is approximately zero around multiples of twice the folding frequency (of the subsample)."*

Comparison with P-3 Processing With this background, we can better evaluate P-3 data acquisition. The important comparison is between the P-3 prefilter shown in Fig. 11-2 with the "optimal" prefilters derived in App. D and shown in Fig. D-1. Because P-3 data is acquired using a 14-bit analog-to-digital converter (ADC), precision is about half that of standard, single-precision arithmetic (23 bit mantissa), and the optimal prefilter corresponding to $p=4$ is a better choice for this comparison. All things considered, the P-3 prefilter is rather humble compared to the $p=4$ prefilter; the passband is not very flat and the transition is too slow. Nonetheless, it is monotone in the passband and has a similar geometric character. Efficiency and speed were important factors in its choice; limited resources prohibited

11. P-3 Data Acquisition

anything much more complicated. We conclude that the P-3 prefilter is of sound design, but there is room for improvement.

Computational Aliasing This is a sinister problem that generally impacts all nonlinear computations on discrete grids. The difficulty is that nonlinear operations tend to generate higher-frequency information, some of which cannot be accurately represented on a fixed grid; unless care is taken, these high frequencies can alias back and contaminate computed answers. This problem is, perhaps, best known in numerical modeling where nonlinear equations tend to generate a cascade of scales that, eventually, cannot be resolved.

To be more specific, consider the (normalized) time series $x(t)=\cos\omega_1t$ and $y(t)=\cos\omega_2t$. From the trigonometric identity:

$$(11.15) \quad \cos\omega_1t \cos\omega_2t \equiv \frac{1}{2}[\cos(\omega_1+\omega_2)t + \cos(\omega_1-\omega_2)t] ,$$

we see that the product $x(t)y(t)$ results in sum and difference frequencies. Consequently, even though we may start with unaliased samples $x_k=x(k)$ and $y_k=y(k)$, the product will be aliased whenever $\omega_1+\omega_2 > \pi$.

So how does this impact us? Recall that wind computation requires a number of multiplications of data dependent quantities. True airspeed is multiplied with flow-angle data which is then rotated into geodetic coordinates, and this rotation requires three more multiplications. Clearly, the *potential* for trouble is high. We emphasize, however, that neither the extent nor the magnitude of the problem is very well understood.

Practical Considerations In App.D it is shown that computational aliasing can be controlled with interpolation and filtering. Although theory is definitive, required procedures are tedious, especially with large data bases (e.g., 10 hr of aircraft data). Consequently, we here explore a compromise. To begin, we observe that an easier, but less accurate, way to reduce computational aliasing is to simply filter *before* computation. The difficulty here is that aliasing is suppressed at the expense of discarding some "good" data as well. At this point, we recall that our data acquisition (11.4) leaves some data aliased anyway, and additional filtering can be justified on this basis. Thus, application of a low-pass filter will improve both problems. But, what filter? In view of discussion following (11.14), the Hanning filter is an obvious choice; it is the simplest filter consistent with

11. P-3 Data Acquisition

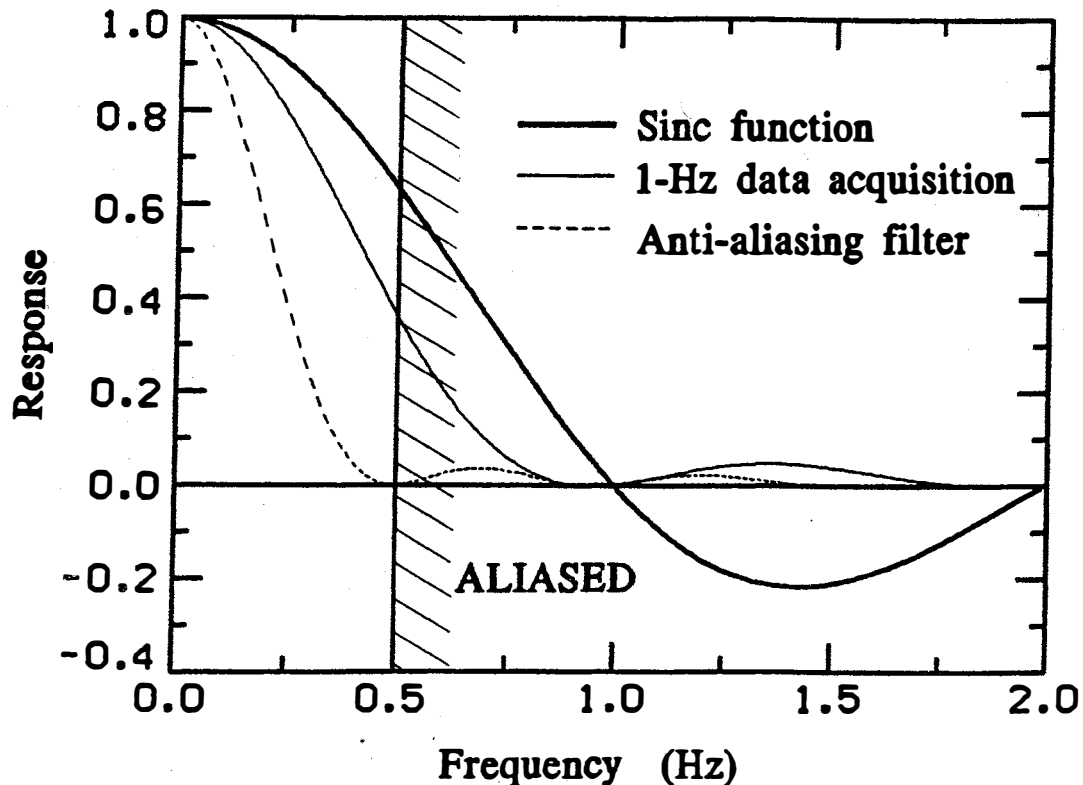


Fig. 11-3. Frequency response of the sinc function $\text{sinc } 2\omega = (\sin 2\omega) / (2\omega)$ (dark line), of the digital prefilter used to obtain "slow" 1-Hz data from "fast" 80-Hz data (light line), and of the "anti-aliasing" filter--the digital prefilter used in combination with the Hanning filter (dashed line).

above theory. In particular, the Hanning filter has response $\cos^2(\omega/2)$ [see Appendix C (C.3)], and vanishes at the folding frequency. Finally, the net effect of using this filter in tandem with our data-acquisition filter is shown in Fig. 11-3 where it is there labeled as an anti-aliasing filter. This terminology is justified for two reasons: first, it suppresses aliasing remaining after data acquisition and reduces phase problems, and second, it safeguards against computational aliasing, especially in wind computations. The improvement in phase problems is seen in Fig. 11-4, where the coherences of temperature T , static pressure p_s , and dynamic pressure q_c are plotted with (dark line) and without (light line) the anti-aliasing filter. These coherences were computed using 31-point averages. In any case, we emphasize that there is no reason to believe that simple procedures of this kind are adequate. Much research remains.

11. P-3 Data Acquisition

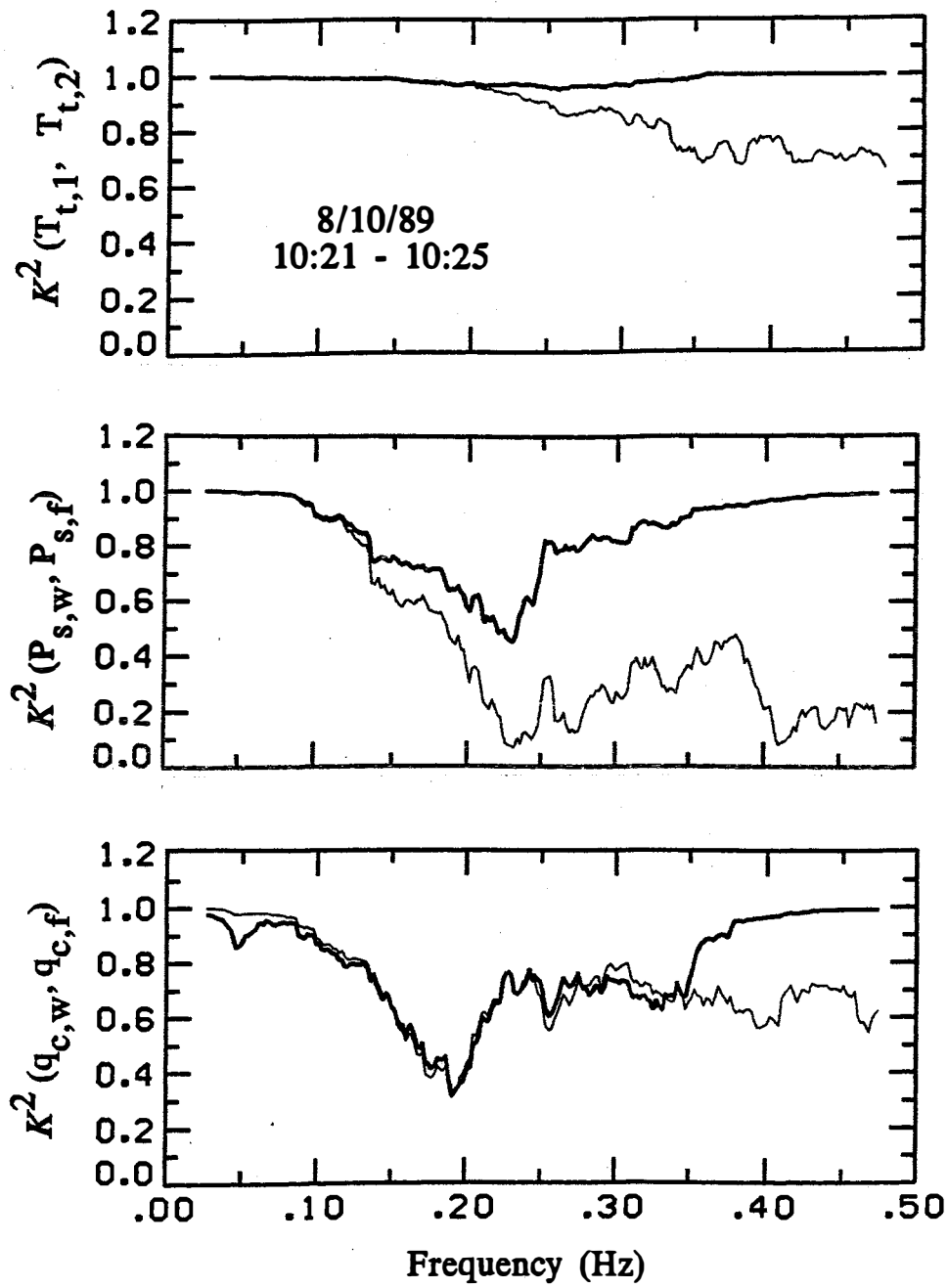


Fig. 11-4. Coherence K^2 of the two total temperature sensors ($T_{t,1}, T_{t,2}$), wingtip and fuselage static pressures ($P_{s,w}, P_{s,f}$), and wingtip and fuselage dynamic pressures ($q_{c,w}, q_{c,f}$) computed with (dark line) and without (light line) the anti-aliasing filter.

12. CORRECTIONS WITH FILTERS

Calibration methods provide one way of improving accuracy in acquired data. However, such methods are applied point-wise and are limited in extent to rescaling measured parameters. We here explore another set of methods based on filtering theory, where one mixes two measurements of the same thing to obtain the best features of both. A short list of applications is

- (1) Correcting horizontal navigation with LORAN-C or GPS.
- (2) Correcting vertical navigation with radar altimetry or GPS.
- (3) Correcting wingtip pressures with fuselage pressures.
- (4) Correcting Lyman-Alpha humidimeters with cooled-mirror hygrometers.

For example, in (2), inertial navigation and radar altimetry both supply information about vertical position, but not with the same accuracy; one instrument (the INS) is accurate at high frequencies, the other (radar altimetry) is accurate at low. The "optimal" blend then consists of data that is accurate everywhere. The mixing filter technique has broad application and has been used by many others in aircraft science. Some of the first use (1) were Gray (1965), and Shapiro and Kennedy (1981); (2) has been documented by Jorgensen et. al. 1985; (3) has been used in P-3 processing (see below); and (4) is as yet untried.

We begin with an overview of some technical aspects of filtering. A short list of relevant issues is:

- | | |
|--|---|
| •Editing?
(a)Shot noise.
(b)Poor SNR. | •Symmetry?
(a)Predictive.
(b)Symmetric. |
| •Operator type?
(a)Linear
(b)Adaptive. | •Missing data?
(a)Least-square curves.
(b)Filtered interpolation. |
| •Classification?
(a)Lowpass.
(b)Highpass.
(c)Notch. | •Boundaries?
(a)Neglect.
(b)Least-square curves.
(c)Mirror-images. |
| •Characteristics?
(a)Passband.
(b)Stopband.
(c)Lobes. | •Implementation?
(a)Versatility.
(b)Memory.
(c)Speed. |

12. Corrections with Filters

Editing Because filters operate globally, they can propagate noise in undesirable ways. This is especially true of **shot noise** which is characterized as being very large, but of short duration. Clearly, it is advantageous to remove this and other sources of error *prior* to filtering, so that effects do not spread. A statistical procedure for doing this is discussed in App. H.

Operator Type A linear filter A is an operator that satisfies $A[ax+by]=aA[x]+bA[y]$ where a and b are scalar constants and x and y are time-series data; all filters used here are of this type. By contrast, adaptive filters are designed to change or adapt to a given time series and do not have this property. Although they are useful in certain applications, such as for computing Doppler shifts, they are not recommended for general use and will not be further discussed here.

Filter Classification The most commonly used filters are lowpass, highpass, and notch. Lowpass filters are used for smoothing and with data acquisition; an algorithm useful to our needs is given in App. F. Highpass filters are the opposite of lowpass filters and can be computed by differencing data with a lowpass filter; highpass filters are often used to remove slowly varying trends. Finally, notch filters are used to remove erroneous oscillations at a specific frequency.

Filter Characteristics Filters are often specified with a passband, a stopband, together with a transition region. The passband characterizes which frequency components should remain unaltered, and the stopband specifies which ones should be attenuated. In particular, the stopband puts limits on unwanted peaks called lobes. As a rule, the sharper the transition and the smaller the lobes, the harder the filter is to implement, requiring more coefficients. This topic is more fully discussed in App. D where certain ideal filters and their approximations are studied in some detail.

Symmetry Most filters in use are either predictive or symmetric. Although symmetric theory is generally more powerful and easier to understand, real-time methods so dominate the literature that symmetric ones have all but been forgotten. We demonstrate the essential difference with data from a cooled-mirror, dew point hygrometer, taken with N43RF on 12/9/87 as part of OCEAN STORMS experiment (based in Seattle Washington). Five minutes of data are shown in Fig. 12-1; they are badly contaminated by a feedback oscillation that controls the cooling of the mirror. This oscillation is known to be fairly stable with a frequency of about 0.175 Hz, and can be removed with a

12. Corrections with Filters

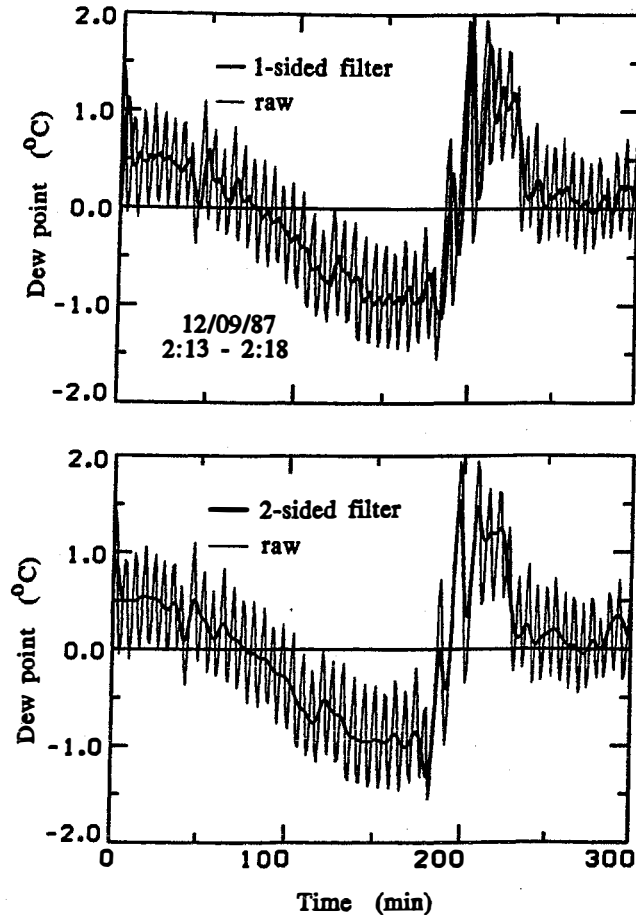


Fig 12-1. Top graph: Raw dew point (light line) and dew point corrected using a 1-sided filter (dark line) for a 5-minute portion of a flight when the dew point sensor suffered an oscillatory feedback error. Bottom graph: Same as the top graph, but the filtering has been performed with a 2-sided (symmetric) filter. Note that the 1-sided filter shifts peaks in the data, while the 2-sided filter does not.

notch filter. The superimposed dark curves in the upper and lower parts of Fig. 12-1 are the result of applying predictive and symmetric filters respectively. More precisely, the lower curve is the result of applying the same predictive filter, both forward and backward in time, and averaging. We observe that the predictive method tends to move peaks around, producing a distortion. By contrast, the symmetric method leaves peaks where they belong, and gives the better answer. In App. C it is shown that this is characteristic of the general case, and *proves* that symmetric filters are superior for post-processing applications.

Missing Data Missing data is a problem that arises surprisingly often; it can result from editing, poor signal-to-noise ratio (SNR), or equipment failure. In spite of this, there appears to be no theory that addresses the

12. Corrections with Filters

problem in any comprehensive way, most likely due to its complexity. At the same time, high-order filters cannot be used with missing data, and neglecting the problem is a poor option.

So, "What can be done?" The obvious solution is to fill in missing regions with interpolation. But, standard interpolation schemes are often unsuitable when data are noisy and/or missing regions are of long duration. In particular, system failure during the course of a flight often results in large noise spikes adjacent to the very regions that need fixing. To gain some insight as to what to do, consider the approach of filling in missing regions by fitting least-square curves. In principle, this can be viewed as a statistical interpolation scheme that reduces uncertainties due to noise. However, curve-fitting procedures can be awkward to use because missing regions tend to occur randomly, in unexpected ways; regions can be of long duration (like half a flight) or short and frequent (like every other point). We observe, however, that fitting least-square curves is a form of smoothing, and the stabilizing effects of smoothing are much easier to achieve with filtering. Filtered interpolation schemes for doing this are discussed in App. G.

Data Boundaries Because data is always of finite duration, every time series has a beginning and an end, and near the boundaries, filter performance *must* change. One scheme is simply to discard points anywhere a formula cannot be fully evaluated. In practice, this can be awkward to do and even when it isn't, long filters (i.e. many coefficients) can result in a substantial loss of data. In addition, discarding points can complicate other procedures, such as integration, that require boundary data.

Using least-square curves near boundaries is an approach with intuitive appeal. However, least-square polynomials tend to become unstable near boundaries, producing large excursions. In addition, such procedures are difficult to interface with convolution procedures (see App. C.).

Another approach is to change or shorten underlying formulas as boundaries are approached. This also turns out to be difficult because changing formulas often produces jump discontinuities — unacceptable behavior for low-pass filters that are supposed to produce smooth results. Nonetheless, normalization procedures can be made to work reasonably well with *low-order* filters having *positive* coefficients (see App. G).

None of the various "solutions" to this problem have proved as

12. Corrections with Filters

satisfactory as simply extending a time series with a mirror-image extension *before* applying a filter. Such extensions also work well in multi-dimensions, and result in linear operators. For lowpass filters, mirror-image extensions produce smooth results without instability, and are accurate near peaks. Also, the mirror-image is a geometric form, familiar to experience, and easy to work with in analysis procedures. In the author's opinion, it is the only *general-purpose* method acceptable with high-order filtering methods, and is an important feature of the lowpass filter documented in App. F.

Implementation Computer algorithms are as much art as science. Nonetheless, some are better than others, and good software can make the difference between success and failure. For example, aircraft data often results in large arrays, and algorithms that require more array space may not be usable because of insufficient memory. Also, speed and efficiency can be limiting factors in real-time applications. Finally, versatility is important in a research environment to determine optimal settings. The lowpass filter presented in App. F was designed to meet these needs.

The Mixing Procedure We now turn to the correction procedure, central to this development. To help formalize ideas, we borrow some notation from turbulence theory. Here, a process x in space and/or time is decomposed into a mean and fluctuating part $x = \bar{x} + x'$; the mean \bar{x} comprises the large-scale features and the fluctuation x' comprises the small-scale ones; alternatively, the mean consists of low frequencies and the fluctuation consists of high ones. Moreover, the maps $x \rightarrow \bar{x}$ and $x \rightarrow x'$ are generally modeled as projections or ideal filters, that is, they are symmetric (in space and/or time) and idempotent: $\bar{\bar{x}} = \bar{x}$ and $x'' = x'$. Note that because $x' = x - \bar{x}$, this decomposition is completely determined by the filter $x \rightarrow \bar{x}$ alone.

For present purposes, two measurements of the same thing, say x_1 and x_2 , are separated into their mean and fluctuating parts: $x_1 = \bar{x}_1 + x'_1$ and $x_2 = \bar{x}_2 + x'_2$. If, moreover, x_1 is more accurate at high frequencies and x_2 is more accurate at low, then an "optimal" blend \hat{x} can be constructed as:

$$(12.1) \quad \boxed{\hat{x} = \bar{x}_2 + x'_1 = x_1 + \overline{\Delta x}} \quad .$$

where $\Delta x = x_2 - x_1$ and $\overline{\Delta x}$ is the low-frequency correction to x_1 . In particular, when $x_1 = x_2$, $\overline{\Delta x}$ vanishes and this construction does nothing. While this formulation captures basic ideas, it is overly simplistic insofar as optimal

12. Corrections with Filters

low-pass filters $x \rightarrow \bar{x}$ can be elusive to find and difficult to verify.

A Simple Example We apply this scheme to correct for what is often called "cold-soaking." When pressure transducers get cold they tend to drift. Sensors mounted on a wing tip boom have shown variations in static pressure as high as 3 mb; drifts in fuselage-mounted sensors of 1 - 2 mb have also been observed (Willoughby *et al.*, 1989). The idea is, therefore, to combine high-frequency data from the boom with low-frequency data from the fuselage. (These data should already be corrected for roll-induced altitude variations.) Thus, if $p_{s,w}$ and $p_{s,f}$ are the static pressures on the wing tip and on the fuselage respectively, the "optimal" blend is $\hat{p}_s = p'_{s,w} + \bar{p}_{s,f}$.

In this application, choosing a filter is relatively simple because errors are small and slowly varying. The exponential filter E_r (with $r=0.95$), discussed in App. C, has proved adequate. To make it symmetric, it is applied both forward and backward in time and averaged: $S_r = (E_r + E_r^*)/2$. Also, the exponential filter is normalized near boundaries to preserve constants (see App. G). We emphasize, however, that such simplicity is the exception; other correction procedures are much more demanding.

Fourier Transforms and Optimality To better understand what is going on, a spectral interpretation is helpful. For this we use the Fourier transform \mathcal{F} , defined on a time series $x(t)$ as:

$$(12.2) \quad \mathcal{F}(x)(\omega) = \frac{1}{\sqrt{2\pi}} \int_{-\infty}^{\infty} x(t) e^{-i\omega t} dt .$$

where ω is (radian) frequency. For the integral to exist, the process x must have finite energy which, in this context, is quite restrictive. Nevertheless, the Fourier transform is a standard tool, useful for illustrating basic concepts. To start, we abbreviate notation for transforms with capitals $X(\omega) = \mathcal{F}(x)(\omega)$, and denote the low-pass mixing filter by A , that is, $\bar{x}_2(t) = A[x_2(t)]$. Thus, if $\mathcal{R}_A(\omega)$ is the frequency response of A , then the Fourier transform of (12.1) is

$$(12.3) \quad \hat{X}(\omega) = [1 - \mathcal{R}_A(\omega)] X_1(\omega) + \mathcal{R}_A(\omega) X_2(\omega).$$

The important observation is that $\hat{X}(\omega)$ is a weighted average of $X_1(\omega)$ and $X_2(\omega)$; more precisely, $\hat{X}(\omega)$ is a convex combination with weights $1 - \mathcal{R}_A(\omega)$ and $\mathcal{R}_A(\omega)$. Ideally, $\hat{X}(\omega)$ is as a smooth "splice" of the Fourier transforms $X_1(\omega)$ and $X_2(\omega)$ that results in a flat and seamless fit.

To make this more explicit, note that X_1 starts out noisy at low

12. Corrections with Filters

frequencies and becomes more accurate at high ones; for X_2 the situation is reversed. In between there should be an overlap region $[\omega_1, \omega_2]$ of common accuracy, and X_1 and X_2 should be (approximately) equal on it. In this situation, *an optimal mixing filter A is one for which the frequency response $\mathcal{R}_A(\omega)$ makes the transition from unity to zero within the overlap region $[\omega_1, \omega_2]$.* When this is the case, $\hat{X}(\omega)$ of (12.3) reduces to $X_2(\omega)$ for $\omega < \omega_1$, and to $X_1(\omega)$ for $\omega > \omega_2$; in between, $\hat{X}(\omega)$, $X_1(\omega)$, and $X_2(\omega)$ should all be about the same. The net result is data that is accurate everywhere. Clearly, such filters are not unique; if we can find one, there are others as well. Such lack of uniqueness can (and does) lead to some confusion.

Readers familiar with spectral analysis will recognize the overlap region $[\omega_1, \omega_2]$ as that region over which the spectral coherence of $X_1(\omega)$ and $X_2(\omega)$ is nearly maximum. Thus, the coherence determines the filter when errors depend only on instrument performance. However, errors can depend on other parameters making filter optimization more difficult. For example, filters best suited for straight-and-level flight can differ from those best suited for maneuvers. In addition, spectral techniques are poorly suited for analyzing data with slowly moving trends that, say, might be modeled as polynomials, exponentials, or partial cycles, and many of the errors of concern fall into this category. As a result, the problem of finding optimal filters is more complicated than it otherwise might be.

13. HORIZONTAL WIND COMPUTATION

Horizontal winds are computed as the difference between aircraft velocity and the relative wind. Therefore, accurate horizontal wind computation requires not only well-calibrated flow angle and pressure sensors, but also accurate aircraft navigation measurements. However, aircraft navigation, using the Inertial Navigation System (INS), is vulnerable to a host of errors which must often be corrected to obtain accurate horizontal winds and aircraft position. Correction of these navigation errors is covered extensively in Masters and Leise (1993), and only a brief overview will be presented here.

Navigation instrumentation Each P-3 aircraft carries two Delco Carousel-IV INS's, operating independently and producing data at 40 Hz. Each INS consists of a gimballed platform containing three gyroscopes (gyros) and three accelerometers, one for each spatial degree of freedom. To minimize the problem of measuring small horizontal accelerations in the presence of gravity, the platform supporting the two horizontal accelerometers is maintained as level as possible (through torquing commands issued by the navigation computer) and is rotated about the local vertical at 1 rpm. The exact mechanical arrangement is called a carousel, free azimuth system. The navigation computer integrates measured accelerations to produce velocities and positions in XYZ or geographic coordinates, where X is east, Y is north, and Z is up along the local vertical. In tandem with this, attitude angles (heading, pitch, and roll) are measured by synchros attached to the gimbals. Because the INS measures accelerations at the fast rate of 40 Hz, it is a good source of high-frequency data; manufacturer specifications are about 38 m and 0.1 kt (0.05 m s^{-1}) for the resolution of position and velocity. However, because velocities and positions must be deduced from integrations, errors tend to accumulate and grow. For an INS, the net result of accumulated error is long-term drift and other forms of low-frequency variations that are difficult to distinguish from real motions.

To complement the INS, an ANI-7000 LORAN-C receiver (manufactured by Advanced Navigation Incorporated) is used. LORAN-C (short for LOng RANGE Navigation) is a method of radio navigation requiring three or more synchronized ground-based stations that transmit phase-locked 100 kHz radio pulses. LORAN-C measures positions at the slower rate of 1 Hz, has a lower resolution (88m), and has poor relative accuracy on a point-to-point basis due to small jump discontinuities. Nonetheless, LORAN-C errors are nearly constant in time with an advertised absolute accuracy of 0.1 nm (0.185 km), provided

13. Horizontal Wind Computation

in time with an advertised absolute accuracy of 0.1 nm (0.185 km), provided data are acquired in regions of good coverage. Because errors do not grow with time, LORAN-C is an accurate source of low-frequency data.

NOAA has also tested Global Positioning System (GPS) receivers on the P-3 aircraft. GPS is a method of radio navigation requiring signals from 3 or more satellites from a constellation of 21 satellites that orbit the Earth at a fixed altitude of 18,000 km. GPS measures positions at 1 Hz, and can achieve accuracies of 25m under favorable conditions. Unlike LORAN-C, GPS has global coverage and is less prone to electrical interference; thus it is a better

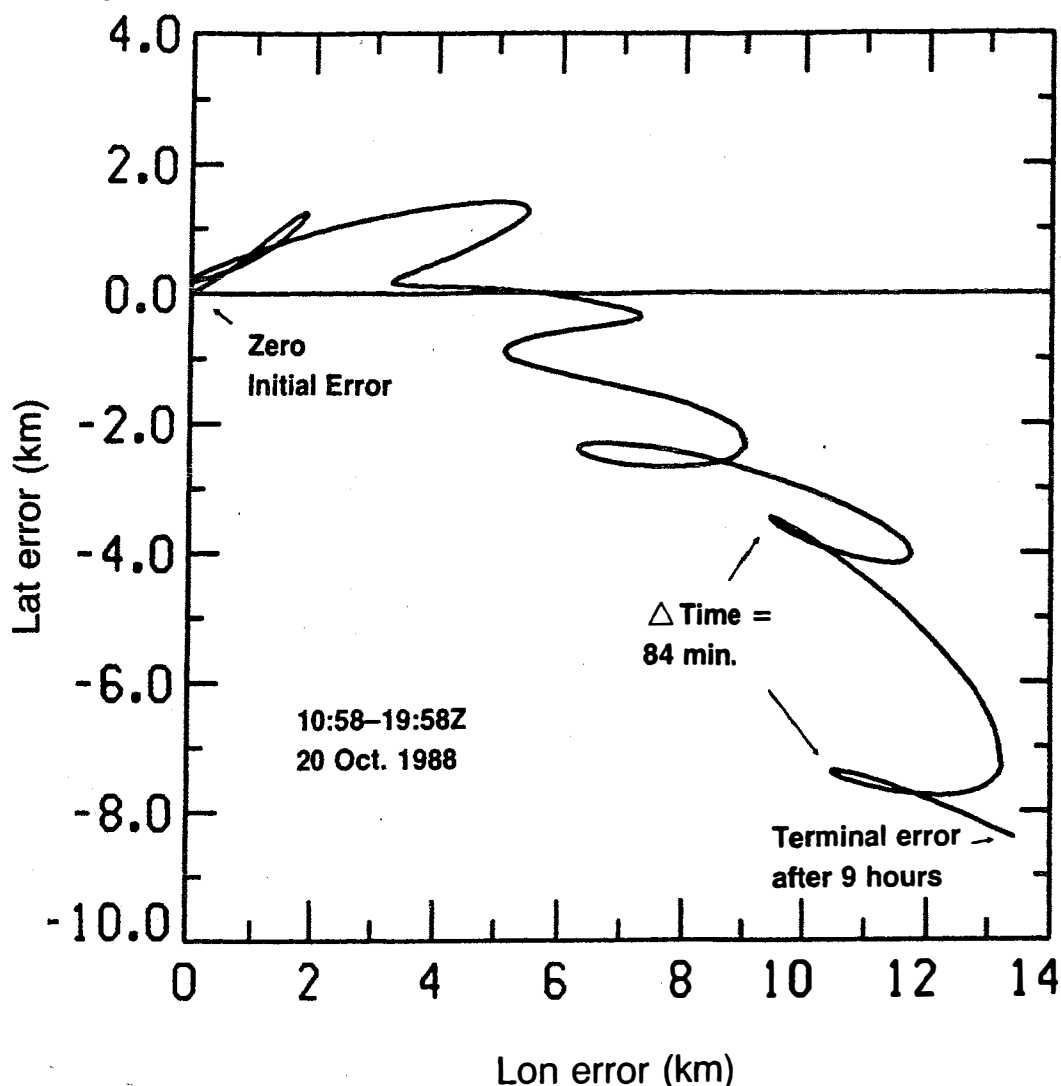


Fig. 13-1. Total (Schuler + drift) INS position error over the course of the 9h flight of October 20, 1988. Such cycloidal motions are easily confused with hurricane tracks which display similar motions with similar time scales.

13. Horizontal Wind Computation

source of low-frequency data. It is anticipated that GPS will replace LORAN-C as the primary source of low-frequency navigation information aboard the P-3's in the near future. However, GPS data was not available for this study and will not be discussed in more detail.

Error sources INS errors can be grouped into low-frequency errors (inertial drift and Schuler oscillation), and other errors (maneuver dependent errors, heading angle errors, and phase lag problems). Fig. 13-1 illustrates the severity of the low-frequency INS drift and Schuler oscillation errors on a typical P-3 flight. At takeoff time, the position error in both latitude and longitude is zero, but as the flight progresses, errors in both latitude and longitude accumulate at approximately 1 km hr^{-1} due to **inertial drift**. Superimposed on this inertial drift error is a sinusoidal oscillation with period 84 minutes called the **Schuler oscillation**. Note that the position errors shown in Fig. 13-1 trace out a cycloidal pattern, similar in time period to patterns observed in hurricane tracks (Willoughby et al. 1984). When velocity errors are added to this cycloidal behavior, locating the velocity center of a hurricane vortex can be a challenging exercise. Of some importance is that accurate data of these kind are essential for hurricane warnings in support of public safety, and navigation error could compromise this mission.

In more detail, the Schuler oscillation is caused by precession of the Z-gyro in an elliptical pattern about the local vertical. Suppose for simplicity that an aircraft is flying with velocity v along a great circle. Then, a small angular error ε in vertical alignment of the inertial platform results in the horizontal-acceleration error $\dot{v}_\varepsilon = g \sin \varepsilon$. At the same time, velocity error v_ε along a great circle can be estimated as $v_\varepsilon = (R+H)\dot{\varepsilon}$ where R is the radius of the earth and H is altitude above mean sea level. Thus, on combining equations $(R+H)\ddot{\varepsilon} = g \sin \varepsilon$, and the small-angle approximation $\sin \varepsilon \cong \varepsilon$ results in a harmonic equation with solutions of the form $\varepsilon(t) = A \cos(\omega_H t + \phi)$ where A and ϕ are amplitude and phase, and where ω_H is the radian frequency $\omega_H = 1/T_H$ computed with $T_H = 2\pi\sqrt{(R+H)/g}$. Although A and ϕ are generally unknown, T_H is fairly constant and can be estimated as $T_H \cong 84.5 \text{ min}$ using $R = 6.378 \times 10^6 \text{ m}$, $g = 9.807 \text{ m/s}^2$, and $H = 0$ (see Broxmeyer 1964, p. 15) In turn, this precession causes sinusoidal variations in the vector velocities. Because, the vector components are the projections of total error onto the horizontal axes, they have similar amplitudes but are 90° out of phase. Predictably, amplitudes tend to increase during a flight, as vertical alignment deteriorates. On the Carousel-IV units, Schuler oscillation peak amplitude errors in position range

13. Horizontal Wind Computation

from 1-7 km, and peak amplitude errors in velocity range from $0.5\text{-}3\text{ m s}^{-1}$.

Inertial drift is characterized as being nearly constant in direction, but with an amplitude that can grow linearly or exponentially with time. However, the sources of such errors are harder to pinpoint. They are generally attributed to mechanical imperfections in the Z-gyro, inaccurate calibration of the INS, and deficiencies in models and numerical algorithms. In any case, the prevalence of drift is easy to verify; typical angular offsets in the Z-gyro result in initial INS velocity errors of about 0.5 m s^{-1} , even when the aircraft is sitting still on the runway. Once airborne, position errors tend to accumulate at about 2 km h^{-1} , although rates as high as 7 km h^{-1} have been observed.

Correcting INS errors INS errors have been corrected by various authors using a variety of techniques. Shaw (1988) was one of the first to demonstrate the feasibility of correcting winds using LORAN-C data sampled at regular intervals. He used 1 Hz data and cubic splines to obtain a smooth fit to low-frequency INS errors. His results were definitive; LORAN-C substantially improved the accuracy of computed winds. Leach and MacPherson (1991) used the somewhat more complicated Kalman filtering approach to correct INS errors using LORAN-C; this method had the additional advantage of being able to estimate errors in heading angle and maneuver correlated errors.

A method of correcting low-frequency INS errors using LORAN-C or GPS has been developed at NOAA. The method is similar in spirit to the methods of Shaw (1988) and Leach and MacPherson (1991), but the implementation is different. Rather than using a curve-fitting procedure, the method is based upon filtering theory, which has the advantage of possessing a spectral interpretation. This allows one to control the spectral content of the data, which is useful in post processing, for example, because it allows one to evaluate problems related to phase lags in the INS. Phase lags occur because the navigation computer must estimate, and otherwise update, parameters prior to output, producing a delay. Delays of 0.08 to 0.7s in INS parameters have been observed by Tjernström and Friehe (1991), and phase lags of similar magnitude have been observed in NOAA's INS data. Delays of this magnitude can cause serious problems in applications requiring high-precision data, such as flux computations. Additionally, the use of symmetric filters does not inject phase lags into the data; application of a causal Kalman filter does.

The correction algorithm The method works by mixing the high-frequency data from the INS with the low-frequency data from LORAN-C to produce data

13. Horizontal Wind Computation

that is accurate at both high and low frequencies. To perform this feat, the filter presented in App.F is used in conjunction with the mixing filter technique (12.1). Comparison with a tracking laser (Masters and Leise, 1993) showed that position errors can be reduced below 0.2 km, and aircraft velocity errors to 0.1-0.3 m s^{-1} . The filter used is tuned to the Schuler component because other errors are less variable and of lower frequency; note, however, that maneuver correlated INS errors do exist, and those corresponding to frequencies higher than the Schuler component will not be corrected. In addition, the 1 rpm revolution of the Carousel IV platform causes oscillations in all INS quantities with a period of 1 minute which will not be removed by the filter.

Correcting the heading angle Even though near-perfect ground velocities can be obtained using the correction procedure, errors in heading remain and can degrade absolute accuracy of computed horizontal winds. For example, an aircraft flying 100 m s^{-1} with a 0.1° error in heading will produce a velocity error of $100 \tan(0.1^\circ) \cong 0.2 \text{ m s}^{-1}$, and larger angle errors produce proportionally larger velocity errors. Since the manufacturer's specified accuracy of heading angle is 0.4° , errors in computed horizontal wind due to heading angle errors could approach 1 m s^{-1} . A method of partially correcting heading angle errors is presented in Masters and Leise (1993). However, full correction of heading angle errors will require an independent source of heading information, or a Kalman filter approach.

Conclusions and recommendations Accurate horizontal wind computation requires navigation data that is accurate at both high and low frequencies. The INS is an excellent source of high-frequency data, and GPS and LORAN-C are excellent sources of low-frequency data. By mixing the high-frequency data from the INS with low-frequency data from GPS or LORAN-C, errors in aircraft velocity can be reduced below 0.3 m s^{-1} . However, heading angle errors and maneuver correlated errors remain and may degrade horizontal wind calculation by as much as 1 m s^{-1} . The only recourse may be to use another, more accurate source of heading, or abandon the symmetric filter and go to a Kalman filtering approach.

However, designing a good Kalman filter is difficult and time-consuming, and one injects phase lags and distorts the spectral content of the data due to the complex, time-varying blend of information used to generate corrected quantities, even when applying the filter forwards and backwards in time to produce a symmetric filter. Kalman filters are superior for real time

13. Horizontal Wind Computation

applications, and should be implemented on the aircraft for in-flight wind computation, but it remains to be proven that Kalman filtering is the best approach to use in post processing applications where winds with highly accurate spectra are needed, such as for flux computations.

A better solution might be to modify the INS, measure all angles and accelerations directly, and compute positions and velocities, instead of relying on the INS to do the computation. One could then use the symmetric filtering technique presented here in post-processing to correct the low frequency errors in the INS using GPS or LORAN-C. The final result would be highly accurate winds with good spectra, free of phase lag errors. Another possibility might be to use one of the new multi-antennae differential GPS systems to obtain attitude angles and low-frequency position information; high-precision accelerometers could then be used for high-frequency position information, since GPS, in spite of its greatly improved capabilities, does not have sufficient resolution at high frequencies to substitute for inertial navigation. Manufacturer's specifications indicate that these multi-antennae GPS systems can measure attitude angles to milliradian accuracy (better than an INS). Again, the mixing filter technique could be applied the the GPS/accelerometer information, to provide accurate winds with good spectra, free of phase lag errors.

14. VERTICAL WIND COMPUTATION

Vertical wind computation is performed by finding the vector sum of W_0 , the aircraft's vertical velocity, and W_r , the vertical relative wind. W_r is computed from true airspeed, attack, and slip angles, while W_0 is computed by integrating the vertical accelerometer output from the INS. The difficulty is that integration processes are inherently unstable; measurement errors, once incurred, tend to accumulate and grow. It is well known in statistics that integrating a white noise process (e.g., round-off error) results in a random walk with *infinite variance*. This error is apparent in Fig. 14-1 (light curve), where the aircraft vertical velocity from integrating the INS accelerometer ranges between 20 and 80 ms^{-1} over the course of a 4 hour flight. Vertical aircraft velocity from the integrated accelerometer must be stabilized by another source of aircraft velocity with good *low frequency* information.

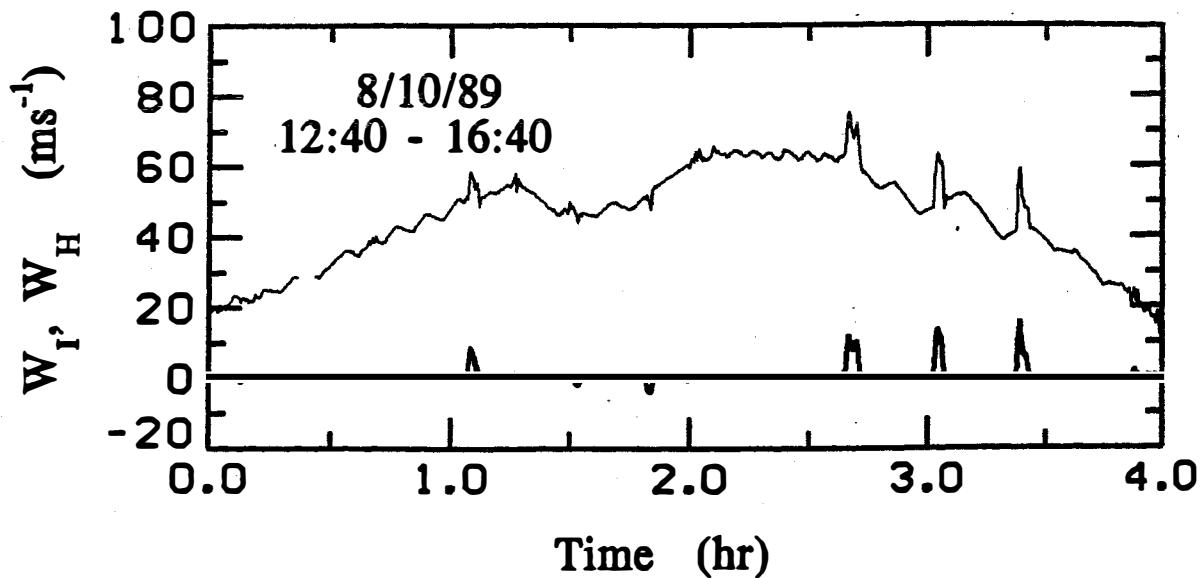


Fig. 14-1. Vertical aircraft velocity computed by integrating INS vertical accelerometer (W_I , light line) and by differentiating radar altimetry (W_H , dark line). Note the poor low frequency behavior of W_I , and the bias of 20ms^{-1} . Data taken from N42RF's calibration flight on 8/10/89.

14. Vertical Wind Computation

Two sources of vertical aircraft velocity with good low frequency information are available: the derivative of either pressure altitude or radar altitude with time. When GPS becomes available in 3 dimensions, one could also use the derivative of GPS altitude. Fig. 14-1 (dark curve) shows that the derivative of radar altitude gives good low frequency information--it remains near zero for the entire 4-hour flight, as one would expect when flying a calibration flight with many legs at constant altitudes. Radar altitude is the preferred measurement to use, since pressure altitude depends on altitude and meteorological conditions, and radar altitude does not. An exception to this rule occurs when flying over land--then one has no choice but to use pressure altitude, as radar altitude will give a measure of the terrain fluctuations beneath the aircraft.

Given the two estimates of vertical aircraft velocity, one from the integrated accelerometer, and one from (for example) differentiated radar

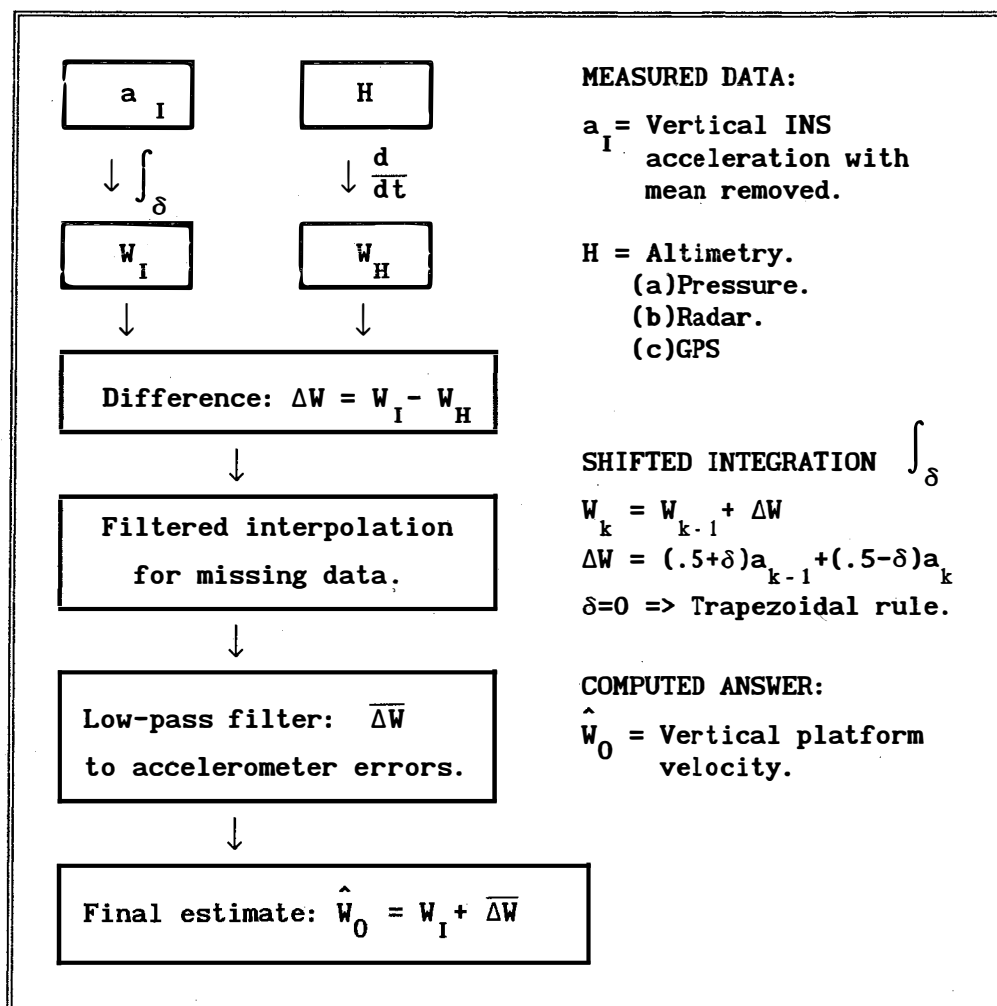


Figure 14-2. Flow chart of method used to compute vertical aircraft velocity from altimetry and INS acceleration.

14. Vertical Wind Computation

altimetry, one can splice them together using (12.1). A filter for doing this is described in App. F. The full correction procedure is outlined in Fig. 14.2. First, the mean acceleration from the entire flight is removed from the raw acceleration, a_I . Acceleration is then integrated using the trapezoidal rule to give the estimate of vertical aircraft velocity W_I (good at high frequencies). Note that the integration can be shifted in time to inject a phase lag, δ , into W_I (discussed at the end of this section). Radar altitude H is differentiated to give the estimate of vertical aircraft velocity W_H (good at low frequencies). The difference $\Delta W = W_I - W_H$ undergoes filtered interpolation to replace missing data (App. G), then it is lowpass filtered to obtain $\overline{\Delta W}$. The final estimate of vertical aircraft velocity is then $\hat{W}_0 = W_I + \overline{\Delta W}$.

The main question is, "how do we tune the filter to give the best vertical winds?" The answer depends on the performance of the two instruments used. In this case, we want to use the good high frequency information from the accelerometer without corrupting the computed velocity with accelerometer integration errors. Conversely, we do not want to use information from the radar altimeter that is too high in frequency, because its resolution is limited to 1 meter (see Fig. 14-3). The correct mix is best determined by

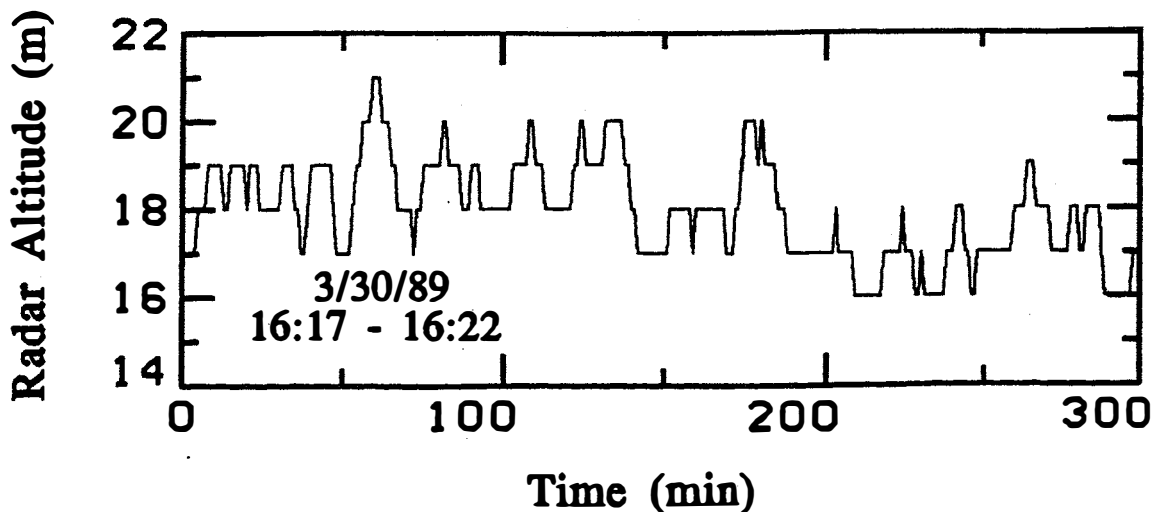


Fig. 14-3. Radar altitude vs. time for N43RF's low-level flight on 3/30/89 over a smooth portion of the polar ice cap. Note the poor high frequency information from radar altimetry--resolution is limited to 1 meter.

14. Vertical Wind Computation

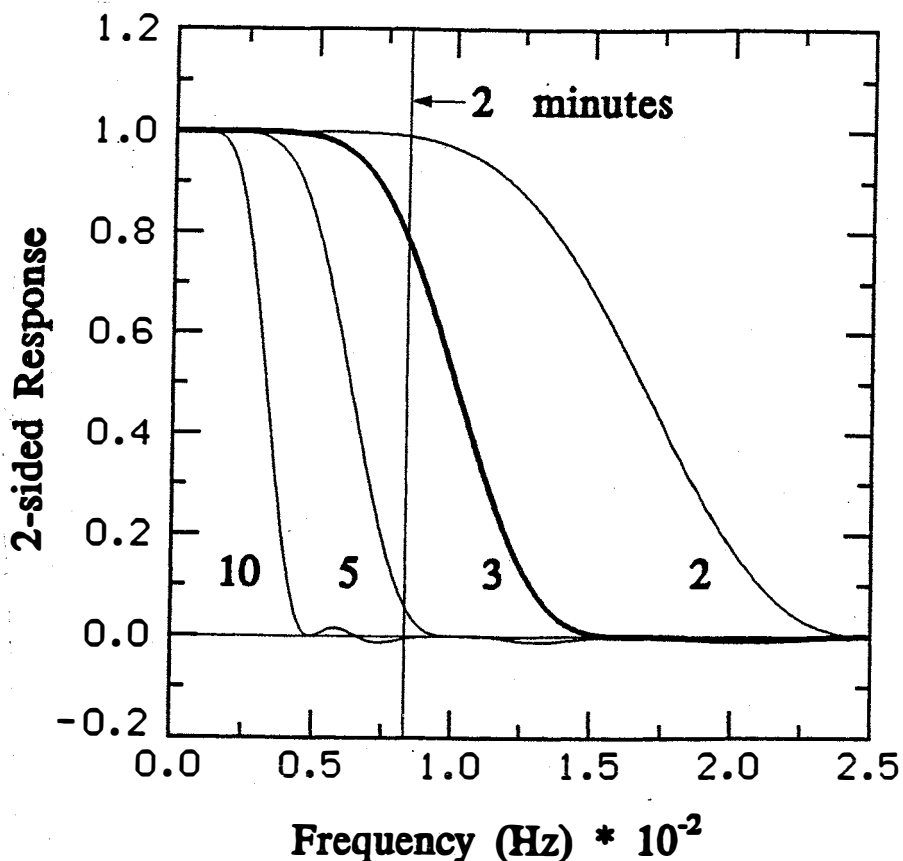


Fig. 14-4. Response curve for filter used to compute vertical aircraft velocity. Response is shown for LNTN=2, 3, 5, and 10; the value of LNTN controls the passband of the filter. LNTN=3 is recommended for best vertical winds.

studying maneuvers in calibration flights, and striving to tune out any observed maneuver-correlated fluctuations in the computed vertical wind.

The filter used to perform the splice has an adjustable length parameter, LNTN, that controls the passband of the filter (see App. F). When LNTN is doubled, the passband is halved. For example, with LNTN set to 5, the filter passes data with periods of 4 minutes or longer; for LNTN=10, only data with periods of 8 minutes or longer are passed (see Fig. 14-4 for the filter's response curve). Vertical winds were computed with a number of LNTN parameters for many different operational and calibration flights to study the best way to tune the filter; a value of LNTN=3 was determined to give the best overall performance. Computed vertical winds using LNTN=3 and LNTN=5 are shown in Fig. 14-5. These winds were computed during constant altitude circle maneuvers performed on N42RF's calibration flight of 8/10/89; six full circles were flown during the time shown. A plot of computed horizontal wind (lower graph) shows the circles quite clearly, as does the plot for vertical winds

14. Vertical Wind Computation

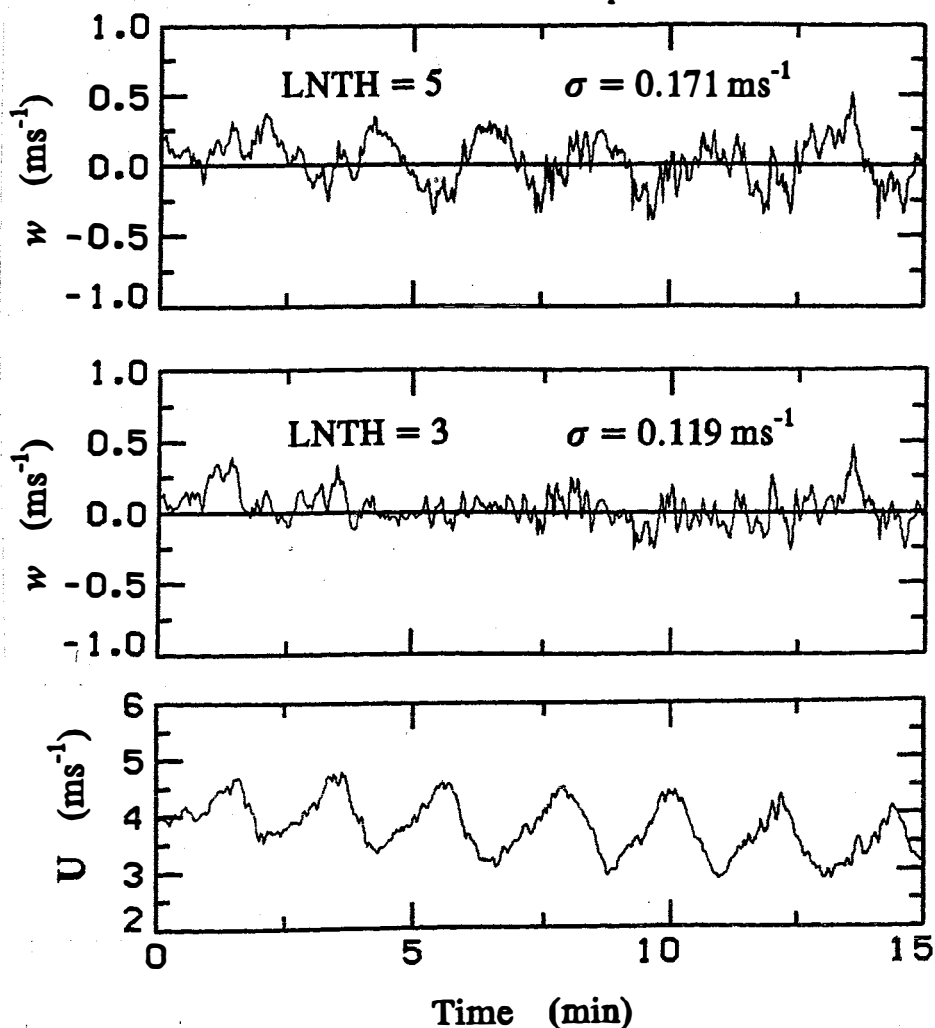


Fig. 14-5. Horizontal wind speed U (lower graph), vertical wind w computed with LNTH=5 (top curve), and w computed with LNTH=3 (middle curve), during a series of 6 circles on N42RF's calibration flight of 8/10/89. LNTH=3 gives vertical winds with less maneuver correlation and lower standard deviation, σ .

computed with LNTH = 5 (middle graph). Vertical winds computed with LNTH = 3 show little or no correlation with maneuvers; furthermore, the standard deviation of the winds is lower than that for LNTH = 5. Further reducing LNTH to 2 gives approximately the same answer as LNTH = 3, but with a slightly higher standard deviation; thus LNTH = 3 appears to be the better choice.

With LNTH = 3, the filter has approximately unity response for data with periods of 3 minutes or greater, zero response for periods less than 1 minute, with intermediate periods passed according to Fig. 14-4. This is similar to the filter used by Jorgensen and LeMone (1989) to compute vertical winds on the P-3's. Their filter (Graham, 1963) had unity response at periods longer than 65 s, zero response at periods shorter than 30 s, and a cosine fall off in between. This response is approximately what one would get by setting

14. Vertical Wind Computation

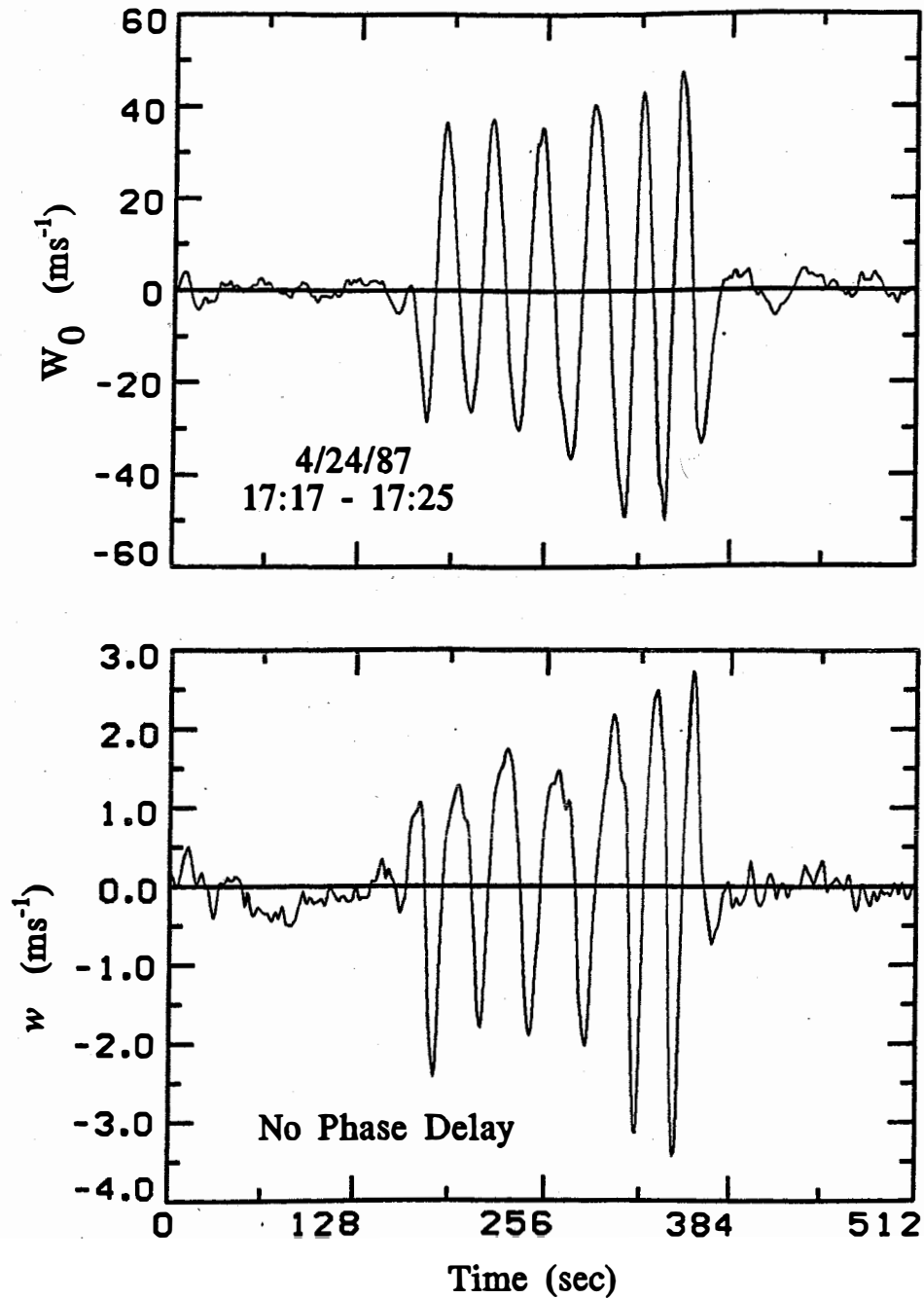


Fig. 14-6. Vertical aircraft velocity W_0 (top curve) and computed vertical wind w with no phase delay added (bottom curve) for the roller coaster maneuver on N43RF's calibration flight of 4/24/87. The maximum error in w is about 5%, and occurs during the maximum rate of change in W_0 , implying that a phase lag may cause the error.

14. Vertical Wind Computation

LNTN = 2 in the filter of App. F. Vertical winds computed using the two schemes have been compared and agree to within 0.1 ms^{-1} .

Phase corrections The final test of a vertical wind tuning technique is to study the "roller coaster" maneuver, where the aircraft rapidly climbs and descends at vertical velocities of 20 ms^{-1} or greater. Computed vertical winds for a roller coaster maneuver during N43RF's calibration flight on 4/24/87 are shown in Fig. 14-6. The aircraft's vertical velocity exceeded 40 ms^{-1} (top graph); this vigorous roller coaster was ideal for studying vertical wind errors. The bottom graph shows the computed vertical wind for the same maneuver. The vertical wind has about 5% error ($\pm 2.0 \text{ ms}^{-1}$), which is quite good; NCAR uses 10% error as their criteria for a successful vertical wind calibration. Close inspection of both graphs shows that the maximum error in vertical wind occurs when the aircraft velocity is changing most rapidly--i.e., when the aircraft velocity is passing through zero. This behavior implies that a phase delay may be causing the vertical wind errors.

Phase delays are known to exist in the P-3 INS data--manufacturer's specifications give phase delays of between 0.025 s and 0.125 s for the various INS parameters. Delays can also occur in the instruments used for relative wind computation--e.g., due to the length of the pressure lines. To see if a phase delay might be causing the observed error, correlation analysis was performed on the vertical aircraft velocity, W_0 , and the vertical relative wind, W_r . Technically, the computation consisted of computing the cross spectrum, zero-filling to interpolate, inverse transforming (with the FFT), and finally using a second-order, time-series interpolation to complete the curve. The result, shown in Fig. 14-7 (top curve), reveals that W_0 lagged W_r by 0.25 seconds. It is unknown exactly where this phase lag is coming from, since it is approximately double the manufacturer's specifications for the phase lag in the vertical accelerometer in the INS. INS phase lags of 0.08 - 0.2 seconds have been observed in vertical accelerometer data from a similar INS, the Litton LTN-72, by Tjernström and Friehe (1991).

This INS phase lag can be corrected by injecting a phase lag of the opposite sign and amplitude into the integration of the INS accelerometer (shown in Fig. 14-2). Vertical winds recomputed after performing this correction are shown in the bottom curve of Fig. 14-7. Vertical wind errors during the roller coaster maneuver were reduced below 1% ($\pm 0.3 \text{ ms}^{-1}$), which is an extraordinary feat. Tests done in other roller coaster maneuvers on both N42RF and N43RF reveal that this phase lag is always present, and ranges

14. Vertical Wind Computation

between 0.1 and 0.4 ms^{-1} . Further research is needed to quantify the magnitude of this phase lag.

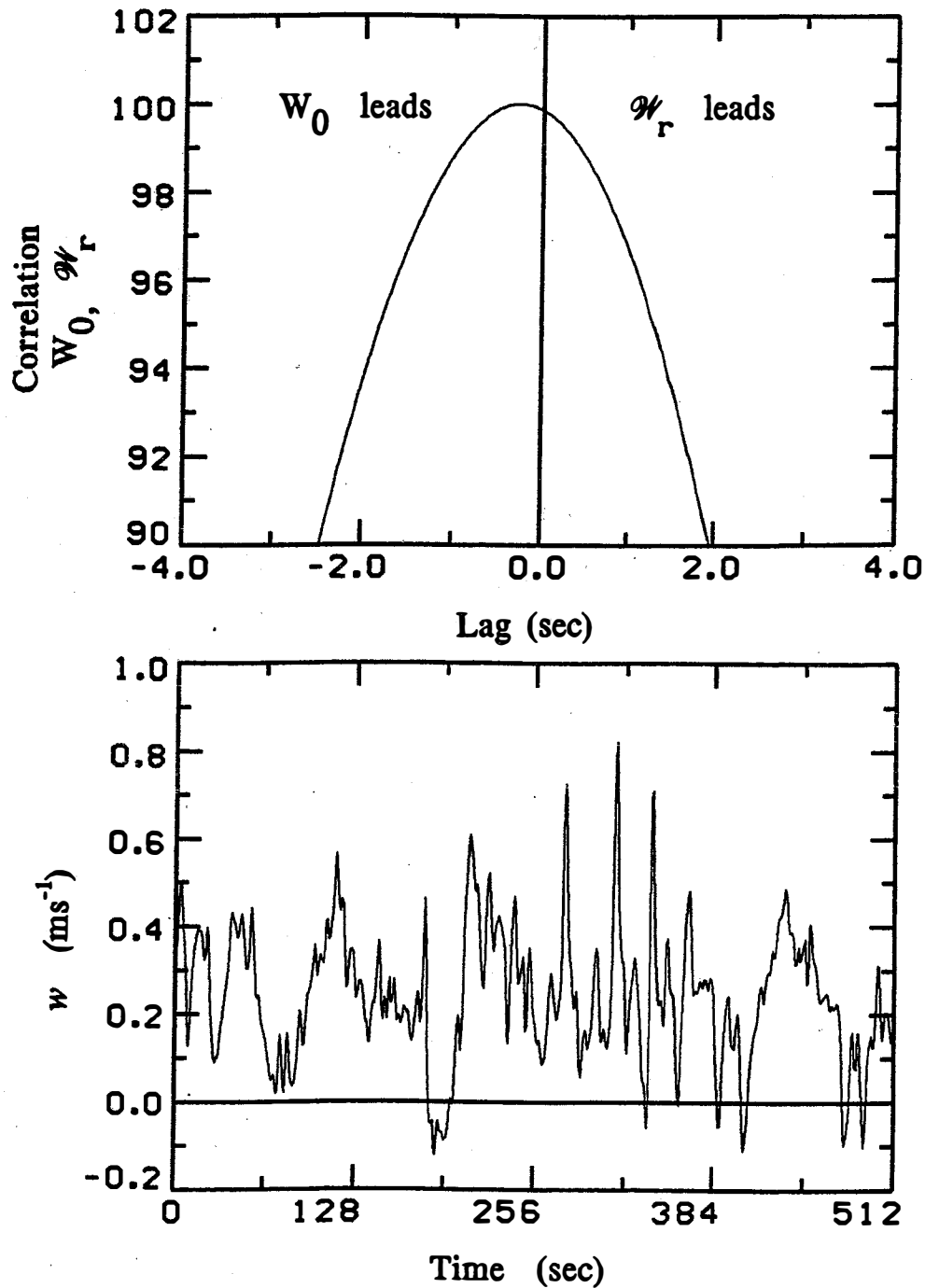


Fig. 14-7. Top graph: Phase delay between the vertical aircraft velocity W_0 and the vertical relative wind W_r computed using correlation analysis, during the roller coaster maneuver of Fig. 14-6. W_0 lags W_r by 0.25 seconds. Bottom graph: Vertical wind w during the roller coaster maneuver recomputed after correcting for the 0.25 second phase delay in W_0 . Relative error in w has been drastically reduced, to below 1%.

15. FLOW DISTORTION AND PHASE

Flow distortion Flow distortion refers to the phenomena of flow around the aircraft changing in rapid, unpredictable ways due to maneuvering or atmospheric turbulence. A sample of this behavior was demonstrated for the slip sensor mounted on top of the fuselage, during yaw maneuvers (Fig. 9-4). Flow distortion can lead to serious problems in wind measurement, because sensors are typically designed and calibrated for a narrow range of attack and slip angles. It is precisely when flow distortion becomes greatest when one is most interested in making accurate wind measurements, as one is typically passing through a turbulent region of great meteorological interest.

Pressure measurements on both the wing tip boom and fuselage have angle of attack and sideslip dependencies that are not correctly compensated for by current calibration methods, and are vulnerable to flow distortion errors. Rosemount Model 855EB-1 pitot-static tubes mounted on the wing tip has a "nose" that is somewhat flanged or scooped out to compensate for small differences in the incidence angle of the relative wind in the measurement; the resulting measurement of total pressure is straightforward and has not produced any noticeable distortions. Static pressure, however, is another story; for this two horizontal ports on opposite sides of the pitot-static tube are manifolded together to supply a static source; the idea is that external air motion will produce equal and opposite pressure forces that cancel. In practice, this works fairly well in straight-and-level flight or, more generally, when only the attack angle is varied; however, this measurement does not work so well in maneuvers or, more generally, when the slip angle is varied (DeLeo and Hagen, 1977).

Curiously, this situation is reversed for static pressure measured along the fuselage. In this case, static ports are located on opposite sides of the fuselage, aft of the wings, and some 15 m behind the nose, in a position relatively free of air motion. Again, these ports are manifolded together to supply a static source; now this measurement is relatively insensitive to slip angle, but tends to vary with attack angle (DeLeo and Hagen, 1978). Differences as great as 2 hPa between uncalibrated fuselage and wingtip static pressures have been observed on roller coaster maneuvers (Fig. 15-1). Recently implemented calibration procedures using a trailing cone (Brown, 1988) have provided the independent reference needed to properly calibrate static pressure.

At large attack and slip angles, differences between uncalibrated wingtip

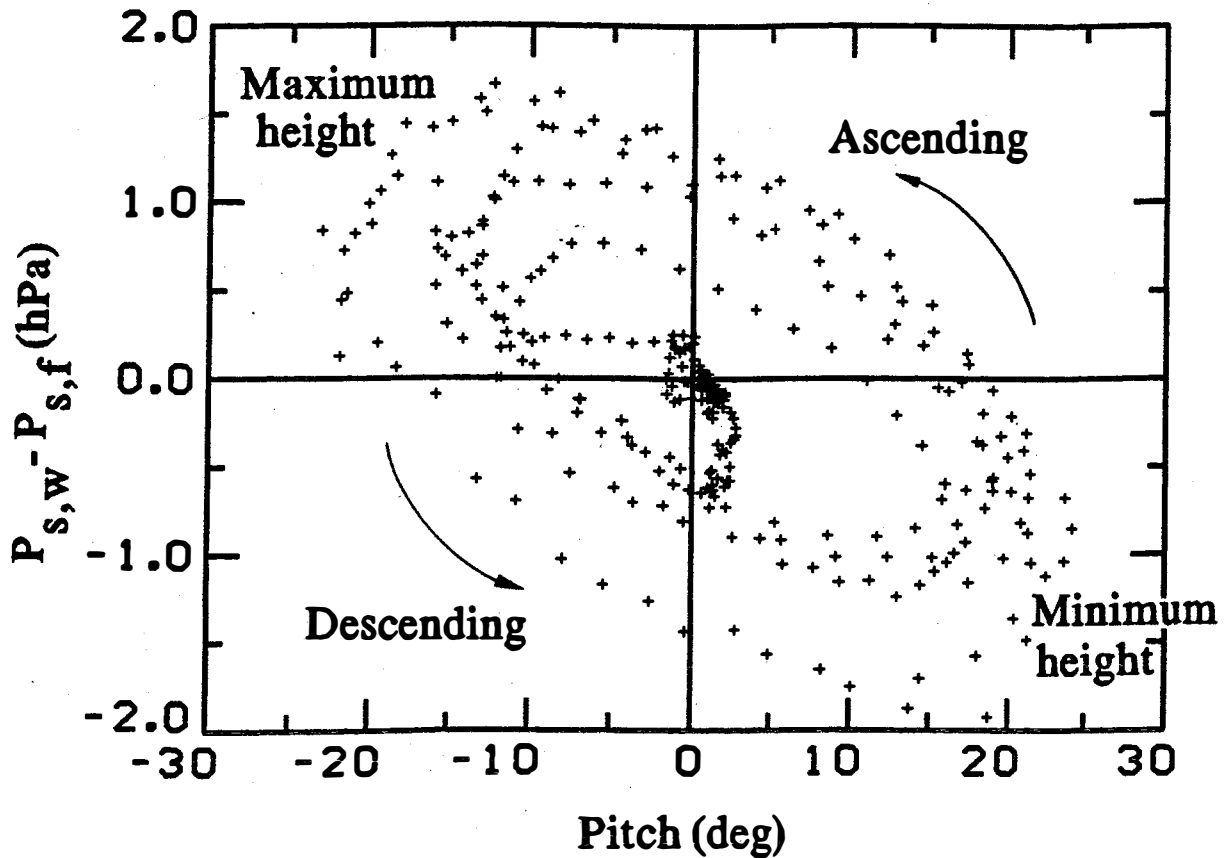


Fig. 15-1. Difference in uncalibrated static pressure between the wingtip and fuselage sensors as a function of pitch angle during the rollercoaster maneuver on N42RF's calibration flight of 4/24/87. The mean has been removed from both static pressures.

and fuselage static pressure can reach 10 hPa, and up to 17 hPa for dynamic pressure. Differences of these magnitudes were encountered during N42RF's penetration of Hurricane Hugo's eyewall on 9/15/89 (Fig. 15-2). Horizontal wind shear of 60 ms^{-1} and vertical wind shear of 15 ms^{-1} were encountered over a 700 meter distance, resulting in extreme flow distortion, slip angles exceeding 6° , attack angles of $\pm 4^\circ$, accelerations between -3.0 and +5.6 gravities, and the failure of one of the aircraft's engines. The 10 hPa and 17 hPa differences in static and dynamic pressure between the wingtip and fuselage static pressures were reduced to only 8 hPa and 14 hPa, respectively, after calibration; errors in flow angles of this magnitude can cause errors in computed horizontal wind of 10 ms^{-1} . Flow distortion and wind measurement errors of this magnitude are rarely encountered, but nevertheless it is important to track down these errors so that opportunities to measure unique meteorological events are not missed.

The majority of this huge discrepancy in measurements on the Hurricane

15. Flow Distortion and Phase

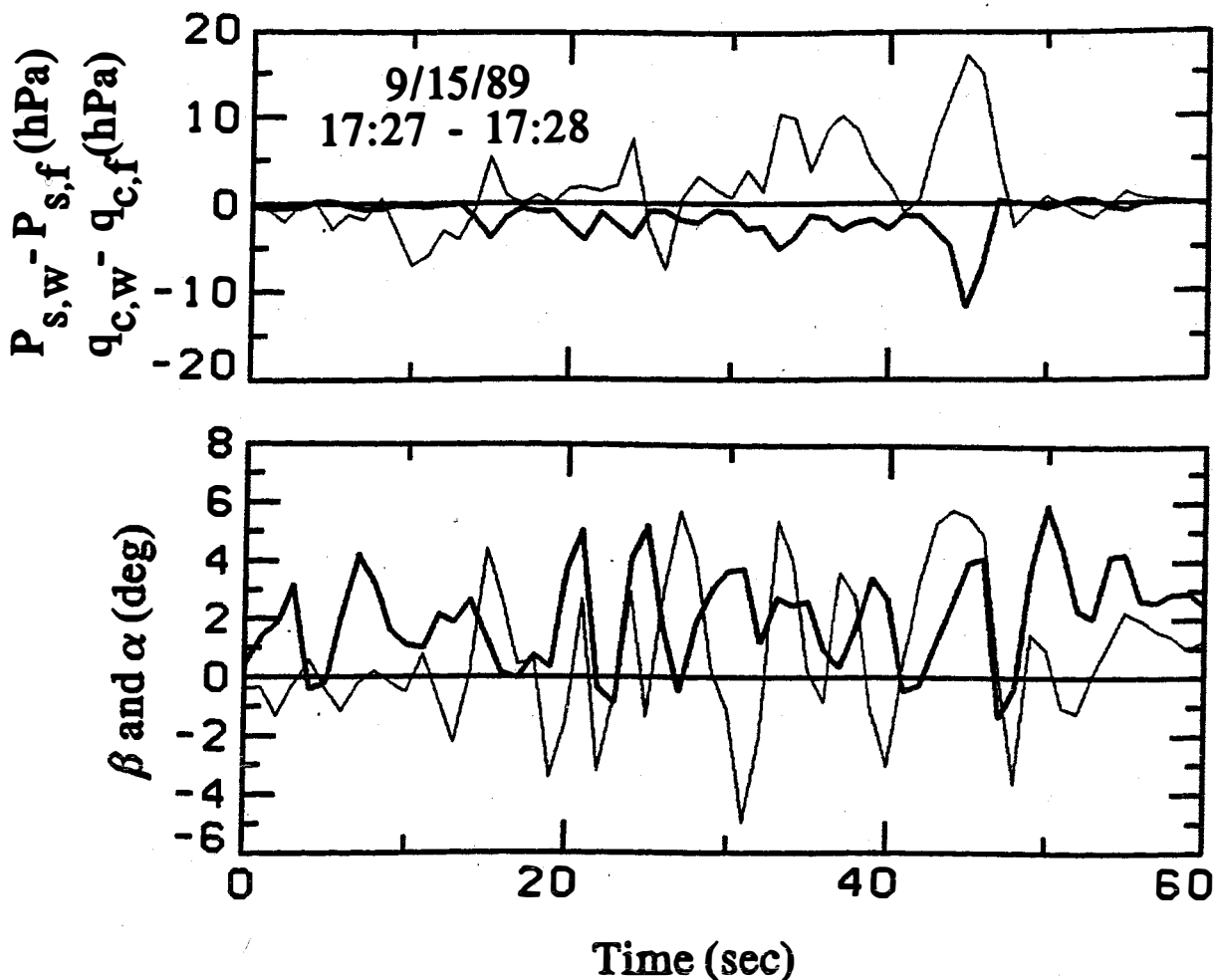


Fig. 15-2. Top graph: Difference between uncalibrated wingtip and fuselage static pressures ($P_{s,w} - P_{s,f}$) and dynamic pressures ($q_{c,w} - q_{c,f}$) during N42RF's penetration of Hurricane Hugo's eyewall on 9/15/89. Bottom graph: Attack and slip angles for the same period.

Hugo flight was subsequently traced to the wingtip boom. Studies of yaw maneuvers on N42RF revealed that the wingtip boom is probably not pointed straight ahead, but has a $2^\circ - 4^\circ$ tilt away from the aircraft fuselage. Thus when the slip angle was $+6^\circ$, the wingtip boom "saw" a slip angle of $8^\circ - 10^\circ$. According to the wind tunnel tests of the wingtip boom (DeLeo and Hagen, 1977), errors in static pressure exceeding 5 hPa can be expected for this situation, depending on the angle of attack. The remainder of the discrepancy may be caused by improper calibration of the fuselage sensor. Studies of the wingtip boom on N43RF reveal that it, too, may not point straight ahead, and thus will be subject to similar errors.

Clearly, more research is needed to determine the attack and sideslip

15. Flow Distortion and Phase

calibration factors for both the wingtip and fuselage pressure sensors. If possible, the tilt of the wingtip boom should be measured on the ground. Yaw maneuvers flown at various angles of attack would also help diagnose the problem.

Phase Phase lags between the time an event occurs and the time it is recorded by the data acquisition system occur to some degree in all instruments. All instruments have a (usually small) phase lag produced by the analog circuitry that processes the signal; in addition, instruments typically have a characteristic response time that may vary with flight conditions or meteorological conditions. For example, the General Eastern cooled mirror dew point instrument used on the P-3's has a response time of approximately 20 s to a 30°F step change in dew point. At low moisture levels, this response time is even slower. Additional phase lags can be caused by the data acquisition computer as it writes the data to tape; for the P-3's, however, these phase lags are probably insignificant (Alan Goldstein, personal communication).

Pressure measurements can have phase lags due to the length of the pressure lines connecting the transducer to the sampling port. An important example of this is the fuselage static pressure--it takes approximately 0.1 s for a pressure impulse travelling the speed of sound to traverse the distance from the fuselage static port to the total pressure transducer located near the copilot's seat (see Fig. A-1). Phase lags in pressure can also be caused by flow distortion; Fig. 15-3 shows the fuselage dynamic pressure $q_{c,f}$ lagged the wingtip dynamic pressure $q_{c,w}$ by 2.2 s during a yaw maneuver on N42RF's

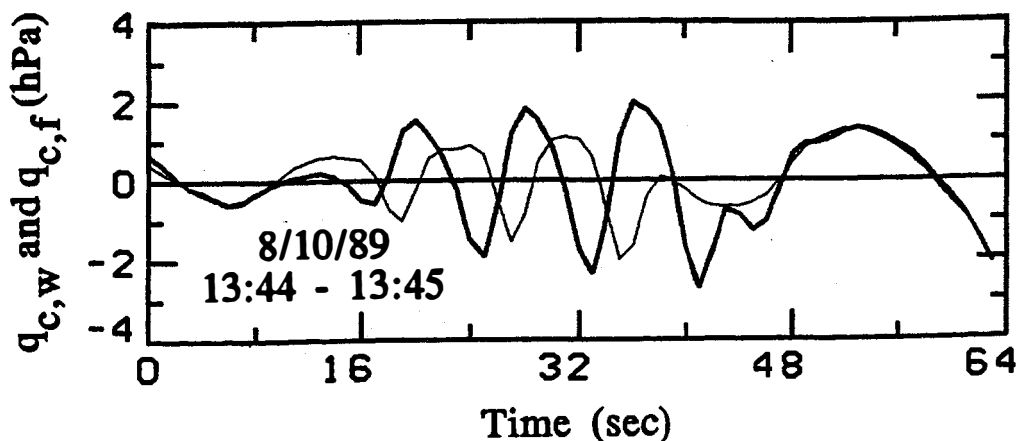


Fig. 15-3. Wingtip dynamic pressure $q_{c,w}$ and fuselage dynamic pressure $q_{c,f}$ during the yaw maneuver on N42RF's calibration flight of 8/10/89. The $q_{c,f}$ lags $q_{c,w}$ by 2.2 seconds.

15. Flow Distortion and Phase

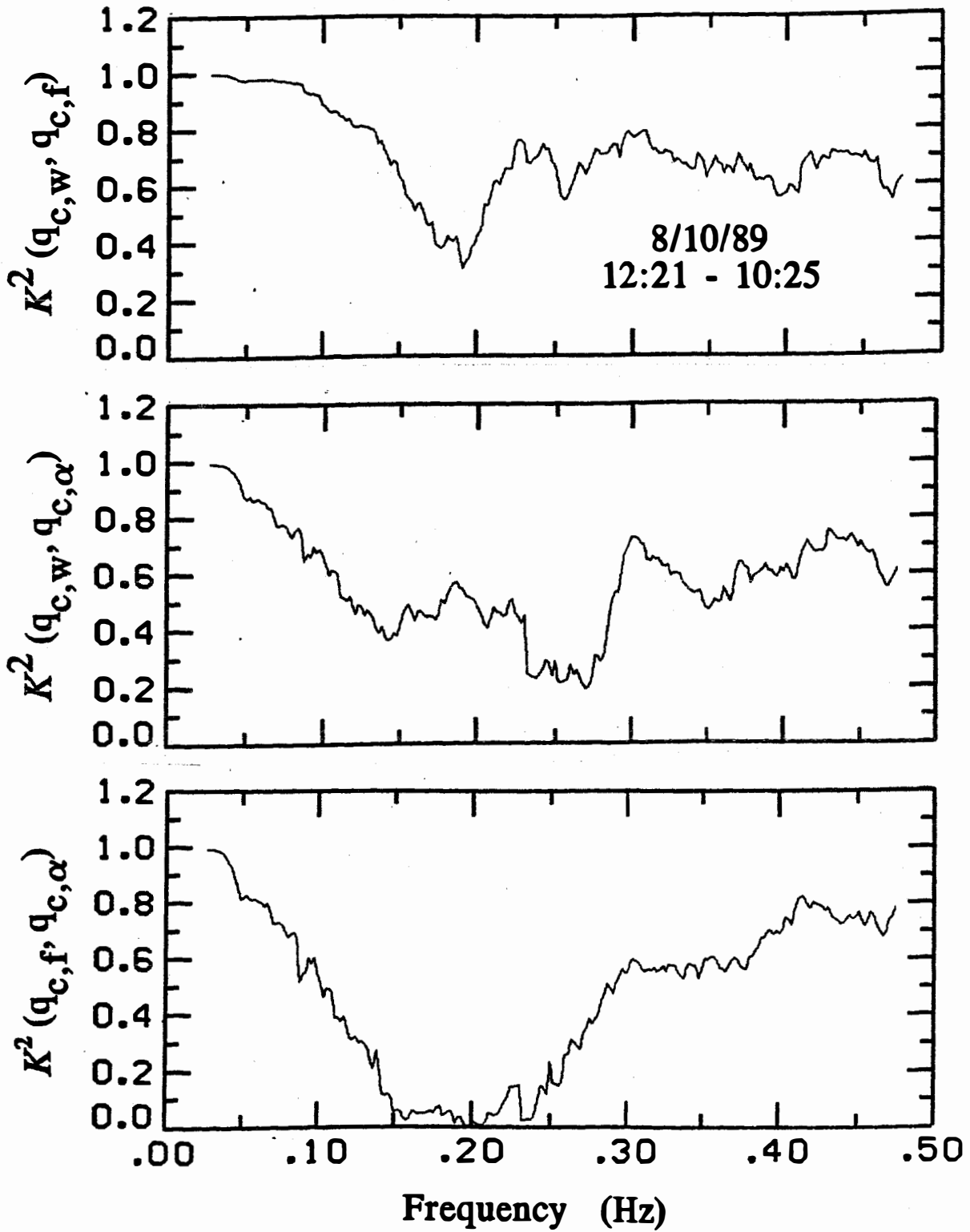


Fig. 15-4. Coherence K^2 for three sets of dynamic pressures: wingtip dynamic pressure $q_{c,w}$ and fuselage dynamic pressure $q_{c,f}$ (top graph); $q_{c,w}$ and dynamic attack pressure $q_{c,\alpha}$ (middle graph); and $q_{c,f}$ and $q_{c,\alpha}$ (bottom graph). Data taken during a straight and level ferry flight on N42RF.

15. Flow Distortion and Phase

calibration flight of 8/10/89. During this same maneuver, $q_{c,w}$ lagged dynamic slip pressure $q_{c,s}$ by 1.6 s. Phase lags between the two total temperature sensors of 0.6 s have also been observed during maneuvers. Even during straight and level ferry flights, phase problems have been found. For example, coherences for three sets of pressure sensors using the same variety of transducer (Fig. 15-4) are quite poor, suggesting that substantial phasing problems exist.

These phase problems are important to identify and correct, because even a small phase lag can lead to substantial error in computed winds, as was shown for the vertical wind in Sec. 14. Horizontal winds can be affected as well; Tjerström and Friehe (1991) showed that INS phase lags of 0.4-0.7 s degraded their horizontal winds. In addition, correction of phase problems is critical for high precision flux measurements requiring fast (10 Hz) data. Much research is needed to quantify and correct phase problems on the P-3's.

16. CONCLUSIONS AND RECOMMENDATIONS

The theory needed to perform high precision wind computations from aircraft has been presented. In particular, a better understanding of fluid geometry led to exact equations of flow angle measurement on the surface of a sphere. Resulting improvements in flow angle measurement will assist in computing horizontal winds and turbulent fluxes to higher accuracy. Symmetric filtering methods were introduced to correct instrument errors, and a detailed description of a high-quality low pass filter to use for these corrections was presented. In addition, FORTRAN subroutines and in-flight examples from NOAA's P-3 aircraft were presented to demonstrate application of the theory.

Horizontal wind accuracy was improved by correcting low frequency INS errors with LORAN-C, using a symmetric filter. Errors in horizontal winds due to aircraft positioning can be reduced to $0.1-0.3 \text{ ms}^{-1}$ using this technique. Similar methods were used to correct vertical winds, and vertical wind errors during strenuous vertical aircraft maneuvers were reduced to a remarkable 1%. However, accurate calibrations of the flow angle sensors remained elusive, probably due to improper sensor location, and relative wind measurement accuracy remains unsatisfactory.

Recommendations Improvements in wind accuracy can be achieved through a combination of improved instrumentation and better understanding of current instrumentation and calibration methods. Particular emphasis should be placed on identifying and correcting phase lags in *all* instrumentation carried on the P-3's; this is especially important for INS quantities. Correction of phase problems is especially critical for obtaining high precision turbulent flux measurements from the newly installed radome gust probe. Additionally, flow distortion problems need to be identified and corrected; failure to do so will cause significant loss of measurement precision at times when one is passing through turbulent regions of greatest interest. In particular, the wingtip boom needs to be recalibrated for slip angle dependencies.

Several unknown error sources need to be studied and corrected. The cause of observed drift in vertical wind over the course of a 9-hour flight needs to be studied. Maneuver dependent and heading angle errors in the INS need to be quantified, possibly through addition of separate accelerometers and an independent source of heading. A Kalman filtering approach to correcting INS errors should also be considered, particularly for real-time application. Finally, an oscillation in the roll angle with a period of approximately 5 seconds has recently been discovered (Fig. 16-1). The cause and importance

16. Conclusions and Recommendations

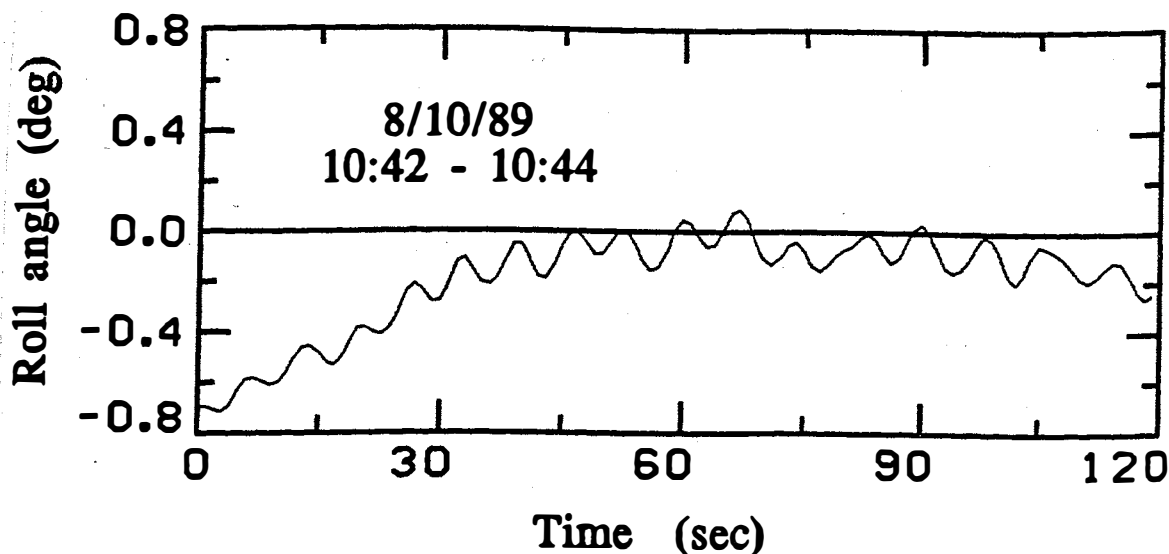


Fig. 16-1. Oscillation in roll angle with a period of approximately 5s observed during a straight and level ferry flight on N42RF. The cause of the oscillation is unknown.

of this oscillation is unknown, but it could adversely affect turbulent flux measurements. Further research is needed to find the cause of this oscillation, to see if it affects other quantities, and to identify other possible troublesome oscillations in P-3 instrumentation.

New instrumentation can substantially improve wind computation accuracy. For true airspeed, direct measurement using a Doppler lidar would be superior to the current indirect method, using Bernoulli's equation. Flow angles can be improved by using radome flow angle sensors, which should be less prone to flow distortion errors. These sensors have recently been installed on the P-3's, but were not available for this work. Horizontal winds can be improved by addition of GPS and an alternate source of heading; a multi-antennae differential GPS system can provide more accurate attitude angles and low-frequency position and velocity information than an INS. Horizontal winds can also be improved by obtaining improved high-frequency velocity information, either by adding new independent high-precision accelerometers or by modifying the INS to measure its accelerometer output directly. Consideration should be given to co-locating the navigation and relative wind instrumentation to reduce flow distortion and phase lag problems. An improved slow response dew point instrument is also needed.

In conclusion, major improvements have been made in P-3 data processing

16. Conclusions and Recommendations

software, calibration methods, and instrumentation. Accuracy of horizontal winds in straight and level flight in the absence of significant turbulence is probably $0.5-1.0 \text{ ms}^{-1}$, if low frequency INS errors are corrected using LORAN-C or GPS. Under the same conditions, vertical wind accuracy is probably $0.3-0.5 \text{ ms}^{-1}$. However, current instrumentation and understanding of P-3 measurement errors is insufficient to insure good data quality for flux measurements, during aircraft maneuvers, and in strong flow distortion conditions associated with penetrations of turbulent weather. Additional research and better instrumentation is needed in order to provide the scientific community the highly accurate wind measurements it needs.

Acknowledgements. Jim Leise died shortly before he finished this work, and I would not have been able to finish it for him without the help of Admiral Francis Moran and Captain Tom Gerish of the Aircraft Operations Center, who arranged to grant me the necessary funds. Many people aided us during the preparation of this paper, and I will do my best to acknowledge those who assisted us. Firstly, we thank Tim Crawford, Ed Brown, and Carl Freihe, who reviewed this document. Harlan Davis and Dick Darby, who laid the foundation of P-3 science, deserve special thanks. Also, we thank Stig Rossby, Tom Gerish, Jim McFadden, Jack Parrish, Barry Damiano, Phil Bogert, Robert Crow, Jim Roles, Alan Goldstein, Jim Dugranrut, Terry Schricker, Jerry Krantz, Terry Lynch, and the entire crew and support personnel of the Aircraft Operations Center, who endured the 5:00 am take off times for calibration flights, the endless racetracks and circles, and the ever-dreaded roller coaster maneuver. Thanks, guys. Without you, this study would not have been possible. Also, we wish to thank our fellow scientists in the aircraft community who assisted us. In particular, we thank Frank Marks Jr., Hugh Willoughby, Pete Black, Bob Burpee, and the entire staff of the Hurricane Research Division of the Atlantic Oceanographic and Meteorological Laboratory; Don Lenschow and Dick Freisen of NCAR; Dave Jorgensen and Peggy LeMone of NOAA's Environmental Research Laboratory; Will Shaw of Battelle Northwest; and Jan Zysko and Bill Jaferis of NASA. Thanks also to Kristi Vandebosch, who did the graphics. And finally, I thank Diana Kennelly, Duane Leise, and Diane Hallinen for their much needed moral support in finishing this work.

Part III
Appendices

Appendix A. P-3 INSTRUMENTATION

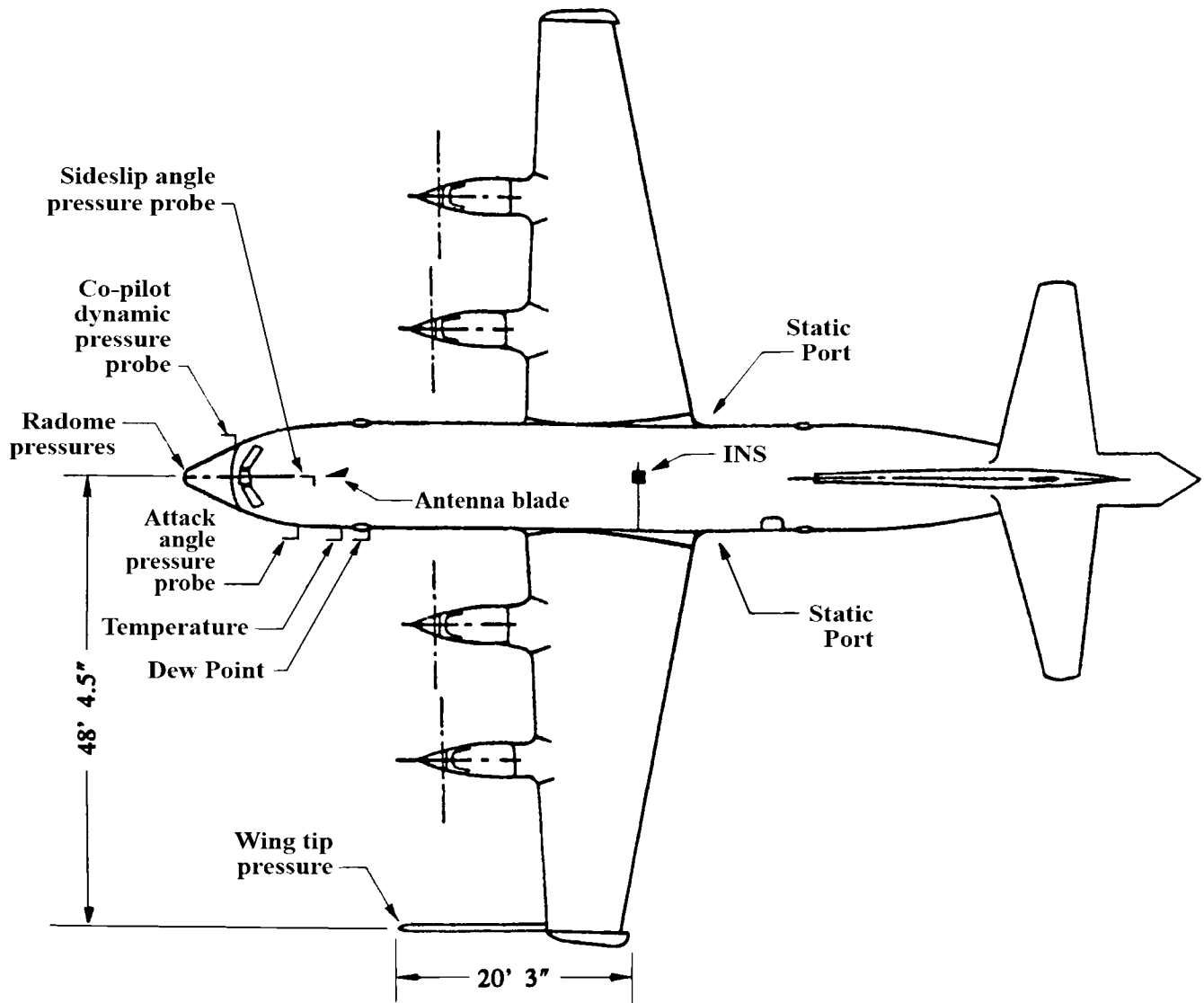


Fig. A-1. Location of P-3 instruments.

Appendix B. INCOMPRESSIBLE FLOW PAST A SPHERE

Theory presented here is for flow past a sphere, needed with flow-angle measurement (see Sec. 6). The model is for incompressible, inviscid flow and yields an exact, closed-form solution (Landau and Lifshitz, 1959, p. 25); by contrast, compressible solutions are rare, even in the inviscid case. Of special interest is that *flow is not restricted to be stationary*.

To begin, incompressible fluids are divergence free $\nabla \cdot \mathbf{V} = 0$. Thus, for potential flow $\mathbf{V} = \nabla \Psi$, Laplace's equation must be satisfied:

$$(B.1) \quad \nabla \cdot \mathbf{V} = \nabla \cdot \nabla \Psi = \nabla^2 \Psi = \frac{\partial^2 \Psi}{\partial x^2} + \frac{\partial^2 \Psi}{\partial y^2} + \frac{\partial^2 \Psi}{\partial z^2} = 0,$$

which can be solved with harmonic function theory.

The problem of interest is to *compute the potential flow past a sphere of radius λ induced by ambient wind of velocity \mathbf{U}* . Here \mathbf{U} can change with time but not with position. Note that this is a model of flow observed in aircraft coordinates from a (spherical) platform moving with *arbitrary* velocity \mathbf{U} . Boundary conditions are:

$$(B.2) \quad \begin{aligned} \text{BC1: } & \nabla \Psi = \mathbf{U} \text{ at large distances.} \\ \text{BC2: } & \mathbf{n} \cdot \nabla \Psi = 0 \text{ at the surface of the sphere.} \end{aligned}$$

where \mathbf{n} is the *outward* unit normal. Thus, ambient flow \mathbf{U} is perturbed in such a way so as not to penetrate the surface.

This problem can be solved, in standard ways, with separation of variables. However, for present purposes, it is easier and more informative to simply verify that the following potential function works:

$$(B.3) \quad \boxed{\Psi = \left[1 + \frac{\lambda^3}{2r^3} \right] \mathbf{U} \cdot \mathbf{r}}$$

where $\mathbf{r} = r\mathbf{n}$ is the position vector of length r in the direction \mathbf{n} . To this end, the following vector identities are useful:

$$(B.4) \quad \begin{aligned} \text{ID1: } & \nabla(\kappa\phi) \equiv \kappa\nabla\phi & \text{ID3: } & \nabla r \equiv \mathbf{n} & \text{ID5: } & \nabla \cdot \phi \mathbf{A} \equiv \nabla\phi \cdot \mathbf{A} + \phi\nabla \cdot \mathbf{A} \\ \text{ID2: } & \nabla(\mathbf{c} \cdot \mathbf{r}) \equiv \mathbf{c} & \text{ID4: } & \nabla\phi(r) \equiv \phi'(r)\mathbf{n}. \end{aligned}$$

where κ and \mathbf{c} are scalar and vector constants, and where ϕ and \mathbf{A} are scalar and vector-valued functions, respectively; in particular, because \mathbf{U} depends only on time, we can use $\mathbf{c} = \mathbf{U}$. Now, velocity $\mathbf{V} = \nabla \Psi$ is obtained with ID2 and ID3 as,

Appendix B. Incompressible Flow Past a Sphere

(B.5)

$$\mathbf{V} = \mathbf{U} - \frac{\lambda^3}{2r^3} [3(\mathbf{U} \cdot \mathbf{n})\mathbf{n} - \mathbf{U}]$$

Similarly, verification that $\nabla \cdot \mathbf{V} = 0$ is tedious but straightforward; we leave this as an exercise (note, $\mathbf{n} = \mathbf{r}/r$). To check boundary conditions, observe that at large distances r , \mathbf{V} agrees with the ambient wind $\mathbf{V} \cong \mathbf{U}$, and near the surface $r = \lambda$, the flow changes to $\mathbf{V} \cong 3[\mathbf{U} - (\mathbf{U} \cdot \mathbf{n})\mathbf{n}]/2$. Consequently, $\mathbf{V} \cdot \mathbf{n} = 0$ at the surface, and there is no flow into it. Of additional interest is that flow speeds up in going around the sphere; specifically when $\mathbf{U} \cdot \mathbf{n} = 0$, the flow satisfies $\mathbf{V} = 3\mathbf{U}/2$ and there is a net velocity increase of $\mathbf{U}/2$.

The subtle step is to relate velocity \mathbf{V} to pressure p . For potential, incompressible flow, Euler's equation (5.3) can be put in the form:

$$(B.6) \quad \nabla \left(\frac{\partial \Psi}{\partial t} + \frac{1}{2} V^2 + gz + \frac{p}{\rho} \right) = 0,$$

where $V^2 = \mathbf{V} \cdot \mathbf{V}$. This is a standard computation, requiring more vector arithmetic. For present purposes, we neglect gravity and integrate

(B.7)

$$\frac{\partial \Psi}{\partial t} + \frac{1}{2} V^2 + \frac{p}{\rho} = f(t)$$

where $f(t)$ is the "constant" of integration. This equation is known as **Bernoulli's equation for potential, incompressible flow**, and should not be confused with Bernoulli's equation (5.6) for isentropic flow; in particular, the adiabatic and incompressibility assumptions are incompatible. Observe that V^2 is determined by (B.5)

$$(B.8) \quad V^2 = \left[1 + \frac{\lambda^3}{2r^3} \right]^2 U^2 - 3 \left[\frac{\lambda^3}{r^3} - \frac{\lambda^6}{4r^6} \right] (\mathbf{U} \cdot \mathbf{n})^2$$

where, as above, $U^2 = \mathbf{U} \cdot \mathbf{U}$. Next, $f(t)$ can be obtained by averaging over spherical surfaces of radius $r = R$ and letting $R \rightarrow \infty$; we denote this limit by $\langle \cdot \rangle_\infty$. It is easily seen that $\langle V^2 \rangle_\infty = U^2$ and $\langle \Psi \rangle_\infty = 0$; thus, $\langle \partial \Psi / \partial t \rangle_\infty = \partial \langle \Psi \rangle_\infty / \partial t = 0$ and $f(t)$ must satisfy:

$$f(t) = \langle f(t) \rangle_\infty = \left\langle \frac{\partial \Psi}{\partial t} \right\rangle_\infty + \frac{1}{2} \langle V^2 \rangle_\infty + \langle p \rangle_\infty / \rho = \frac{1}{2} U^2 + p_s / \rho.$$

where $\langle p \rangle_\infty = p_s$ is the static pressure. When this expression is used in (B.7), the pressure difference $p - p_s$ on the surface of the sphere is computed by evaluating terms at $r = \lambda$

Appendix B. Incompressible Flow Past a Sphere

(B.9)

$$p - p_s = \frac{\rho}{8} [9(\mathbf{U} \cdot \mathbf{n})^2 - 5U^2] - \frac{3\rho\lambda}{2} \mathbf{n} \cdot (\partial \mathbf{U} / \partial t)$$

Here, $p=p(\mathbf{n})$ is pressure on the surface in the direction \mathbf{n} . Recall that this is the solution for inviscid, incompressible flow. A more realistic model would be adiabatic.

For application to flow-angle measurement, \mathbf{U} is replaced with the relative wind $\mathcal{Z}_r = \tau \dot{\mathbf{e}}_r$ where, as before, $\tau = \|\mathcal{Z}_r\|$ is true airspeed and $\dot{\mathbf{e}}_r$ is the vector direction. The radius λ is now the (local) radius of a spherically shaped sensor or probe which could be the front part of a radome. In any case, (B.9) can be written

$$(B.10) \quad p - p_s = \frac{\rho\tau^2}{8} [9(\dot{\mathbf{e}}_r \cdot \mathbf{n})^2 - 5] - \frac{3\rho\lambda}{2} \mathbf{n} \cdot (\partial \mathcal{Z}_r / \partial t)$$

After all this, we show that the acceleration term can generally be neglected, anyway. Consider the relative error computed as the ratio of the second term to the first:

$$\text{Relative Error} = |3\lambda \mathbf{n} \cdot (\partial \mathcal{Z}_r / \partial t)| / \left| \frac{1}{4} \tau^2 [9(\dot{\mathbf{e}}_r \cdot \mathbf{n})^2 - 5] \right|$$

For a worst-case analysis, suppose that the wind direction coincides with the pressure direction $\dot{\mathbf{e}}_r \cdot \mathbf{n} = -1$ and there is no angular acceleration, that is, $\partial \mathcal{Z}_r / \partial t = \|\partial \mathcal{Z}_r / \partial t\| \dot{\mathbf{e}}_r$. Thus, with an acceleration equal to gravity g , the relative error reduces to $3\lambda g / \tau^2$. Finally, with a nominal true-airspeed of 100 m/s and $g \cong 10 \text{ m/s}^2$, this error is about $3 \cdot 10^{-3} \lambda$. Because the radius λ is substantially less than a meter in practical applications, we conclude that the acceleration term can safely be omitted. Nonetheless, the reader should be wary of situations where the difference $9(\dot{\mathbf{e}}_r \cdot \mathbf{n})^2 - 5$ is small and the acceleration term becomes the dominant factor.

Appendix C. DIGITAL FILTERS AND SYMMETRY

Mathematically, a filter is a linear operator that transforms one time series into another by **convolution**. Simply stated, convolution is a generalized moving-average; it is a concept natural to both measurement and signal processing. For example, weather radars transmit with a fixed beam pattern and the resulting backscatter is spatially averaged or convolved by this pattern. Data can also be convolved in time; pressure and temperature sensors require a small, but finite, amount of time to respond to physical stimuli; the net effect is an averaging process that can again be modeled as a convolution. For a filter, the salient feature is that the same computation is applied over and over (such as in differencing), by sliding it along the data.

Of special interest here are predictive filters and symmetric ones. **Predictive filters** are used in real-time applications because they are **causal**, that is, they use data only from the past (or present). In practice, they can either be implemented digitally, say with a computer, or built directly into an analog device (like in radio). A simple example is the **exponential filter** defined

$$(C.1) \quad y_n = r y_{n-1} + (1-r)x_n$$

where $\{x_k\}$ is a given time-series of data, y_n is the filtered answer, and r is a parameter that controls the amount of "feedback" from y_{n-1} . We remark that feedback filters that depend only on present data x_n are called autoregressive (**AR**); however, for more general autoregressive filters, feedback can depend on all previous filtered values y_{n-k} ; $k > 0$. Next, it is informative to track the iteration backwards in time

$$(C.2) \quad \begin{aligned} y_n &= r^2 y_{n-2} + (1-r)[x_n + r x_{n-1}] \\ &= r^3 y_{n-3} + (1-r)[x_n + r x_{n-1} + r^2 x_{n-2}] \\ &\dots \\ &= (1-r) \sum_{k=0}^{\infty} r^k x_{n-k} \end{aligned}$$

which is an infinite moving-average (**MA**) filter that converges for $|r| < 1$. Because powers are related to exponentials as $r^k = \exp(k \log r)$, the reason for calling this the exponential filter is clear. In passing, we remark that this example is characteristic of the general case, "Any (convergent) AR filter can be represented as an MA filter;" however, the converse is not true, "There are MA filters cannot be implemented as AR filters." We remark that many of the filters of interest are in this latter category.

Appendix C. Digital Filters and Symmetry

By contrast, **symmetric filters** use data from both the past and the "future", and are usually restricted to digital implementation; they are commonly used in post-processing and analysis. A simple example is the Von-Hann or Hanning filter:

$$(C.3) \quad y_n = \frac{1}{4}(x_{n-1} + 2x_n + x_{n+1})$$

which is often used for smoothing. With general-purpose (i.e., broad-spectrum) applications, symmetric filters are superior in almost every way. However, because they require data from the "future", they can be more difficult to implement. Nonetheless, (short) symmetric filters can be realized in near-real-time with fast digital processors or analog delay loops.

Symmetric Structure A brief, but useful, analysis of symmetric structure can be obtained with a Taylor's series analysis. To begin, the Taylor's series expansion for the function $f(t)$ about $t=0$ is:

$$(C.4) \quad f(h) = \sum_{k=0}^{\infty} \frac{1}{k!} f^{(k)}(0) h^k$$

where $f^{(k)}(0)$ is the k -th derivative at 0. Of some importance is that odd derivatives cancel when $f(h)$ and $f(-h)$ are averaged:

$$(C.5) \quad \begin{aligned} \frac{1}{2} [f(h)+f(-h)] &= \sum_{k=0}^{\infty} \frac{1}{(2k)!} f^{(2k)}(0) h^{2k} \\ &= f(0) + \frac{1}{2} f^{(2)}(0) h^2 + O(h^4) \end{aligned}$$

where $O(t)$ is the notation used in Sec. 10. Observe that (C.5) can be computed to about the same level accuracy as (C.4), with only half the computation, and shows the great utility of symmetric formulas in numerical procedures.

Next, solving for $f(0)$ gives:

$$(C.6) \quad f(0) = \frac{1}{2} [f(h)+f(-h)] - \frac{1}{2} f^{(2)}(0) h^2 - O(h^4),$$

which, in turn, can be converted into a numerical estimate \hat{x}_n of $f(nh)$:

$$(C.7) \quad \hat{x}_n = \frac{1}{2} [x_{n+1} + x_{n-1}] - \frac{1}{2} x_n'' ,$$

where x_n'' is a numerical estimate of $f^{(2)}(nh)$. Note that this is an interpolation formula, provided x_n'' does not depend on x_n .

To continue, a useful filter y_n results by averaging (C.7) with x_n :

$$(C.8) \quad y_n = \frac{x_{n-1} + 2x_n + x_{n-1}}{4} - \frac{1}{4} x_n'' .$$

Appendix C. Digital Filters and Symmetry

Note that if x''_n is set to zero, (C.7) reduces to linear interpolation, and (C.8) reduces to the Hanning filter (C.3).

The more interesting case is when the second derivative is nonzero because then the filter can respond to local curvature. Here numerical estimates x''_n should be exact on cubic polynomials; a standard one is:

$$x''_n = \frac{x_{n+2} - 2x_n + x_{n-2}}{4}$$

When substituted into (C.8), a cubic filter results that is qualitatively similar to more advanced filters developed later (e.g., App. F). Of special importance is the close relationship between interpolation and filtering.

Formal Definition A deeper understanding of filtering procedures requires the **shift operator** \mathcal{E} which denotes translation by one unit. More generally, \mathcal{E}^τ is translation of a time series $x(t)$ by τ units

$$\mathcal{E}^\tau x(t) = x(t+\tau).$$

Positive τ is forward translation, negative τ is backward translation, and $I = \mathcal{E}^0$ is the identity or do-nothing operation. A digital filter, as an operator, can then be represented as weighted sums of shifts. For example, the exponential filter (C.2) can be represented $E_r = (1-r) \sum_{k=0}^{\infty} r^k \mathcal{E}^{-k}$ and the Hanning filter (C.3) is $H = (\mathcal{E}^{-1} + 2I + \mathcal{E})/4$. More generally, a digital filter A is an operator of the form

$$(C.9) \quad A = \sum_k a_k \mathcal{E}^{-k} \quad \Leftrightarrow \quad A[x(t)] = \sum_k a_k x(t-k).$$

where the (possibly complex) weights a_k are called the **filter coefficients**. (When summation limits are omitted, it is understood that sums are over all required integers, positive and/or negative.) Observe that $A[x(t)]$ is evaluated by "moving" the computation with t which, as noted above, is characteristic of convolution. Here, infinite sums must converge (in some sense). Also, we continue to use subscript notations for the discrete case: $x_k = x(k)$ and $A_k[x] = A[x(k)]$.

We next compute the composition of two filters A and B , applied in succession

$$B[A[x(t)]] = B \sum_k a_k x(t-k) = \sum_k a_k B[x(t-k)] = \sum_k a_k \sum_j b_j x(t-k-j)$$

or, letting $n=k+j$

Appendix C. Digital Filters and Symmetry

$$B[A[x(t)]] = \sum_k a_k \sum_n b_{n-k} x(t-n) = \sum_n \left[\sum_k a_k b_{n-k} \right] x(t-n)$$

which is polynomial multiplication, in disguise! Indeed, when polynomials $p(z)$ and $q(z)$ are multiplied, all coefficients of a power of z are grouped together and *summed*. Applied to filters, this means

$$(C.10) \quad A = \sum_k a_k e^{-k} \quad \& \quad B = \sum_k b_k e^{-k} \quad \Rightarrow \quad AB = \sum_n c_n e^{-n}$$

$$\text{where } c_n = \sum_k a_k b_{n-k} = \sum_k a_{n-k} b_k .$$

In particular, polynomial multiplication commutes $AB=BA$, and so, *filter composition and polynomial multiplication are the same thing*. It is, therefore, not surprising that the coefficients c_n are computed using the same convolution rule as (C.9). We remark that c_n , as computed in (C.10), is also known as the Cauchy product, giving convolution yet another name.

Frequency analysis is the principle tool used to study filters. It is a form of spectral analysis based on the complex exponentials $e^{i\omega t} = \cos(\omega t) + i\sin(\omega t)$, where $i = \sqrt{-1}$ is the imaginary unit and ω is the (radian) frequency. In this context, the complex exponentials are called **frequency components**. An important property of digital filters is that they always preserve frequency content; although a filter can delay or annihilate a given component, it cannot generate new ones. More precisely, when a digital filter A is applied to a component $e^{i\omega t}$, there is always some (complex) number, say $\mathcal{R}_A(\omega)$, which depends only on frequency ω so that for all time t

$$(C.11) \quad \boxed{A[e^{i\omega t}] = \mathcal{R}_A(\omega) e^{i\omega t}} .$$

The function $\mathcal{R}_A(\omega)$ is called the **frequency response** of the filter because it completely characterizes what the filter does to the time series $e^{i\omega t}$. In more general contexts, $e^{i\omega t}$ is called an eigenfunction (of the operator A), and $\mathcal{R}_A(\omega)$ is called the eigenvalue.

As a simple example, we compute the response $\mathcal{R}_H(\omega)$ of the Hanning filter

$$(C.12) \quad \begin{aligned} H[e^{i\omega t}] &= \frac{1}{4}(e^{i(t-1)\omega} + 2e^{i\omega t} + e^{i(t+1)\omega}) \\ &= \frac{1}{4}(e^{-i\omega/2} + e^{i\omega/2})^2 e^{i\omega t} \\ &= \cos^2(\omega/2) e^{i\omega t} ; \end{aligned}$$

thus, $\mathcal{R}_H(\omega) = \cos^2(\omega/2)$. It should be observed that complex functions are used

Appendix C. Digital Filters and Symmetry

to expedite computation; by equating real and imaginary parts, the effect of filtering the trigonometric components $\cos(k\omega)$ and $\sin(k\omega)$, as *real* time series, can be inferred; in the present case they are both attenuated by the amount $\mathcal{R}_H(\omega)$.

Closer inspection of the eigenvalue computation reveals that *the frequency response can always be computed by substituting $e^{i\omega}$ for \mathcal{E}* ; thus,

$$(C.13) \quad \boxed{A = \sum_k a_k \mathcal{E}^{-k} \Rightarrow \mathcal{R}_A(\omega) = \sum_k a_k e^{-ik\omega}} .$$

provided that the trigonometric series converges in the usual least-squares sense. For example, the response of the exponential filter, as computed in (C.2), is $\mathcal{R}_E(\omega) = (1-r) \sum_{k=0}^{\infty} r^k e^{-ik\omega}$ and converges insofar as it can be summed as a geometric series

$$(C.14) \quad \mathcal{R}_E(\omega) = \frac{1-r}{1-re^{-i\omega}} = \frac{(1-r)(1-re^{i\omega})}{(1-r)^2 + 4r\sin^2\omega/2} .$$

Unlike (C.12), this response is a complex function. When this happens, it is useful to express it in polar form: $\mathcal{R}(\omega) = |\mathcal{R}(\omega)| e^{i\phi(\omega)}$ where $|\mathcal{R}(\omega)|$ denotes the **amplitude** and $\phi(\omega)$ denotes the **phase** computed as the inverse tangent $\tan^{-1}(\text{Im } \mathcal{R} / \text{Re } \mathcal{R})$ of the imaginary to real parts of $\mathcal{R}(\omega)$. In the present case, $|\mathcal{R}_E(\omega)|^2 = (1-r)^2 / [(1-r)^2 + 4\sin^2\omega/2]$. (Phase computation is usually left to computers.) Note well that *nonzero phase means that components $e^{it\omega}$ are shifted or delayed in time by the amount $\Delta t = -\phi(\omega)/\omega$, that is, $e^{it\omega} e^{i\phi(\omega)} = e^{i(t-\Delta t)\omega}$ ($\omega=0$ excluded). As can be seen from (C.14), the exponential filter E_r delays different frequency components by different amounts, a feature common to *all* predictive filters.*

From the eigenvalue property (C.11), it follows that the response of two filters, applied one after the other, is the product of the responses. But, applying two filters in succession is the same as composition which is also the same as multiplication; thus,

$$(C.15) \quad \boxed{\mathcal{R}_{AB}(\omega) \equiv \mathcal{R}_A(\omega) \mathcal{R}_B(\omega)} .$$

Because, filter multiplication is computed using the convolution rule, this result is generally known as the **convolution theorem**. In the special case when $A = \mathcal{E}$, the identity $\mathcal{R}_{AB}(\omega) \equiv e^{i\omega} \mathcal{R}_B(\omega)$ is known as the **shift theorem**.

To effectively describe symmetry, we need the **operator adjoint** A^* defined on filters A as:

Appendix C. Digital Filters and Symmetry

(C.16)

$$A^* = \sum_k a_k^* \mathcal{E}^k \quad \Leftrightarrow \quad A = \sum_k a_k \mathcal{E}^{-k}$$

where a^* denotes the **complex conjugate** of a . In particular, $\mathcal{E}^* = \mathcal{E}^{-1}$ and the adjoint has the effect of reversing time. Moreover, it is idempotent $A^{**} = A$ and distributes over addition, scalar multiplication, and filter products: $(A+B)^* = A^* + B^*$, $(cA)^* = c^* A^*$, and $(AB)^* = A^* B^*$. Also, it is easily verified that *the response of the adjoint is the conjugate of the response* $\mathcal{R}_{A^*} = \mathcal{R}_A^*$.

To proceed, a filter has **even symmetry** if it is self-adjoint $A^* = A$; examples are filters of the form $(A+A^*)$, $i(A-A^*)$, and AA^* . The Hanning filter (C.3) is an example of even symmetry. A filter has **odd symmetry** if it is skew symmetric $A^* = -A$; examples are filters of the form $A-A^*$, $i(A+A^*)$, and iAA^* . The centered difference $(\mathcal{E} - \mathcal{E}^{-1})$ is an example of odd symmetry. A filter is simply called **symmetric** if it is either even or odd. Symmetric filters are never causal (except for real multiples of the identity) and, conversely, causal filters are never symmetric. Consequently, *symmetry and causality are mutually exclusive concepts*.

Now, the response of a filter with even symmetry is pure real because $\mathcal{R}_A^* = \mathcal{R}_{A^*} = \mathcal{R}_A$, and the response of a filter with odd symmetry is pure imaginary because $\mathcal{R}_A^* = \mathcal{R}_{A^*} = \mathcal{R}_{-A} = -\mathcal{R}_A$. It turns out that the converse is also true because *filter coefficients a_n can be computed as Fourier coefficients of the frequency response*:

$$(C.17) \quad a_n = \frac{1}{2\pi} \int_{-\pi}^{\pi} \mathcal{R}_A(\omega) e^{in\omega} d\omega,$$

provided that this integral is well defined. Thus, if $\mathcal{R}_A(\omega)$ is pure real, then $a_{-n} = a_n^*$, and A has even symmetry; if $\mathcal{R}_A(\omega)$ is pure imaginary, then $a_{-n} = -a_n^*$, and A has odd symmetry.

An important consequence of this is that *no predictive filter can have a frequency response that is either pure real or pure imaginary*. But, smoothing filters are ideally modeled with responses that are pure real, and derivative operators are ideally modeled with responses that are pure imaginary. *Thus, predictive filters used for smoothing and/or differentiation can, and will, create time distortions that cause frequency components to shift and peaks to move around*. By contrast, symmetric filters tend to leave features where they belong.

The superiority of symmetric methods should by now be clear; above results

Appendix C. Digital Filters and Symmetry

are definitive. In closing, we remark that the response map has many properties in addition to those discussed. Suffice it to say that theory generally parallels the Fourier transform.

Appendix D. SAMPLING AND INTERPOLATION

This section deals with more advanced, theoretical aspects of sampling and interpolation. In particular, we show how numerical interpolation can be used to improve on Shannon's Sampling Theorem. Results are then applied to obtain an "optimal" class of filters, especially well suited to data acquisition. Finally, a solution of the computational aliasing problem discussed in Sec. 11 is presented.

Analog Prefilters Because analog filters are implemented in real time they are predictive and spoilers of symmetry. The question arises, "Can we do without them?" Here, theory supplies a definitive answer. Basically, what is needed is an ideal, low pass filter that restricts frequency content to an interval of the form $[-\Omega, \Omega]$; more precisely, we need a frequency response $\mathcal{R}_\Omega(\omega)$ that satisfies

$$(D.1) \quad \mathcal{R}_\Omega(\omega) = \begin{cases} 1, & |\omega| < \Omega \\ 0, & |\omega| > \Omega \end{cases}$$

The value of $\mathcal{R}_\Omega(\omega)$ at $\omega = \Omega$ is left indeterminate. Filters of this kind are called **band limited** and the interval $[-\Omega, \Omega]$ is called the **passband** of the filter; likewise, the region of zero response is called the **stopband** (with practical methods there is a transition region as well). Now, it turns out that *band-limited filters do not have digital representations*. Instead, the corresponding time-domain filter \mathcal{P}_Ω must be realized as an integral operator

$$(D.2) \quad \mathcal{P}_\Omega[x(t)] = \int_{-\infty}^{\infty} \frac{\sin \Omega(t-s)}{\pi(t-s)} x(s) ds$$

which is again recognized as convolution, but for a continuous variable. Note that \mathcal{P}_Ω is also a projection operator, that is, it is idempotent $\mathcal{P}_\Omega^2 = \mathcal{P}_\Omega$ and symmetric (also, self-adjoint) $\mathcal{P}_\Omega^* = \mathcal{P}_\Omega$; in other words, applying \mathcal{P}_Ω twice gives the same answer as does reversing time.

For present purposes, the operator \mathcal{P}_Ω is the theoretical counterpart of an analog prefilter. Because it does not have a digital representation, analog filters cannot be replaced with digital ones. For data sampled at regular intervals, the only recourse is to sample above the frequency response of the instrument or sensor; however, in this situation, the sensor is implicitly functioning as an analog filter anyway and little has changed. We therefore conclude that *analog prefilters are a necessary part of sampling any*

Appendix D. Sampling and Interpolation

continuous process. Also, it is worth remarking that phase distortion produced by an analog prefilter can, in principle, be removed in post processing by running a matched digital filter backwards in time. Although this is seldom done, it is a procedure of practical value.

Interpolation A good place to start is with Shannon's Sampling Theorem (Hamming, 1977, p. 135) which gives a criterion for data to be correctly sampled; basically, it says that *unaliased time series can always be interpolated.* More precisely, if $x_k = x(k)$ is a sample of a (weakly stationary) process $x(t)$, then $x(t)$ can be reconstructed from the interpolation:

$$(D.3) \quad x(t) = \sum_{k=-\infty}^{\infty} \frac{\sin \pi(t-k)}{\pi(t-k)} x_k$$

provided that data is unaliased. Here, convergence is in the least-squares sense, like a Fourier series. Observe that this formula requires bi-infinite data x_k from both the past and the "future." By contrast, there is no analogous predictive formula that uses data only from the past (and/or present).

An important special case is for interpolation to midpoints $t=n+1/2$; in this case, (D.3) simplifies to

$$(D.4) \quad x_{n+1/2} = \frac{2}{\pi} \sum_{k=0}^{\infty} \frac{(-1)^k}{2k+1} [x_{n+k+1} + x_{n+k}] .$$

Note that for constant data x , the interpolate \hat{x} must be the same and (D.4) reduces to the well-known expression: $\pi/4 \sum_{k=0}^{\infty} (-1)^k / (2k+1)$. Unfortunately, the series (D.4) converges very slowly and is not very useful in practice. Nonetheless, it has value in its structure, and practical methods that share this structure tend to be of high quality. In this regard, **Bessel's midpoint interpolation** is one of the best; for an index p , it interpolates polynomials of degree $2p-1$ to midpoints as

$$(D.5) \quad \hat{x}_{n+1/2} = \sum_{k=0}^{p-1} c_{p,k} \frac{(-1)^k}{2k+1} [x_{n+k+1} + x_{n+k}]$$

where the $c_{p,k}$ are weights, expressed in terms of binomial coefficients as

$$c_{p,k} = \frac{p}{4^{2p-1}} \binom{2p}{p} \binom{2p-1}{p-k-1} ; k=1,2,\dots,p-1.$$

Examples

Appendix D. Sampling and Interpolation

$$p=1, \text{ Linear: } \hat{x}_{1/2} = [x_0 + x_1]/2$$

$$p=2, \text{ Cubic: } \hat{x}_{1/2} = [9(x_0 + x_1) - (x_{-1} + x_2)]/16$$

$$p=3, \text{ Quintic: } \hat{x}_{1/2} = [150(x_0 + x_1) - 25(x_{-1} + x_2) + 3(x_{-2} + x_3)]/256$$

We remark that in the limit as $p \rightarrow \infty$, Bessel's formula (D.5) converges to the "ideal" value (D.4); this limit, therefore, provides a different convergence pattern to the same final answer. Additionally, it converges in situations where (D.4) does not (e.g., polynomials), and can be viewed as a generalization of the sampling theorem to a broader (nonstationary) class of functions and processes.

We observe that the basic difference between (D.3) and (D.4) are the weighting coefficients $c_{p,k}$ which impart a Gaussian-like taper to the troublesome term $1/(2k+1)$. This taper is evident in Table D-1 which shows total values of $b_{p,k} = (-1)^k c_{p,k} / (2k+1)$ for even values of p .

$k \setminus$	$b_{2,k}$	$b_{4,k}$	$b_{6,k}$	$b_{8,k}$	$b_{10,k}$
0	0.5625000	0.5981445	0.6106682	0.6170455	0.6209080
1	-0.0625000	-0.1196289	-0.1453972	-0.1599748	-0.1693386
2		0.0239258	0.0436192	0.0575909	0.0677354
3		-0.0024414	-0.0103855	-0.0186983	-0.0260521
4			0.0016155	0.0048477	0.0086840
5			-0.0001202	-0.0009153	-0.0023684
6				0.0001106	0.0005010
7				-0.0000064	-0.0000766
8					0.0000075
9					-0.0000004

Table D-1. Coefficients for Bessel's midpoint interpolation.

Note that the top row $b_{p,0}$ is converging to $2/\pi = 0.6366198$ and can be used as a measure of how well (D.5) approximates the ideal (D.4).

Next, because single-precision (23-bit mantissa) arithmetic has about seven significant digits of precision, we see that there is a practical limit on the order of this interpolation; indeed, for $p \geq 10$, the smallest coefficients get lost in roundoff error and further increasing p could actually result in loss of precision. We therefore conclude that interpolation corresponding to $p=8$ is about optimal for single-precision arithmetic. (A more precise answer requires numerical simulations for specific applications.)

Half-band Filters An ideal low pass filter that *reduces* the passband to $\Delta < \pi$ has a frequency response $\mathcal{R}_\Delta(\omega)$ defined

Appendix D. Sampling and Interpolation

$$(D.6) \quad \mathcal{R}_\Lambda(\omega) = \begin{cases} 1, & 0 \leq |\omega| < \Lambda \\ 0, & \Lambda < |\omega| \leq \pi \end{cases} .$$

Here, $\mathcal{R}_\Lambda(\omega)$ is extended to the rest of the real line by periodicity, and is *not* band limited. It turns out that periodicity is a necessary condition for filter to have a digital representation; in the present case, straightforward computation using (C.13) shows:

$$(D.7) \quad \boxed{P_\Lambda = \frac{\Lambda}{\pi} \left[I + \sum_{k>0} \frac{\sin k\Lambda}{k\Lambda} (e^{k\Lambda} + e^{-k\Lambda}) \right]}$$

As above, P_Λ is a projection operator.

A half-band filter is then obtained by setting $\Lambda = \pi/2$, and another calculation shows that $y_n = P_{\pi/2, n}[x]$ simplifies to:

$$(D.8) \quad y_n = \frac{1}{2} \left\{ x_n + \frac{2}{\pi} \sum_{k=0}^{\infty} \frac{(-1)^k}{2k+1} [x_{n+2k+1} + x_{n-2k-1}] \right\} ,$$

What is remarkable is that the sum in brackets is the same midpoint interpolate \hat{x} as (D.4) above, except that now it is computed from a subsample consisting of every other point. This result is of considerable value in application; it shows how to approximate ideal, half-band filters. For present purposes, we approximate (D.8) with polynomial filters $y_n^{(p)}$ of degree $2p-1$ defined:

$$(D.9) \quad \boxed{y_n^{(p)} = (x_n + \tilde{x}_n^{(p)})/2}$$

where $\tilde{x}_n^{(p)}$ denotes the $2p-1$ order Bessel interpolation (D.5) applied to the subsample $\{x_{n+2k}\}$ consisting of every other point. For example, when the first Bessel interpolation $\tilde{x}_n^{(1)} = (x_{n-1} + x_{n+1})/2$ is used, we get the Hanning filter (C.3).

More generally, response curves for higher-order interpolation filters are shown in Fig.D-1 for $p=1,2,4,8,16,32$. In all cases the responses $\mathcal{R}^{(p)}(\omega)$ are unity at $\omega=0$ and zero at $\omega=\pi$. Additionally, curves are monotone decreasing and "skew symmetric" about $\omega=\pi/2$, that is:

$$(D.10) \quad \mathcal{R}^{(p)}(\pi/2-\epsilon) + \mathcal{R}^{(p)}(\pi/2+\epsilon) = 1 .$$

"Optimal" Data-Acquisition For application to data acquisition, data is

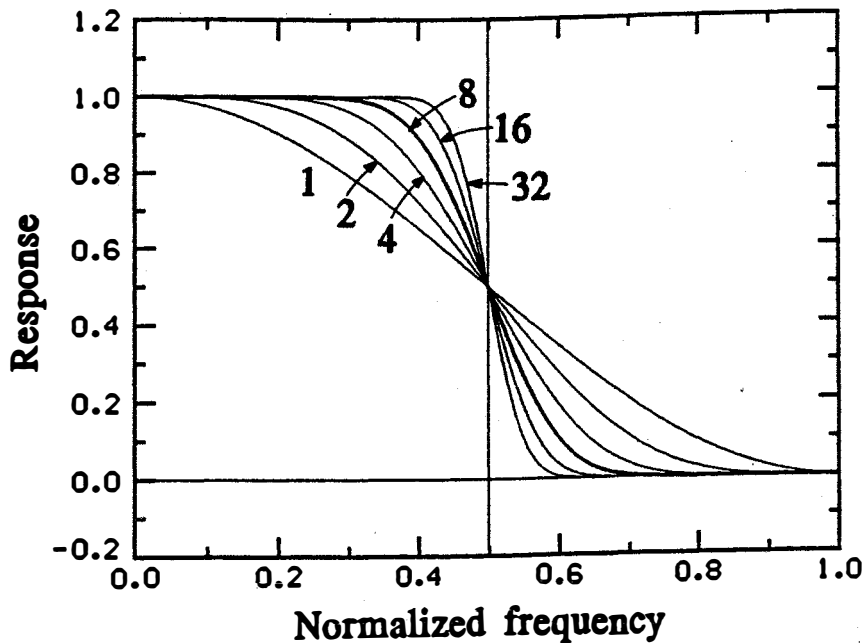


Fig. D-1. Response curves for "ideal" higher-order Bessel interpolation passband filters, with $p=1, 2, 4, 8, 16, 32$.

prefiltered with a half-band filter (D.9), and then subsampled to every other point. We argue that this decimation procedure is well suited, if not optimal, for scientific application. First, as noted above, the passband is monotone which is important because otherwise there would be peaks or ripples that could get passed on to acquired data, leading to confusion. Second, because these filters vanish at multiples of $\omega=\pi$, folding does not corrupt the DC component ($\omega=0$). (See Sec. 11.)

But filters with these properties can be obtained in many ways, so "What makes those of (D.9) so special?" The answer is that they are polynomial filters, and *polynomials are exceptionally well suited to data acquisition because they are invariant to subsampling*. In other words, any (regular) subsample of a polynomial of degree n is another polynomial sample with the same degree. By contrast, trigonometric functions do not share this property.

In addition, the filters $y_n^{(p)}$ of (D.9) are qualitatively similar to the ideal half-band filter (D.8), and converge to the ideal filter as $p \rightarrow \infty$.

Appendix D. Sampling and Interpolation

Finally, it is easy to prove that any other polynomial filters with the above properties and having the same number of coefficients would be the same. Consequently, the filters (D.9) are unique, therefore optimal, by this set of standards.

Another way to judge a data-acquisition filter is by what it does to white noise. In this situation, decimation procedures should preserve the white-noise property (at least in the mean). However, for this to be true the response $\mathcal{A}(\omega)$ of a symmetric filter A would have to satisfy:

$$(D.11) \quad [\mathcal{A}(\pi/2-\varepsilon)]^2 + [\mathcal{A}(\pi/2+\varepsilon)]^2 = 1 .$$

in contradiction to (D.10). To better understand this condition, we model a white noise sample as having constant power which is the same as having constant (real) amplitude c and random phase. Thus, components sampled at radian frequencies $\omega=\pi/2-\varepsilon$ and $\omega=\pi/2+\varepsilon$ have complex form $ce^{i\phi}$ and $ce^{i\psi}$. After filtering and subsampling, the $\omega=\pi/2+\varepsilon$ component folds back to $\omega=\pi/2-\varepsilon$, and the complex amplitude is

$$a(\pi/2-\varepsilon) = c[\mathcal{A}(\pi/2-\varepsilon)e^{i\phi} + \mathcal{A}(\pi/2+\varepsilon)e^{i\psi}] .$$

In turn, power is proportional to the amplitude squared:

$$|a(\pi/2-\varepsilon)|^2 = c^2[\mathcal{A}^2(\pi/2-\varepsilon) + \mathcal{A}^2(\pi/2+\varepsilon) + 2\mathcal{A}(\pi/2-\varepsilon)\mathcal{A}(\pi/2+\varepsilon)\cos(\phi-\psi)].$$

Finally, if \mathbf{E} is the expectation over all such samples, that is, over all possible ϕ and ψ , we get

$$\mathbf{E}|a(\pi/2-\varepsilon)|^2 = c^2[\mathcal{A}^2(\pi/2-\varepsilon) + \mathcal{A}^2(\pi/2+\varepsilon)]$$

and so $\mathbf{E}|a(\pi/2-\varepsilon)|^2 = c^2$ as claimed when (D.11) is satisfied, showing that decimation preserves the white-noise property.

By contrast, this same analysis applied to the filters $\mathcal{R}^{(p)}$ results in the equation:

$$\mathbf{E}|a(\pi/2-\varepsilon)|^2 = c^2[r^2 + (1-r)^2]$$

where $r = \mathcal{R}^{(p)}(\pi/2-\varepsilon)$. We remark that for application to spectral analysis, this curve can be used to "calibrate" a power spectrum so that white noise will, indeed, appear white (at least in the mean).

So which are better, polynomial filters or filters that preserve white noise? We cannot have both. In this regard, choosing a filter based on what it does to noise is a dubious criterion. Moreover, it is not difficult to show that such filters are inconsistent with the ideal filter (D.8) at the sampling

Appendix D. Sampling and Interpolation

frequency $\omega=\pi/2$, even in the limit. We conclude that such filters are of limited value in data-acquisition procedures.

Application to Computational Aliasing In Sec. 11 we saw that when two time series are multiplied together, sum and difference frequencies result. On a discrete grid, higher frequencies cannot be accurately resolved, and they fold back to lower frequencies, creating a distortion. So what, if anything, can be done? *The key observation is that continuous time series $\hat{x}(t)$ and $\hat{y}(t)$ can be recovered using the Sampling Theorem (D.3); once done, the aliasing associated with multiplication goes away. However, continuous interpolation is a theoretical ideal, and the practical question is, "How much is really needed?" It turns out that interpolation to midpoints is enough. This is because midpoint interpolation doubles the number of grid points and, in so doing, doubles the number of frequencies that can be resolved. At the same time, multiplication also doubles frequency content. Thus, *midpoint interpolation is the minimum amount required to avoid aliasing from multiplication.* For example, consider the sequence $(1, -1, 1, -1, \dots)$ sampled at the folding frequency; then squaring gives a constant sequence which is nonsense. By contrast, interpolation will yield 0 at midpoints resulting in the new sequence $(1, 0, -1, 0, \dots)$; now squaring gives a meaningful answer.*

In summary, multiplicative aliasing can be controlled by (I) interpolating to midpoints, (II) multiplying the interpolated time series, and (III) decimating the answer back to the grid we started from. Because practical methods are never ideal, some aliasing will result, the extent of which can be controlled with higher-order methods. More complicated nonlinearities will generally not have such explicit solutions. Nonetheless, they are still amenable to the same scheme, but may need to be "tuned" with numerical simulations. All things considered, this is a most satisfactory solution, both in theory and in practice.

Some Operator Identities The utility and power of above theory can only be fully appreciated in the context of operators. Although time and space do not permit a full treatment of this elegant topic, we here outline central results; in particular, we show one way to derive the Bessel formula (D.5). To begin, we borrow the notations μ and δ from classical numerical analysis to denote the mean and difference operators: $\mu=(e^{1/2}+e^{-1/2})/2$ and $\delta=e^{1/2}-e^{-1/2}$ which have frequency responses: $\cos \omega/2$ and $2i \sin \omega/2$, making it easy to convert, back and forth, between operator identities and trigonometric ones. For application to polynomial theory, the important observation is that the

Appendix D. Sampling and Interpolation

iterated operator δ^p annihilates polynomials of degree $p-1$ (or less).

The first identity of importance is:

$$(D.12) \quad \frac{\mu}{\sqrt{1+\delta^2/2}} = \mu \sum_{k=0}^{\infty} (-1)^k \beta_k \left[\frac{\delta}{2} \right]^{2k}$$

where β_k is expressed in terms of binomial coefficients as $\beta_k = \frac{1}{2^{2k}} \binom{2k}{k}$. Note that this identity is derived from the Taylor's series expansion of $(1+x)^{-1/2}$. Also, because $\cos^2 \omega/2 + \sin^2 \omega/2 = 1$, there is a corresponding operator identity: $\mu^2 - \delta^2/2 = I$, and (D.12) can be interpreted as converging to the identity operator I . A useful interpretation of (D.12) is that the infinite series is undoing or deconvolving the averaging operator μ .

When (D.12) is truncated at $k=p-1$, the resulting operator, say B_p , is exact on polynomials of degree $2p-1$:

$$(D.13) \quad B^{(p)} = \mu \sum_{k=0}^{p-1} (-1)^k \beta_k \left[\frac{\delta^{1/2} \delta^{-1/2}}{2} \right]^{2k},$$

and has response $\cos(\omega/2) \sum_{k=0}^{p-1} \beta_k \sin^{2k}(\omega/2)$. Although not obvious, (D.12) is equivalent to Bessel's interpolation (D.5). One way to establish this is to show that the frequency responses of (D.5) and (D.13) are both equivalent to:

$$(D.14) \quad \mathcal{B}^{(p)}(\omega) \equiv 1 - 2p \beta_p \int_0^{\omega/2} \sin^{2p-1} \alpha \, d\alpha,$$

which also shows that Bessel's midpoint interpolation is maximally flat at $\omega=0$. This is a lengthy computation, requiring the following intermediate identity (easily verified in operator form):

$$(D.15) \quad \sin^{2p-1}(\omega/2) \equiv \frac{-1}{4^{p-1}} \sum_{k=1}^p (-1)^k \binom{2p-1}{p-k} \sin(2k-1)\omega/2,$$

[Hint: differentiate (D.14) and the response of (D.5), then sum; also integrate (D.14) by parts to get the response of (D.13).]

Finally, we present an important identity for the optimal filter of (D.9), that is, for the operator $I^{(p)} = (I + \tilde{B}^{(p)})/2$ where $\tilde{B}^{(p)}$ is the Bessel operator $B^{(p)}$ applied to every other point. Observe from (D.13) that

$$(D.16) \quad \tilde{\mathcal{B}}^{(p)}(\omega) \equiv \mathcal{B}^{(p)}(2\omega) \equiv \cos \omega \sum_{k=0}^{p-1} \beta_k \sin^{2k} \omega$$

Appendix D. Sampling and Interpolation

The following identity for the frequency response $\mathcal{F}^{(p)}(\omega)$ of the operator $I^{(p)}$ can then be established with a straightforward, but tedious, proof by induction:

$$(D.17) \quad \mathcal{F}^{(p)}(\omega) \equiv \cos^{2p}(\omega/2) \sum_{k=0}^{p-1} \binom{p+k-1}{k} \sin^{2k} \omega/2 ; p \geq 1.$$

Observe that the frequency response is parameterized with ω in (D.15), but changes to $\omega/2$ in (D.17). Implicitly, this identity shows that the filters are maximally flat at $\omega=0$.

The practical significance of (D.17) is that optimal filters can always be factored. For $p=1$, $I^{(1)}$ is the Hanning filter with frequency response $\mathcal{F}^{(1)}(\omega) = \cos^2(\omega/2)$. For $p=2$, the filter $I^{(p)}$ can be factored

$$I^{(2)} = \left[\frac{\mathcal{E} + 2I + \mathcal{E}^{-1}}{4} \right]^2 \left[\frac{-\mathcal{E} + 4I - \mathcal{E}^{-1}}{2} \right]$$

which is the composition of the square of the Hanning filter with another symmetric operator. More generally, the p -th power of the Hanning filter can always be factored out of $I^{(p)}$; the remaining filter can then be further factored into "quadratic" terms: $aI + b(\mathcal{E} + \mathcal{E}^{-1}) + c(\mathcal{E}^2 + \mathcal{E}^{-2})$ with real coefficients a , b , and c .

Appendix E. ENHANCED TRIANGLE FILTERS

The purpose of this appendix is to discuss a class of high-quality, low-pass filters capable of isolating or separating out slowly moving trends (see Oppenheim and Schaffer, 1975, and Leise, 1981). Because such trends can often be modeled as polynomials, filters that leave polynomials unchanged are a good choice. Formally, **polynomial filters** are characterized as leaving invariant all polynomials of a given degree (or less). To make this mathematically precise, we introduce the notation \mathbf{k}^P to denote the bifinite sequence of integers raised to the power p :

$$(E.1) \quad \mathbf{k}^P = (\dots, (-k)^P, (-k+1)^P, \dots, -1, 0, 1, \dots, (k)^P, (k+1)^P, \dots) .$$

Otherwise said, \mathbf{k}^P is the discrete analog of the continuous monomial $x(t)=t^P$. In this context, *necessary and sufficient conditions for a filter F to be a polynomial filter of degree n are:*

$$(E.2) \quad \boxed{F[\mathbf{k}^P] = \mathbf{k}^P ; p=0,1,2,\dots,n} ,$$

and we can now begin to appreciate the significance of polynomial filters; *they have (low order) monomials \mathbf{k}^P as an additional set of eigenvectors.* More generally, all (low-order) polynomials are eigenvectors; however, monomials are linearly independent, like the complex eigenfunctions $e^{i\omega t}$, and deserve emphasis.

Our approach here is to compute symmetric, polynomial filters from triangle filters. There are several reasons for doing this: (I) we are familiar with triangle filters from Sec. 11, (II) frequency analysis is straightforward, and (III) triangle filters are very efficient to implement.

Our first task is to understand the mechanics of making triangle filters into polynomial filters. In Sec. 11 we learned that triangle filters T_N with a single vertex always have odd length ($N=2L-1$) and can be represented as the filter product $T_N=R_L^2$ where R_L is the (centered) running average of length L . Because the notation T_{2L-1} is somewhat unwieldy, we shall omit subscripts when context is clear. In any case, the present goal is to find a correction filter, say, C for which the filter product $P=TC$ is a polynomial filter. It is useful to represent this correction as follows:

$$(E.3) \quad C \cong \sum_k c_{2k} \delta_h^{2k}$$

where $\delta_h = e^{h/2} - e^{-h/2}$ is the centered difference operator for step size h .

Appendix E. Enhanced Triangle Filters.

This representation is analogous to a Taylor-series expansion; its principle advantage is that powers of δ_h annihilate low-order polynomials. To continue, note that the eigenfunction conditions (E.2) completely determine the unknown coefficients c_{2k} ; specifically, polynomial filters of degree $2n+1$ are completely determined by the following system of equations:

$$(E.4) \quad \sum_{k=0}^n c_{2k} T_0 \delta_h^{2k} [k^p] = 0 ; p=0, 2, 4, \dots, 2n$$

where, consistent with our simplified notation, $T_0 = T_{2L-1,0}$ is the filtered value at time $t=0$. Additionally, because $\delta_h^{2k} [k^p] = 0$ for $2k > p$, the system (E.4) decouples and the unknowns c_{2k} can be computed recursively; in particular, the c_{2k} are independent of n .

Note that triangle filters are already polynomial filters of degree one, and so $c_0 = 1$. However, other constants must be computed. To begin, we let $m_L^{(p)} = T_0 [k^p]$ denote the p -th moment of the triangle filter $T = T_{2L-1}$. Clearly, these moments vanish when p is odd, and when p is even they satisfy:

$$(E.5) \quad m_L^{(p)} = \frac{2}{L^2} \sum_{k=1}^{L-1} k^p (L-k)$$

Required sums $\sum_k k^r$ can be found in tables, and the first few values of $m_L^{(p)}$ can be shown to be:

$$(E.6) \quad m_L^{(0)} = 1; \quad m_L^{(2)} = (L^2 - 1)/6; \quad m_L^{(4)} = (L^2 - 1)(2L^2 - 3)/30$$

Computation of $\delta_h^{2k} [k^p]$ is a tedious but straightforward task which we leave to the reader; some low-order results are:

$$(E.7) \quad \delta_h^2 [k^2] = 2h^2 k^0; \quad \delta_h^2 [k^4] = 2h^4 k^0 + 12h^2 k^2; \quad \delta_h^4 [k^4] = 24h^4 k^0$$

With this background, we can now compute c_2 from (E.4)

$$(E.8) \quad \begin{aligned} T_0 [k^2] + c_2 T_0 \delta_h^2 [k^2] &= 0 \\ \Leftrightarrow m_L^{(2)} + 2h^2 c_2 m_L^{(0)} &= 0 \\ \Leftrightarrow c_2 &= -m_L^{(2)} / (2h^2 m_L^{(0)}) \\ &= -(L^2 - 1) / (12h^2) \end{aligned}$$

To emphasize the dependence on L , we here change notation to $c_L = -c_2$, in which case the cubic filter can be written:

Appendix E. Enhanced Triangle Filters.

$$(E.9) \quad \boxed{P_L^{(3)} = T_{2L-1}(I - c_L \delta_h^2); \quad c_L = (L^2 - 1)/(12h^2)} .$$

Now, it turns out that such filters can be improved through factorization; in the present case, we use the identity: $T_{4L-1} \equiv \mu_L^2 T_{2L-1}$ where $\mu_h = \frac{1}{2}(\mathcal{E}^{h/2} + \mathcal{E}^{-h/2})$ is the averaging operator for step size h . We then observe that if μ_L^2 and T_{2L-1} are independently enhanced to become cubic filters, the resulting composition $Q_{2L}^{(3)}$ is be another cubic filter with improved characteristics. It is a straightforward exercise to show:

$$(E.10) \quad \boxed{Q_{2L}^{(3)} = T_{4L-1} (I - \frac{1}{4} \delta_L^2) (I - c_L \delta_h^2)} .$$

To complete this discussion, we need a condition on h . The answer is to choose h at about half the size of L ; more precisely $h = [(L+1)/2]$ where square brackets here denote integer truncation. Insight into this choice can be obtained by analyzing the cubic filter for the cases $L=2$ and $L=3$.

The Triangle-Filter Algorithm Knowing how the triangle filter is implemented is part of understanding its limitations. Here, $T_{2L-1}[x]$ is computed with a double integration of $\delta_L^2[x]$ based on the identity:

$$(E.11) \quad \boxed{(\delta_L/L)^2 \equiv \delta_1^2 T_{2L-1}} .$$

(Remember that T_{2L-1} is also normalized by L^2 .) For example, with $L=3$ this is the same as the polynomial identity:

$$\mathcal{E}^3 - 2I + \mathcal{E}^{-3} \equiv (\mathcal{E} - 2I + \mathcal{E}^{-1})(\mathcal{E}^2 + 2\mathcal{E} + 3I + 2\mathcal{E}^{-1} + \mathcal{E}^{-2}) .$$

Again, we revert to our simplified notation $T_k[x] = T_{2L-1, k}[x]$ and define differences $D_k[x] = T_k[x] - T_{k-1}[x]$; because $\delta_L^2[x]$ is considered as already computed, the double integration takes the form:

$$(E.12) \quad \begin{aligned} D_k[x] &= D_{k-1}[x] + \frac{1}{L^2} \delta_{L, k-1}^2[x] \\ T_k[x] &= T_{k-1}[x] + D_{k-1}[x] \end{aligned} .$$

and $T_k[x]$ can be recursively computed from initial values $T_0[x]$ and $D_0[x]$.

A shortcoming of this integration is that it tends to propagate roundoff error generated in the computation of $\delta_L^2[x]$ and cannot be reversed. (Recall from statistics that integrating a white noise process, such as roundoff

Appendix E. Enhanced Triangle Filters.

error, generates a random walk with infinite variance.) The computer algorithm presented in the next appendix uses an error-correction procedure to help control this problem.

The Composite Filter By now it should be evident that algorithms discussed are all well suited to machine implementation. Rather than trying to design or force a filter to a given set of specifications, we have pursued methods of exceptional performance. Our design strategy is to construct high-quality algorithms from a collection of finely tuned parts. Our present goal is to complete this task.

Without further distraction, the low-pass filter of interest, say, F_L approximately satisfies $F_L \cong Q_{2L}^{(3)} P_L^{(3)}$ where $Q_{2L}^{(3)}$ controls the shape of the passband while $P_L^{(3)}$ reduces the size of the stopband. This would be the answer except for the presence of a rather large lobe (about 20 dB); to reduce it, we modify $P_L^{(3)}$ to obtain another cubic filter, here denoted $R_L^{(3)}$. This computation is rather technical and not very informative. Consequently, we simply state final formulas:

$$(E.13) \quad F_L = Q_{2L}^{(3)} R_{2H}^{(3)}; \quad H = [(L+1)/2]$$

$$Q_{2L}^{(3)} = T_{4L-1} \left(I - \frac{1}{4} \delta_L^2 \right) (I - c_L \delta_H^2); \quad c_L = (L^2 - 1)/(12H^2)$$

$$R_{2H}^{(3)} = T_{4H-1} \frac{1}{3} (\mathcal{E}^H + I + \mathcal{E}^{-H}) (I - d_H \delta_H^2); \quad d_H = \frac{1}{3} + (4H^2 - 1)/(12H^2)$$

which form the basis of the computer algorithm presented next.

Appendix F. A MIRROR-IMAGE FILTER ALGORITHM

We here apply the computations of App. E to construct a useful algorithm. Because the formulas for F_L of (E.13) are complicated and not very intuitive, this algorithm is better understood by its properties and here the following list speaks for itself:

Properties of F_L

- (1) Symmetric (no phase shifting).
- (2) Mirror-image extension.
- (3) Multidimensional.
- (4) Cubic filter (good with trends).
- (5) First-order approximation: $F_L \cong T_{4L-1}$
- (6) Versatile (a different filter for each L).
- (7) Small lobes (40 dB = 2 decimal digits).
- (8) Requires no additional array space.
- (9) Very efficient ($\cong 7N$ multiplications).
- (10) Easy to use (minimal preparation).

Note, however, that round-off error can be a problem with large arrays. This difficulty, and ways around it, are discussed in some detail below.

The computer code that implements F_L consists of the following four FORTRAN subroutines listed in Figs. F-1 through F-4.

```
SUBROUTINE CMIR3(Y,N1,N2,N3,LNTH1,LNTH2,LNTH3)
SUBROUTINE CMIR1(Y,NY,LNTH,JUMP)
SUBROUTINE TANGLE(Y,NY,LNTH,JUMP)
SUBROUTINE MIRROR(Y,NY,COEFF,LSTEP,JUMP)
```

Note that JUMP is not a user parameter; rather, it is a bookkeeping parameter for multidimensional arithmetic. It should be set to unity for use with time series. (See the listings for an explanation of other parameters used in the calling sequences.) For technical reasons these subroutines are discussed in reverse order.

Subroutine MIRROR This is the core algorithm used to implement the mirror-image filter:

$$(F.1) \quad M_L = \mathcal{E}^L + cI + \mathcal{E}^{-L}$$

without additional array space. Here $c=COEFF$ is a specified constant and $L=LSTEP$ is a given step parameter. The idea is to replace a given time series x with the computed answer $M_L[x]$ (like an FFT) and, in so doing, circumvent

Appendix F. A Mirror-Image Filter Algorithm

the need for additional memory. The trick is to calculate and update $x_k \rightarrow x_{k+L}$ along (mirror-image) equivalence classes $\text{MOD}(L)$. Unfortunately, explicit details are intricate and beyond the scope of this outline. Nonetheless, it is an algorithm that can safely be used as a "black box."

Subroutine TANGLE This subroutine implements the double integration (E.12) for the triangle filter. Here the second difference δ_L^2 is computed using the mirror-image filter M_L with $c=-2$. The important insight is that by integrating mirror-image values, the triangle filter also becomes a mirror-image algorithm as well.

As previously noted, integration tends to propagate roundoff error. To control such errors, two integrations are performed from the center of a time series outward, toward both boundaries. In turn, errors at the boundaries are then computed (by comparison with exact, mirror-image values) and a correction step is employed that removes much of it. The net effect is to integrate, both forward and backward in time, and weight the respective answers by their distances from computed initial data. In addition, all initializations, integrations, and error corrections are done with double-precision (64 bit), floating-point arithmetic.

Subroutine CMIR1 This subroutine implements the formulas (E.13). Recall that one triangle filter is used to control the shape of the passband while another is used to control the stopband. This composition is then enhanced to become a cubic polynomial filter, and an additional lobe-reduction step is used to attenuate lobes to about 40 dB. The next result is a mirror-image filter that is exact on cubic polynomials (boundary regions excluded) and requires no additional array space.

CMIR1 only requires about $7N$ multiplications for an array $Y(N)$ of length N . Consequently, this is an $O(N)$ procedure; by contrast, the FFT is an $O(N \log N)$ procedure. It is worth remarking, however, that with the widespread use of math coprocessors, multiplication is not much more expensive than any other operation. Thus, multiplication can be misleading as an indicator of speed.

Finally, to implement CMIR1, An adjustable length parameter LNTN is passed to the subroutine to control the passband of the filter. The LNTN parameter has a linear effect; when LNTN is doubled, the passband is halved. For example, operating the filter on an array of 1-Hz time series data with LNTN set to 5 will result in data with periods of approximately 25 seconds or longer being passed; for LNTN=10, only data with periods of 50 seconds or

Appendix F. A Mirror-Image Filter Algorithm

longer are passed. When using data averaged into 10-second bins, as in the vertical wind computation, the above figures are multiplied by a factor of 10 (see Fig. 14-4 for the filter's response curve in this case).

Subroutine CMIR3 This is a multidimensional driver for subroutine CMIR1. Implementation is by the method of lines, that is, CMIR1 is applied to all lines, in all directions. The amount of filtering in different dimensions can be controlled with the length parameters LNTH1, LNTH2, and LNTH3. Although this code is only configured for three dimensions or less, it is easily modified to more.

Because CMIR3 inherits properties from CMIR1, it is also a mirror-image algorithm and reproduces cubic multinomials (away from boundaries). We remark that the mirror-image extension is especially useful in higher dimensions; it unfolds in such a way as to produce continuous extensions to infinity, in all directions. Also, all multidimensional, convolution procedures commute with one another, simplifying both theory and application.

Roundoff Error Even with the error-correction used in TANGLE, roundoff error is a potential problem with large arrays. Error can, however, be monitored and/or controlled with a correction procedure. With notation as above, correction consists of first computing $y_n = F_{L,n}[x]$, then the difference $\varepsilon_n = x_n - y_n$, and finally the corrected values $z_n = y_n + F_{L,n}[\varepsilon]$. In operator form this is the filter $G_L = F_L + F_L(I - F_L)$. Note that effects of roundoff error will show up as a low-frequency trend in the difference $\varepsilon_n = x_n - y_n$. In turn, such error is captured in $F_L[\varepsilon]$ which, when added back, corrects most of the problem. (The reader is referred to App.G for more discussion on iterations of this kind.)

Another benefit of this correction is that it improves the frequency response, and converts the cubic filter into a sixth-order one. (However, lobes are increased by about 3 dB.) Because of the improved accuracy, it is used with P-3 data in the computation of vertical winds. Note that this procedure requires additional storage (not necessarily array space) to compute $F_L[\varepsilon]$. In any case, the author has not observed roundoff error to be a significant problem with array sizes up to about 4K (the largest used in P-3 processing).

Appendix F. A Mirror-Image Filter Algorithm

```

SUBROUTINE CMIR3(Y,N1,N2,N3,LNTH1,LNTH2,LNTH3)
C *****Jim Leise 2/88
C Hello,
C I am your friendly 3-D, Cubic Mirror-Image Replacement filter;
C I smooth Y(N1,N2,N3) according to how you set my lengths
C LNTH1, LNTH2, and LNTH3 (LE. Nk/2); it may help to know that I
C annihilate components of period/wavelength 2*LNTHk. I give you
C back the (smoothed) answer in the same array and I have no need
C for (extra) memory. My defaults are transparent; to suppress
C action in a given dimension, set the respective LNTH's to zero;
C for 1-D or 2-D data, set the excess parameter(s) Nk to one.
C Mathematically, I have been enchanced to commute with cubics --
C that makes me a third-order algorithm. Near boundaries, I use
C mirror-image extensions; they are continuous (in all dimensions)
C and keep me stable. Finally, you should be pleased to hear that
C my lobes are small (down 40 dB) and that I am fast. Have at it!
C DIMENSION Y(*),NY(3),LNTH(3)
C
NY(1)=N1          ! Index for cyclic rotation on faces
NY(2)=N2          ! of cube. Filter lines are initialized
NY(3)=N3          ! as points on such faces.
LNTH(1)=LNTH1    ! Note: NY(k)=1 => do nothing.
LNTH(2)=LNTH2    !           LNTH(k)=0 => do nothing.
LNTH(3)=LNTH3
JUMP=1           ! Initialize subsampling.
DO 30 NDIM=1,3   ! Cycle faces (needed or not).
IF(NY(NDIM).LE.1 .OR. LNTH(NDIM).LE.0)GO TO 30
  NYD=NY(NDIM)   ! Save to reset NY(NDIM).
  NY(NDIM)=1     ! Specify face of cube.
  DO 20 K1=1,NY(1) ! Loop
    DO 20 K2=1,NY(2) ! through
      DO 20 K3=1,NY(3) ! face.
        KSTRT=K1+N1*((K2-1)+N2*(K3-1))
        =====
        CALL CMIR1(Y(KSTRT),NYD,LNTH(NDIM),JUMP)
        =====
C
C
20  CONTINUE
    NY(NDIM)=NYD ! Reset.
    JUMP=JUMP*NY(NDIM) ! Update subsampling.
30  CONTINUE
END

```

Appendix F. A Mirror-Image Filter Algorithm

```

SUBROUTINE CMIR1(Y,NY,LNTH,JUMP)
C *****Jim Leise 2/88
C 1-D, Cubic Mirror-Image Replacement filter: Smooth Y(NY*JUMP)
C according to the length parameter LNTH using a mirror extension.
C The only restrictions on use is 2*LNTH.LE.NY; JUMP is used to
C import data for multidimensional use; set JUMP=1 for 1-D data.
C The LNTH parameter has a linear effect; when LNTH is doubled,
C the passband is halved. In more detail, if [L] denotes a
C running average of length L=LNTH, the first-order filter is
C [2L]*[2L]*[L]*[L], '*'=convolution
C This convolution is then improved with cubic enhancement,
C i.e., the central filter is modified to commute with cubic
C polynomials. Also, there is a correction step to suppress the
C (spectral) side lobes to about 40 dB. Functionally, this code
C is a driver for subroutines MIRROR and TANGLE. Total
C multiplications used by this algorithm is about 7*NY.
C DIMENSION Y(*)
C
C IF(LNTH.LE.0 .OR. 2*LNTH.GT.NY)RETURN ! Check setup.
C.... Cubic enhancement of top step + large triangle.
C ===== ! =====
CALL MIRROR(Y,NY,-6.0, LNTH, JUMP) ! 4*(I-0.25*d**2)
CALL TANGLE(Y,NY, 2*LNTH, JUMP) ! T[4*L-1]
C ===== ! =====
YNORM=-1./(4.*FLOAT(2*LNTH)**2) ! Initialize norm.
C.... Cubic enhancement of small triangle.
IF(LNTH.EQ.1)GO TO 10 ! "Short" samples.
LHALF=(LNTH+1)/2 ! Halve LNTH.
CL=(FLOAT(LNTH)**2-1.)/(12.*FLOAT(LHALF)**2)
P = 1.+2.*CL
Q =-CL
C ===== ! =====
CALL MIRROR(Y,NY,P/Q, LHALF, JUMP) ! (I-CL*d**2)/Q
C ===== ! =====
YNORM=YNORM*Q ! Update norm.
C.... Lobe suppression + small triangle + enhancement.
DH=1/3.+(FLOAT(2*LHALF)**2-1.)/(12.*FLOAT(LHALF)**2)
P = 1.+2.*DH
Q =-DH
C ===== ! =====
CALL MIRROR(Y,NY,1.0, LHALF, JUMP) ! (I+E+Einverse)
CALL TANGLE(Y,NY, 2*LHALF, JUMP) ! T[4*LHALF-1]
CALL MIRROR(Y,NY,P/Q, LHALF, JUMP) ! (I-DH*d**2)/Q
C ===== ! =====
YNORM=YNORM*Q/(3.*FLOAT(2*LHALF)**2)
10 DO 20 K=1,1+(NY-1)*JUMP, JUMP ! Normalize.
20 Y(K)=YNORM*Y(K) ! ...
END

```

Appendix F. A Mirror-Image Filter Algorithm

```

SUBROUTINE TANGLE(Y,NY,LNTH,JUMP)
C *****Jim Leise 1/88
C 1-D TRIANGLE FILTER ALGORITHM. Filter Y(NY) with a triangle
C filter (defined by LNTH) and a mirror-image extension:
C TRIANGLE =[LNTH]*[LNTH] e.g. [3]*[3]=(1,2,3,2,1)
C where [L]=running average of length L and '*'=convolution.
C Internally, this algorithm requires NY multiplications which
C are done via the mirror filter algorithm MIRROR. External
C normalization by LNTH**2 is required to complete the filter.
C JUMP is used to import data for multidimensions; set JUMP=1
C for 1-D data. Restriction on use: 2*LNTH.LE.NY & NY.LE.16384.
C DOUBLE PRECISION SL,SR,TL,TR,SB,DB,DF,TB,TF
C DIMENSION Y(*)
C
IF(LNTH.LE.1)RETURN
N2=NY/2 ! N2=halfway pointer.
J1=LNTH*JUMP ! Subsampled LNTH step.
Jcntr=1+N2*JUMP ! Subsample pointer.
IF(Jcntr.LE.J1)RETURN ! Indexing check.
Jstop=1+(NY-1)*JUMP ! Subsampled end.
C.... Compute I.C.'s for double integration.
SL=Y(1) ! Initialize Left Sum.
SR=Y(Jstop) ! Initialize Right Sum.
TL=SL ! Initialize Left Triangle.
TR=SR ! Initialize Right Triangle.
DB=Y(Jcntr)-Y(Jcntr-J1) ! Initialize "Difference."
SB=Y(Jcntr) ! Initialize Back Sum.
TB=SB ! Initialize Back Triangle.
DO 10 K=JUMP,(LNTH-1)*JUMP,JUMP
SL=SL+Y(1+K)+Y(1+K-JUMP) ! Left integral.
SR=SR+Y(Jstop-K)+Y(Jstop-K+JUMP) ! Right integral.
TL=TL+SL ! Second integral.
TR=TR+SR ! ...
DB=DB+Y(Jcntr+K)-Y(Jcntr-K) ! Difference mod(2*K).
SB=SB+Y(Jcntr+K)+Y(Jcntr-K) ! First Integral.
10 TB=TB+SB ! Second integral.
C.... Get the mirror-image second difference.
C ===== ! =====
CALL MIRROR(Y,NY,-2.0,LNTH,JUMP) ! Y(K) <= Y(K+L)-2Y(K)+Y(K+L)
C ===== ! =====
C.... Double integration: center ==> boundaries.
DF=DB+Y(Jcntr) ! Initialize F-Difference.
TF=TB ! Initialize F-Triangle.
Y(Jcntr)=TF ! Save answer.
KB=Jcntr-JUMP ! Initialize B-counter.
DO 50 KF=Jcntr+JUMP,Jstop,JUMP
TB=TB-DB ! Integrate Backwards.
TF=TF+DF ! Integrate Forwards.
DB=DB-Y(KB) ! Update Backward Difference.
DF=DF+Y(KF) ! Update Forward Difference.
Y(KB)=TB ! Save answer.
Y(KF)=TF ! ...
50 KB=KB-JUMP ! Update backward counter.

```

Appendix F. A Mirror-Image Filter Algorithm

```
IF(KB.EQ.1)THEN                                ! Parity check to terminate.
  TB=TB-DB                                       ! NY even => done.
  Y(1)=TB                                       ! ...
ENDIF
..... Linear error correction: slope=(exact-integrated)/points.
DB=(TL-TB)/N2                                   ! Backward error slope.
DF=(TR-TF)/(NY-N2-1)                           ! Forward error slope.
TB=0.                                           ! Initialize B-correction.
TF=0.                                           ! Initialize F-correction.
KB=Jcntr-JUMP                                   ! Backward counter.
DO 60 KF=Jcntr+JUMP,Jstop,JUMP
  TB=TB+DB                                       ! Increment B-correction.
  TF=TF+DF                                       ! Increment F-correction.
  Y(KB)=Y(KB)+TB                                 ! Do B-correction.
  Y(KF)=Y(KF)+TF                                 ! Do F-correction.
60  KB=KB-JUMP                                   ! Update counter.
IF(KB.EQ.1)THEN                                ! Parity check to terminate.
  TB=TB+DB                                       ! NY even => done.
  Y(1)=Y(1)+TB                                   ! ...
ENDIF
END
```

Appendix F. A Mirror-Image Filter Algorithm

```

SUBROUTINE MIRROR(Y,NY,COEFF,LSTEP,JUMP)
C *****Jim Leise 10/85; 1/90.
C MIRROR-IMAGE FILTER: Implement the (replacement) filter
C   Y(K) <= Y(K-LSTEP) + COEFF*Y(K) + Y(K+LSTEP)
C on Y(NY) using a mirror-image extension (NY operations).
C Set JUMP=1 for 1-D data, or use multidimensional driver.
C DIMENSION Y(*)
C
KSTEP=MAX0(1,MIN0(LSTEP,NY/2))      ! Setup check.
NYJ=1+(NY-1)*JUMP                    ! Subsampled end.
JSTEP=KSTEP*JUMP                      ! Subsampled stepsize.
Jtest=NYJ-JSTEP                       ! Test parameter.
C -----
C.... KCLASS=MIRROR-IMAGE EQUIVALENCE CLASS MOD(JSTEP).
DO 70 KCLASS=1, (KSTEP+1)/2
Kstrt=KCLASS                          ! Initialize Kstrt.
C.... CYCLE Kstrt MOD(LSTEP) TO POSITION PAST 2*NY AND CHECK CLASS.
20 Kstrt=KSTEP-MOD(MOD(NY-Kstrt,KSTEP)+MOD(NY,KSTEP),KSTEP)
IF(Kstrt.LT.KCLASS .OR. KSTEP-Kstrt+1.LT.KCLASS)GO TO 70
IF(Kstrt.GT.KCLASS)GO TO 10           ! Continue search.
C.... EQUIVALENCE CLASS NEW: Kstrt=KCLASS.
Save =Y(1+(Kstrt-1)*JUMP)             ! Saved to close loop.
Ynow =Y(1+(KSTEP-Kstrt)*JUMP)         ! Initialize.
20 Jstrt=1+(Kstrt-1)*JUMP              ! Save for loop check.
Jnow =Jstrt                            ! Initialize.
30 Jnxt =Jnow+JSTEP                    ! Update pointer.
C.... FORWARD STEPS -----
40 Yold=Ynow                            ! Update data.
Ynow=Y(Jnow)                            ! ...
Y(Jnow)=COEFF*Ynow+(Yold+Y(Jnxt))
Jnow=Jnxt                                ! Update index.
IF(Jnxt.LE.Jtest)GO TO 30              ! Implicit loop to end.
Jnxt=(NYJ-Jnxt)+Jtest+JUMP             ! Reflect &
IF(Jnxt.EQ.Jnow)GO TO 60               ! Check for coincidence.
C.... BACKWARD STEPS -----
50 Yold=Ynow                            ! Update data.
Ynow=Y(Jnow)                            ! ...
Y(Jnow)=COEFF*Ynow+(Yold+Y(Jnxt))
Jnow=Jnxt                                ! Update pointer.
Jnxt=Jnow-JSTEP                          ! ...
IF(Jnxt.GT.0)GO TO 50                  ! Implicit loop to start.
Jnxt=2-Jnxt-JUMP                        ! Reflect &
IF(Jnxt.EQ.Jnow)GO TO 60               ! Check for coincidence.
C.... CLOSE CYCLIC LOOP: [Save,?Y(Jnow),Yold] <= past.
IF(Jnxt.NE.Jstrt)GO TO 40              ! Check for closed loop.
Y(Jnow)=COEFF*Y(Jnow)+(Ynow+Save)      ! Finish cyclic loop.
GO TO 70
C.... OR, TOGGLE COINCIDENT REFLECTIONS? -----
60 Y(Jnow)=COEFF*Y(Jnow)+(Ynow+Y(Jnow)) ! Finish coincidence.
Kstrt =1+KSTEP-Kstrt                    ! Reflect Kstrt.
Ynow =Save                               ! Reinitialize.
IF(Kstrt.NE.KCLASS)GO TO 20            ! Do other half.
70 CONTINUE
END

```

Appendix G. FILTERED INTERPOLATION

We here discuss several methods of interpolating missing values when data is noisy.

Missing Data and the Exponential Filter Recall that the exponential filter (C.1) requires an infinite amount of data from the past so, "How do we get it started?" It must be modified or normalized near data boundaries in such a way that constant time series remain constant. What makes this normalization really significant is that it works, more generally, for random missing data. The net result is a smoothing filter that works even when data are incomplete.

The useful feature of the exponential filter E_r is that it is a filter with *positive* coefficients, a property important to normalization. To begin, suppose that $\{x_n\}$ is a time series with some missing values. Let $\{x_n^+\}$ denote the time series in which the missing values are replaced with zeros, and let δ_n^+ be the indicator or delta function that is unity at good values x_n and zero at missing ones. Then, sums S_n and counters C_n are computed using the recursive form (C.1) of the exponential filter, here parameterized with $\gamma=1-r$:

$$(G.1) \quad \begin{aligned} S_n &= (1-\gamma)S_{n-1} + \gamma x_n^+ \\ C_n &= (1-\gamma)C_{n-1} + \gamma \delta_n^+ \end{aligned}$$

and the normalized filter y_n is the quotient:

$$(G.2) \quad y_n = S_n / C_n .$$

Note that when data are complete, C_n converges to unity as $n \rightarrow \infty$, and so for large n , normalization does nothing. However, for small values, normalization helps adjust for an unknown past. Specifically, to get the filter started, S_0 and C_0 are initialized to zero and data is indexed so that the first value x_1 is good one. We denote this extension by E_γ^+ , that is, $y_n = E_\gamma^+(x)$. To obtain a symmetric procedure, E_γ^+ is applied in both directions and averaged to get S_γ^+

$$S_\gamma^+ = [E_\gamma^+ + (E_\gamma^+)^*] / 2 .$$

Although this is not a high-quality method, it is useful as an intermediate step.

A First-Order Method In principle, S_r^+ can generate values at missing points; however, the interpolation so produced is unsatisfactory insofar as it is constant over missing intervals and produces jump discontinuities at points of transition. Nonetheless, because data has been smoothed, noise has been suppressed and interpolation across missing regions is more stable.

Appendix G. Filtered Interpolation

Specifically, if x_n and x_m are good values that border missing ones, then the linear interpolates $y_{n+1}, y_{n+2}, \dots, y_{m-1}$ are computed from filtered end points $y_n = S_{\gamma, n}^+(x)$ and $y_m = S_{\gamma, m}^+(x)$. Finally, *smoothed values are replaced with original data and only the linear interpolates are retained*. In this way, a versatile (first-order) filtered interpolation scheme is obtained that can be implemented as a sequence of simple steps.

Iterative Improvement Linear interpolation is a low-order method and may not always be adequate to achieve desired effects (such as needed to determine peaks). We here consider a stable way of generating improvements, based on higher-order filtering. Results can be viewed as a sequence of successive approximations. Thus, let $I^{(1)}$ denote the above procedure, that is, $I_n^{(1)}[x] = x_n$ at good values and $I_n^{(1)}[x]$ is the linear interpolate at missing ones. In turn, a higher-order filter (such as in App. F) is applied to the time series $\{I_n^{(1)}[x]\}$ to improve the estimates at missing points. Again, good values are put back and an improved operator $I^{(2)}$ results; if A denotes the higher-order filter, then $I_n^{(2)}[x] = x_n$ at good values and $I_n^{(2)}[x] = A_n I_n^{(1)}[x]$ at missing ones. Clearly, this iteration can be continued ad-infinitum (with the same filter). Although this procedure tends to be stable, it can be slow to converge which means that if desired effects are not achieved in one or two steps, the filter is probably not very well matched to the problem.

A Causal Method So far, algorithms have been of the safe variety, suitable for automated data processing. However, when working interactively, it is often better to use less stable methods that are more flexible and faster converging. For this exposition, we restrict attention to the case where data are complete, having no missing values.

To begin, the exponential filter $y_n = E_{\gamma, n}[x]$ can be improved by smoothing the difference $\varepsilon_n = x_n - y_n$ and adding it back to y_n ; the resulting operator is $E_{\gamma}^{(2)} = E_{\gamma} + E_{\gamma}(I - E_{\gamma})$. More generally, higher-order corrections can be obtained through iteration:

$$(G.3) \quad \begin{aligned} \varepsilon_n^{(k)} &= (1-\gamma)\varepsilon_{n-1}^{(k)} + (x_n - y_n^{(k)}) \\ y_n^{(k+1)} &= y_n^{(k)} + \varepsilon_n^{(k)}, \end{aligned}$$

where $y_n^{(1)} = y_n$ and $\varepsilon_n^{(1)} = \varepsilon_n$ above. If $E_r^{(k)}$ denotes the operator $E_{\gamma, n}^{(k)}[x] = y_n^{(k)}$, then mathematical induction can be used to establish:

$$(G.4) \quad E_{\gamma}^{(k)} = I - (I - E_{\gamma})^k.$$

In turn, the frequency response is:

Appendix G. Filtered Interpolation

$$(G.5) \quad \mathcal{R}_\gamma^{(k)}(\omega) = 1 - [1 - \mathcal{R}_\gamma(\omega)]^k$$

which converges to unity as $k \rightarrow \infty$, whenever $|\mathcal{R}_\gamma^{(k)}(\omega)| < 1$.

The interesting thing is that the operator $(I - E_\gamma)^k$ always annihilates polynomials of degree $k-1$ (we leave this as an exercise). As a consequence, $E_\gamma^{(k)}$ is a polynomial filter of degree $k-1$.

Analysis of $E^{(2)}$ We have just seen that the $E_\gamma^{(2)}$ is a polynomial filter of degree one and can track straight lines. To compute the operator, first observe that E_γ^2 can be obtained by squaring E_γ as an infinite series:

$$E_\gamma = \gamma \sum_{k=0}^{\infty} (1-\gamma)^k \mathcal{E}^{-k} \quad \Rightarrow \quad E_\gamma^2 = \gamma^2 \sum_{k=0}^{\infty} (k+1)(1-\gamma)^k \mathcal{E}^{-k}$$

and so

$$(G.6) \quad E_\gamma^{(2)} = 2E_\gamma - E_\gamma^2 = \gamma \sum_{k=0}^{\infty} [2 - (k+1)\gamma](1-\gamma)^k \mathcal{E}^{-k}$$

Observe that the factors $[2 - (k+1)\gamma]$ are monotone decreasing with a zero at $k = O_\gamma \equiv 2/\gamma - 1$; this zero is useful as a length scale.

We apply the scaling parameter O_γ to model the number of steps required for $E_\gamma^{(2)}$ to stabilize after starting up. When applied to straight lines ($x_k = k$), there is a transient error that starts at zero, attains a maximum, and then decays exponentially back to zero. Steps or iterations N_γ required for convergence to a 1% relative error level are shown in Table G-1. More precisely, N_γ is the smallest number of steps for which $k \geq N_\gamma \Rightarrow |1 - E_\gamma^{(2)}[x]/k| < 0.01$. The important observation is that N_γ is asymptotically proportional to O_γ , that is, $N_\gamma^0 = N_\gamma / O_\gamma \cong 2.64$.

Another application of O_γ is to characterize maximum amplitudes $|\mathcal{R}_\gamma^{(2)}(\omega)|$ of (G.5). Here, the amplitude starts out at unity ($\omega=0$), attains a maximum, and then decreases toward zero. Maximums are shown in Table G-1, together with the normalized wavelength $\lambda_N = 1/f_N$ (scaled in units of points per cycle) at which the maximums occur. Again the normalization $\lambda_N^0 = \lambda_N / O_\gamma$ is asymptotically constant with a value of about 4.44. Observe that the relatively large maximums (about 1.15) are typical for predictive polynomial filters, and shows why such filters should be used with caution.

Appendix G. Filtered Interpolation

γ	O_γ	N_γ	N_γ^0	$ \mathcal{R}_\gamma^{(2)} _{\max}$	λ_N	λ_N^0
0.001	1999.0	5273	2.638	1.155	8874.5	4.439
0.002	999.0	2635	2.638	1.154	4437.3	4.442
0.003	665.7	1756	2.638	1.154	2955.3	4.440
0.004	499.0	1317	2.639	1.154	2216.5	4.442
0.005	399.0	1053	2.639	1.154	1774.9	4.448
0.006	332.3	877	2.639	1.154	1480.2	4.454
0.007	284.7	751	2.638	1.153	1263.4	4.437
0.008	249.0	657	2.639	1.153	1108.0	4.450
0.009	221.2	584	2.640	1.153	986.8	4.461
0.010	199.0	525	2.638	1.153	884.6	4.445
0.020	99.0	262	2.646	1.151	442.3	4.468
0.030	65.7	174	2.650	1.149	293.7	4.473
0.040	49.0	130	2.653	1.147	219.7	4.484
0.050	39.0	103	2.641	1.145	175.5	4.500
0.060	32.3	86	2.660	1.143	145.7	4.506
0.070	27.6	73	2.648	1.141	124.6	4.520
0.080	24.0	64	2.667	1.139	108.8	4.534
0.090	21.2	56	2.639	1.137	96.5	4.546
0.100	19.0	51	2.684	1.135	86.7	4.562
0.200	9.0	24	2.667	1.116	42.2	4.684
0.300	5.7	15	2.647	1.097	27.3	4.810
0.400	4.0	11	2.750	1.079	19.8	4.951
0.500	3.0	8	2.667	1.061	15.3	5.092

Table G-1. Some characteristic features of the filter $E_\gamma^{(2)}$. Here O_γ is the zero crossing of the filter coefficients, N_γ is the number of iterations required for 1% accuracy after starting up, and λ_N is the wavelength, (in points per cycle) of the maximum frequency response. The normalized values $N_\gamma^0 = N_\gamma / O_\gamma$ and $\lambda_N^0 = \lambda_N / O_\gamma$ show the usefulness of O_γ as a length scale.

The TREND Algorithm The algorithm of interest here combines the filter $z_n = E_{\gamma,n}^{(2)}[x]$ at good values with the prediction $z_n = 2z_{n-1} - z_{n-2}$ at bad ones. A flow chart for this algorithm, called TREND, is given in Fig. G-1, and a FORTRAN subroutine is given in Fig. G-2; note that this subroutine uses a 5-point buffer to hold intermediate results. By changing buffers, the same code can be used for different applications.

At this point, it is convenient to streamline the normalization procedure

(G.1) as:

$$(G.7) \quad \begin{aligned} s_n &= (1-\gamma)s_{n-1} + x_n \\ c_n &= (1-\gamma)c_{n-1} + 1 \end{aligned}$$

Appendix G. Filtered Interpolation

$$y_n = s_n / c_n .$$

which requires two less multiplications, but does not distinguish between good values and bad ones. Also, the limit for $\gamma=0$ is different.

This normalization is shown in the flow-chart of Fig. G-1 for the TREND algorithm. Note that missing values are predicted from smooth ones, producing feedback which can go on forever.

Appendix G. Filtered Interpolation

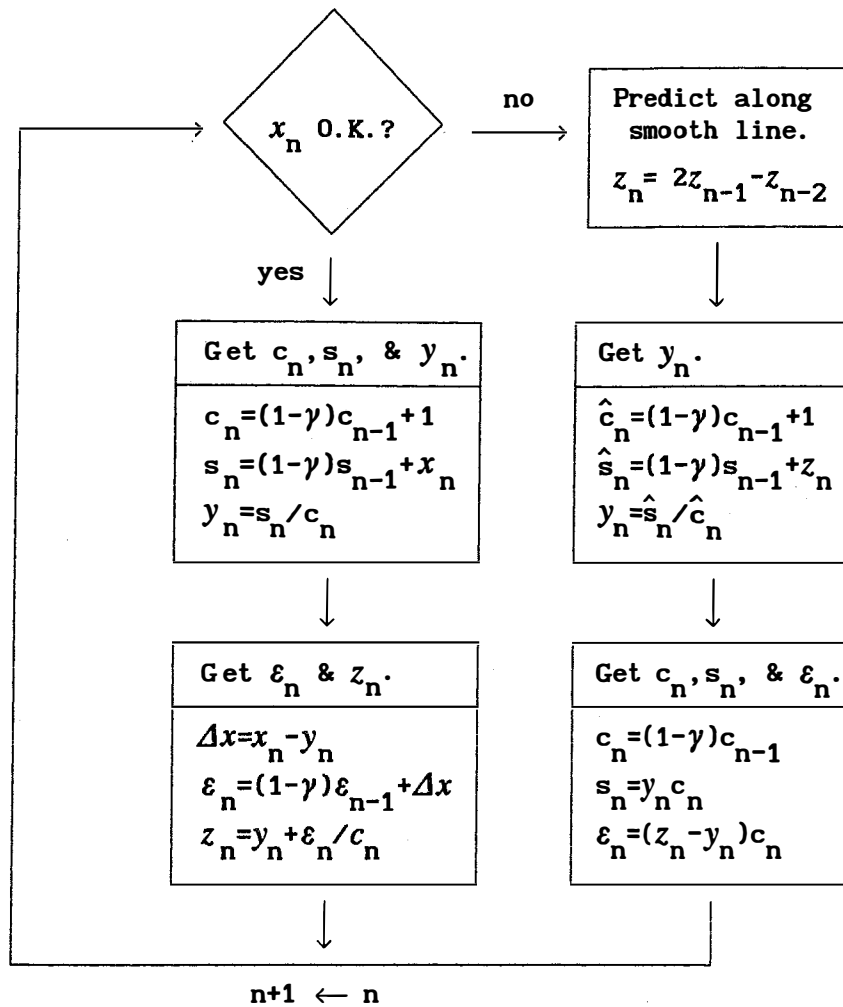


Figure G-1. Flow chart for TREND algorithm. Here $\{x_n\}$ are given data, y_n is the exponential filter and z_n is the corrected (final) one. When data are missing, z_n is a prediction, c_n is a shift, and y_n , s_n , and ϵ_n are computed to be consistent with the filtering process. Note that c_{n-1} , s_{n-1} , ϵ_{n-1} , z_{n-1} , and z_{n-2} are all saved variables. A FORTRAN subroutine is given in Fig. G-2 .

Observe that when data are complete, the TREND algorithm is simply an implementation of $z_n = E_{\gamma, n}^{(2)}[x]$ and normalization is done in the usual way. However, when prediction is used, the intermediate values c_n , s_n , y_n , and ϵ_n require explanation. To help motivate what is going on, suppose that at missing values c_n and s_n are both shifted $c_n = (1-\gamma)c_{n-1}$ and $s_n = (1-\gamma)s_{n-1}$. But then, the mean filter $y_n = c_n / s_n$ would be the same as y_{n-1} , and would remain unchanged over an entire region of missing values. Consequently, when a good

Appendix G. Filtered Interpolation

value is encountered, there would be an inconsistency causing a jump. Another approach would be to use the prediction z_n as valid data $x_n = z_n$; however, the prediction $z_n = 2z_{n-1} - z_{n-2}$ is already smooth, and using it as data would have the effect of smoothing twice, creating a different kind of jump.

The procedure shown in the flow chart of Fig. G-2 is a combination of these two approaches. When a bad value is encountered, c_n is shifted $c_n = (1-\gamma)c_{n-1}$, but y_n is computed as though the prediction z_n was valid data; once done, s_n is forced to be consistent $s_n = y_n c_n$. In turn, the correction ε_n is computed as $\varepsilon_n = (z_n - y_n)c_n$. Now, over regions of missing data, y_n will converge to z_n and ε_n will converge to zero. The net effect is a smoother transition between bad regions and good ones. Also, when missing regions are large, c_n will converge to zero and the algorithm will reinitialize.

In summary, we see that TREND is an attempt to handle a variety of missing-data problems, and in such a way that straight-line behavior is accurately reproduced. Clearly, no predictive algorithm can do so much, over such varied conditions, and still remain stable; suffice it to say that TREND can go unstable, especially with larger values of γ . Nonetheless, when symmetrized, TREND has performed well in a variety of applications.

It is worth remarking that there are many variations of this procedure, especially with the prediction; another useful one is: $z_n = z_{n-1} + z_{n-2} - z_{n-3}$ which is more stable. Also, higher-order procedures similar to (G.3) can be constructed directly with TREND, and there is little motivation for configuring more primitive code to do this. Finally, it is often useful to apply this filter twice, to help further smooth out jumps caused by transitions.

Appendix G. Filtered Interpolation

```

FUNCTION TREND(Ynow,WT, Buff5)
C *****JIM LEISE 7/87, 6/90
C Linear TREND estimate: Filter and/or predict values of a time
C series with present value of YNOW. The filter is determined by
C the weight parameter WT (0<WT<1); small values result in more
C smoothing; large values in less. BUFF5(5) is a work buffer that
C must be dimensioned (externally) to 5 and initialized with WT=0:
C                               DUM=TREND(DUM,0.,BUFF5)
C Bad or missing values are defined with a flag (YNOW=FLAG). For
C such values, TREND is returned as a predicted value -- provided
C it has already been given some good data.
DIMENSION Buff5(5)
DATA FLAG/-1.E+38/

C.... ===== INITIALIZE =====
TREND=Ynow           ! Set default.
IF(WT.EQ.0.)THEN    ! Check for startup.
  Buff5(1)=0.       ! Preset to zero.
  Buff5(2)=0.       ! ...
  Buff5(3)=0.       ! ...
  Buff5(4)=FLAG     ! Mark as empty.
  Buff5(5)=FLAG     ! Mark as empty.
RETURN
ENDIF

C.... ===== MEAN FILTER =====
IF(Ynow.NE.FLAG)THEN ! DATA O.K.
  Ydat=Ynow          ! Use it.
ELSE                ! DATA MISSING.
  IF(Buff5(5).NE.FLAG)THEN ! Both buffers set?
    Ydat=2*Buff5(4)-Buff5(5) ! PREDICT on line.
  ELSEIF(Buff5(4).NE.FLAG)THEN ! Any data at all?
    Ydat=Buff5(4)          ! Yes, use TREND.
  ELSE                    ! No data yet.
    RETURN                ! Exit.
  ENDIF
ENDIF

CT=1.-WT
Buff5(1)=1. + CT*Buff5(1) ! Update counter.
Buff5(2)=Ydat + CT*Buff5(2) ! Update mean buffer.
YMEAN=Buff5(2)/Buff5(1)   ! MEAN FILTER.

C.... ===== CORRECTED FILTER =====
IF(Ynow.NE.FLAG)THEN ! DATA O.K.
  Buff5(3)=(Ydat-YMEAN)+CT*Buff5(3) ! Correction buffer.
  TREND=YMEAN+Buff5(3)/Buff5(1)    ! Corrected filter.
ELSE ! DATA MISSING.
  Buff5(1)= Buff5(1)-1.           ! Shifted to
  Buff5(2)= YMEAN*Buff5(1)        ! be inverse
  Buff5(3)=(Ydat-YMEAN)*Buff5(1)  ! consistent.
  TREND=Ydat                      ! Use prediction.
ENDIF
Buff5(5)=Buff5(4)                ! Update and save
Buff5(4)=TREND                   ! for prediction.
END

```

Figure G-2. FORTRAN listing of TREND algorithm.

Appendix G. Filtered Interpolation

The PATCH Routine We now return to the problem of configuring a method for interactive use. Here, the TREND algorithm works well when applied both forward and backward in time. Note that the quality of a prediction is a function of which direction it comes from. Because of this, respective predictions are weighted according to their distances from valid data. If missing regions occur at the beginning or end of a time series, results are predictive. A FORTRAN subroutine for this procedure, called the PATCH algorithm, is given in Fig. G-3. Note that this is an array oriented procedure requiring additional workspace.

Internal to a data set, the PATCH algorithm approximates cubic interpolation. The interesting feature is that values produced are quite sensitive to the weighting parameter $\gamma=1-r$, especially when interpolating over large regions. In fact, this procedure can become unstable, producing excessively large values. Nonetheless, this instability can be an advantage because the same mechanism gives the algorithm the flexibility required to model sharp peaks and other transient behavior. In this context, γ must be determined interactively by trial and error and by a skilled user. *In particular, this method is not recommended for automated data processing.*

Appendix G. Filtered Interpolation

```

SUBROUTINE PATCH(Y,WORK,N,WT)
C *****Jim Leise 6/88, revised 12/89.
C This algorithm interpolates/extrapolates over missing/flagged
C data in Y(N) -- i.e. values Y(K)=FLAG are replaced; other
C values are returned unchanged. WORK(N) is a work array required
C by the algorithm. On exit, it contains the input Y array (FLAGS
C and all). The weight parameter WT should be set/input between
C zero and one. Larger values produce smoother splines (smaller
C jumps) and larger peaks; smaller values are more stable.
C DIMENSION Y(N),WORK(N),BUFF5(5)
C DATA FLAG /1.E-38/

C
L=N+1           ! L = backwards counter.
KSTRT=0        ! Preset KSTRT for test.
DO 10 K=1,N
WORK(K)=FLAG   ! Initialize WORK(*) to flags.
IF(Y(K).NE.FLAG)KSTOP=K ! Location of first good data.
L=L-1         ! Update L.
10 IF(Y(L).NE.FLAG)KSTRT=L ! Location of last good data.
IF(KSTRT.EQ.0)RETURN ! No data.

C
C.... ==>, forward prediction and gap counter.
DUM=TREND(DUM,0.,BUFF5) ! Initialize TREND/BUFF5.
DO 20 K=KSTRT,KSTOP ! Loop forward.
IF(Y(K).EQ.FLAG)THEN ! Data not OK.
KOUNT=KOUNT+1 ! KOUNT>0 <=> bad data.
Y(K)=TREND(FLAG,WT,BUFF5) ! TREND predicts on flags.
ELSE ! Data OK.
KOUNT=0 ! KOUNT=0 <=> good data.
DUM=TREND(Y(K),WT,BUFF5) ! Data-base call.
ENDIF
20 WORK(K)=KOUNT ! Needed later.

C
C.... <==, backward prediction and weighted averaging.
DUM=TREND(DUM,0.,BUFF5) ! Reinitialize TREND/BUFF5.
DO 30 L=KSTOP,KSTRT,-1 ! Backward loop.
IF(WORK(L).NE.0.)THEN ! Missing data detected.
IF(SCALE.EQ.0.)SCALE=1./(WORK(L)+1.)
WEIGHT=SCALE*WORK(L) ! Linear weighting.
YNOW=TREND(FLAG,WT,BUFF5) ! Get backward prediction.
Y(L)=(1.-WEIGHT)*Y(L)+WEIGHT*YNOW ! Save answer.
WORK(L)=FLAG ! Return flags to WORK(*).
ELSE ! Good data detected.
SCALE=0. ! Reset scale.
WORK(L)=Y(L) ! Good Y(*) ==> WORK(*).
DUM=TREND(Y(L),WT,BUFF5) ! Data-base call.
ENDIF
30 CONTINUE

```

(continued on next page)

Appendix G. Filtered Interpolation

```

C
C.... All internal gaps are filled. Now do the ends.
      IF(KSTOP.EQ.N)GO TO 50          ! Far endpoint OK.
      DUM=TREND(DUM,0.,BUFF5)        ! Reinitialize TREND/BUFF5.
      DO 40 K=KSTRT,N                ! Loop forwards.
      YNOW=TREND(Y(K),WT,BUFF5)      ! Data-base call.
40    IF(K.GT.KSTOP)Y(K)=YNOW        ! Prediction ==> Y(*).
C
      50 IF(KSTRT.EQ.1)RETURN         ! Starting endpoint OK.
      DUM=TREND(DUM,0.,BUFF5)        ! Reinitialize TREND/BUFF5.
      DO 60 L=KSTOP,1,-1             ! Loop backwards.
      YNOW=TREND(Y(L),WT,BUFF5)      ! Data-base call.
60    IF(L.LT.KSTRT)Y(L)=YNOW        ! Prediction ==> Y(*).
C
      END

```

Figure G-3. FORTRAN listing of algorithm for filtered interpolation. Again WT corresponds to γ . Also WORK(N) is needed work space. Note that this algorithm could be implemented as a predictive method, applied in both directions, and without the use of arrays.

Two-Parameter Methods The PATCH algorithm is especially useful for combining two measurements of the same thing. For example, radar altimetry H_r is superior for computing vertical winds over water. However, when islands or other obstructions are encountered, data are invalidated and require fixing. When problems are of short duration (<30 min), pressure altimetry H_p can be used instead, provided it is adjusted so as not to produce jump discontinuities. The exact procedure is as follows:

- Step 1: Edit out bad regions in H_r .
- Step 2: Compute the difference $\Delta H = H_r - H_p$ of remaining good data.
- Step 3: Interpolate bad regions in ΔH with PATCH to get ΔP .
- Step 4: Replace bad values in H_r with $H_p + \Delta P$.

Here a flag structure is used to distinguish between good and bad data (e.g., FLAG=-1.0 E+38) In particular, ΔH is flagged whenever H_r is bad, and the PATCH algorithm replaces these flags with interpolates.

The net effect is to adjust the mean trend in H_p with ΔP to match the mean trend in H_r . Once done, the two measurements can be spliced together to produce a smooth and seamless fit. In particular, *high frequencies are unaltered* by this process.

A sample of the result of two-parameter editing and patching is shown in Fig. G-4. The difference in latitude between two independent sources of

Appendix G. Filtered Interpolation

navigation information, LORAN-C and INS, is plotted (light line). Data was taken from N43RF's flight of 12/9/87 over coastal Washington state. Large excursions in the difference are apparent. These excursions, caused by poor signal-to-noise ratios in the LORAN-C unit, required that the LORAN-C data be edited, using INS data. Spikes in LORAN-C were edited out and patched over using steps 1 through 4, above. The resulting corrections in the patched areas are shown as the dark curve in Fig. G-4.

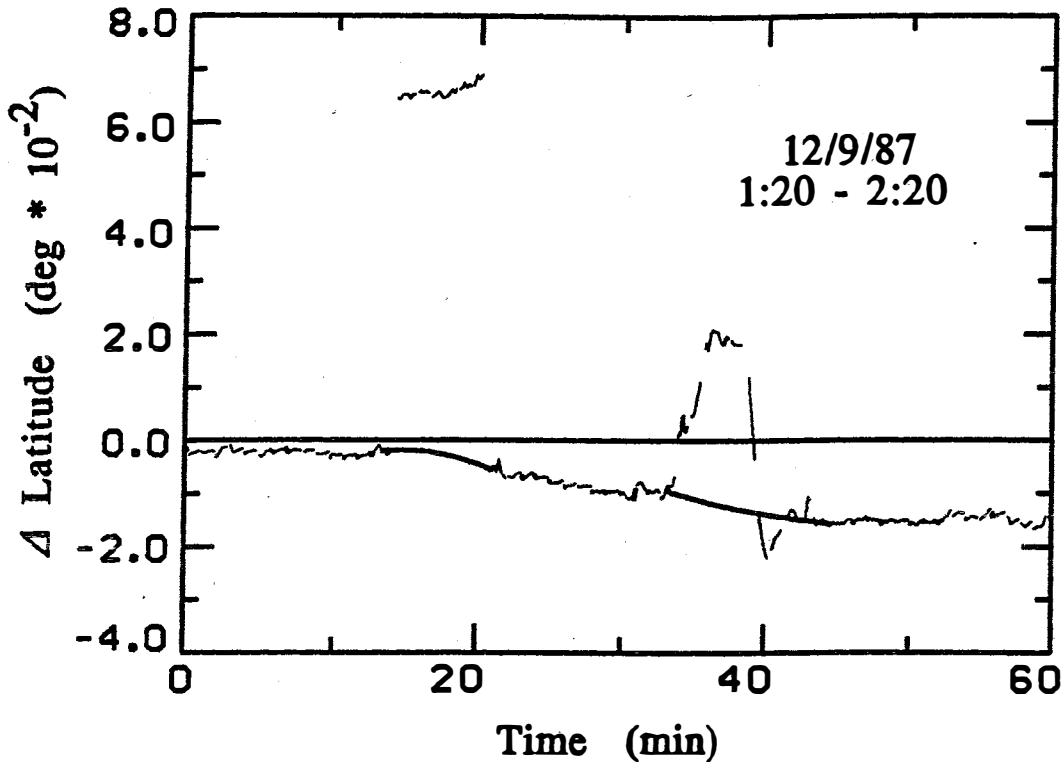


Fig. G-4. Difference in latitude between LORAN-C and INS (light line). Data was taken from N43RF's flight of 12/9/87 over coastal Washington state. Large excursions in the difference are caused by poor signal-to-noise ratios in the LORAN-C unit. Spikes in LORAN-C were edited out and patched over, using filtered interpolation (dark lines).

Appendix H. STATISTICAL EDITING

Automatic editing procedures for removing shot noise are an integral part of data processing, and should generally precede filtering procedures; recall that because filters act globally, they can spread effects of noise to other data, compounding the problem.

The statistical editing of interest here is based on Chebyshev's inequality:

$$(H.1) \quad P\{ |X-\mu| \geq \varepsilon\sigma \} \leq \frac{1}{\varepsilon^2}$$

where P , μ , and σ are the probability, mean, and standard deviation of a random variable X ; ε is an adjustable parameter that determines the size of the editing window. This inequality is especially useful because it is a simple geometric statement about the underlying probability distribution function. As such, it is an inequality that applies in many different situations, for different random variables, and with different probabilities.

Configuring editing procedures around this inequality is relatively straightforward; values $X=X_k$ that satisfy (H.1) are judged as bad. However, the mean and standard deviation must first be estimated from sample statistics:

$$(H.2) \quad \hat{\mu} = \frac{1}{N} \sum_{k=1}^N X_k \quad \text{and} \quad \hat{\sigma} = \frac{1}{N-1} \left[\sum_{k=1}^N X_k^2 - N\hat{\mu}^2 \right]^{1/2}$$

where $\{X_k : k=1,2,\dots,N\}$ is a discrete sample of size N . Note that division by $N-1$ rather than N in the computation of $\hat{\sigma}$ accounts for the degree of freedom present in $\hat{\mu}$. Because the underlying distribution is usually not known, values of ε can be determined experimentally; once done, they rarely need changing.

This method is exceptionally effective with P-3 data when applied to the difference of two similar measurements. For example, data from the two INS's should, in principle, be the same. However, for unknown reasons, spikes or shot noise sometimes occur in one but not in the other, and such spikes are easy to detect in the difference. An additional feature of two-parameter editing is that once a bad value is detected, the other one can be used to correct it. A flow chart for doing this is shown in Fig. H-1, and a FORTRAN subroutine is given in Fig. H-4. Note that bad values are replaced with mean-adjusted good ones, and averages are computed from good data only.

An important property of this scheme is that it is independent of amplitude scaling; in other words, for a fixed value of ε and any constant $c \neq 0$, the random variables X and cX will be edited exactly the same way.

Appendix H. Statistical Editing

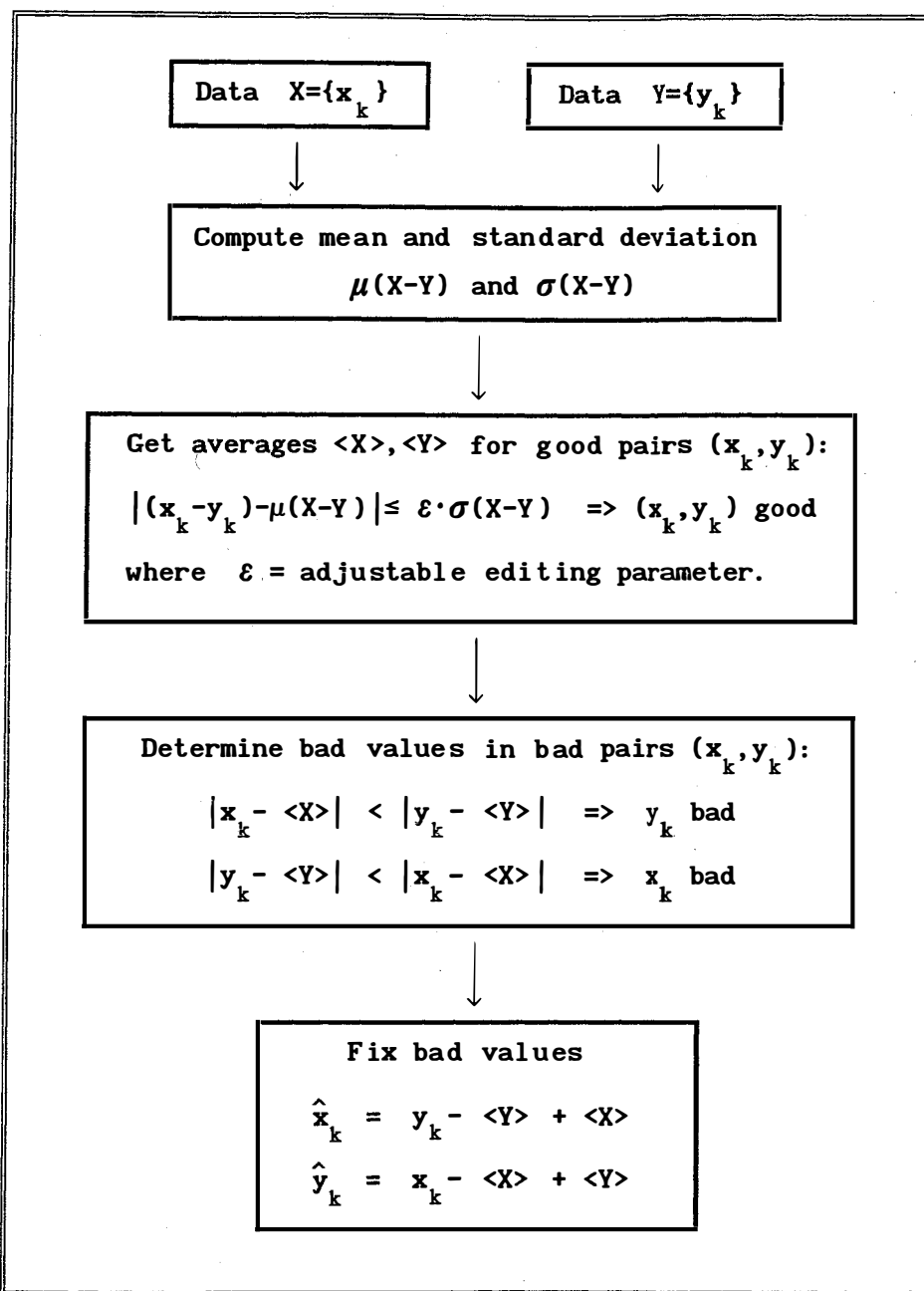


Figure H-1. Flow chart for two-parameter statistical editing based on Chebyshev's inequality. ϵ is a user set parameter that controls the relative size of the editing window. The averages $\langle X \rangle$ and $\langle Y \rangle$ are computed only from points passing as good. A FORTRAN subroutine for this algorithm is given in Fig.H-4.

Appendix H. Statistical Editing

For technical reasons, our two-parameter editing is applied to 20-second samples (i.e., 20 points), but each value is subject to two editing steps. This is accomplished by updating two 10-second buffers as shown in Fig. H-2.

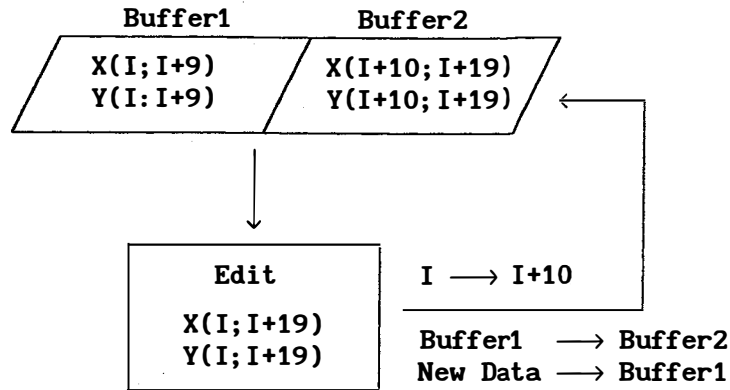


Figure H-2. 10-second updating procedure used with statistical editing. Note that each value is subjected to two editing steps, increasing sensitivity to noise and producing better results.

This two-step procedure helps compensate for the small data base of 20-points, making the statistical procedure more reliable. Recall from Sec. 11 that the triangle prefilter can spread out effects of shot noise to adjacent points. More precisely, shot noise consisting of one point gets spread out to three after decimation. The largest or center value is usually easy to detect, but the smaller, adjacent ones are not. Using a two-step editing procedure helps solve this problem; on the first step the largest value is corrected; once done, the smaller values are easier to detect.

We demonstrate this procedure with data from the 1989 calibration flight discussed in Sec. 9. This flight lasted about 7 hr and produced 26820 samples of 1 Hz data. Shown in Table H-1 are the number of points detected as bad for 4 quantities for which two separate instruments made measurements: pitch (ϕ_1, ϕ_2), acceleration (a_1, a_2), static pressure ($p_{s,w}, p_{s,f}$), and total temperature ($T_{t,1}, T_{t,2}$). Note that the wing-tip static pressure $p_{s,w}$ was roll adjusted prior to editing (see Sec. 10). For comparison, the number of points that would be deleted from a (large) normal distribution with *one* editing step are also shown. Note that these statistics reflect instrument performance; in our example, they indicate that $p_{s,w}$ and $T_{t,1}$ were working better than $p_{s,f}$ and $T_{t,2}$.

Appendix H. Statistical Editing

ϵ	Normal	ϕ_1	ϕ_2	a_1	a_2	$p_{s,w}$	$p_{s,f}$	$T_{t,1}$	$T_{t,2}$
1.50	3584	2731	3037	3363	3286	2646	3893	2579	4062
1.75	2149	1403	1566	1999	1996	1487	2212	1382	2325
2.00	1541	642	696	1090	1078	712	1094	660	1154
2.25	655	288	275	560	534	359	466	278	488
2.50	333	154	98	284	259	157	177	99	189
2.75	160	106	47	129	116	60	69	33	75
3.00	72	86	23	62	57	23	25	16	24

Table H-1. Total points edited for the 1989 calibration flight.

Another useful way to analyze these data is to normalize with the first column of Table H-2. Now values are expressed as the percentage of points relative to the normal distribution. This presentation is useful because it better shows vertical structure in the table, that is, it better shows how changing ϵ affects the statistics. For example, changes in the behavior of p_s and T_t around $\epsilon=2.00$ indicates a transition in the kind of "noise" sensed by the editing procedure.

ϵ	ϕ_1	ϕ_2	a_1	a_2	$p_{s,w}$	$p_{s,f}$	$T_{t,1}$	$T_{t,2}$
1.50	0.762	0.847	0.988	0.917	0.738	1.086	0.720	1.133
1.75	0.653	0.729	0.930	0.939	0.692	1.029	0.643	1.082
2.00	0.417	0.452	0.707	0.700	0.462	0.720	0.428	0.749
2.25	0.440	0.420	0.855	0.815	0.548	0.712	0.424	0.745
2.50	0.463	0.294	0.853	0.778	0.472	0.532	0.297	0.568
2.75	0.663	0.294	0.806	0.725	0.375	0.431	0.206	0.469
3.00	1.194	0.320	0.861	0.798	0.320	0.347	0.222	0.333

Table H-2. Percentage of points edited out relative to the normal distribution. Values were computed from Table H1 by normalizing with the first column, for example, $0.762 \approx 2731/3584$.

In Table H-3, statistical editing of pitch is shown for each 10 min interval of the flight for the editing parameters $\epsilon=2.25$ and $\epsilon=3.00$. This is the usual output in P-3 processing (only one ϵ , however). Experiment and use have shown that ϵ should generally be restricted to the the range $2.25 \leq \epsilon \leq 3.00$, with $\epsilon=3.00$ the preferred value for editing large fliers only. Observe that at about $\epsilon=2.25$, the relative number of points edited in ϕ_1 and ϕ_2 changes, demonstrating the lower bound.

Appendix H. Statistical Editing

Time Interval	ϕ_1 ($\epsilon=2.25$)	ϕ_2	ϕ_1 ($\epsilon=3.00$)	ϕ_2	Time Interval	ϕ_1 ($\epsilon=2.25$)	ϕ_2	ϕ_1 ($\epsilon=3.00$)	ϕ_2
10:00	11	3	5	3	13:40	10	8	1	1
10:10	5	3	2	0	13:50	5	7	1	1
10:20	3	4	0	0	14:00	8	5	2	2
10:30	2	4	0	0	14:10	7	5	2	0
10:40	6	5	2	0	14:20	8	5	2	0
10:50	4	4	2	0	14:30	7	9	7	0
11:00	12	2	4	0	14:40	9	2	6	0
11:10	6	6	2	0	14:50	2	8	0	0
11:20	4	4	2	0	14:00	8	3	2	0
11:30	6	4	2	1	15:10	4	10	4	1
11:40	6	9	2	1	15:20	9	4	0	1
11:50	5	9	1	3	15:30	4	5	0	0
12:00	10	6	2	0	15:40	5	2	2	1
12:10	4	6	0	0	15:50	3	7	0	0
12:20	6	11	2	2	16:00	7	6	0	0
12:30	4	15	2	0	16:10	5	9	0	0
12:40	7	6	4	0	16:20	3	7	0	0
*12:50	13	3	5	1	16:30	6	12	0	1
13:00	4	5	0	0	16:40	8	6	3	0
13:10	7	4	2	0	16:50	4	7	0	0
13:20	13	5	6	0	17:00	5	10	1	1
13:30	3	4	0	0	17:10	11	10	6	3

Table H-3. Breakdown of editing into 10-minute intervals. This breakdown is particularly useful for showing when and how often an instrument malfunctions.

As a test case, we examine the interval from 12:50 Z to 13:00 Z marked with an asterisk in Table H-3. This example is of special interest because it occurred during one of our dual-racetrack maneuvers used in our calibration. For $\epsilon=3$, ϕ_1 is seen to have five bad values while ϕ_2 has only one. Recall that because our prefilter spreads noise to adjacent values, there could be as many as $2 \times 3 = 6$ points that require fixing. A plot of the difference $\phi_1 - \phi_2$ is shown in Fig. H-3 and shows the presence of two large spikes.

In concluding this material we emphasize that errors of this kind are easy to miss in routine analysis, and left undetected, effects can propagate to other parameters. In the present case, errors in pitch are transmitted to computed vertical winds as shown in Fig. H-3; clearly, the 1.5 m/s error shown is intolerable. Note that, to first order, a 1° error in the pitch angle translates to about a 1 m/s error in the vertical wind which is useful as an order-of-magnitude estimate.

Appendix H. Statistical Editing

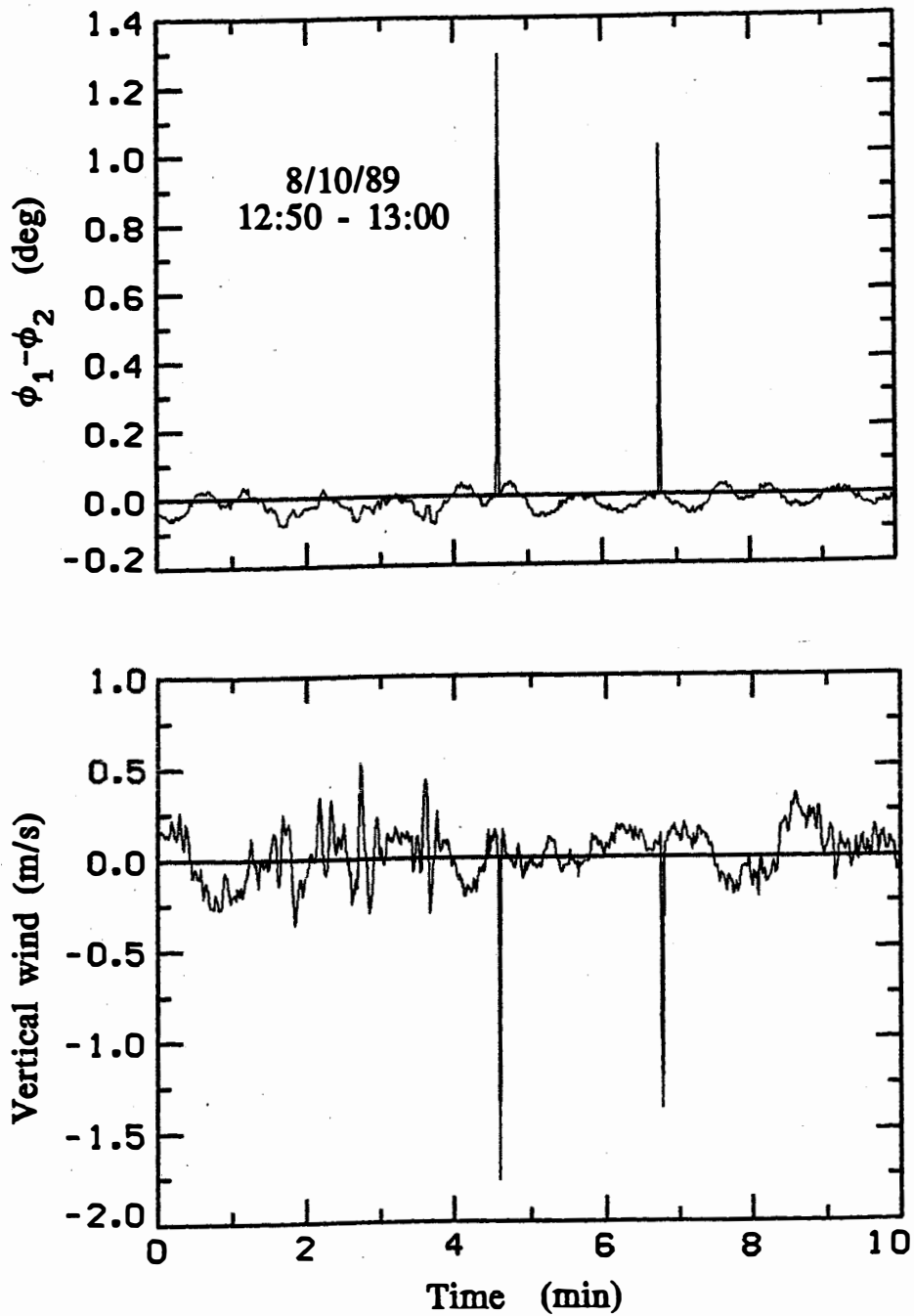


Fig. H-3. The difference between pitch angles measured by two independent INS units (top graph) reveal that one of the units is generating erroneous spikes. These spikes, if undetected, can contaminate computed quantities, such as vertical wind (lower graph). Data taken from N42RF's calibration flight on 8/10/89.

Appendix H. Statistical Editing

```

SUBROUTINE EDIT2(Y1,Y2,N,SD,NBAD1,NBAD2)
C *****JIM LEISE 7/87
C Given two similar types of data arrays Y1(N) and Y2(N), this
C routine edits for flyers(shot noise) and fixes the errors.
C INPUT: Y1(N),Y2(N) = Two similar data arrays (Flags OK).
C SD = Editing parameter (Try 2.0, 2.5, 3.0)
C OUTPUT: NBAD1,NBAD2 = Point-counters for number of fixes.
C Bad values are detected when a difference Y2(K)-Y1(K) varies
C more than SD standard deviations from the mean difference.
C In turn, the value of Y1(K) or Y2(K) that varies most from its
C respective mean is judged as bad and fixed by swapping (mean
C adjusted) values between the arrays.
DIMENSION Y1(N),Y2(N)
DATA FLAG/-1.E+38/

C
NBAD1=0 ! Initialize bad-data counter.
NBAD2=0 ! ...
IF(SD.LE.0.)RETURN ! Silly call.
C.... Compute the (sample) variance of Y2-Y1.
DY=0. ! Initialize mean.
VAR=0. ! Initialize variance.
KOUNT=0 ! Initialize counter.
DO 10 K=1,N ! Compute mean and variance.
IF(Y1(K).EQ.FLAG .OR. Y2(K).EQ.FLAG)GO TO 10
KOUNT=KOUNT+1 ! Update counter.
DK=Y2(K)-Y1(K) ! Get difference.
DY=DY+DK ! Difference sum.
VAR=VAR+DK**2 ! Second-moment sum.
10 CONTINUE
IF(KOUNT.LE.N/2)RETURN
DY=DY/KOUNT ! Sample mean.
VAR=(VAR-KOUNT*(DY**2))/(KOUNT-1.) ! Sample variance.
ERR=SD*SQRT(ABS(VAR)) ! Error tolerance.
IF(ERR.LE.0.)RETURN ! Constant data.

C
C.... Get Y1 & Y2 averages free of errors.
S1=0. ! Initialize Y1 sum.
S2=0. ! Initialize Y2 sum.
KOUNT=0 ! Initialize counter.
DO 20 K=1,N
IF(Y1(K).EQ.FLAG .OR. Y2(K).EQ.FLAG)GO TO 20
DK=Y2(K)-Y1(K) ! Get current difference.
IF(ABS(DY-DK).LE.ERR)THEN ! Statistical test.
KOUNT=KOUNT+1 ! Update counter.
S1=S1+Y1(K) ! Accumulate Y1 sum.
S2=S2+Y2(K) ! Accumulate Y2 sum.
ENDIF
20 CONTINUE
IF(KOUNT.LE.1)RETURN
AVE1=S1/KOUNT ! Get mean of good Y1's.
AVE2=S2/KOUNT ! Get mean of good Y2's.

```

(continued on next page)

Appendix H. Statistical Editing

```
C
C.... Do the fixes.
      DY=AVE2-AVE1                ! Get mean difference.
      DO 30 K=1,N
      IF(Y1(K).EQ.FLAG .OR. Y2(K).EQ.FLAG)GO TO 30
      DK=Y2(K)-Y1(K)              ! Get current difference.
      IF(ABS(DY-DK).LE.ERR)GO TO 30 ! Statistical test.
      IF(ABS(Y1(K)-AVE1) .LT. ABS(Y2(K)-AVE2))THEN
      Y2(K)=Y1(K)+DY              ! Y2 bad, adjust.
      NBAD2=NBAD2+1              ! Update diagnostic counter.
      ELSE
      Y1(K)=Y2(K)-DY              ! Y1 bad, adjust.
      NBAD1=NBAD1+1              ! Update diagnostic counter.
      ENDIF
30 CONTINUE
C
      END
```

Figure H-4. FORTRAN listing of subroutine for two-parameter statistical editing. Here SD corresponds to ϵ in the text. Note that this code allows for flags (marking missing data). Also, counters NBAD1 and NBAD2 of bad data are returned. A flow chart of this algorithm is given in Fig.H-1.

REFERENCES

Axford, D. N., 1968: On the accuracy of wind measurements using an inertial platform in an aircraft, and an example of a measurement of the vertical mesostructure of the atmosphere. *J. Appl. Meteor.*, **7**, 645-666.

Broxmeyer, C., 1964: *Inertial Navigation Systems*, McGraw-Hill, 254 pp.

Brown, E. N., C. A. Friehe, and D. H. Lenschow, 1983: The use of pressure fluctuations on the nose of an aircraft for measuring air motion. *J. Climate Appl. Meteor.*, **22**, 171-180.

———, E. N., 1988: Position error calibration of a pressure survey aircraft using a trailing cone. NCAR Tech. Note NCAR/TN-313+STR, National Center for Atmospheric Research, Boulder, Colorado.

Crawford, T. L., R. T. McMillen, and R. J. Dobosy, 1990: Development of a "generic" mobile flux platform with demonstration on a small airplane. NOAA Tech. Memo. ERL ARL-184, U.S. Dept. of Commerce, NOAA, Environmental Research Laboratories, Boulder, CO, 81 pp.

———, and R.J. Dobosy, 1992: A sensitive fast-response probe to measure turbulence and heat flux from any airplane. *Boundary-Layer Meteorology* **59**, 257-278.

DeLeo, R. V., and Hagen, F. W., 1977: Wind tunnel calibration of Rosemount Model 855EB-1 aerodynamically compensated pitot-static tube for NOAA. Rosemount report 27722, 19 February 1977, Rosemount, Inc.

DeLeo, R. V., and Hagen, F. W., 1978: The use of multiple output aerodynamically compensated sensors on aircraft. Rosemount report 37812, Rosemount, Inc.

Denaro, R.P., and G.J. Geier, 1988: GPS/inertial navigation system integration for enhanced navigation performance and robustness. The NAVSTAR GPS system, AGARD-LS-161, 7-1 to 7-12.

References

- Dutton, J. A., 1976: *The Ceaseless Wind*, McGraw-Hill, 579 pp.
- Hamming, R.W., 1977: *Digital Filters*, Prentice-Hall, 226 pp.
- Graham, R. J., 1963: Determination and analysis of numerical smoothing weights. NASA Tech. Rep. TR-179, Office of Technical Services, Dept. of Commerce, Washington DC, NTIS N65-13828.
- Gray, W.M., 1965: Calculations of cumulus vertical draft velocities in hurricanes from aircraft observations. *J. Appl. Meteor.*, **4** 463-474.
- Jorgensen, D.,P., E.J. Zipser, and M.A. LeMone, 1985: Vertical motions in intense hurricanes. *J. Atmos. Sci.*, **42**, 839-856.
- , and M. A. LeMone, 1989: Vertical velocity characteristics of oceanic convection. *J. Atmos. Sci.* **46**, 621-640.
- Landau, L. D., and E. M. Lifshitz, 1959: *Fluid Mechanics*, Pergamon Press, 536 pp.(English translation, J. B. Sykes).
- Leach, B. W., and J. I. MacPherson, 1991: An application of Kalman filtering to airborne wind measurement. *J. Atmos. Ocean. Tech.*, **8**, 51-65.
- Leise, J.A., 1981: A multidimensional scale-telescoped filter and data extension package. NOAA Tech. Memo. ERL WPL-82, U.S. Dept. of Commerce, NOAA, Environmental Research Laboratories, Boulder, CO, 20 pp.
- Lenschow, D.H., 1972: The measurement of air velocity and temperature using the NCAR Buffalo Aircraft Measuring System. NCAR, NCAT-TN/Edd-74, 39 pp.
- , 1986: Aircraft measurements in the boundary layer. *Probing the Atmospheric Boundary Layer*, Lenschow, D. H., Ed. Amer. Meteor. Soc., 39-55.
- Masters, J.M., and J.A. Leise, 1993: Correction of Inertial Navigation with LORAN-C on NOAA's P-3 aircraft. *J. Atmos. Ocean. Tech.*, in press.

Appendix I

Papers citing Leise and Masters before 2013

- Dobosy, R., et al., 2013: Calibration and quality assurance of an airborne turbulence probe in an aeronautical wind tunnel. *Journal of Atmospheric and Oceanic Technology*, **30** (2), 182–196.
- Eckman, R., 1999: Computation of flow angles and dynamic pressure on a BAT Probe. ARL/FRD contribution, Available on web, NOAA, Air Resources Laboratory, Field Research Division, 4 pp., Idaho Falls (Idaho), USA. URL <http://www.noaa.inel.gov/Personnel/Eckman/docs/flowangles.pdf>.
- French, J., G. Crescenti, and T. Crawford, 2000: Data report: Long-EZ (N3R) participation in the 1999 Shoaling Waves Experiment (SHOWEX). Tech. rep., Air Resources Laboratory, NOAA.
- Giebel, G., U. Paulsen, J. Reuder, A. la Cour-Harbo, C. Thomsen, J. Bange, and M. Buschmann, 2009: Autonomous aerial sensors for wind power meteorology. *System*, **32** (2), 573–585.
- Hill, T., R. Wade, and J. Moncrieff, 2009: A simple but effective approach for calibrating the best-air-turbulence probe for aircraft windspeed measurements, URL <http://www.sages.ac.uk/home/>

homes/thill/Hill_JAOT_2009.pdf, available from University of Edinburgh UK.

Isaac, P., J. McAneney, R. Leuning, and J. Hacker, 2004: Comparison of aircraft and ground-based flux measurements during OASIS95. *Boundary-layer meteorology*, **110** (1), 39–67.

Metzger, S., W. Junkermann, K. Butterbach-Bahl, H. Schmid, and T. Foken, 2011: Corrigendum to “Measuring the 3-D wind vector with a weight-shift microlight aircraft” published in *Atmos. Meas. Tech.*, 4, 1421–1444, 2011. *Atmospheric Measurement Techniques*, **4** (7), 1515–1539.

van den Kroonenberg, A., T. Martin, M. Buschmann, J. Bange, and P. Vörsmann, 2008: Measuring the wind vector using the autonomous mini aerial vehicle M2AV. *Journal of Atmospheric and Oceanic Technology*, **25** (11), 1969–1982.

Vellinga, O. S., R. J. Dobosy, E. J. Dumas, B. Gioli, J. A. Elbers, and R. W. A. Hutjes, 2013: Calibration and quality assurance of flux observations from a small research aircraft. *Journal of Atmospheric and Oceanic Technology*, **30** (2), 161–181.

Zulueta, R., W. Oechel, H. Loescher, W. Lawrence, and K. T. Paw U, 2011: Aircraft-derived regional scale CO₂ fluxes from vegetated drained thaw-lake basins and interstitial tundra on the Arctic Coastal Plain of Alaska. *Global Change Biology*, **17** (9), 2781–2802.

Zulueta, R. C., W. C. Oechel, J. G. Verfaillie, S. J. Hastings, B. Gioli, W. T. Lawrence, and K. T. Paw U, 2013: Aircraft regional-scale flux measurements over complex landscapes of mangroves, desert, and marine ecosystems of Magdalena Bay, Mexico. *Journal of Atmospheric and Oceanic Technology*, 1266–1294, doi:10.1175/JTECH-D-12-00022.1.